PROPERTIES AND APPLICATIONS IN CHEMICAL SENSING: MODIFICATION OF POROUS SILICON INTERFACES

A Thesis
Presented to
The Academic Faculty

by

Caitlin Baker

In Partial Fulfillment
of the Requirements for the Degree
Doctor of Philosophy in the
School of Physics

Georgia Institute of Technology
December 2015

PROPERTIES AND APPLICATIONS IN CHEMICAL SENSING: MODIFICATION OF POROUS SILICON INTERFACES

Approved by:

Professor James L. Gole, Advisor
School of Physics
Georgia Institute of Technology

Professor Jennifer Curtis
School of Physics
Georgia Institute of Technology

Professor Peter Hesketh
School of Mechanical Engineering
Georgia Institute of Technology

Professor Flavio Fenton
School of Physics
Georgia Institute of Technology

Professor Dragomir Davidovic
School of Physics
Georgia Institute of Technology

Date Approved: August 4 2015

To my husband,

Andrew Baker,

for his support and encouragement.

ACKNOWLEDGEMENTS

Firstly I would like to thank my advisor, Prof. James Gole for his encouragement and guidance throughout my graduate work. I also thank Prof. Peter Hesketh for allowing me the use of his laboratory space and equipment as well as for many insightful discussions on gas sensor technology. I want to acknowledge and thank Neil Hardy for his extensive work and collaboration on redesigning the sensor contact apparatus. I would like to thank Arthur Lin for helping to collect gas sensing data, organizing the data filing system, as well as contributing many hours discussing and developing theoretical sensor models. I thank my committee members, Prof. Hesketh, Prof. Davidovic, Prof. Curtis, and Prof. Fenton, for reading this dissertation and providing valuable feedback. Finally, I thank my parents, Cathy and Kevin Smith, and my husband, Andrew Baker, for their constant support.

TABLE OF CONTENTS

LIST OF TABLES

LIST OF FIGURES

SUMMARY

Sensor and microreactor technology plays a major role in the detection, monitoring, and transformation of materials at interfaces. We study the dynamics of acid/base interaction of gas analytes with the majority charge carriers of nanostructure modified extrinsic semiconductor interfaces. Nanostructures are deposited on highly sensitive surface layers, created by forming an array of nanopore-coated micropores on p- or n- type silicon semiconductors. The balance of physisorption and chemisorption is achieved by following the tenants of the inverse hard and soft acid/base interaction model to select metal oxide nanostructures for deposition.

Chapter 1 introduces the concept of chemical sensors and provides a rationale for the research outlined in this thesis. Chapter 2 provides the necessary background on porous silicon (PSi), the key material utilized for fabrication of highly sensitive chemical sensors, and an overview of the current applications of PSi devices. The fabrication and characterization methods of the PSi sensors are outlined in Chapter 3. An extended discussion of these topics are published in the following:

- C. Baker and J. L. Gole, "Interface Modifications of Porous Silicon for Chemical Sensor Applications," *JSM Nanotechnol Nanomed* **2**, 1021 (2014). Reproduced with permission, Creative Commons License.

- C. Baker and J. L. Gole, "PSi-Based Microreactors," Copyright 2016. From *Porous Silicon: Opto- and Microelectronic Applications*, edited by G. Korotcenkov. Reproduced by permission of Taylor and Francis Group, LLC, a division of Informa plc.

Chapter 4 explores a simulated model of the PSi sensing interface, in the interest of defining the physical and chemical processes associated with the interaction of the

PSi surface and select inorganic gas analytes. Chapter 5 provides an in depth study of these interactions. Sensitivity enhancements of the PSi sensor response to low concentrations H_2S and CO, aligned with the recently developing Inverse Hard/Soft Acid/Base (IHSAB) concept are presented. Also, a study of the selectivity of the PSi sensor to inorganic analytes in the presence of volatile organic chemicals is presented. These results are published in the following:

- C. Baker, W. Laminack, and J. L. Gole, "Sensitive and selective detection of H2S and application in the presence of toluene, benzene, and xylene," *Sensors and Actuators B: Chemical* **212**, 28 (2015). Reprinted with permission from Elsevier.

- C. Baker and J. L. Gole, "Selective detection of the inorganic NO_x, SO_2, and H_2S in the presence of volatile BTEX contaminants toluene, benzene, and xylene," *Air Quality, Atmosphere & Health*, 1-9 (2015). With kind permission from Springer Science+Business Media.

Chapter 6 introduces two proof-of-concept studies of using the PSi sensor, and the accompanying IHSAB model, as an interfacial dynamics analysis device. First, the PSi sensor is examined as a support for magnetic materials and the magnetically enhanced inorganic gas sensing is discussed. Second, the interactions of Group IIA metal decorated PSi sensors with the inorganic analytes NH_3 and NO are utilized to explore the chemical states of the deposited materials. These studies are published in the following journal articles:

- C. Baker, W. Laminack, T. Tune, and J. Gole, "Magnetically induced enhancement of reversibly responding conductometric sensors," *Journal of Applied Physics* **115**, 164312 (2014). Reprinted with permission. Copyright 2014, AIP Publishing LLC.

- T. C. Tune, C. Baker, N. Hardy, A. Lin, T. J. Widing, and J. L. Gole, "Formation of nanostructured Group IIA metal activated sensors: The transformation of Group IIA metal compound sites," *Applied Surface Science* **337**, 216 (2015). Reprinted with permission from Elsevier.

Extending the application of the PSi sensors to the identification of organic solvents, Chapter 7 presents a study of impedance spectroscopy of the PSi interface. An equivalent circuit model is developed for both n-type and p-type PSi sensors allowing an exploration of the physical and chemical changes of the sensing interface upon exposure to various organic solvents. The changes to the individual equivalent circuit elements are monitored and compared. This allows for a calculation of changes to the circuit elements as a function of time to view how the organic solvents interact during absorption and evaporation phases.

CHAPTER I

INTRODUCTION

Chemical sensors are devices that undergo a measurable physical change upon exposure to a particular gas phase or liquid phase analyte. A complete sensor device both interacts with the analyte species (recognition) and translates the response corresponding to this interaction into a measurable quantity (transduction) [18]. Ideal sensors are those that exhibit a change proportional to the concentration of the analyte, are rapidly responding, and are reversible. Significant resources have been expended by both academic and national research labs on developing sensors with these ideal characteristics, with an emphasis on enhancing both sensitivity (a larger response to lower analyte concentrations) and selectivity (the ability of a sensor to detect and identify an analyte in the presence of other species) [13,163,187]. Chemical sensors offer an alternative to traditional analytical methods such as spectrometry, chromatography, and biochemical techniques as they are designed to be inexpensive, mobile, simple to use and to repair. The development of chemical sensors is a multidisciplinary endeavor, requiring expertise in fields such as physics, chemistry, computer science, electrical engineering, and biology. Major research challenges in the field, such as species characterization against complex background environments, sensitivity and selectivity at ppb concentrations, and complete electronic nose (e-nose) devices, necessitate a better understanding of bulk and surface properties of gas sensing materials, better design of integrated electronics, and advanced statistical and data analysis methods for sensing arrays.

There is an ever-increasing demand for sensitive and selective gas sensing with applications in environmental air quality and pollution monitoring, occupational health

and safety, industrial manufacturing process monitoring, agriculture, automotive exhaust monitoring, and air-conditioning of enclosed spaces, such as airplanes and spacecraft [32,67,68,101,138]. Gas sensors also have enormous potential in the health care industry, as breath analysis can be used for rapidly accessed non-invasive disease detection and point-of-care applications [18,101,182,197,221,286].

In 1970, the United States Congress established the Environmental Protection Agency (EPA) and the Clean Air Act Amendments (CAAAs), which were subsequently revised and strengthened in 1977 and 1990 [106]. In 1996, the European Council created a series of Directives to assess and manage air quality [19]. The Occupational Safety and Health Administration (OSHA), founded in 1970, has set personal exposure limits (PELs) for air contaminants including volatile organic compounds such as BTEX (benzene, toluene, ethylbenzene and xylene), ethanol, methanol, propanol, and methane, and inorganic pollutants such as ammonia carbon dioxide, carbon monoxide, hydrogen sulfide, sulfur dioxide, nitrogen oxides, and phosphine. These limits are summarized in Table A.4. Consequently, a major focus of research involves the development of a low cost, low power, sensitive, ambient air sensor array suitable for identification of the quality of breathable air in the environment and for detection of hazardous gases and odors and, if necessary, their liquid precursors [68,118].

Nitrogen oxides (NO, NO_2, NO_x) are toxic gases associated with air pollution, combustion, and respiratory disease [68,197]. Monitoring of automotive and industrial combustion exhaust, responsible for acid rain, photochemical smog, and corrosion, involves the detection of NO_x and SO_2 [68]. There is also an increasing demand for the detection of fuel combustion products CO (toxic and odorless) and CO_2 (a global warming factor) [68]. Phosphine (PH_3), an extremely toxic gas, is used in agriculture for fumigation and also represents an unfortunate byproduct in the production of methamphetamines [26,32].

Exhaled nitric oxide is of particular importance in the health industry, specifically diagnostics. NO is correlated with asthmatic conditions such as airway inflammation and has the potential to provide rapidly accessed noninvasive disease detection [286]. Additionally, an asthmatic attack produces large quantities of NO, which can combine with O_2 to produce NO_2. NO is also a dominant indicator for pulmonary inflammation related to type II diabetes [209]. As such, a mass produced portable sensor device, capable of detecting separately small changes in NO and NO_2 concentrations in the breath, could dramatically improve in-home and point-of-care testing.

The air quality in enclosed livestock barns can strongly affect both the health of the animals as well the health of human operators in the industry [83, 260]. The decomposition of nitrogenous compounds in manure, represented by non-degraded proteins, produces ammonia (NH_3) [45]. In poultry operations, specifically in broiler chicken houses, NH_3 polluted air can reach high enough concentrations to cause Chronic Respiratory Disease in chickens and even death [260]. Workers reported experiencing eye and upper respiratory irritation in chicken houses [83,230]. This suggests that the ability to detect NH_3 selectively at low ppm levels at room temperature can represent a valuable asset where farm animals are sequestered.

Hydrogen sulfide (H_2S) is a toxic and flammable gas used as a process gas in many chemical research and industrial applications. H_2S is found naturally in hydrocarbon reserves, which include oil reservoirs [62, 194]. Similar to NO, H_2S is recognized as a signal molecule in biological processes such as a neuromodulator, neuroprotectant, and smooth muscle relaxation signaling [126, 137]. OSHA recognizes that acute symptoms of H_2S exposure include nausea, headaches, bronchial constriction, and drowsiness. Prolonged exposure can cause pulmonary edema, serious eye damage, unconsciousness, and even death. H_2S is particularly dangerous analyte because, while the odor threshold for detection in humans is as low as 0.1 ppm, the loss of

sense of smell due to olfactory fatigue or paralysis occurs at concentrations well below toxic concentrations [62]. Therefore, detection of low ppm levels of H_2S is a significant motivator for the development of chemical sensors. Of equal importance is the selective detection of H_2S in the presence of volatile organic compounds, especially the BTEX compounds toluene, benzene, and xylene [62]. A significant source of anthropogenic H_2S is as a by-product of the combustion of sulfur-containing fuels, the purification of natural gas, and the refinement of crude oil [31, 58]. As a result, stringent regulations are in place to control sulfur air pollution from fuels [31]. For instance, the United States Code of Federal Regulations lists a maximum allowed sulfur content of 15 ppm for diesel fuel refiners [1].

Chemical sensors are also developed for the purpose of detecting volatile organic compounds (VOCs), in both liquid and gas phase. The sources of VOCs are both natural and anthropogenic; a majority (over 90%) of VOCs result from transportation, solvent use, vegetation, production processes, and combustion power [39, 72]. Organic solvents are used in many applications including anesthetics in the medical industry, research laboratories, dry cleaning, house and car painting, and common consumer products such as laundry products, personal care products, cleaning supplies, and air fresheners [37, 108, 239, 246, 285]. Solvents represent a major contaminant of ground water due to both ubiquitous use across so many industries and indiscriminant disposal. Liquid-phase detection and identification is thus necessary for monitoring and evaluating treatment methods such as phytoremediation [246]. In indoor settings, building materials, indoor furnishings, and chemical products release VOCs [235, 257]. In particular, the BTEX compounds represent a major environmental concern in urban areas. Common urban sources of BTEX compounds include fuel stations, service stations, and automotive emissions [39]. Exposure to VOCs, especially benzene, ethylbenzene, and toluene, even below recommended levels, represent significant risk factors for the development of childhood asthma [227]. Benzene is a

known carcinogen, toluene may affect the reproductive and central nervous systems, and the xylenes are known for respiratory and neurological effects [62].

Analytical techniques for chemical gas sensing include Fourier Transform Infrared Spectroscopy (FTIR), gas chromatography (GC), and mass spectrometry (MS). Gas chromatographs separate gaseous species by passing analyte samples through a column. These analytes will stream at different rates depending on their physical and chemical characteristics. The separated species can then be identified by a mass spectrometer, where an applied magnetic field will characteristically deflect a molecule's path depending on its mass and charge. GC-MS is a highly accurate method for species identification. FTIR, which collects IR absorption spectra of gaseous samples, is advantageous for monitoring pollutant gases as spectra can be collected and measured *in-situ*, indoors or outdoors. Large libraries of FTIR spectra exist for various compounds, including over 130 different pollutants [67]. However, GC, MS, and FTIR suffer from complexity of operation, high cost of operation and maintenance, and are bulky and non-mobile.

Metal oxide (MOX) semiconductors have been extensively studied as chemical gas sensors since the first report of a hydrogen-sensitive MOX semiconductor field effect transistor in 1975 [129,173,245,269]. MOX gas sensors, which are well known for their variable electrical conductivity in the presence of different gas atmospheres, are widely used as an alternative to the above mentioned analytical methods due to advantages such as compact size, simple electronics, and low cost of production [50, 68, 245]. Typical MOX sensors are in the form of thin or thick film SnO_2, TiO_2, WO_3, ZnO, Fe_2O_3, and In_2O_3 [50, 68]. Selectivity, a common problem for MOX sensors, can in some cases be potentially addressed by the addition of noble metals such as Pd, Pt, Au, and Ag [50]. Reduction of the crystallite size through an exploration of nanostructured MOXs, and thus a reduction in grain size, also improves sensor performance [50, 67, 245]. However, MOX sensors suffer from several key disadvantages;

MOX sensors must be operated at elevated temperatures of 150 °C to 500 °C and lack compatibility with integrated circuit technology [68,85,110,117,269,284]. As most integrated circuits are built on silicon, MOXs deposited onto silicon wafers can only be heated to around 150 °C [68]. Additionally, selectivity to different gases often requires operating the MOX sensors at different precisely defined temperatures [68, 85, 110].

Porous silicon (PSi) based gas sensors have attracted attention as an alternative to MOX sensors due to their unique combination of advantageous properties [142]. Electrochemically fabricated by anodic etching in an HF solution, PSi features high surface area, luminescence properties, and a chemically active surface. By adjusting the etch parameters, the morphology, pore size, and porosity can be changed and reasonably controlled [236]. PSi is compatible with well-established microfabrication techniques and therefore easily integrated with microelectronic platforms. Additionally, PSi gas sensor devices can be operated at room temperature and do not require a heating element [85, 110]. However, for applications requiring elevated temperature environments, such as identification of combustion products, PSi sensors can operate in a heat sunk configuration [13, 85].

As an analog to chemical sensing, PSi is also a promising material for microreactor technology operating both as a surface-area-enlarger and a heterogeneous catalyst support. Freshly prepared PSi features a hydrogen-terminated surface, which can act as a reducing agent to easily form noble metal catalyst nanoparticles throughout the porous structure [192]. Additionally, deep quantum confinement due to the presence of nanometer-sized features, surface bound fluorophors, and the ability to absorb a broad spectrum of light make PSi an excellent candidate for photocatalysis [164, 217, 244]. As an added benefit for microreactor technology, PSi can serve as a thermal insulation barrier, which allows for local heating [238, 282].

This thesis will discuss design of PSi chemical sensors, the enhancement of the sensitivity and selectivity through metal oxide nanostructure depositions, and probe

the applications of this technology as a tool to explore interface interaction dynamics. Using the nanostructure-directed modification of the Lewis acid/base character of an analyte-extrinsic PSi semiconductor interface, we have developed the ability to control the degree of electron transduction (and therefore energy transfer) between an extrinsic semiconductor interface and interacting analyte gases. Based on the inversion of the hard/soft acid/base theory (HSAB), the careful selection of nanostructure directed modifications can enhance or impair electron transduction, which can be made to precisely control the increase or decrease the sensor response to a given analyte. This concept has led creation of a general road map, the Inverse Hard/Soft Acid Base (IHSAB) concept, for sensor design [94]. Beyond controlling electron transduction as a function of nanostructure deposition [92], in-situ modification of the deposited nanostructures has been explored [146, 151]. We have demonstrated that the change in conductometric response allows a more detailed monitoring of the interaction of various materials deposited to an extrinsic semiconductor interface in contrast to standard characterization methods such as X-ray photoelectron spectroscopy (XPS) and energy dispersive X-ray spectroscopy (EDX). We are now extending the application of PSi sensors to the identification of organic solvents using modifications of impedance spectroscopy. Through the use of an equivalent circuit model [8], we can explore the physical changes of the PSi sensors with a diversity of distinctly interacting metal oxide nanostructure depositions and upon exposure to various organic solvents. Through mobile PSi sensor device development and formulation of a table cataloging materials' effects on interface interactions, we can create a complete interfacial analysis system with applications as a materials characterization tool, a research project starter, and a classroom demonstration of basic and advanced solid state and condensed matter physics concepts.

CHAPTER II

BACKGROUND AND LITERATURE REVIEW

First discovered during an investigation of electropolishing methods for Si, porous silicon (PSi) is formed by electrochemical etching in a solution containing hydrofluoric acid. PSi is generally classified by pore size; micropores or nanopores refer pore diameters below 2 nm, mesopores refer to diameters between 2 nm and 50 nm, and macropores are defined as pores with diameters above 50 nm [142]. However, the morphology of the PSi featured in this thesis consists of hybrid ∼2 µm diameter pores with ∼10 nm diameter porous walls, which will be referred to as micro- or nanopores.

PSi can be fabricated from p-type or, under illumination, n-type silicon and the morphology, pore size, pore depth, and porosity can be controlled by adjusting etch parameters such as current density, etch duration, and etch solution. Figure 2.1 shows a scanning electron microscope (SEM) cross-sectional image comparing p-type and n-type PSi morphology. PSi morphology also depends on the bulk Si properties such as doping level, resistivity of the Si wafer, and crystal orientation.

PSi is an extremely versatile material with a wide range of applications including (but not limited to) optoelectronics, magneto-optical devices, microelectronics, microreactors, biomedical and pharmaceutical research, photovoltaics, chemical filtering and chemical sensing [104, 110, 142, 238, 282]. PSi can also be utilized as a template for the formation of nanostructured materials [104]. In particular, PSi is a great material for chemical sensing featuring an ideal combination of a large internal surface area as high as 500 m^2 cm^{-2}, a crystalline structure perfectly compatible with integrated circuit technology, and ease of fabrication in a range of morphologies [104,142]. Additionally, PSi is a desirable sensor material as the transduction process can use

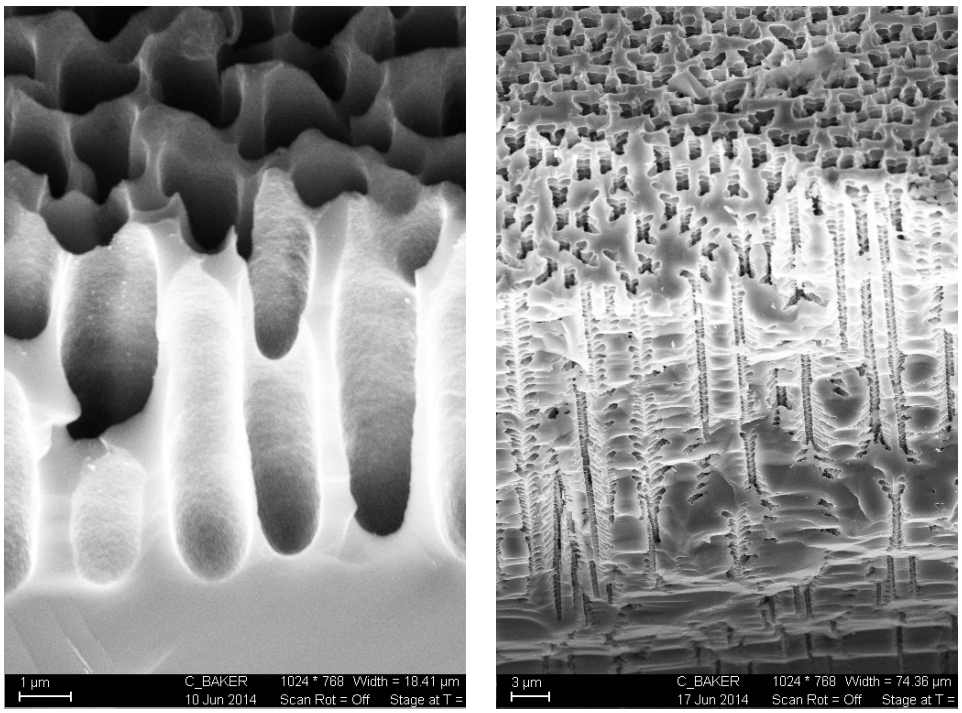

(a) (b)

Figure 2.1: SEM micrograph of a cross-sectional view of PSi layers formed from (a) p-type and (b) n-type silicon. The samples are beveled at 45 deg. C. Baker, unpublished.

both conductometric properties and optical properties [8, 85, 128, 142]. As a result, PSi offers the possibility to mass produce compact, low-cost, easy-to-use, and fully integrated chemical sensor arrays.

2.1 History of Porous Silicon

Porous silicon (PSi) was discovered in 1956 at Bell Labs during research on electropolishing Si in a hydrofluoric acid (HF) solution [258, 259]. The attempted electropolish produced a matte black, brown or red stain assumed to be a thick layer of Si suboxide [55, 258]. In 1957, Fuller and Ditzenberger [78] reported the fabrication of similar matte films in $HF-HNO_3$ solutions in the absence of an applied electrical bias. In 1958, Turner at Bell Labs [255] determined the critical minimum current density required to electropolish Si. Dissolution of Si at current densities below the critical value would form a thick stain layer instead. Turner also suspected that, due to the absence of discontinuity in the cell resistance during the layer formation, the layer was likely porous [255]. However, the porous nature of the film was not investigated further or confirmed until over a decade after this original suggestion [272]. Later, Archer [9] performed additional detailed studies of the mysterious colored stain films grown on Si during etching in $HF-HNO_3$ solutions and determined that the film consisted of either elemental silicon or silicon hydride for p-type or n-type silicon respectively. The stain films first became known as PSi almost ten years later when Watanabe et al. [271, 272] reported the isolation by oxidized porous silicon (IPOS) technique for bipolar integrated circuits. PSi was formed on both p- and n-type silicon and subsequently oxidized to create an insulating film. For the first time, a relationship between the porous layer thickness and anodization time was reported as well as a relationship between current density and layer growth rate [271].

The application of PSi as a dielectric isolation material was explored in the late

1970s [10, 125, 261]. The development of the full isolation by porous oxidized Si (FIPOS) process [124] stimulated increased interest in PSi for silicon-on-insulator (SOI) applications in integrated circuit technology [22, 251, 253]. During an investigation of PSi properties for SOI applications, Pickering et al. reported PSi photoluminescence spectra with band energies within the visible light range at 4.2 K [211]. However, it was Canham's seminal paper in 1990 on the photoluminescence (PL) of PSi in the visible spectrum at room temperature that generated a dramatic rise in the popularity of PSi research [35]. Canham ascribed the red PL of mesoporous silicon to quantum size effects. The PL properties were supported by the independent research of Lehman and Gösele a year later by comparing the increased band gap of PSi to that of bulk Si, which was also attributed to quantum size effects [157]. Subsequent research suggested that the wavelength of the emitted light might depend on porosity; porosity above 70% emits shorter wavelength green/blue light and porosity around 50% emits longer wavelength red light [35, 142, 157]. However, this relationship was shown to be superficial.

The mechanism for producing PL emission in PSi has been a subject of controversy stimulating numerous research investigations [215]. Various suggested mechanisms range from radiative recombination of electrons and holes that are quantum confined on nanostructures [55, 267] to suggesting that small non-passivated Si crystallites with surface states are responsible for the PL effect [140]. However, in contrast to the theories focussed on the semiconductor size effects, Gole et al. [89–91, 99] demonstrated substantial evidence that PL was actually due to surface conditions. They explained that surface-bound emitters or fluorophors are the dominant source for PSi PL, which was supported by an extensive set of experimental results correlated with time-dependent density functional theory (TD-DFT) calculations [89, 91, 99]. This explanation was further supported by the observation of PL after only 10 s of PSi

etching, a time scale much too short for any significant pore formation but sufficient for the formation of surface-bound emitters [64]. For many years, worldwide excitement surrounded research on the phospholuminescence of PSi with significant interest in potential applications in optoelectronics and the potential for a fully integrated light-emitting diode [49, 215].

Following the exploration of PL mechanisms in PSi, numerous research endeavors were conducted on the various parameters of PSi that are sensitive to the surrounding atmosphere. One of the earliest applications of PSi as a sensor was as a humidity sensor that experienced a measurable change in conductance with changing humidity [70,179]. The capacitance of p-type PSi was found to increase by 440 % when exposed to 0 % to 100 % relative humidity [70]. The large surface area sensitive to adsorption and capillary condensation and the transduction of that sensitivity through optical and electrical characteristics combine to create highly effective sensor systems [55, 70, 180]. With the advent of numerous studies concerning the feasibility for the detection low concentrations of analyte gases, PSi has been rapidly becoming a pivotal material of interest in the chemical sensing field. PSi has been demonstrated as an effective sensor for NO_2 in the low-ppm regime [20, 21, 28, 181, 202] as well as other harmful atmospheric pollutants [163, 197, 198, 233]. Currently, continued PSi sensor research focuses on the ability to control and transform the PSi interface for the purpose of increased sensitivity and selectivity, which is fundamental for creating an effective chemical sensor [13, 27, 92, 128, 142, 167, 197].

2.2 Intrinsic and Extrinsic Semiconductors

To understand the details of PSi formation and applications, the properties of semiconductors must first be discussed. Intrinsic (pure) semiconductors are defined by conductivity that lies between that of conductors and insulators. The chemical potential, or "Fermi level," sits in the band gap between the valence and conduction

band. The existence of the band gap makes for a poor conductor up to moderate temperatures. While charge carrier population increases with temperature, the introduction of impurities is generally a more useful method of increasing conductivity [226]. In reality, all semiconductors have impurities and/or defects, and it is the extrinsic properties of these impurities that make them useful for electronic devices [176].

For semiconductors of elements from the tetravalent group IV elements of the Periodic Table (such as silicon and germanium), trivalent elements from group III and pentavalent elements from group V can be impurity dopants [226]. By doping silicon with a group V element, such as phosphorus, the dopant atom replaces a silicon atom in the crystal lattice. As phosphorous has five valence electrons, compared to the four valence electrons of the silicon atom it replaced, each group V dopant atom will contribute one extra weakly bound electron. The energy levels for these extra electrons lie slightly below the conduction band. Since at even moderate temperatures the electrons are easily excited into the conduction band, the energy levels are termed *donor levels* and group V dopants are labelled *donors*. As a result of the electrons excited from the donor levels into the conduction band, the majority charge carriers of this type of semiconductor are electrons. Therefore, extrinsic semiconductors with donor impurities are referred to as *n-type*, after the negative charge of the majority charge carriers. At high enough temperatures to excite electrons from the valence band, minority charge carriers, holes, are formed [226]. The band structure of an n-type semiconductor at 300 K is shown in Figure 2.2a. Note the large carrier concentration of electrons (red shaded region) in comparison with the concentration of holes (blue shaded region).

In contrast, by doping silicon with an element with one less valence electron, such as boron, an electron vacancy is created bound to the dopant atom. It is important to note that, similar to the extra weakly bound electron in donor atoms, the vacancy is not a charge carrier. However, as the energy level of the vacancies lie just above

the valence band, an electron from a neighboring atom can be easily excited into the vacancy, creating a hole in the valence band. Therefore, the trivalent impurity levels are called *acceptor levels* and the impurities are referred to as *acceptors*. An analogous description of this process is considering the vacancy as a weakly bound hole that can be 'excited' into the valence band. The majority charge carriers are positively charged holes, and thus extrinsic semiconductors with acceptor impurities are called *p-type*. Electrons excited to the conduction band are considered the minority charge carriers [226]. Figure 2.2c demonstrates the band structure and carrier concentrations for p-type semiconductors.

2.2.1 Carrier concentrations and conductivity

The density of states, Fermi distribution, and carrier concentrations of intrinsic and n- and p-type extrinsic semiconductors at 300 K are shown in Figure 2.2. The Fermi distribution is described by the Fermi-Dirac distribution, or Fermi function, at thermodynamic equilibrium,

$$f(\mathcal{E}) = \frac{1}{1 + \mathrm{e}^{(\mathcal{E}-\mu)/k_B T}} \tag{2.1}$$

where k_B is the Boltzmann constant, T is the temperature, and μ is the chemical potential or "Fermi level." The Fermi distribution gives the probability that a state at energy E is populated at thermodynamic equilibrium. At the energy of the Fermi level, $f(\mathcal{E} = \mu)$ is equal to 1/2 for all temperatures.

The density of charge carriers, electrons in the conduction band and holes in the valence band, is the most important property of a semiconductor and depends on the chemical potential, which in turn depends on temperature and extrinsic impurities [11]. Regardless of semiconductor purity, the density of electrons in the conduction

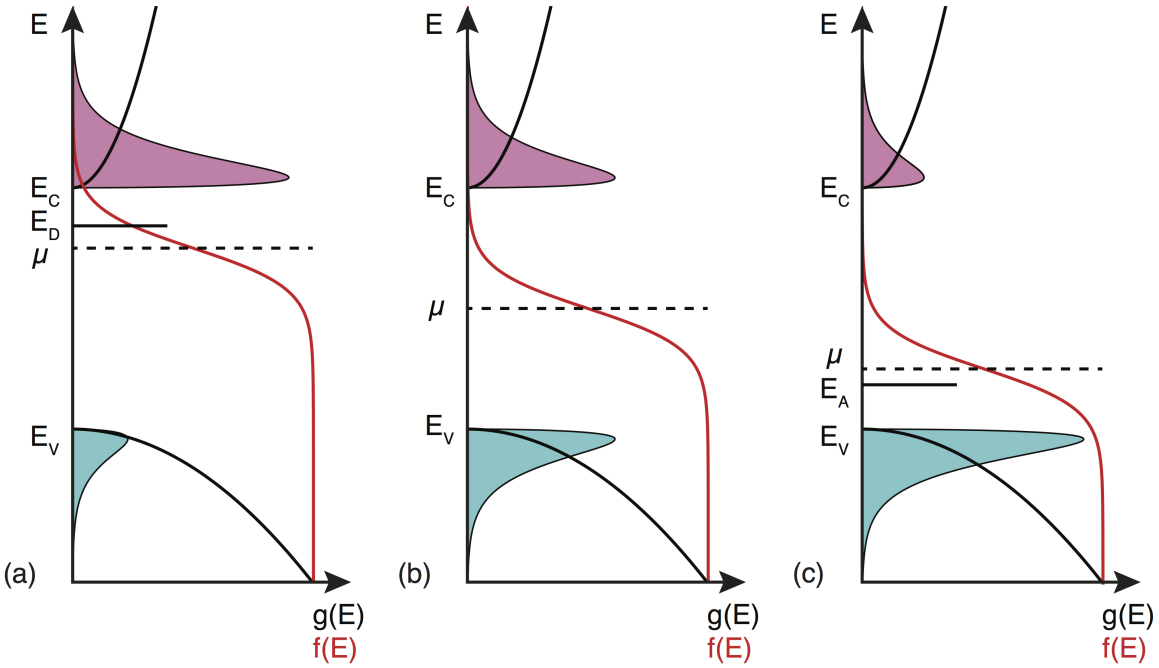

Figure 2.2: Density of states ($g(\mathcal{E})$, black line), Fermi distribution ($f(\mathcal{E})$, red line), and carrier concentrations of electrons ($n_c(T)$, red shaded) and holes ($p_v(T)$, blue shaded) of (a) n-type, (b) intrinsic, and (c) p-type semiconductors at 300 K.

band and holes in the valence band are given by

$$n_c(T) = \int_{\mathcal{E}_c}^{\infty} \mathrm{d}\mathcal{E}\, g_c(\mathcal{E}) f(\mathcal{E})\,, \tag{2.2a}$$

$$p_v(T) = \int_{-\infty}^{\mathcal{E}_v} \mathrm{d}\mathcal{E}\, g_v(\mathcal{E})\,(1 - f(\mathcal{E}))\,. \tag{2.2b}$$

The density of states in the conduction band ($\mathcal{E} > \mathcal{E}_c$) and valence band ($\mathcal{E} < \mathcal{E}_v$) are $g_c(\mathcal{E})$ and $g_v(\mathcal{E})$, respectively. Although information about the impurity levels is required to determine the chemical potential (and thus precise carrier concentrations), useful information is available regardless of the precise value. As long as the chemical potential is far enough away from either the conduction or valence bands,

$$\mathcal{E}_c - \mu \gg k_B T\,, \tag{2.3a}$$

$$\mu - \mathcal{E}_v \ll k_B T\,, \tag{2.3b}$$

then the Boltzmann approximation may be used to solve the previous integrals:

$$f(\mathcal{E}) \approx \mathrm{e}^{-(\mathcal{E}-\mu)/k_B T} \qquad \mathcal{E} > \mathcal{E}_c\,, \tag{2.4a}$$

$$1 - f(\mathcal{E}) \approx \mathrm{e}^{-(\mu-\mathcal{E})/k_B T} \qquad \mathcal{E} < \mathcal{E}_v\,. \tag{2.4b}$$

This condition holds true for a wide range of chemical potential values, even for small energy gaps. Semiconductors that satisfy this condition are called "non-degenerate" and semiconductors that do not satisfy this condition are "degenerate." The density of states for the conduction and valence band can then be written as,

$$g_{c,v}(\mathcal{E}) = \frac{1}{2\pi^2}\left(\frac{2m_{c,v}}{\hbar^2}\right)^{3/2}\sqrt{|\mathcal{E}-\mathcal{E}_{c,v}|}\,, \tag{2.5}$$

where m_c and m_v are the effective masses of electrons and holes. Using the Boltzmann approximation [176, 226], the concentration of charge carriers are

$$n_c(T) = N_c(T)\mathrm{e}^{-(\mathcal{E}_c-\mu)/k_B T}\,, \tag{2.6a}$$

$$p_v(T) = P_v(T)\mathrm{e}^{-(\mu-\mathcal{E}_v)/k_B T}\,, \tag{2.6b}$$

where,

$$N_c(T) = 2\left(\frac{m_c k_B T}{2\pi\hbar^2}\right)^{3/2}\,, \tag{2.7a}$$

$$P_v(T) = 2\left(\frac{m_v k_B T}{2\pi\hbar^2}\right)^{3/2}\,. \tag{2.7b}$$

It is of note that the product of the electron and hole charge carrier densities is independent of the chemical potential. This relation,

$$n_c p_v = N_c P_v \mathrm{e}^{-(\mathcal{E}_c-\mathcal{E}_v)/k_B T} = N_c P_v \mathrm{e}^{-\mathcal{E}_g/k_B T}\,, \tag{2.8}$$

is known as the "law of mass action," which means that knowing the density of one carrier type is sufficient to know the density of the other.

For intrinsic semiconductors, the electron and hole concentrations are the same, or $n_c(T) = p_v(T) \equiv n_i(T)$. The mass action law becomes $n_c p_v = n_i^2$ and, therefore,

the intrinsic carrier concentration can be written as

$$n_i = 2\left(\frac{k_B T}{2\pi\hbar^2}\right)^{3/2} (m_c m_v)^{3/4}\, \mathrm{e}^{-\mathcal{E}_g/2k_B T}\,. \tag{2.9}$$

Using Equation (2.9), the intrinsic electron concentration in silicon ($\mathcal{E}_g = 1.124\,\mathrm{eV}$) at room temperature is approximately $1 \times 10^{10}\,\mathrm{cm}^{-3}$, shown by,

$$n_i = 2\left(\frac{k_B(300\,\mathrm{K})}{2\pi\hbar^2}\right)^{3/2} ((1.09m_0)(1.15m_0))^{3/4} \exp\left(\frac{-1.124\,\mathrm{eV}}{2k_B(300\,\mathrm{K})}\right) \tag{2.10}$$

$$= 1.074 \times 10^{16}\,\mathrm{m}^{-3} \tag{2.11}$$

$$\approx 1 \times 10^{10}\,\mathrm{cm}^{-3}\,, \tag{2.12}$$

where $k_B = 8.62 \times 10^{-5}\,\mathrm{eV/\ K}$, $\hbar = 6.58 \times 10^{-16}\,\mathrm{eV\,s}$, and $m_0 = 5.11 \times 10^5\,\mathrm{eV/c^2}$ [105]. Additionally, the chemical potential can be found by combining Equations (2.6) and (2.9) with the fact that $-n + p = 0$,

$$\mu_i = \frac{\mathcal{E}_v + \mathcal{E}_c}{2} + \frac{3}{4}k_B T \ln\left(\frac{m_v}{m_c}\right)\,. \tag{2.13}$$

However, at $300\,\mathrm{K}$, $m_v \cong 1.06m_c$ and $\mathcal{E}_g \gg k_B T$, so the intrinsic chemical potential can be approximated as:

$$\mu_i = \frac{\mathcal{E}_v + \mathcal{E}_v + \mathcal{E}_g}{2} + \frac{3}{4}k_B T\mathcal{O}(1) \tag{2.14}$$

$$\mu_i = \mathcal{E}_v + \frac{\mathcal{E}_g}{2} + \frac{3}{4}k_B T\mathcal{O}(1) \tag{2.15}$$

$$\mu_i \approx \mathcal{E}_v + \mathcal{E}_g/2\,, \tag{2.16}$$

where $\mathcal{O}(1)$ represents terms with values on the order of 1.

For extrinsic semiconductors with an impurity density Δn, the law of mass action still holds, but now $n_c - p_v = \Delta n$. The charge carrier densities can be written in terms of the intrinsic properties, as

$$n_c(T) = n_i \mathrm{e}^{(\mu-\mu_i)/k_B T}\,, \tag{2.17a}$$

$$p_v(T) = n_i \mathrm{e}^{-(\mu-\mu_i)/k_B T}\,. \tag{2.17b}$$

The Boltzmann approximation is still valid for extrinsic semiconductors, given that certain conditions are met. Recall that in the intrinsic case, as long as $\mathcal{E}_g \gg k_B T$, then μ_i satisfies the non-degeneracy assumption (Equation 2.3), which requires μ_i to reside far from both $\mathcal{E}_c$ and $\mathcal{E}_v$. For extrinsic semiconductors to also satisfy this assumption, the extrinsic chemical potential must also be far away from both $\mathcal{E}_c$ and $\mathcal{E}_v$. This is typically the case, except in cases of extreme extrinsic behavior, in which Δn is many orders of magnitude larger than n_i [11]. This will be demonstrated through a derivation of the a relation between chemical potential and impurity density (Equation 2.20d). In practice, semiconductors are doped with either acceptor or donor impurities and so one carrier type will dominate. To determine the carrier densities and chemical potential as explicit functions of temperature, impurity concentrations must be considered.

The donor and acceptor levels can be estimated by recognizing that the ionization energy of the impurity atom is similar to that of the Coulomb interaction. The key difference is that the interaction is screened by the dielectric constant of the intrinsic semiconductor and the free electron mass is replaced by m^*/m,

$$\mathcal{E} = \frac{m^*}{m}\frac{1}{\epsilon^2} \times 13.6\,\mathrm{eV}\,. \tag{2.18}$$

For p-type silicon doped with boron, the acceptor level resides approximately 0.043 eV to 0.046 eV above the valence band [11, 121, 186] and for n-type silicon doped with phosphorus, the donor level resides approximately 0.043 eV to 0.044 eV below the conduction band [11, 121]. It is important to note that exciting an electron from the donor level into the conduction band or a hole into the valence band from the acceptor level (or "ionizing" an impurity) is possible with significantly less thermal energy than exciting an electron across the intrinsic energy gap. As such, at moderate temperatures (in particular at room temperature, which is of interest for this thesis) almost all of the impurities will be ionized. The additional charge carrier density, Δn, will be

equal to the difference between the density of N_d donor impurities and N_a acceptor impurities. The condition for using the Boltzmann approximation (Equation (2.4)) must be modified to

$$\mathcal{E}_d - \mu \gg k_B T\,, \tag{2.19a}$$

$$\mu - \mathcal{E}_a \ll k_B T\,, \tag{2.19b}$$

which is easily satisfied at the moderate temperatures being considered. Combining Equation (2.17) with $\Delta n = N_d - N_a = n_c - p_v$ allows the chemical potential to be written as an explicit function of temperature:

$$N_d - N_a = n_c - p_v \tag{2.20a}$$

$$= n_i(T)\mathrm{e}^{(\mu-\mu_i)/k_BT} - n_i(T)\mathrm{e}^{-(\mu-\mu_i)/k_BT} \tag{2.20b}$$

$$= n_i(T)\left(\mathrm{e}^{(\mu-\mu_i)/k_BT} - \mathrm{e}^{-(\mu-\mu_i)/k_BT}\right) \tag{2.20c}$$

$$= 2n_i(T)\sinh\frac{\mu-\mu_i}{k_BT}\,. \tag{2.20d}$$

Equation 2.20d demonstrates the condition that if μ_i is far from both $\mathcal{E}_c$ and $\mathcal{E}_v$ (satisfying the non-degeneracy assumption), then μ will be as well, unless $\Delta n = N_d - N_a$ is many orders of magnitude larger than n_i.

The chemical potential, as a function of temperature, is shown in Figure 2.3 for n-type ($N_d > N_a$) and p-type ($N_a > N_d$) semiconductors. For n-type semiconductors, as the temperature rises from 0 K , the chemical potential will gradually lower, first dropping below the donor level as all donor electrons are excited to the conduction band. At high enough temperatures (600 K) , a significant number of electrons have been excited across the gap energy and the carrier densities revert to that of the intrinsic semiconductor, where $n_c \cong p_v$. For p-type semiconductors, a similar process occurs where the number of electrons excited to the conduction band is approximately equal to the total number of holes in the valence band (due to electrons excited to both the conduction band and acceptor level).

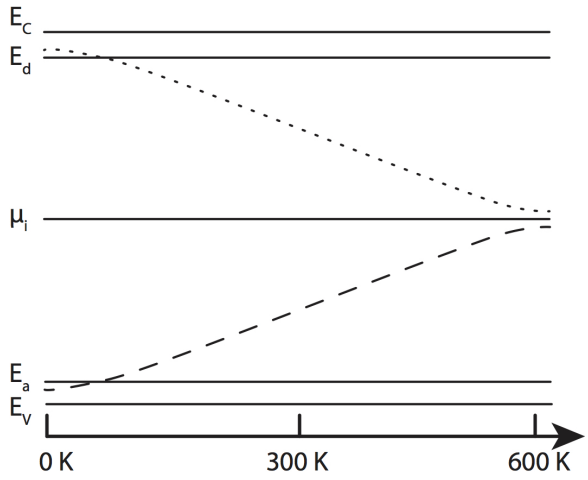

Figure 2.3: $\mu(T)$ for n-type (dotted line) and p-type (dashed line) semiconductors. Note that $\mu \to \mu_i$ at temperatures greater than 600 K (300 °C).

In general, the conductivity of a semiconductor can be written as,

$$\sigma = n_c e \mu_c + p_v e \mu_v \,, \tag{2.21}$$

where μ_c and μ_v are the carrier mobilities in the conduction and valence band. In intrinsic semiconductors, $n_c = p_v = n_i$, and so the conductivity of an intrinsic semiconductor is given by

$$\sigma_i = n_i e \left(\mu_c + \mu_v\right) \,, \tag{2.22}$$

As the mobilities vary with temperature ($\mu_{c,v} \propto T^{-3/2}$) the conductivity can be written as

$$\sigma_i = \sigma_{0i} \mathrm{e}^{-E_g/2k_B T} \,, \tag{2.23}$$

where σ_{0i} is a constant. For extrinsic semiconductors, first let $\mu - \mu_i \equiv e\phi_F$ for convenience, where ϕ_F is the potential difference between the extrinsic and intrinsic Fermi level, so that the carrier densities can be written as simply

$$n_c(T) = n_i \mathrm{e}^{e\phi_F/k_B T} \,, \tag{2.24a}$$

$$p_v(T) = n_i \mathrm{e}^{-e\phi_F/k_B T} \,. \tag{2.24b}$$

Thus, the conductivity for an *extrinsic* semiconductor with arbitrary impurity doping

is

$$\sigma_{\text{extrinsic}} = n_i e \left(\mu_c \mathrm{e}^{e\phi_F/k_B T} + \mu_v \mathrm{e}^{-e\phi_F/k_B T} \right) , \tag{2.25}$$

where ϕ_F is dependent on the impurity doping density through Equation (2.20d).

2.2.2 Space charge region

A key feature of semiconductors is the behavior at the interface when in contact with another material, such as a metal, another semiconductor, or electrolyte solution. In general, the semiconductor and the contact material will have different Fermi levels, that will equalize to establish thermodynamic equilibrium [107,226]. Figure 2.4 demonstrates the shift of Fermi levels when an n-type semiconductor is brought into contact with a metal with both a lower and higher Fermi level than the semiconductor. Considering the example of a metal-semiconductor interface, the band bending can be understood from an examination of the work functions of each material. The work function, ϕ, is defined as the energy separation between the Fermi level and vacuum level. The electron affinity, χ, is the energy required remove an electron from the semiconductor, measured from the bottom of the conduction band to the vacuum level (also shown in Figure 2.4). This useful quantity is often defined as it has a clear physical meaning (in comparison to the semiconductor work function).

As demonstrated in Figure 2.4a, when an n-type semiconductor with work function ϕ_{s} comes into contact with a metal with a greater work function, ϕ_{m}, electrons will flow from the semiconductor to the metal until the Fermi level, μ, is continuous across both materials [107,226]. Electrons leaving the the donor levels in the semiconductor near the interface will create a *depletion layer* (a region that is depleted of charge carriers) with positive space charge, shown in Figure 2.4a with width, w. This positive space charge induces an accumulation of negative charge (an *accumulation layer*) in the metal at the junction. The positive and negative space charge layers form a dipole layer that grows until the electric field between them is strong enough to

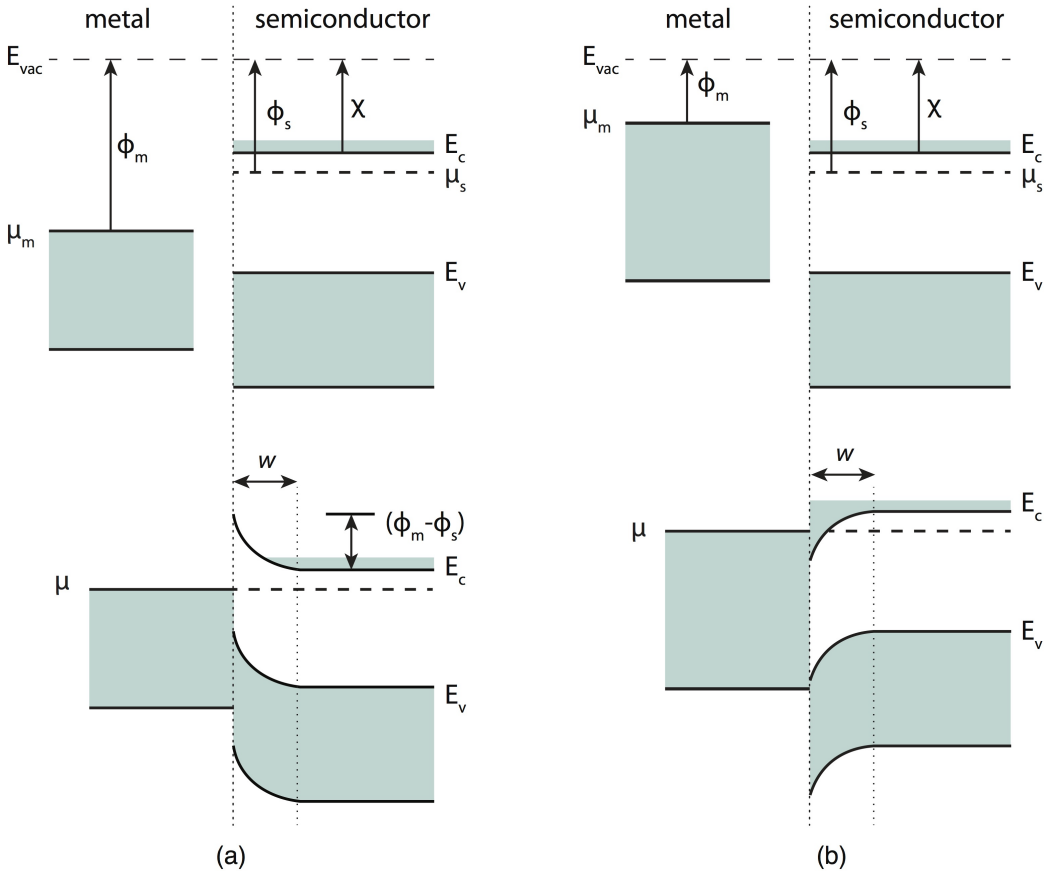

Figure 2.4: Band structure of metal-semiconductor interface (top) before and (bottom) after contact: (a) for $\phi_{\mathrm{m}} > \phi_{\mathrm{s}}$, a rectifying contact is formed; for $\phi_{\mathrm{m}} < \phi_{\mathrm{s}}$, an ohmic contact is formed.

inhibit further electron movement [226]. The depletion layer in the semiconductor is highly resistive; the upward bending of the energy bands form a potential energy barrier with height $e(\phi_{\mathrm{m}} - \phi_{\mathrm{s}})$. The upward bending of the energy bands can be understood as electrons moving closer to the negative space charge layer in the metal must experience an increase in energy. Only the few electrons in the semiconductor conduction band with enough energy to pass over the potential barrier can flow into the metal.

Figure 2.5 demonstrates the effect of applying a bias voltage, V, or external voltage, to the n-type semiconductor-metal junction where $\phi_{\mathrm{m}} > \phi_{\mathrm{s}}$. A reverse bias (Figure 2.5b), where the semiconductor is made positive with respect to the metal, lowers the Fermi level of the semiconductor and widens the depletion layer. While electron flow from the metal into the semiconductor is unchanged from the zero-bias condition, the potential barrier for electrons traveling from the semiconductor into the metal increases to $e(\phi_{\mathrm{m}} - \phi_{\mathrm{s}}) + eV$. This high potential barrier almost completely prevents electron flow. In the case of a forward bias (Figure 2.5c), the Fermi level of the semiconductor is raised and thus the potential barrier for electrons traveling from the semiconductor to the metal is lowered by eV. Again, the electron flow from the metal to the semiconductor is unaltered. Under this forward bias voltage, the conventional current (opposite the direction of electron flow) increases exponentially with applied voltage. Therefore, this type of metal-semiconductor interface is referred to as a *rectifying contact*: a junction in which a large current flows in one direction and only a small current flows in the opposite direction. In the case of a p-type semiconductor-metal interface, a rectifying junction is formed when $\phi_{\mathrm{m}} < \phi_{\mathrm{s}}$, with similar considerations given to the flow of electronic holes.

Alternatively, in the case of an n-type semiconductor coming into contact with a metal with a smaller work function (Figure 2.4b), the potential difference will cause electrons to flow from the metal into the semiconductor until thermal equilibrium is

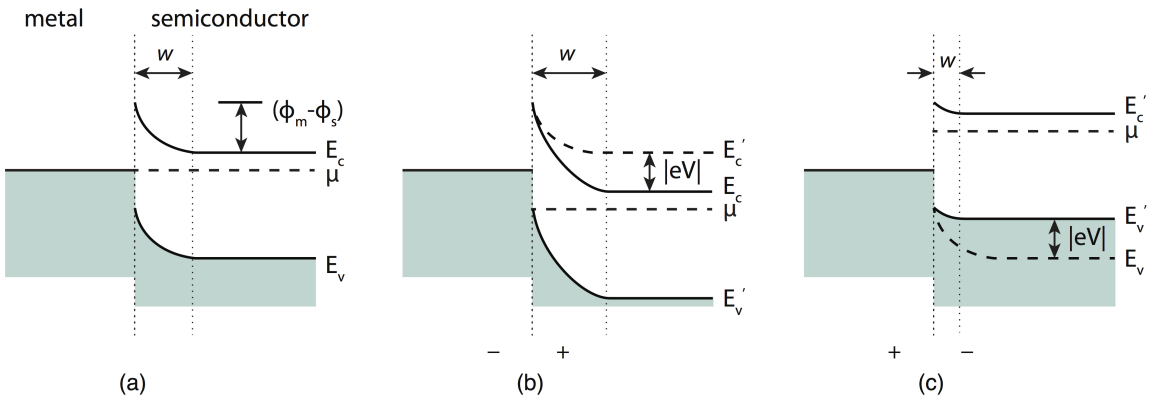

Figure 2.5: (a) zero bias, (b) reverse bias, and (c) forward bias applied to an n-type semiconductor-metal junction where $\phi_{\mathrm{m}} > \phi_{\mathrm{s}}$. The magnitude of the applied bias is $|eV|$.

reached. Therefore, an electron accumulation layer (negative space charge) will form in the semiconductor at the junction and a depletion layer (positive space charge) will form in the metal. The energy bands of the semiconductor will then bend downwards representing the decrease in energy of electrons as they move towards the positive charge in the metal near the junction. As there is no potential energy barrier and electrons can move freely in either direction across the junction, this type of junction is referred to as an *ohmic contact* [226]. For p-type semiconductors, an ohmic contact is formed when $\phi_{\mathrm{m}} > \phi_{\mathrm{s}}$.

However, this ideal interface description, with no consideration of semiconductor surface states, does not hold up to experimental measurements [107, 226, 256]. In reality, metal-semiconductor junctions almost always form rectifying junctions, regardless of relative sizes of work functions. Semiconductor surface states trap charge and pin the surface chemical potential to the surface state energy. The chemical potential of the bulk semiconductor, generally at a different value to the surface, must then bend near the surface to remain continuous [176]. Surface states can be due to discontinuities in the crystal lattice at the cleaved surface, absorbed impurity atoms, oxide layers, or other physical defects [226].

Figure 2.6 demonstrates the band bending within the space charge regions (depletion, accumulation, or inversion layers) due to surface state electron or hole traps. Similar to the case of an n-type semiconductor coming into contact with a metal of a larger work function, the negatively charged surface states (surface electron traps) will create a depletion layer. This potential energy barrier will exist regardless of any metal contact. At large enough surface state concentrations, electrons can also be removed from the valence band creating electronic holes. If the concentration of holes at the surface becomes larger than the electron concentration, then the layer becomes p-type in character, and the layer is referred to as an *inversion layer*. An accumulation layer can be formed in an n-type semiconductor in the presence of surface hole traps. Again, this analysis is inverted for p-type semiconductors.

The band bending and potential barrier, $\phi(x)$, can be found by starting with Poisson's equation,

$$\frac{\mathrm{d}^2}{\mathrm{d}x^2}\phi(x) = \frac{eN_D}{\epsilon_s} \tag{2.26}$$

where x is the distance from the interface into the semiconductor, ϵ_s is the static dielectric constant of the semiconductor, and eN_D is the space charge density provided by the ionized donors in the depletion layer [107,176]. Solving for the potential energy gives,

$$\phi(x) = \frac{eN_D}{2\epsilon_s}(x - x_0)^2\,, \tag{2.27}$$

which provides the parabolic bending shown in Figure 2.6. The potential energy barrier height is provided by $e\phi(x = 0)$:

$$e\phi(x = 0) = \frac{e^2 N_D}{2\epsilon_s}x_0^2\,. \tag{2.28}$$

Therefore, the depletion layer width, $w \equiv x_0$, is defined as,

$$w = \sqrt{\frac{2\epsilon_s\phi_B}{eN_D}}\,, \tag{2.29}$$

where $\phi_B \equiv \phi(x = 0)$ is the barrier energy barrier height. Plugging in typical values

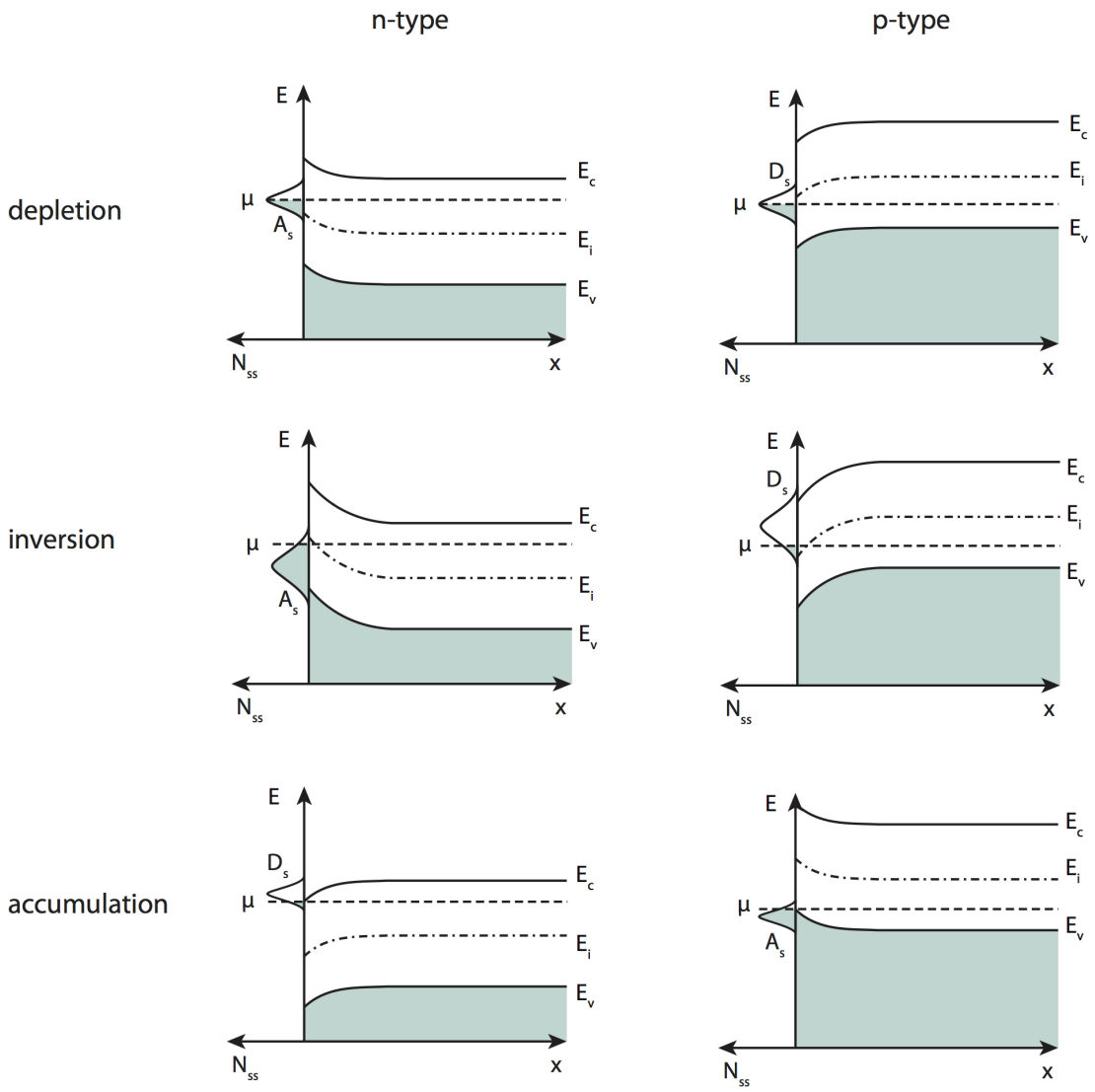

Figure 2.6: Schematic plots of the band structure for n-type and p-type semiconductors at low temperature for depletion, inversion, and accumulation space charge layers due to surface states. The inversion layer occurs when the midband, E_i, crosses the Fermi energy, μ. Here E_c and E_v are the conductance and valence band edges. The number of surface acceptors (A_s) and surface donors (D_s) as a function of energy are shown.

for n-type semiconductors of $\epsilon_s/\epsilon_0 = 10$, $\phi_B = 0.3\,\text{eV}$, and $N_D = 10^{18}\,\text{donors/cm}^3$ gives a depletion layer width of only 18 nm [176].

For the purpose of fabricating semiconductor devices, ohmic contacts must be produced [226]. Techniques for ensuring ohmic contacts include removal of oxide layers from Si by dipping in hydrofluoric acid (HF), surface cleaning, and careful deposition of the metal contact. Heavy doping of the surface of the semiconductor prior to the application of a metal contact is a common method of producing ohmic contacts [226]. For example, increasing the donor concentration at the surface of an n-type semiconductor can counteract the depletion region caused by electron surface traps.

2.3 Fabrication and Formation of PSi

The process of fabricating PSi involves a electrochemical reaction consisting of direct dissolution, oxide formation, and subsequent dissolution of the oxide, typically under the influence of an applied current density [142]. A uniform reaction at sufficiently high current density results in electropolishing, the creation of a completely flat surface free of any defects [17]. The etch reaction can also proceed non-uniformly across the entire exposed surface or in highly localized regions with self-organization, resulting in PSi.

Electroless PSi etching is possible using methods such as stain etching or metal-assisted etching [141, 143]. Stain etching methods consist of immersing Si in an HF solution containing an oxidizing agent such as HNO_3 or $NaNO_2$ [141]. The oxidizing agent performs the function of generating electronic holes at the Si surface, forming an intermediate SiO_2, which is then dissolved by the fluoride component in the solution. Metal-assisted etching uses noble metals (Pd, Pt, Au, Ag) to catalyze the silicon oxidation reaction [141]. However, metal-assisted stain etching suffers limited controllability, uniformity and reproducibility since the etching process is highly

dependent on the physical characteristics of the metal film [143].

PSi can also be formed through dry etching methods, such as reactive ion etching (RIE). Deep reactive ion etching (DRIE) of silicon creates a high aspect ratio nanostructuration on the silicon surface called black silicon, a type of porous silicon named for its light absorbing properties [172, 225]. Roumanie et al. [225] estimated that the planar surface area of the silicon surface increased by a factor of 15 after the formation of black silicon, greatly increasing the potential active surface area of a deposited catalyst. However, the dry etching method of producing PSi is typically limited to producing macropores and nanostructures with characteristic lengths greater than 50 nm. This is due to the fact that the process of pore formation via RIE requires a masking layer to define the pore spacing and cross-sectional shape/area. The masking pattern, and therefore the subsequent pore morphology, is dependent on the existing limitations of photolithography technology [143]. While electroless and dry etching methods are promising, electrochemical etching methods are the most widely studied and offer the ability to fabricate a large variety of well-controlled morphologies.

2.3.1 Etch process and chemistry of pore formation

The electrochemical process, which involves the dissolution of silicon wafers in an aqueous HF solution, is performed in either a single or double cell configuration (Figure 2.7). Galvanostatic anodization is preferred over potentiostatic anodization for greater control and reproducibility [55]. The etch cell is made of HF-resistant materials, such as Teflon or high density polyethylene and a rubber gasket is placed between the wafer and etch cell to ensure the maintenance of the etch solution. For single cell configurations, a Pt cathode is submerged into the HF solution and the Si wafer acts as the anode with a backside metallic contact. A simple metallic contact, used by the Gole group, is a steel plate covered with aluminum foil. The aluminum foil can be inexpensively replaced as needed and combined with the flat steel plate,

securely clamped onto the sensor-gasket-etch cell configuration, creates a good electrical contact. The contact should be ohmic to obtain the greatest consistency of etch. Double etch cells produce better etch uniformity than single cells because the contact is electrolytic on both sides of the silicon wafer, removing the need for backside metallization. However, besides being more complicated in design and set-up than single cells, double etch cells are potentially rate limited by the backside electrochemical reaction [142]. For example, the electrolyte contact on the backside of a p-type silicon wafer is reverse biased, hindering current flow. This can be overcome by backside illumination or by using highly doped p^+-type Si, but these additional etching requirements can limit the range of potential pore structures [143].

While many different theoretical models of the porosification mechanism have been proposed [41, 74–76, 157, 204, 236], a complete common point of view has yet to be established. However, the experimental process of forming various pore morphologies is well understood. In general, it is agreed that the dissolution oxidation reaction,

$$\mathrm{Si} + 6\,\mathrm{F}^- + 2\,\mathrm{H}^+ + 2\,\mathrm{h}^+ \longrightarrow \mathrm{SiF}_6^{2-} + \mathrm{H}_2\,, \tag{2.30}$$

requires both electronic holes and an electrolyte solution capable of dissolving oxides [104, 142, 229]. Silicon reacts spontaneously in water or air to form silicon dioxide, SiO_2, an insulating and surface passivating film. Therefore, HF, which can dissolve the silicon oxides, is an essential component of the etch solution [229]. The dissolution of Si in the presence of HF is still slow, requiring either strong oxidizing agents (stain etching) or electrochemically driven oxidation [110, 229]. Figure 2.8 displays a representative current density-potential curve of Si in an HF-based solution with three defined regions. Region I encompasses the initial exponential rise in current density versus increasing potential, corresponding to PSi formation. Region II is a transition region leading into Region III, which is the electropolishing regime [287].

As long as the system proceeds in Region I of Figure 2.8, the reaction described in Equation (2.30) proceeds along a two-electron electrochemical oxidation reaction,

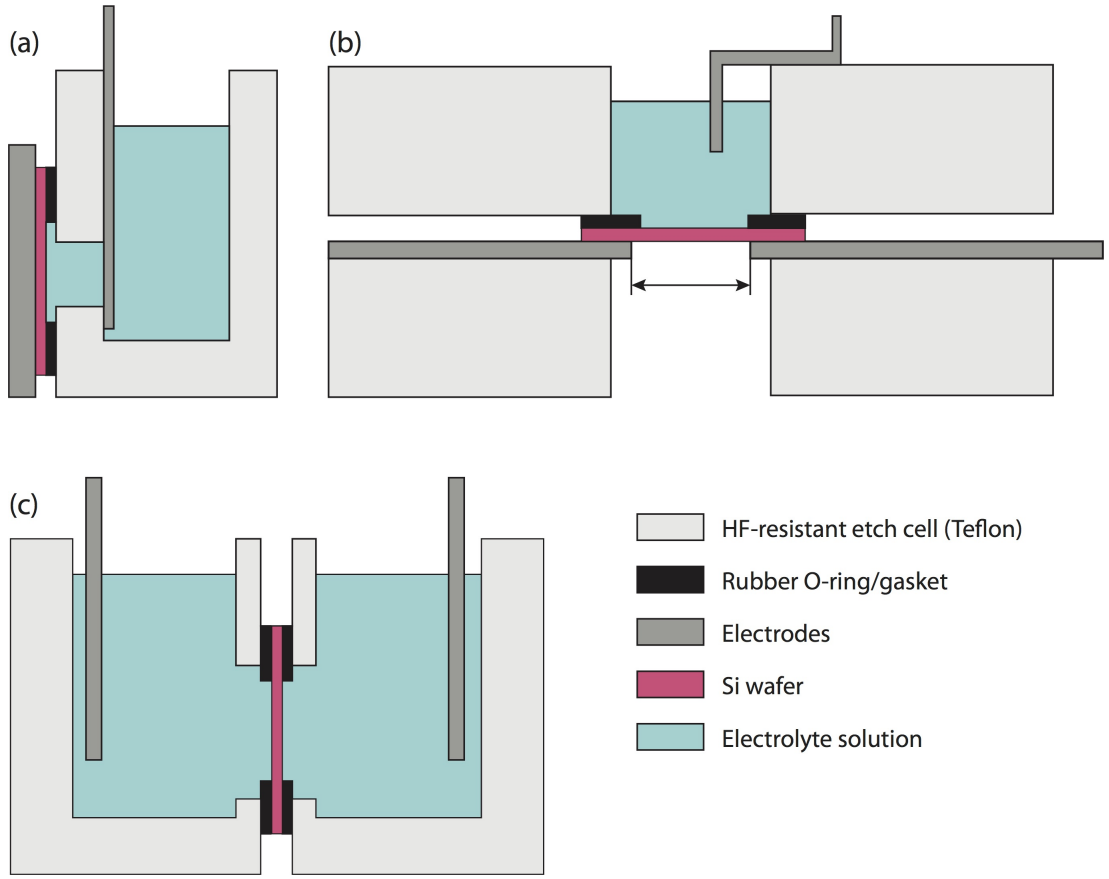

Figure 2.7: Cross-section schematics of a (a) vertical and (b) horizontal electrochemical single cell and (c) double cell for etching PSi in an HF-based solution. The electrodes submerged in the electrolyte solution are typically Pt. The backside wafer contacts for single etch cells shown here are steel plates. The horizontal single etch cell is used for etching under frontside or backside illumination (note the opening in the steel backside contact indicated by the arrows).

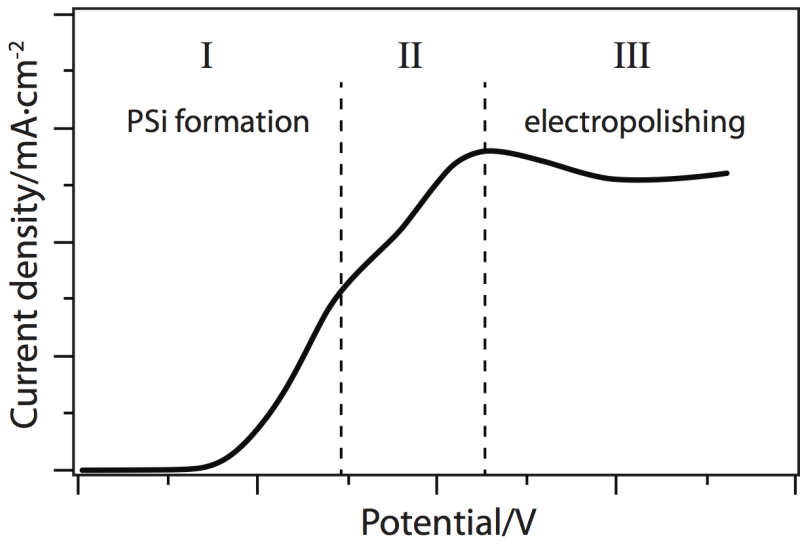

Figure 2.8: Typical anodic IV-curve measured on a moderately doped p-type Si in 1 % HF solution. Adapted with permission from X. G. Zhang (2004) Morphology and Formation Mechanisms of Porous Silicon, J. Electrochem. Soc. 151, C69-C80. Copyright 2004, The Electrochemical Society.

given by,

$$\text{Electrochemical step: } \mathrm{Si} + 2\,\mathrm{F^-} + 2\,\mathrm{h^+} \longrightarrow [\mathrm{SiF_2}] \tag{2.31}$$

$$\text{Chemical step: } [\mathrm{SiF_2}] + 4\,\mathrm{F^-} + 2\,\mathrm{H^+} \longrightarrow \mathrm{SiF_6^{2-}} + \mathrm{H_2}\,, \tag{2.32}$$

where electronic holes, $\mathrm{h^+}$, in the Si valence band are the oxidizing equivalents of the two electrons supplied by the cathode or counter electrode (typically Pt). The cathodic reduction half-reaction balances the anodic dissolution oxidation reaction (Equation 2.31). The silicon surface is inert to hydrofluoric acid attack, thus requiring the electrochemical step given by Equation (2.31) [157]. An electronic hole ($\mathrm{h^+}$), driven by the applied bias, reaches the surface and allow nucleophilic attach on the Si−H bond and subsequent formation of a Si−F bond. The large electronegativity of the fluoride atom destabilizes the adjacent Si−H bond, resulting in another $\mathrm{F^-}$ attack and Si−F bond, which releases an $\mathrm{H_2}$ molecule. The chemical step described by Equation (2.32) proceeds as the recently formed Si−F bonds destabilize the backside Si−Si bonds, which are easily attacked by HF. Lehmann and Gösele [157] explain

that after the first Si atom is removed from an otherwise atomically flat Si surface, the subsequent pore formation will occur preferentially at that location. This is due to a change in the electric field distribution that causes the holes (h^+) required for dissolution to focus at the pore tip (Figure 2.9). The holes (h^+) are supplied by the valence band of the Si. While plentiful in p-type Si, n-type Si requires illumination to generate the necessary holes. In the electropolishing regime (Region III), the electrochemical etching reaction follows a four-electron oxidation reaction given by,

$$\mathrm{Si} + 6\,\mathrm{F}^- + 4\,\mathrm{h}^+ \longrightarrow \mathrm{SiF}_6^{2-}\,. \tag{2.33}$$

Here the electronic holes, h^+, in the silicon valence band are the oxidizing equivalents of the four electrons supplied by the cathodic reduction half-reaction occurring at the counter electrode. In this region, the current density has exceeded the critical current density, j_{PSL}, the maximum current density that can form porous silicon layers (PSL) [156].

The electrolyte solution for HF electrochemical etching is commonly either aqueous or organic [74]. Aqueous electrolytes refer to those from the $\mathrm{HF}-\mathrm{H_2O}$ system as well as ions of fluorine containing salts, such as $\mathrm{NH_4F}$, in water-based etch solutions. Often, ethanol, acetic acid, or surfactants are added to the aqueous solution depending on the desired pore morphology. Alternatively, organic solvents, most commonly acetonitrile (MeCN), dimethylformamide (DMF), or dimethylsulfoxide (DMSO), are combined with HF for an organic electrolytic etch solution. Water present in the organic electrolyte etch solution is supplied by the standard 49 % HF solution. Tetrabutylammonium-perchlorate (TBAP) can be added to MeCN as a salt to improve conductivity. Organic electrolytes are important as they aid recent advances in producing p-type microporous silicon [74].

Crystallographic orientation greatly influences PSi formation. A large single crystal, produced via the Czochralski (CZ) process or float zone (FZ) process, is cut at various angles to produce individual Si wafers coinciding with a particular crystal face

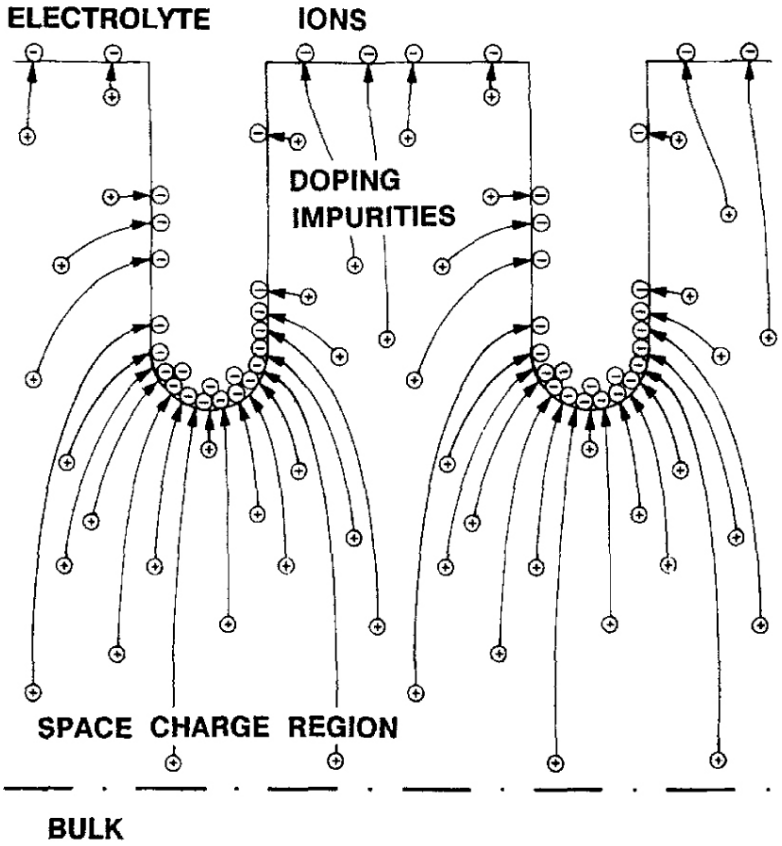

Figure 2.9: Illustration of electric field lines in the space charge region around pores during anodization in an electrolyte, demonstrating the collection of electronic holes (h^+) at the pore tips. Reprinted with permission from V. Lehmann and H. Föll (1990) Formation Mechanism and Properties of Electrochemically Etched Trenches in n-Type Silicon, J. Electrochem. Soc. 137, 653-659. Copyright 1990, The Electrochemical Society.

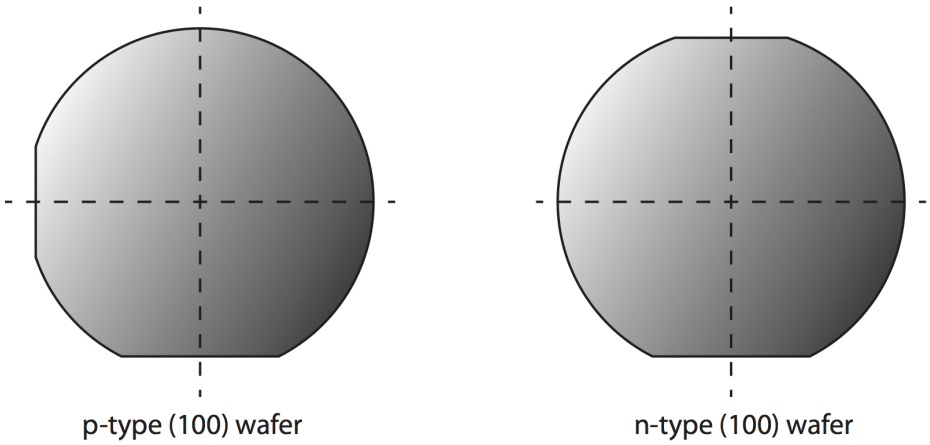

Figure 2.10: Schematic of p-type and n-type (100) wafers with fiducial flats. Dashed lines indicate the (110) natural cleavage planes.

(Figure 2.10) [65]. Crystal planes are indicated on the wafer by fiducial flats; p-type (100) wafers have a major flat parallel the to (110) plane and a minor flat offset by 90°; n-type (100) wafers have a major flat parallel the to (110) plane and a minor flat opposite. PSi growth is anisotropic and propagates primarily in the $\langle 100 \rangle$ direction of the Si crystal and secondarily in the $\langle 113 \rangle$ direction [224]. This is due to the differential chemical stability of the different crystalllographic faces during dissolution. The (111) face is capped with hydrogen atoms bonded perpendicularly to the surface where the (100) face contains strained Si−H bonds [229].

Theoretical models seek to describe both the initiation of pore formation as well as the subsequent growth. Through an analysis of the morphological stability of independently varied etch parameters, Kang and Jorné [132] developed an extensive theoretical model to predict the relationship between applied etch conditions and the resultant PSi morphology. This model confirmed the significance of the supply of holes in the silicon wafer, suggesting that PSi formation is simultaneously dependent on both materials and process. Kang and Jorné also propose that pore nucleation is due to planar surface instability to small perturbations. Other theories for pore nucleation include near-surface variations in vacancy-type defects [51] and selectively etched hydrogen-induced structural micro-defects [6]. Beale et al. [23] propose that

a Schottky barrier between the silicon and electrolyte interface exists due to surface states. As a result, the dissolution of silicon preferentially occurs at the pore tips where the intensity of the electric field is higher, lowering the Schottky barrier. Other mechanisms explaining pore growth include a correlation of the space charge region (SCR) width with the distance between pores and the current burst model [74, 159].

First proposed by Lehmann and Föll [156], the *space charge region pore formation model* explains the formation of n-type macropores. The authors explain that the space charge region at the Si surface will bend around newly formed pore tips (Figure 2.9). The electronic holes required for dissolution are focused at the pore tips were the space charge region is thinnest [74,156]. This focussing of holes at the pore tips is enhanced for the case of n-type anodization with backside illumination, as the holes will be generated primarily from the back side of the space charge region following the preferential path to the pore tips. In this case, large constant diameter macropores will grow [74]. This model has been extensively studied by Lehmann and coworkers [155, 156, 158] and a quantitative formula has been created to reliably predict and refine n-type macropore formation. This successful formula relates pore morphology parameters, such as the cross-sectional area of the pore and spacing between pores, to the applied current density and critical current density, j_{PSL} [155]. However, the SCR model is insufficient to describe the formation of macropores in general. In particular, this is true for the case of macropores formed in organic electrolyte solution, which do not typically have a characteristic peak current density, j_{PSL} [74].

The current burst model explains that low frequency current oscillations are due to spacially and temporally inhomogeneous current. Each current burst isolated to a nm sized region is composed of a sequence of direct dissolution, oxidation, and then oxide dissolution [74]. Hydrogen passivation will then occur if another current burst does not follow in the same location. However, subsequent current bursts tend to occur in the same locations as previous bursts, creating a pore-producing cycle.

Chazalviel et al. [41] explain that theoretical models are often separated into silicon electrochemical theories and physical theories focussed on the semiconducting character of silicon and hole availability. However, these categorically separated anodization models are only able to provide general qualitative predictions. A robust quantitative model requires a framework that incorporates chemical and physical aspects simultaneously [41].

2.3.2 Pore morphology

While a robust quantitative model for the formation of PSi has not yet been given [104,142], extensive studies of the dissolution process have led to the ability to create a wide variety of PSi morphologies tailored to particular applications [74,75,132]. Due to the drastic difference in the number of holes, porosification of n-type Si produces a different set of morphologies than does p-type [74, 75]. Traditionally, n-type Si is used to fabricate large diameter macropores through the application of backside illumination generating the necessary holes at pore tips [104]. Highly doped p^+ and n^+ silicon yields dendridic mesopores, and p-type PSi commonly consists of micropores [104,142,229]. However, all three pore geometries can be formed by a variety of etch conditions. In particular, p-type macropores, formed using an organic electrolyte etch solution, are being investigated as an alternative to the involved process of forming n-type macropores [38,74]. Advantages of using p-type Si to produce macropores include a simpler etch setup (no need for backside illumination) and no known limitations to the parameter space (for example, no limits on etch rate or pore depth have been established for p-type macropore formation) [74]. PSi can be formed as a single layer with no porosity gradient by the application of a single value of current density or as multi-layers of varied pore diameters by sinusoidally modulating the current density [104,134,275].

Demonstrated in even the earliest studies of porous silicon [271], the depth of the

pores formed during dissolution increases with etch time, as shown in Figure 2.11. However, the growth rate decreases with etch duration eventually limiting the maximum depth for a particular set of parameters. For long etch durations, the electrolyte becomes exhausted at the pore tips where the dissolution takes place due an to increasing difficulty of diffusion of electrolyte molecules into the deep pores [74,104,156]. Similarly, the average pore diameter and porosity (the distance between pores) increases with applied current density, as explained by the SCR pore formation model proposed by Lehmann and Föll [156], which is demonstrated in Figure 2.12. Also shown in Figure 2.12, Granitzer et al. [103] investigated the four-fold symmetry of self-assembled pores and the relationship between this regularity and current density. This relationship of a monotonically increasing pore-diameter and regularity of pore-arrangement is explained by the higher electric field strength at the pore tips with larger current densities [104]. Granitzer et al. [103, 104] found that the regular arrangement of the pores only occurred within a specific window of current densities, holding all other etch-parameters constant. The current density must be above a critical value, that required for pore diameters of approximately 30 nm. Below this value, the pore spacing is greater than the pore diameters, leading to an enhancement of dendritic pore growth, all of which contributes to an irregular pore arrangement [104].

By the application of sophisticated etching techniques, advanced PSi morphologies can be constructed. Pores with enhanced regularity, smooth walls, and a high aspect ratio, demonstrated in Figure 2.13, are achieved by pre-patterning the Si wafer prior to anodization. Llorca et al. [168] have developed a lithographic patterning process to produce periodic macropores for utilization as a membrane microreactor. Taking advantage of the channel structure of PSi, bulk silicon can be removed to expose the backside of a PSi layer to create a flow-through-PSi membrane reactor [168, 214, 238]. The square array of 220 µm deep pores, shown in Figure 2.13, was lithographically

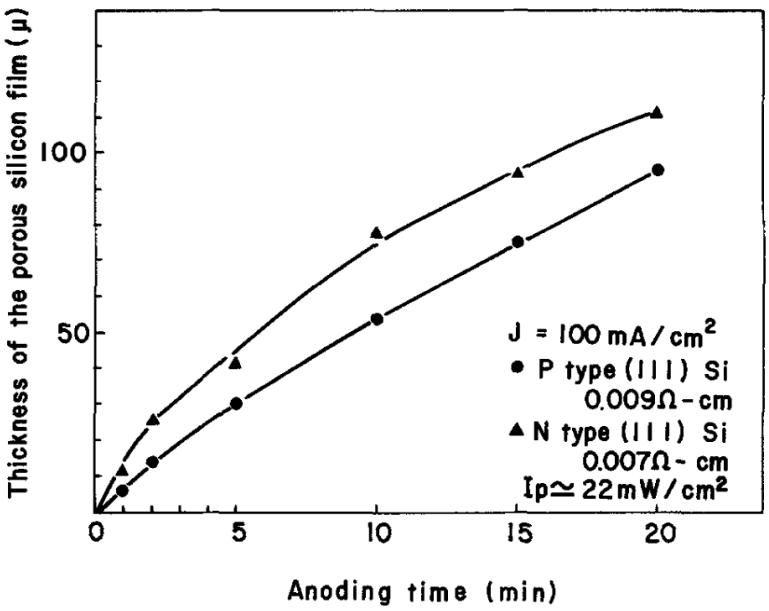

Figure 2.11: Relation between PSi thickness and anodizing time for p- and n-type silicon. Reprinted with permission from Watanabe et al. (1975) Formation and Properties of Porous Silicon and Its Application, J. Electrochem. Soc. 122(10) 1351-1355. Copyright 1975, The Electrochemical Society.

prestructured on n-type (100) silicon wafers. Pre-defining the position of pores is essential for PSi membrane reactors to ensure that membranes can be stacked without dead-end channels [214]. An earlier study on the fabrication of PSi membranes for the purpose of hydrocarbon reforming used an SiN_x etch mask to pre-define pore locations [214]. Inverted pyramids, created by tetramethylammonium hydroxide (TMAH) etching, guided the subsequent electrochemical etch to create pores every 4 µm. With a solution of 5 wt% HF and 0.1 mmol Triton X-100 surfactant, the etch was carried out at 288 K for 330 min with backside illumination. The etch current was reduced as the etch progressed to compensate for the restricted diffusion of HF into the growing high aspect ratio pores. To turn the pore structure into a membrane of channels, the backside of the silicon was etched away by a TMAH solution at 358 K. The recently created front-side porous structure was protected from the TMAH etch by oxidation in O_2 at 1373 K, and the resultant oxide was removed by HF as a final step [168].

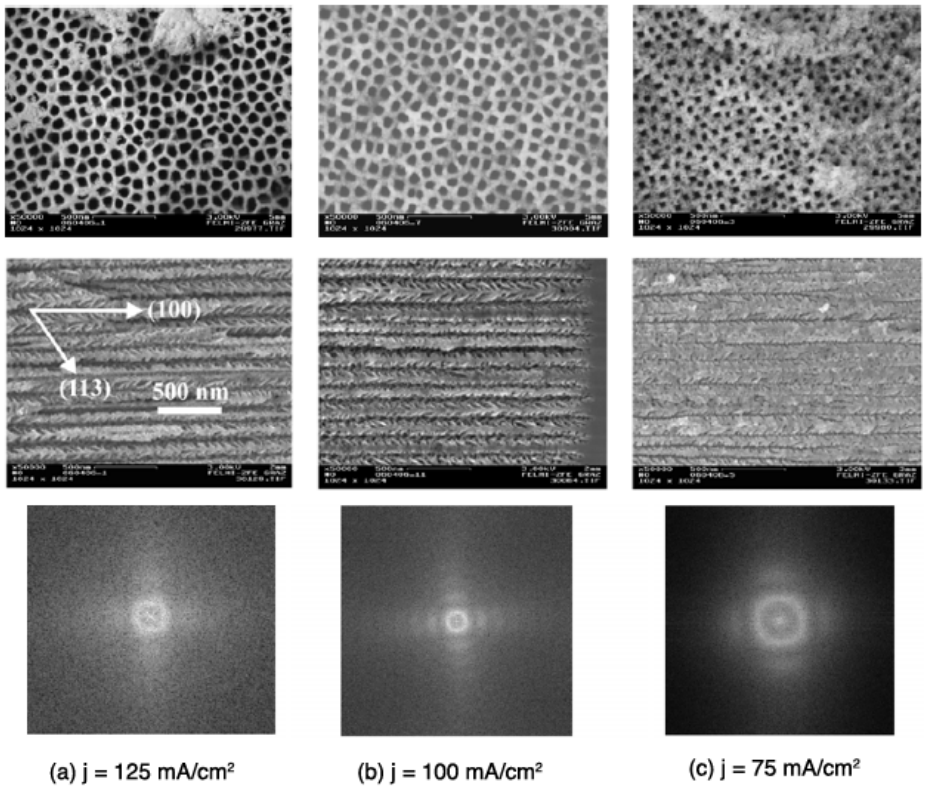

Figure 2.12: Relation between PSi pore diameter, pore spacing and regularity with current density for n-type Si anodized in 10 wt% HF and current density of (a) 125 mA/cm^2, (b) 100 mA/cm^2, and (c) 75 mA/cm^2. Top row: SEM of top view of PSi samples showing variation of pore diameters and pore spacing; middle row: SEM of cleaved edge of PSi samples; bottom row: Fourier transform of top view SEM images showing decreasing regularity with decreasing current density. Reprinted from Physica E: Low-dimensional Systems and Nanostructures, 38(1-2), P. Granter, K. Rumpf, P. Pölt, A. Reichmann, H. Krenn, Self-assembled mesoporous silicon in the crossover between irregular and regular arrangement applicable for Ni filling, 205-210, Copyright 2007, with permission from Elsevier.

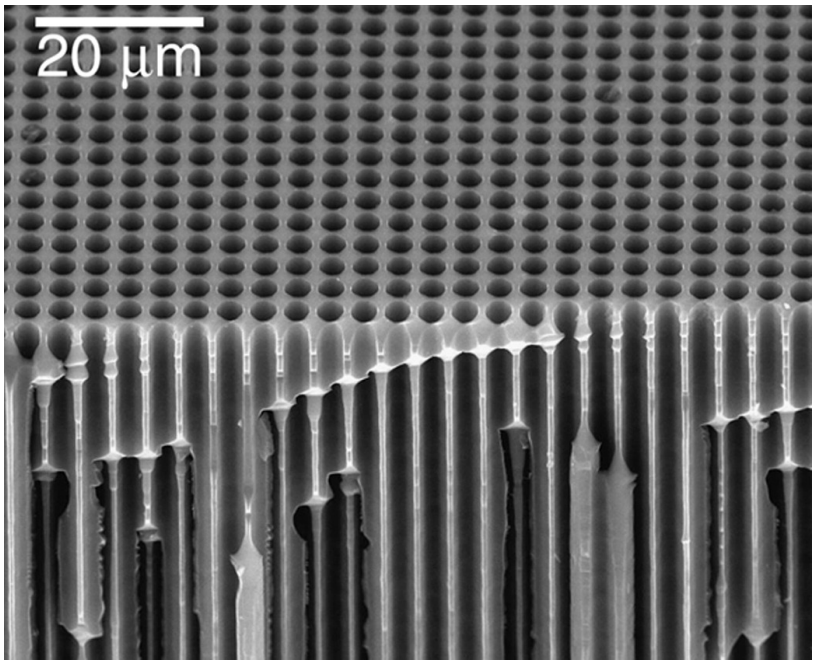

Figure 2.13: SEM image of lithographically patterned n-type macroporous silicon membrane. Reprinted from Journal of Catalysis, 255, Llorca J., Casanovas A., Trifonov T., Rodrguez A., and Alcubilla R., First use of macroporous silicon loaded with catalyst film for a chemical reaction: A microreformer for producing hydrogen from ethanol steam reforming, 228-233, Copyright 2008, with permission from Elsevier.

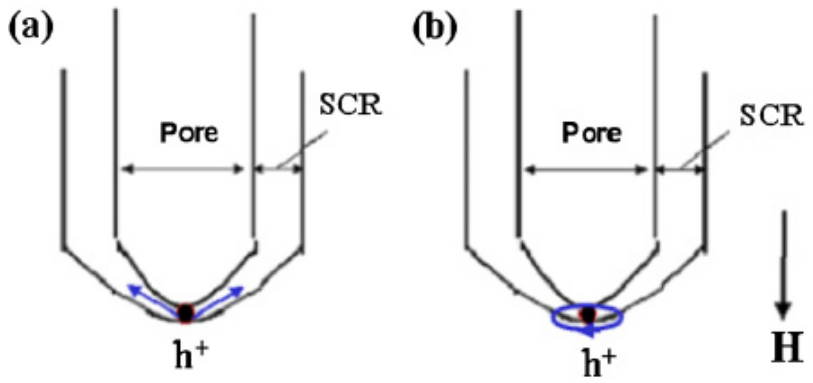

Figure 2.14: Schematic of the motion of holes generated at the pore tips by tunneling (a) without and (b) with an external magnetic field. Reprinted from Japanese Journal of Applied Physics, 47, Hippo et al., Formation Mechanism of 100-nm-Scale Periodic Structures in Silicon Using Magnetic-Field-Assisted Anodization, 7398-7402, Copyright 2008, with permission from IOP Science.

Alternatively, with the utilization of an external magnetic field during anodization of pre-patterned PSi, Hippo et al. [114] have created highly directional and high aspect ratio pores with diameters under 100 nm. Mesoporous silicon formation typically requires highly doped silicon. As doping density increases, the space charge region experiences greater fluctuations, causing pore growth to deviate from the intended unidirectional path. Under the application of a magnetic field parallel to the direction of desired pore growth, the induced Lorentz force confines the electronic holes to the cyclotron radius (Figure 2.14). As a result, pore growth is limited to the pore-tip, restricting the subsequent pore radius. The magnetic field confinement of the holes also suppresses dendridic growth [114].

Multi-layered PSi is created by varying the anodization current density during the etch (Figure 2.15) [104,275]. As dissolution occurs primarily at the pore tips, the adjusted current density will only affect subsequent pore growth and leave the already formed pore structure for the most part unaltered [104, 275]. A key application for multi-layered PSi is as an optical chemical sensor. The layers of different porosity exhibit unique reflectivity and chemical sensing is based on monitoring changes in the refractive index and peak shift of these PSi layers exposed to various species

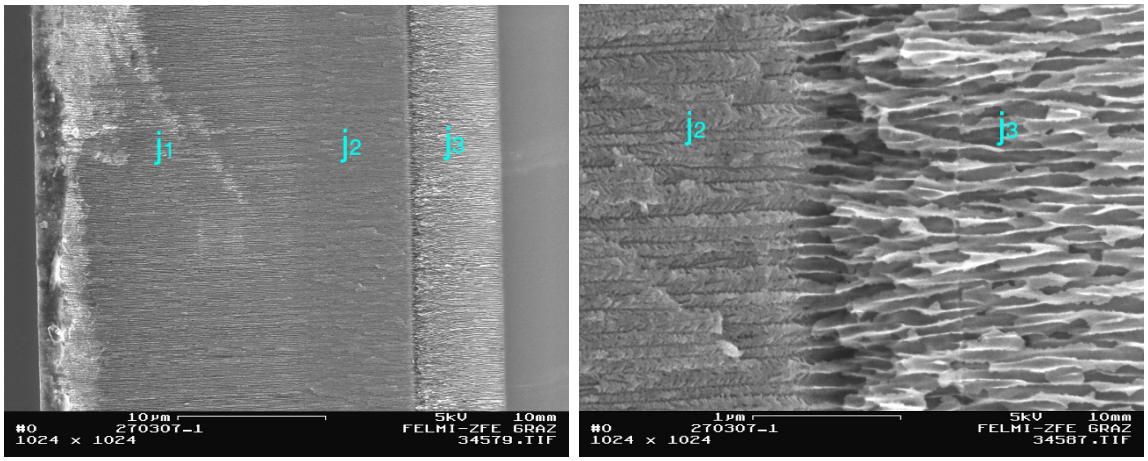

(a) (b)

Figure 2.15: (a) PSi with three layers of different porosities, etched with three changing current densities ($j_1 = 75\,\mathrm{mA/cm^2}$, $j_2 = 50\,\mathrm{mA/cm^2}$, and $j_3 = 125\,\mathrm{mA/cm^2}$). (b) Zoomed-in boundary between layers etched with current densities j_2 and j_3. Reprinted with permission from P. Grantzer and K. Rumpf (2010) Porous Silicon - A Versatile Host Material, Materials 3, 943-998, Creative Commons License.

[134, 200, 275]. Multi-layered PSi, where the deeper layers have sequentially smaller diameters, is particularly useful for monitoring biomolecules. The depth to which biomolecules can penetrate the porous layers is limited by their size, thus creating different optical signals for different sizes of biomolecules. Pacholski et al. [200] created a double-layer of PSi with a top layer of large pores that could support the diffusion of large protein molecules, and a smaller bottom layer into which only the smaller sucrose molecule could penetrate (Figure 2.16). Reflected light from the multi-layers contain three superimposed interference patters (Figure 2.16), which are resolved by fast Fourier Transform (FFT) of the reflectivity spectrum. The peaks in the FFT indicate positioning of large and small molecules in the size-selective membrane. Therefore, the reflectance spectra of the bottom layer could be used as an on-chip reference channel to detect certain large proteins in the presence of smaller sucrose molecules [200].

The technique of creating PSi multi-layers can also be applied to the fabrication of microfilters or micromembranes. In contrast to the PSi membrane fabrication method

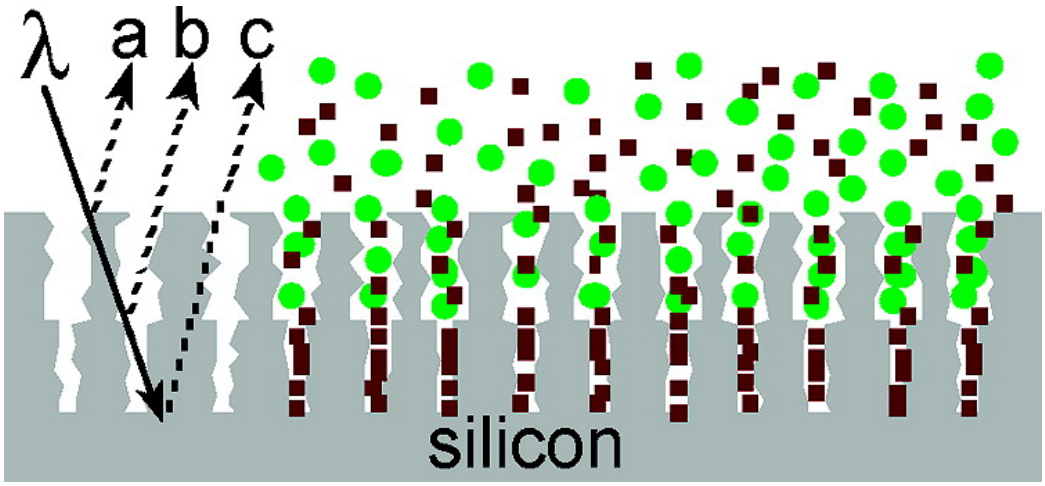

Figure 2.16: Schematic of the porous Si double-layer biosensor consisting of a top layer with large pores and a bottom layer with smaller pores. The three different interfering light beams are shown. Interference of beams a and b occurs from reflections at the interfaces bordering layer 1, interference of beams b and c originates from layer 2, and interference of beams a and c originates from layer 3. Analyte-containing solution is introduced at the top of the structure. Reprinted with permission from Journal of the American Chemical Society, 127, Pacholski et al., Biosensing Using Porous Silicon Double-Layer Interferometers: Reflective Interferometric Fourier Transform Spectroscopy, 11636-11645. Copyright 2005, American Chemical Society..

described by Llorca et al. [168] and others [238], which requires additional steps of protecting the PSi layer, removing the backside bulk silicon, and then subsequent removal of the PSi protectant, an increase of the current density after an initial PSi layer is created can fabricate a PSi membrane in a single etch procedure [34]. The microfilters are etched in a 1:15 volumetric ratio of 49 % HF and DMF in two contiguous stages of current densities. The first stage corresponds to formation of the porous structure of the microfilter with a moderate current density and long etch duration to create deep pores, which will correlate with the durability of the final microfilter. The second stage of the etch is performed at a significantly higher current density, 3 times to 4 times that of the first stage, for a duration of around 300 s. This causes a rapid widening of the pores at the pore tips to the extent that the pore diameter exceeds that of the pore spacing, cutting off the porous structure formed in the first stage from the bulk-Si. Recent work on optimizing the fabrication

process has reliably produced large (approximately $1\,cm^2$) robust microfilters that easily lift off from the bulk-Si by rinsing with MeOH (Figure 2.17).

Careful selection of appropriate electrochemical etch conditions can produce PS with a hybrid morphology of macropores covered with a nanoporous layer [88, 219, 244]. For example, Su et al. [244] developed a hierarchical macroporous silicon with a nanoporous surface (NP-MPSi) by anodic etching of n-type silicon in a 49 % HF/ ethanol solution with a volume ratio of 1:1 at a current density of $50\,mA/cm^2$ under front-side irradiation of a Xe lamp. A pore size analyzer revealed that about 80 % of the pore volume was due to pores with a diameter less than 20 nm, 60 % of which had diameters less than 5 nm. In the context of chemical gas sensing, Gole et al. [88] developed a hybrid PSi surface referred to as nano-/micropores, so named for the pores with diameters of approximately 1 µm to 2 µm with walls coated with pores of diameter below 50 nm. While the micropores allow for rapid Fickian diffusion of gas molecules into the porous silicon structure, the nanoporous layer is optimal for providing an extremely high surface area for sensing and for the deposition of nanostructured metal oxides, which control and focus a variable and efficient analyte interaction with the PSi interface [146]. The hybrid pores will be the foundation for the chemical sensors described in this thesis and the procedure for fabricating these hybrid nano-/micropores, shown in Figure 2.18, will be discussed in detail in section 3.1.4.

2.3.3 Surface chemistry

The surface of freshly prepared PSi is predominantly consists of silicon hydrides (SiH, SiH_2, or SiH_3) and trace amounts of oxygen and fluorine [229]. During the dissolution process, the applied bias will cause holes to drift to the Si-solution interface, resulting in a positively charged Si atom, which is then complexed with a fluoride ion [220]. The large electronegativity of fluoride creates a highly polarized bond, destabilizing the

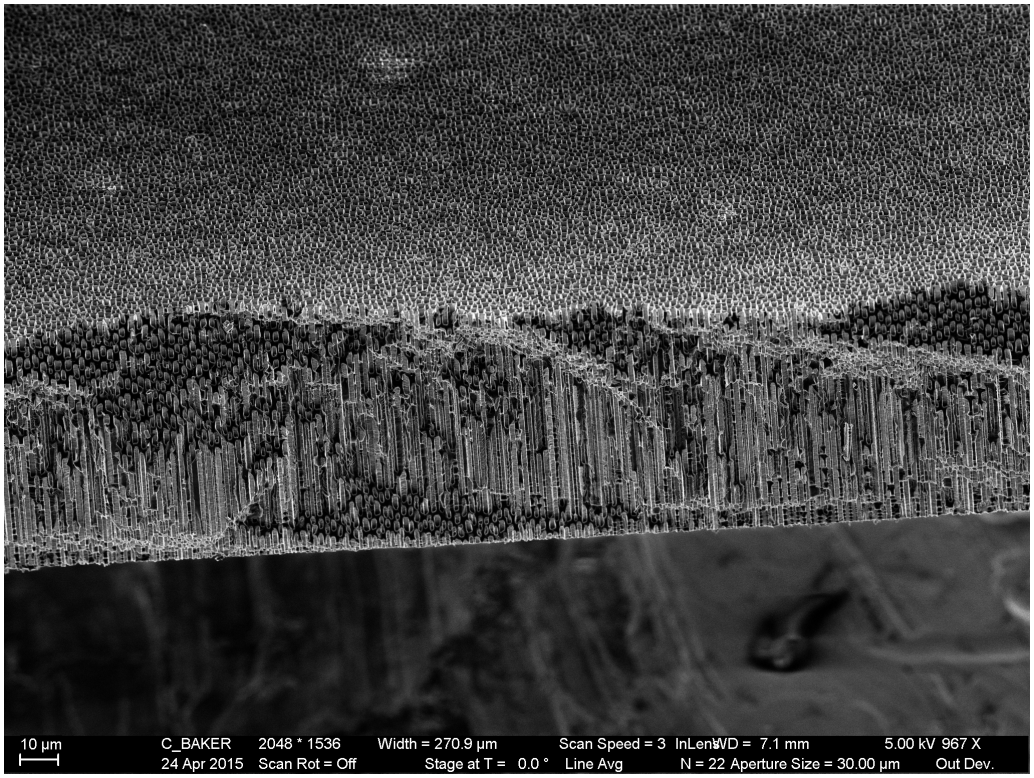

(a)

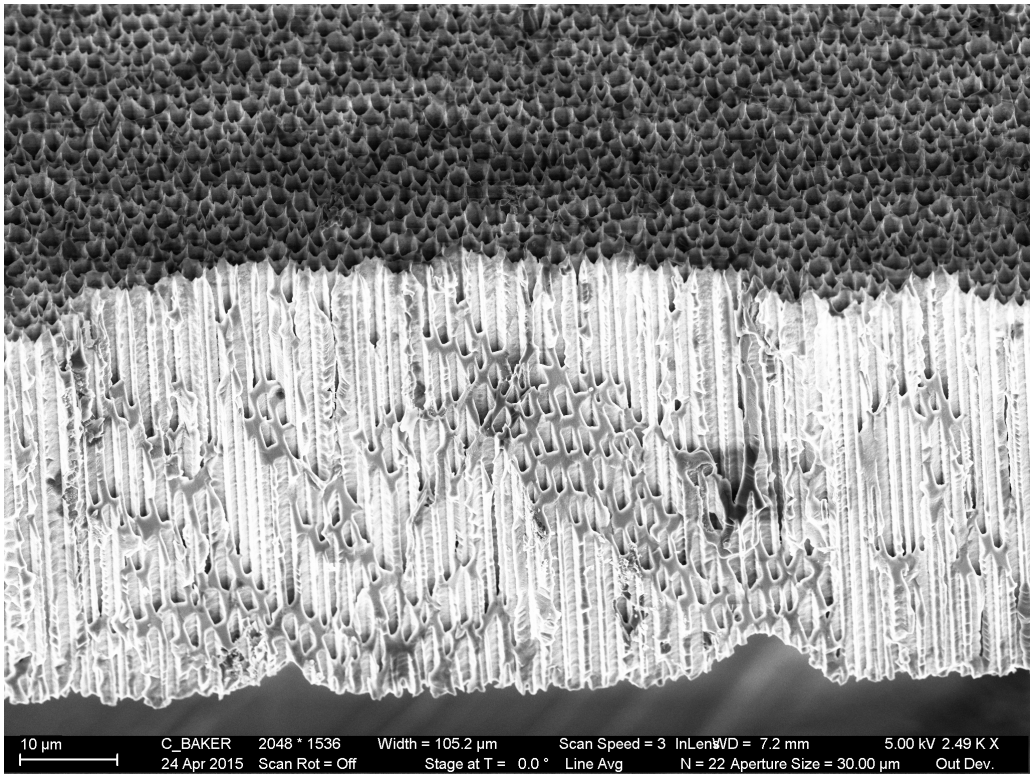

(b)

Figure 2.17: SEM images of PSi microfilters fabricated from p-type silicon, beveled at 45°. The microfilters, with a width of approximately 30 µm, were fabricated with etch conditions of (a) a current density of 9 $\mathrm{mA/cm^2}$ for 7500 s followed by 22 $\mathrm{mA/cm^2}$ for 300 s and (b) 6.5 $\mathrm{mA/cm^2}$ for 7300 s followed by 22 $\mathrm{mA/cm^2}$ for 300 s. C. Baker, unpublished.

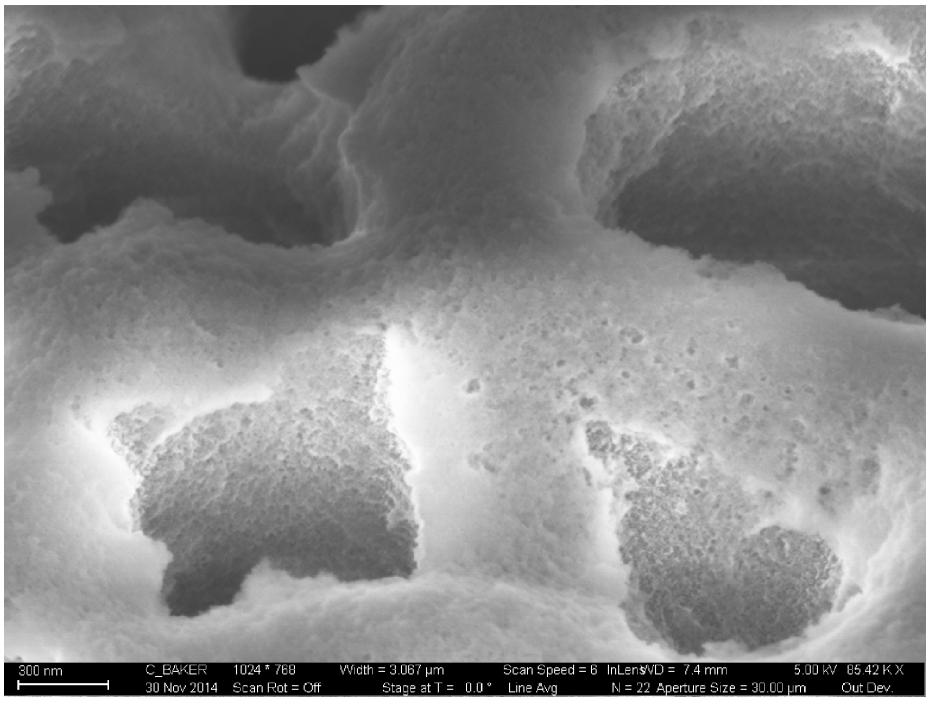

Figure 2.18: SEM image of hybrid nano-/microporous PSi fabricated from p-type (100) Si (7 Ω cm to 13 Ω cm). C. Baker, unpublished.

adjacent Si−H bond, leading to a difluoride terminated surface. The fluoride surface bonds will destabilize the backside Si−Si bonds, and the silicon fluoride is dissolved into the electrolyte solution as SiF_6^{2-}, leaving behind a newly formed stable hydrogen terminated surface [216]. After exposure to air, the PSi surface rapidly oxidizes. The PSi can be completely oxidized through exposure to wet or dry oxygen at elevated temperatures [168, 282]. The resultant oxide can also be easily removed by soaking in dilute HF [15, 168]. As such, the unique surface of PSi can be utilized in a wide range of applications. In particular, PSi is an excellent support of various materials.

Catalytic activity is often dependent on the support surface. A wide range of catalyst supports has been studied to enhance the activity of metal catalysts. Catalyst supports are often inert, enhancing the catalytic activity by providing a high surface area per volume for dispersed catalysts, and are thermally, chemically, and mechanically stable [169, 213]. However, semiconductor supports, traditionally reducible oxides, offer the ability to electronically interact with metal catalysts to further enhance

catalytic sites. PSi is a desirable choice for a catalyst support due to the high surface area porous structure and the semiconducting properties of bulk silicon [213]. PSi can also enhance the activity of supported photocatalysts. Under irradiation, the small band gap (2.0 eV) of PSi contributes additional electron-hole pairs to supported photocatalysts [247]. Additionally, the hydrogen-terminated surface of PSi is ideal for the reduction of metal salts to form metal nanoparticle catalysts [66, 166, 192, 212]. The process of reducing a metal salt into nanoparticles on a PSi surface can be described as follows, using a metal chloride precursor [131, 133]:

1. decomposition of a metal chloride salt in an aqueous acidic solution

$$\mathrm{MCl_z} \longrightarrow \mathrm{M^{z+}} + \mathrm{ZCl^-} \tag{2.34}$$

   where M represents a noble metal,

2. hole injection into the valence band through a coupled redox reaction,

$$\text{oxidation:}\ \ \mathrm{Si} + 2\,\mathrm{H_2O} + 2\,\mathrm{h^+} \longrightarrow \mathrm{Si(OH)_2} + 2\,\mathrm{H^+} \tag{2.35}$$

$$\text{reduction:}\ \ \mathrm{M^{z+}} \longrightarrow \mathrm{M} + \mathrm{zh^+}\,, \tag{2.36}$$

3. electron injection into the conduction band through a second coupled redox reaction,

$$\text{oxidation:}\ \ \mathrm{Si(OH)_2} \longrightarrow \mathrm{SiO_2} + 2\,\mathrm{H^+} + 2\,\mathrm{e^-} \tag{2.37}$$

$$\text{reduction:}\ \ 2\,\mathrm{H^+} + 2\,\mathrm{e^-} \longrightarrow \mathrm{H_2}\,. \tag{2.38}$$

Polisski et al. [212, 213] demonstrated the importance of the hydrogen-terminated surface for Pt nanoparticle deposition by attempting a metal salt reduction on hydrogen-effused PSi powder samples. Removal of the hydrogen-termination at the PSi surface was performed by heating the samples to 400 °C. Fourier-transform infrared (FTIR) spectroscopy was used to confirm the absence of hydrogen-termination on the heated

samples. While FTIR peaks corresponding to $Si-H_x$ bonds were present in the FTIR spectra for the freshly prepared PSi powders, the $Si-H_x$ peaks were absent from the spectra of the heated samples. The hydrogen-effused samples did not participate in any reductive activity, confirming the importance of $Si-H_x$ groups in nanoparticle formation. Copper and silver nanoparticles have also been successfully reduced from metal salts onto a hydrogen-terminated PSi layer [66, 166].

2.4 Porous Silicon Chemical Sensors

PSi has attracted significant attention for chemical sensor applications due to its unique surface chemistry, high surface area, tailorable morphology, and facile integration with silicon based technology. Upon exposure to a chemical species, PSi can transduce the interaction via a change in optical or electrical properties, allowing the detection of a range of organic solvents [8, 123], organic vapors [44, 127, 128, 134, 167, 189], as well as inorganic gas pollutants [28, 174, 250, 278, 279]. In general, inorganic vapors are detected at significantly lower concentrations than that of organic vapors [13]. A key area of the development of PSi chemical sensors is not only improving sensitivity but selectivity, the ability to differentiate between multiple species present in an environment. In recent studies, selectivity is enhanced by simultaneously measuring and comparing signals from multiple transduction mechanisms. This is exemplified by the combination of optical and conductance measurements. While this method shows some promise, these studies are preliminary in nature and struggle with optimizing the porous structure for both methods of transduction [128]. Alternatively, increasing or decreasing the sensitivity to individual gas analytes for allows for the creation of a complete sensing array [92]. The following sections will outline recent advances in the development of sensitive and selective PSi chemical sensors with a focus on improvements through interface modification.

2.4.1 Optical transduction

Optical transduction represents one of the most widely studied properties of PSi in the context of chemical sensing [142]. PSi sensors based on monitoring photoluminescence (PL) quenching with respect to changes in surrounding gas are extremely sensitive. Threshold sensitivities to alcohol vapor concentrations below 4 ppm have been reported [46] and detection of 70 ppb NO_2 [109] and 440 ppb SO_2 [136] have been achieved. However, PSi sensors based on PL quenching suffer from saturation at concentrations above 50 ppm, excluding the ability to discern and distinguish higher vapor concentrations [115]. Other disadvantages of PL-based sensors include low selectivity and a low degree of reversibility, limiting their applicability for commercial devices [109, 142].

In contrast, optical PSi sensors based on monitoring the change in refractive index in the presence of chemical vapors are a promising sensor design. These Bragg reflector-based sensors utilize multi-layered PSi created by alternating current densities during anodization, illustrated in Figure 2.19. Optical sensors have fast response times and do not require electrical components near the PSi sensing interface, which is desirable for detection of highly flammable gases. Jalkanen et al. [127] have developed an optical Bragg reflector based sensor, constructed from multi-layered PSi, to detect various organic vapors. The multi-layered PSi sensor interface is formed by anodizing a p^+-type (100) silicon wafer (0.01 Ω cm to 0.02 Ω cm) in a 1:1 HF/ethanol solution. The current density was modulated between 10 mA/cm^2 and 100 mA/cm^2 with a 20 s period. The Bragg reflector operates on the principle that light reflected off the various PSi layers of different morphology will form an interference pattern with distinct bands of high reflectivity at particular wavelengths. A redshift in the interference peak signals the presence of chemical vapors, which increases in magnitude with increasing vapor concentration [127]. However, selectivity, the ability to

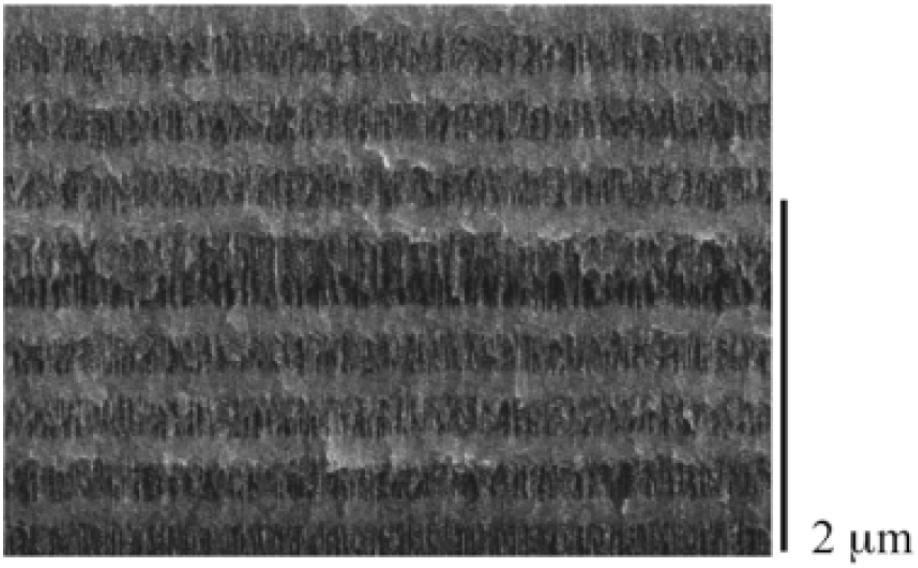

Figure 2.19: SEM image of porous silicon layers consisting of 4 period Bragg mirrors. Alternating layers of 165 nm, 50 % porosity (5 mA/cm^2 for 32 s) and 190 nm, 70 % porosity (35 mA/cm^2 for 11 s) porous silicon layers constitute the Bragg mirrors. The defect layer located between the two Bragg mirrors has a thickness of 205 nm and a porosity of 75 % (50 mA/cm^2 for 8 s). Reprinted with permission from Physica Status Solidi (a), 197, S.M. Weiss and P.M. Fauchet, Electrically tunable porous silicon active mirrors, 556-560, Copyright 2003, with permission from John Wiley and Sons.

distinguish between signals from different vapors, is low and would require the monitoring of other properties of the reflectance spectra, such as spectral shape or response time. A typical complete sensor device setup involves an InGaAs-photodetector for observing the changes in reflected IR radiation, introduced via a bifurcated optical fiber.

Chemical instability due to the natural oxidation of a PSi surface is detrimental to the optical transduction mechanism. Oxidation leads to a gradual blue shift of the reflectance peak (drift of the sensor baseline) and can also diminish sensitivity. Jalkanen et al. [127] describe a method of thermal carbonization to passivate the PSi layers for improved stability. The freshly prepared PSi layer is sealed into a quartz tube and exposed to a continuous flow of a 1:1 volumetric ratio of acetylene and nitrogen. The PSi layer is then simultaneously raised to 500 °C in a furnace for 10 min,

then cooled under just nitrogen to complete the carbonization process. Carbonization below 600 °C creates a stabilized sensor resistant to humidity. In contrast, a hydrophilic surface is created by carbonization above 680 °C, which is ideal for for a sensor sensitive to humidity changes [127, 128].

The delicate method of reflectance monitoring involves challenges including reproducibility due to the imprecise positioning of optical fibers. To improve reproducibility of the monitoring of optical property changes, Karcali et al. [134] have developed an elegant fabrication process to integrate a fiber optic cable directly into the bulk Si. The new design (Figure 2.20) features more robust reflectivity measurements by eliminating measurement error from the variation in fiber optic cable alignment angle. Once the device is fabricated, each subsequent experiment can be quickly and easily assembled. In contrast to the traditional experimental setup (Figure 2.20a), which requires the PSi sensor to be secured to a"basement" or base layer and a carefully positioned fiber optic cable, the new design (Figure 2.20b) can be flexibly positioned. This is optimal for sampling vapors in difficult to access environments.

The first fabrication step involves hole milling by reactive ion etching (RIE) of the insulator backside (handle layer) of a silicon on insulator (SOI) wafer. A thin oxide layer between the silicon and insulator is used to reliably stop the RIE process [134]. The porous layer is formed by electrochemical anodic etching in a 1:2 HF (40 %) and ethanol (95 %) solution. The etching current density is set to 600 $\mathrm{mA/cm^2}$ for 120 s to thin the silicon layer by electro-polishing. The current density is then adjusted linearly from 100 $\mathrm{mA/cm^2}$ to 20 $\mathrm{mA/cm^2}$ for 10 s, to create an index profile to suppress undesired reflections. This is followed by 876.8 s of sinusoidally modulated current of 19 $\mathrm{mA/cm^2}$ to 21 $\mathrm{mA/cm^2}$ to fabricate the detection multilayers. A final linear change over 5 s from 20 $\mathrm{mA/cm^2}$ to 0.2 $\mathrm{mA/cm^2}$ again eliminates unwanted reflections [134]. The fiber optic cable is then integrated into the PS sensor by fixing with epoxy at an optimized position. The authors admit that this new design necessitates a "thorough

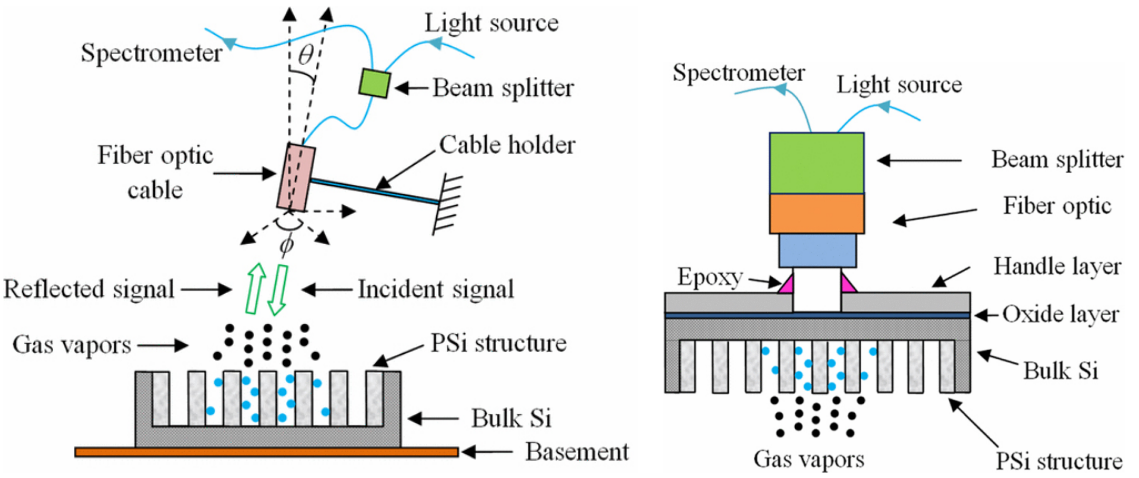

Figure 2.20: Comparison of optical measurement schematics of (a) a conventional reflectance PSi sensor and (b) an integrated PSi sensor. ©2013 IEEE. Reprinted, with permission, from T. Karacali, U.C. Hasar, I.Y. Ozbek, E.A. Oral, H. Efeoglu, Journal of Lightwave Technology, 31, 2013.

and methodological preparation" [134]. This extensive process of device fabrication could represent a significant barrier to adaptation into ready applications.

PSi sensor device optical measurements were compared for ethanol, methanol, propanol, and butanol. The mean and standard deviation of wavelength shifts in reflectivity for each organic vapor are listed in Table 2.1. The measurements from the integrated PSi sensor had a lower variance for all vapors [134]. Both the integrated and conventional PSi sensor reported unique reflectivity wavelength shifts for butanol, propanol, ethanol, and methanol. The integrated PSi sensor, as opposed to a conventional PSi sensor, was able to detect distinct reflectivity wavelength shifts for 1-propanol versus 2-propanol. However, the conventional PS sensor could differentiate between 1-butanol and 2-butanol where the integrated PSi sensor could not [134].

In the interest of obtaining selectivity of optical sensors to different chemical species, Jalkanen el al. [127] propose monitoring multiple aspects of the reflectance spectra. In addition to an observed redshift, the *shape* of the spectra was also slightly altered in response to the various vapors. The full width at half maximum (FWHM)

Table 2.1: Wavelength shifts in reflectivity measurements (in nm). The difference in the standard deviations of the conventional and integrated sensor are also provided.

Organic solvent	Conventional Sensor	Integrated Sensor	STD Difference
1-butanol	40.00 ± 1.35	39.00 ± 0.93	0.42
2-butanol	39.00 ± 1.25	39.00 ± 0.85	0.40
1-propanol	38.00 ± 1.10	37.00 ± 0.77	0.33
2-propanol	38.00 ± 0.98	36.00 ± 0.68	0.30
Ethanol	35.00 ± 0.90	34.00 ± 0.63	0.27
Methanol	30.00 ± 0.80	28.00 ± 0.55	0.25

of the spectra was measured to compare the degree of spectral shape alteration with acetone, decane, and methylamine having the strongest effect [127]. While is it normal for the FWHM value to increase with a redshift in the spectra, the FWHM change due to the organic vapors was greater than expected, in the case of acetone, or the inverse of that expected, in the case of decane. Instead, adsorbate affinity to PSi layers with different indexes of refraction, related to porosity, is a possible reason for the FWHM change [127]. Selectivity of the optical sensors to acetone and methylamine is illustrated in Figure 2.21, by analyzing both the redshift and spectral shape change.

2.4.2 Conductometric transduction

Conductometric based PSi chemical sensors, sensitive to resistance changes as a function of gas analyte concentration, represent one of the simplest and least expensive methods to construct a complete chemical sensing device [85, 142]. Resistance is a function of both charge carrier mobility and density, the latter of which changes in response to the surrounding gas analytes. This corresponds to an adjustment of the position of the Fermi level in the PSi sensor. The precise response mechanism for the transduction of the interaction with gas analytes through a change in charge carrier concentration is a subject of contrasting opinions and a rich topic of continuing study [8, 25, 142, 241]. The presentation of a full fundamental response mechanism

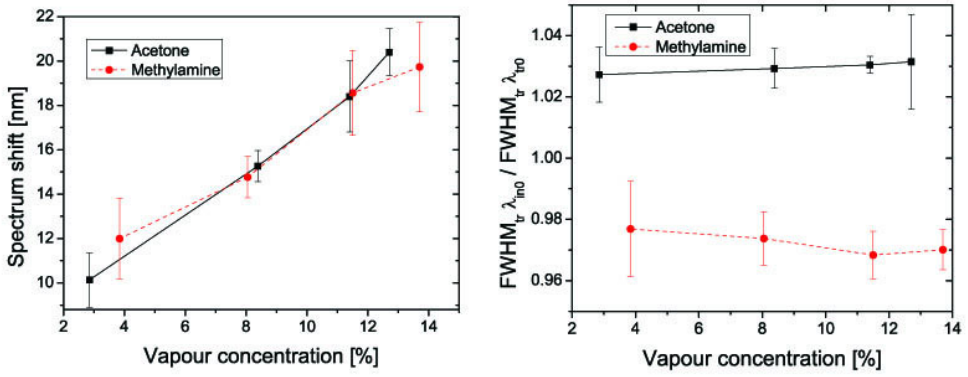

(a) The spectral redshifts measured under acetone and methylamine vapour exposure.

(b) Relative change of the normalized FWHM value as a function of acetone and methylamine vapour concentration.

Figure 2.21: Comparison of redshift and FWHM reflectance spectral change in response to acetone and methyl amine at various concentrations to demonstrate optical sensor selectivity. Reprinted with permission from Optics Express, 17, Jalkanen et al. Optical gas sensing properties of thermally hydrocarbonized porous silicon Bragg reflectors, 5446-5456, Copyright 2009, with permission from the Optical Society of America.

is discussed in detail in Chapter 4. In general, Gole and Ozdemir [94] describe the changes in the extrinsic semiconductor charge carrier populations that occur in the presence of inorganic gas analytes as follows. An analyte acting as a Lewis base can donate electrons to the PSi interface. For p-type PSi, the majority charge carriers, electron holes, combine with the donated electrons and are reduced in number therefore increasing the resistance of the PSi sensor. In contrast, for n-type PSi, the majority charge carriers are electrons and so the electron transfer from analytes increases the majority charge carrier population, thus decreasing resistance [94]. Device electronics, potentially fully integrated with the PSi sensing interface on a single Si wafer, can be easily expanded into an array of conductometric PSi sensors with only a minimal increase in overall device size [147]. Careful considerations for conductometric PSi sensors include developing ohmic contacts and choosing optimal direct current (DC) or alternating current (AC) electrical operating conditions [142]. Ohmic contacts, characterized by a low-resistance or non-rectifying junction between the metal

contact and PSi semiconductor, are essential for producing a low-power device, preferable in particular for portable applications [163, 233]. In general, a resistance-based PSi sensor is operated in DC mode.

Development of both the sensitivity and selectivity of conductometric PSi sensors has been explored through select modifications of the PSi interface. Yan et al. [279] have studied room temperature detection of NO_2 with a PSi layer enhanced by ZnO electrochemical deposition. The PSi sensors were exposed to various concentrations of gas by injecting the analyte gas into an enclosed chamber. The PSi layer was fabricated by a double cell anodic etching of p-type silicon wafers in a 1:2 HF and DMF solution with a current density of $100\,mA/cm^2$. Pt electrodes 100 nm thick were deposited onto the PSi surface by RF magnetron sputtering [279]. The final, relatively large, sensor measured $4\,mm \times 16\,mm$ with two $3\,mm \times 3\,mm$ Pt electrodes. SEM characterization revealed that the morphology of the deposited ZnO nanostructures depended on the pH value of the electrochemical solution [279]. As seen in Figure 2.22, a pH value of 6 resulted in nanosheets of ZnO, a pH value of 6.5 resulted in nanorods, and a pH of 7 encouraged the formation of dendritic ZnO nanostructures.

The resistance change response of the PSi/ZnO sensors was compared showing samples with ZnO nanosheets to have the greatest increase in sensitivity and a sample with dendritic ZnO to have almost the same sensitivity as PSi. Yan et al. [279] propose that the reason for the better gas sensing properties of the nanosheets is due to either possible higher surface area or a more apparent interface effect between the nanosheets and PSi, since the thickness of the sheets is much smaller than the diameter of the nanorods. Additionally, the ZnO nanostructured PS sensors exhibited a high selectivity to NO_2 over NH_3, H_2S, and organic vapors. The sensor response to 1 ppm NO_2, defined as $S = R_g/R_0$ where R_g and R_0 denote the resistance of the sensor in the test gas and in clean air, respectively, was approximately 3 times larger than 10 ppm NH_3 and 4 times larger than 10 ppm H_2S. However, it should be

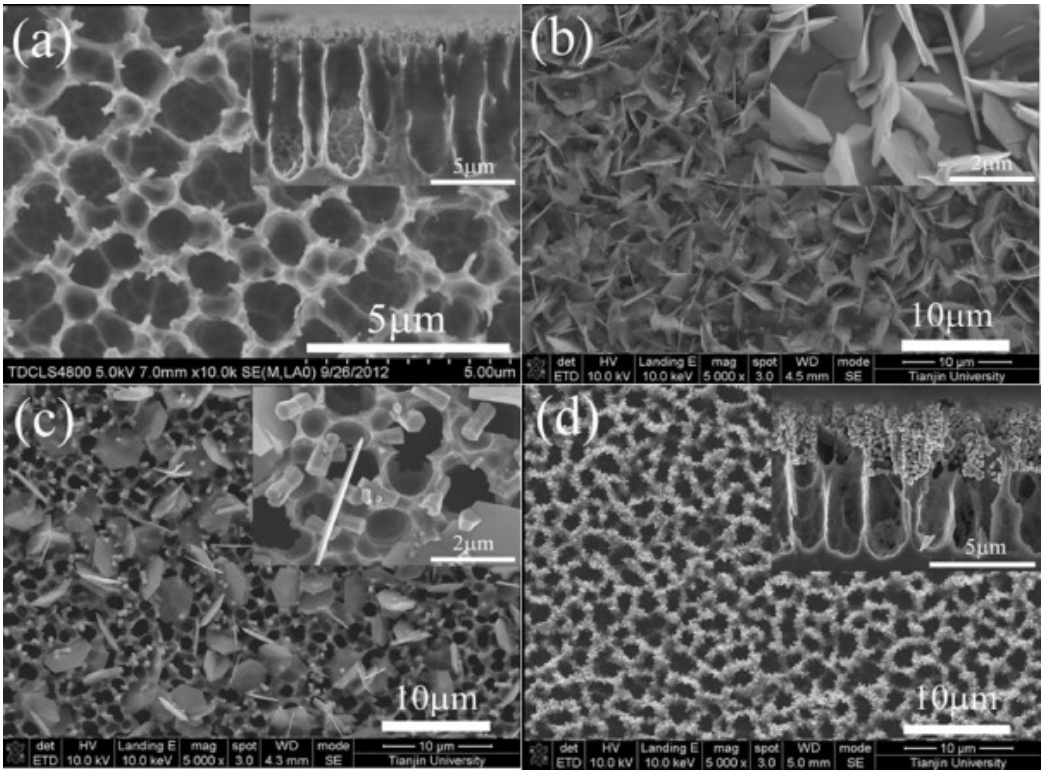

Figure 2.22: SEM images of PS and ZnO nanostructures/PS: (a) PS; (b) pH 6, nanosheets; (c) pH 6.5, nanorods; (d) pH 7, dendritic nanostructures; the inset in (a) and (d) are cross-sectional view of the corresponding products. The inset in (b) and (c) are the high magnification SEM images of the corresponding products. Reprinted from Electrochimica Acta, 115, Yan et al., Electrochemical deposition of ZnO nanostructures onto porous silicon and their enhanced gas sensing to NO_2 at room temperature, 297-305, Copyright 2014, with permission from Elsevier.

noted that PSi sensors, even without surface modification, have been shown to be more sensitive to NO_2 than other gas species [14, 20, 21, 202]. The sensor response to methanol, ethanol, and acetone was negligible [279].

Tungsten oxide nanowires also appear to enhance the response to NO_2 [174]. Ma et al. [174] prepared PSi/WO_3 nanostructured sensors by first coating PSi with a thin film of tungsten by magnetron sputtering. Tungsten is deposited up to 150 nm thick on PSi, and then forms nanowires by annealing under oxygen and argon at temperatures of 600 °C to 750 °C for 1 h. The resistance change of the PSi/WO_3 nanowire sensor was measured in response to NO_2, NH_3, ethanol, and acetone. The sensor showed selectivity to NO_2 with a sensor response approximately 6 times greater for 5 ppm NO_2 than 50 ppm NH_3, 100 ppm of ethanol, and 100 ppm of acetone. The optimal testing temperature of 100 °C is analogous to traditional metal oxide devices. The sensor response to the other gas analytes was negligible [174].

Similarly, the PSi sensor response to NO_2 was enhanced by the addition of TeO_2 nanowires [278]. Tellurium powder was thermally evaporated onto the PSi sample for 2 h at 400 °C. The response (change in resistance) of the PSi/TeO_2 sensor to 1 ppm of NO_2 was approximately 5.7 times the response of blank PSi [278]. This result demonstrates the potential for signal improvement with the proper deposition of nanostructured metal oxides, but the use of TeO_2, an extremely dangerous material, and the complexity of the approach used to prepare the surface does not justify its use over similarly sensitive surfaces.

Nanopore coated microporous PSi interfaces have been created to detect low ppm levels of NH_3, NO_x, CO, SO_2, H_2S, and PH_3 [15, 163, 197, 198]. These are rapidly responding, reversible, and sensitive sensors, which operate at room temperature. Selectivity to different gas analytes has been established with the deposition of select metal oxide nanoparticles. These nanoparticles direct a reversible electron transduction, predicted by the now developing IHSAB principle [92, 94]. The metal oxide

nanoparticles are amenable to in-situ modification, thus extending the range of selective responses and providing additional applications through the modification of the metal oxide nanostructures at the PSi gas sensor interface. The details of fabrication are described in section 3.1.

Metal oxide deposition on the PSi interface has been shown to increase or decrease the resistance response of the PSi sensors to inorganic analyte gases depending on the combination of analyte and decorating metal oxide. The recently implemented Inverse Hard/Soft Acid/Base (IHSAB) model, which predicts the interaction of acidic, basic, and amphoteric gas analytes with nanostructure treated p- and n-type PS sensor interfaces [92], complements the tenants of the HSAB concept [207] and serves as an explanation of this phenomenon.

Figure 2.23 shows the estimated positions of deposited nanostructures (acids) and analytes (bases) on the IHSAB scale relative to p- or n-type PSi. The interaction strength is correlated with the relative acidity and basicity of the reactants, as strong acids react with strong bases and weak acids interact with weak bases, resulting in significant ionic and covalent bonding, respectively. We wish to minimize this bond formation. A nanostructure-treated PSi gas sensor can be made to behave in a physisorption/weak chemisorption dominated mode, and the IHSAB concept can be used to explain this behavior. Here, the physisorption (electron transduction) process is found to dominate for primarily strong acid-weak base and weak acid-strong base interactions. The emphasis is to impede bond formation by creating a molecular orbital mismatch. By assessing trends within the IHSAB framework, appropriate selections can be made for the modification of the PSi hybrid interface with nanostructured metal/metal oxide deposits to create a range of sensitivities for a number of gases [87]. A weak interaction with minimal chemical bonding occurs if the donor orbital (highest occupied molecular orbital, HOMO) energy is not well matched with the acceptor (lowest occupied molecular orbital, LUMO) energy. As the

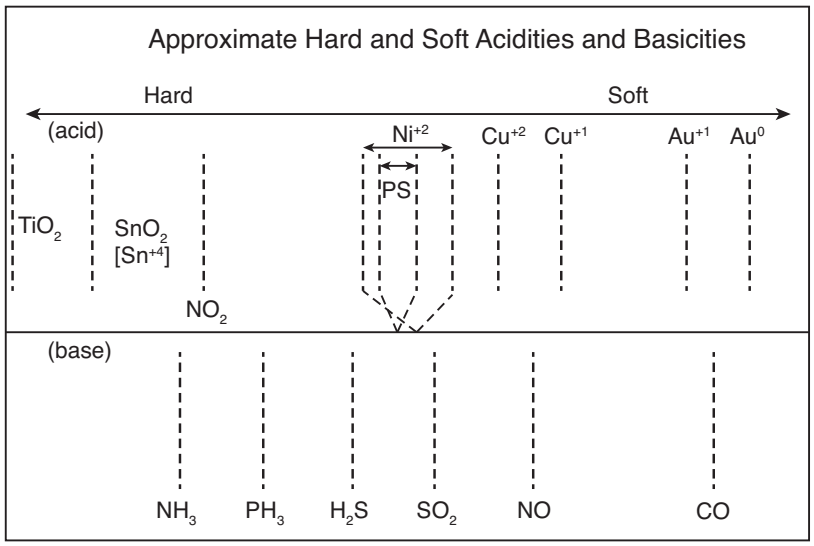

Figure 2.23: IHSAB scale and estimated hard and soft acidities and basicities based on response changes relative to a p- and n-type PSi interface. Reprinted with permission from ChemPhysChem, 13, J.L. Gole, E.C. Goude, and W. Laminack, Nanostructure-driven Analyte-Interface electron transduction: A general approach to sensor and microreactor design," 549-561, Copyright 2012, with permission from John Wiley and Sons.

HOMO (donor)-LUMO (acceptor) energy gap decreases, there will be more charge transfer and a stronger Lewis acid-base interaction. The greater the separation, the greater the orbital mismatch, leading to the greater response of the sensor [87]. As dictated by the IHSAB scale, Au_xO will produce the largest response to NH_3 and TiO_2 and SnO_2 will produce the largest response to CO. The IHSAB principle may, in fact offer an alternate explanation to the observations of Yan et al. [279].

Figure 2.24 demonstrates the effect of nanoparticles on the detection of PH_3. If nanoparticles of NiO, which lie just the the soft side of PSi on the IHSAB scale (Figure 2.23) are deposited on a p-type PSi sensor, they slightly enhance the response to PH_3. The NiO nanostructure shifts the PSi interface toward a position slightly farther away from PH_3, increasing the inverse hard/soft relation and improving the physisorption directed response. As a further demonstration of the IHSAB principle, a p-type PSi sensor decorated with Au_xO nanoparticles enhances the response to PH_3 to an even greater degree. This is due to the fact that Au_xO lies even further away

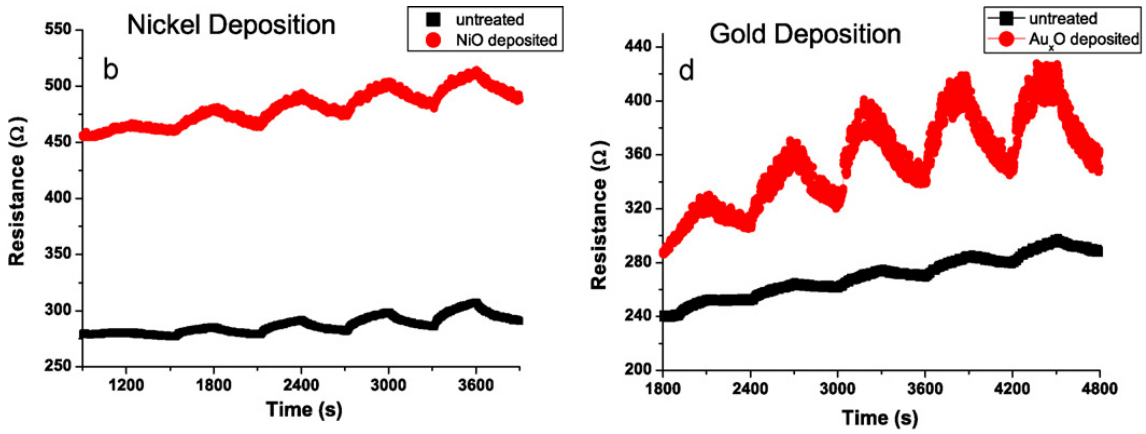

Figure 2.24: Comparison of resistance response to 1 ppm to 5 ppm of NH_3 of untreated p-type PSi (black line) and NiO (left) and Au_xO (right) treated PSi interfaces (red line). Reprinted from Sensors and Actuators B: Chemical, 151, S. Ozdemir and J. L. Gole, A phosphine detection matrix using nanostructure modified porous silicon gas sensors, 274-280, Copyright 2010, with permission from Elsevier.

from PH_3 on the IHSAB scale (Figure 2.23) than both PSi and NiO, representing an increase in orbital mismatch. Acting as a base, PH_3 contributes electrons to a p-type PSi sensor, which combine with and thus decrease the concentration of the majority charge carriers (electronic holes), corresponding to an increase in resistance [198].

The IHSAB model guides the choice of metal oxide nanoparticles deposited onto the PSi micro-/nanoporous interface to create an array of selectively tuned sensors [87]. The relative change in response to NO and NH_3 for an n-type PSi sensor resulting from various nanostructure depositions is summarized in Table 2.2, where the change is described by [87],

$$\Delta = \frac{\Delta R(\text{deposited})/R_0(\text{deposited})}{\Delta R(\text{untreated})/R_0(\text{untreated})}\,. \tag{2.39}$$

This array has recently been expanded by in-situ modification of the deposited metal oxide nanostructures. The metal oxide nanostructure islands on the PSi sensors have been functionalized using triethlyamine in a manner similar to the nitridation of TiO_2 described previously [151]. The sensor is then aged for 24 h in a desiccator before testing, thus allowing unreacted triethlyamine to evaporate. The in-situ modification of the deposited metal oxides changes the reversible interaction with NO, NH_3, and

Table 2.2: Response change, Δ, due to nanostructure depositions on n-type PSi sensor. The changes in response correlate with shifting the position of the PSi sensor on the IHSAB relative to the target analyte gas species. An increase in response indicates a greater mismatch position on the IHSAB scale and thus orbital mismatch.

	Nanostructured Deposition		
Analyte Gas	TiO_2	NiO	Au_xO
NO	-12[a]	4	1.5–2
NH_3	3.5–4	1.5	3

[a] Recorded signal results as the strong acid TiO_2 attracts electrons from the amphoteric NO radical, forcing NO to act as an acid rather than a base.

other analytes in accordance with relative shifts predicted on the IHSAB scale and result from the creation of oxynitrides [98, 150].

Nitridation shifts the position of a NiO decorated PSi sensor toward the soft acid side of the IHSAB scale [150], farther away from NH_3. This enhances the hard/soft inverse matching, increasing the response shown in Figure 2.25b as manifest by a larger decrease in resistance in the presence of NH_3. In contrast, the NiO treated PSi interface moves closer to NO upon nitridation. This enhances the molecular orbital matchup, decreasing the sensor response. This is shown in Figure 2.25a as a smaller decrease in resistance in the presence of NO [149].

Sulfur group functionalization is also facilitated on the metal oxide decorated PS interface following a similar deposition process as that applied for nitridation [146, 150]. Exposure to diethyl sulfide and/or ethane or butane thiol, analogous to the nitridation process, now produces a more complex functionalization. Rather than a change in basicity or acidity of the metal oxide/PS interface, the interaction with the gas analytes suggests a change in molecular electronic structure explained by the IHSAB model [146, 150]. The sulfur and nitrogen donate electron density, shifting the metal oxide interface towards the softer acid end of the IHSAB scale (Figure 10). When applied to TiO_2 decorated PSi, the doped TiO_2 moves closer to the fixed

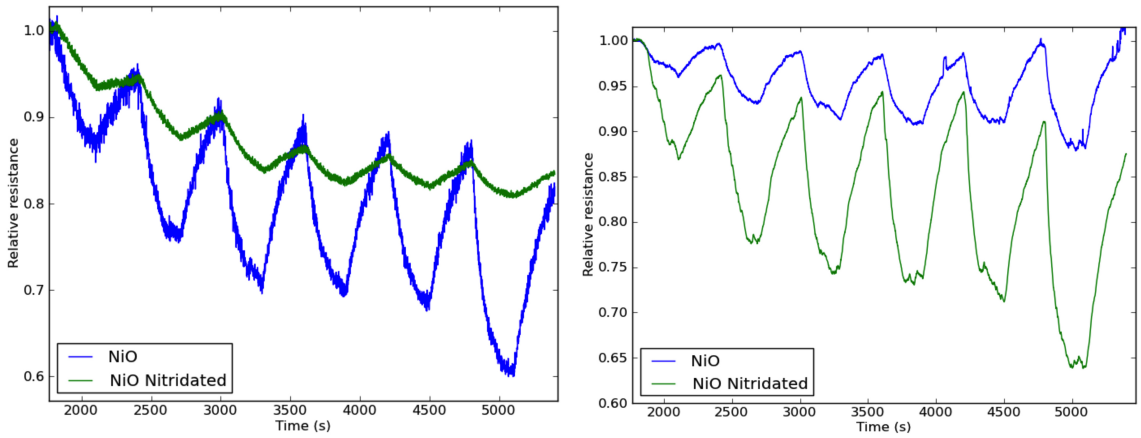

(a) (b)

Figure 2.25: Response of NiO/PSi sensor (blue) and nitridated NiO/PSi sensor (green) to (a) NO and (b) NH_3. Reprinted with permission from W. Laminack and J.L. Gole (2013) Nanostructure-directed chemical sensing: The IHSAB principle and the effect of nitrogen and sulfur functionalization on metal oxide decorated interface response. Nanomaterials 3, 469-485, Creative Commons License.

position of NH_3 or NO, decreasing the interface/analyte orbital mismatch and the sensor signal decreases. However for NiO, which lies equidistant between NH_3 and NO on the IHSAB scale, a sulfur/nitrogen induced shift to the softer acid side increases the orbital mismatch with NH_3, increasing the sensor response, and decreases the orbital mismatch with NO, decreasing the sensor response (Figure 12). Laminack and Gole encourage the application of these results to form "materials sensitivity matrices" for a given analyte to facilitate sensing gas analyte mixtures [146, 150, 151].

Light enhanced PSi gas sensing has also been studied [120, 149]. Hui-Qing et al. [120] have measured the enhancement of PSi sensor response to NO_2 in the presence of UV radiation. PSi at different levels of porosity are formed by electrochemical anodization of p^+-type silicon wafers (0.01 Ω cm to 0.012 Ω cm) in 1:1 HF and ethanol with current densities of 40 mA/cm^2, 60 mA/cm^2 and 80 mA/cm^2. The porosities, measured by the gravimetric method, were 65.2 %, 71.1 %, and 76.8 % respectively. To measure the potential change in sensor response to NO_2 due to illumination, a UV lamp was introduced in the enclosed testing chamber. UV radiation was found

to increase the relative resistance change of the PSi sensors in the presence of NO_2. The PSi with the highest porosity was observed to have the greatest enhancement of sensor response, which was observed to increase by a factor of 4 to 1 ppm of NO_2. Hui-Qing et al. [120] suggest that this is due to the large number of photo-generated charge carriers of the p^+-type PSi facilitating the reduction and oxidation chemistry of the analyte and PSi sensor interface [120].

With the high cost and limited accessibility of UV photons, in combination with studies of the effects of metal oxide deposition and in-situ nitridation, Laminack and Gole [149] take advantage of the visible-light absorbing spectrum of $TiO_{2-x}N_x$. TiO_2 and $TiO_{2-x}N_x$ are fractionally deposited to porous silicon, fabricated from n-type silicon wafers as described previously [92]. The metal oxide/PSi and nitridated metal oxide/PSi sensors are tested in response to NH_3 and NO_2. As a base, NH_3 donates electrons to n-type PSi, increasing the majority charge carriers, thus decreasing the resistance. Both white light and UV light were shown to have no effect on the resistance response of the PSi sensor prior to metal oxide deposition. Upon deposition of the hard acid TiO_2, the interface is shifted to the hard acid end of the IHSAB scale and the response to NH_3 increases. After *in-situ* conversion to $TiO_{2-x}N_x$, the interface obtains a more basic character reducing the capture of the NH_3 donated electrons and the sensor response. In the presence of UV light, the response for the TiO_2 decorated PSi sensor improves by over 100 % whereas visible light has no effect. In contrast, as shown in Figure 2.26, the response to NH_3 is increased in the $TiO_{2-x}N_x$ modified PSi sensor for both UV and white light [25]. Laminack and Gole [149] explain that UV and white light, which can now be absorbed by $TiO_{2-x}N_x$, causes the $TiO_{2-x}N_x$ to become more acidic, enhancing the electron withdrawing power and thus increasing the sensor response.

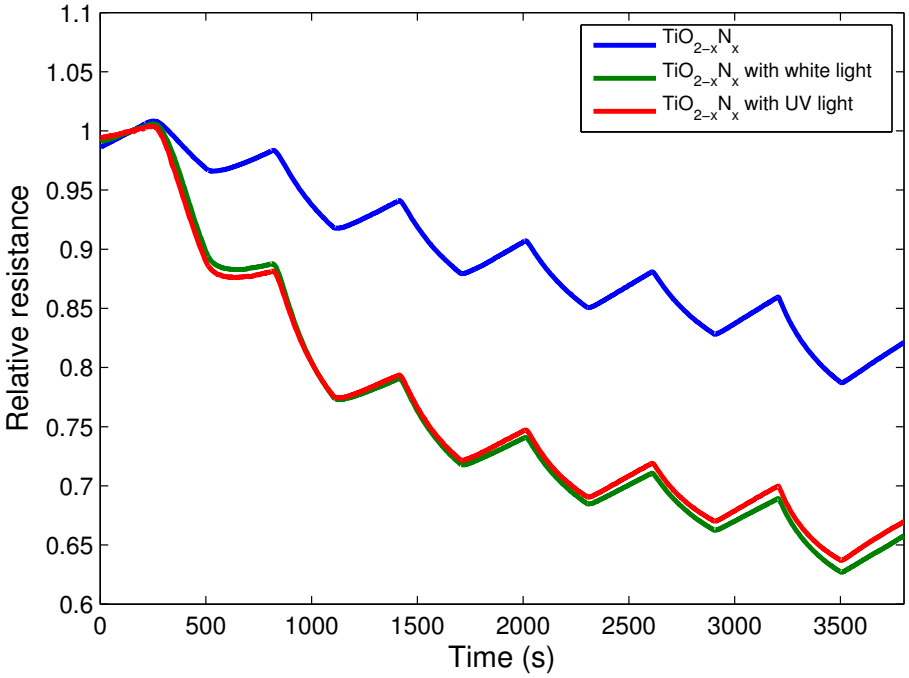

Figure 2.26: Relative resistance response to NH_3 by $TiO_{2-x}N_x$ decorated n-type PS sensor under UV and white light. Reprinted with permission from Advanced Functional Materials, 23, W. Laminack and J.L. Gole, Light Enhanced Electron Transduction and Amplified Sensing at a Nanostructure Modified Semiconductor Interface, 5916-5924, Copyright 2013, with permission from John Wiley and Sons.

2.4.3 Impedance transduction

Beyond measuring the changes in resistance across a PSi sensor operating with direct current, complete impedance spectra can provide additional insights into the interactions between chemical analytes and a PSi interface. Impedance-based PSi sensors have been used for detection of organic solvents [8, 123, 167] and organic vapors [189] by monitoring changes in the impedance magnitude, phase angle, conductance, and capactitance as a function of frequency, for static experimental conditions, or as a function of time for dynamic conditions. Additional features, such as changes in the characteristic frequency of maximum complex impedance components and characteristic time of charge accumulation have also been used as detection signals [189]. A compete analysis of the impedance characteristics of a PSi sensor involves the development of an equivalent circuit model (Figure 2.27), ideally based on real features of the PSi interface.

Archer et al. [8] developed a PSi sensor for the purpose of detecting a range of liquid phase organic solvents with various dielectric constants, dipole moments, electronic polarizability, and bond character. The PSi sensor was fabricated from p-type silicon (10 Ω cm to 20 Ω cm) in a 4 wt% HF in DMF with a current density of 4 mA/cm^2 to create pores with a diameter of ∼1 µm. An etch duration of 70 min produced pore depths of 20 µm. Molecules interacting with the PSi interface cause a change in current, which the authors attribute to a change in carrier concentration in the crystalline silicon (c-Si) substrate. Archer et al. [8] created a space charge region modulation (SCRM) model to explain this change. The SCRM model is modeled after a field effect transistor (FET), where current flows through a channel from a source to drain terminal due to an applied voltage. The current, proportional to the number of charge carriers and the dimensions of the channel, can be modulated by applying an electric field to a gate terminal between the source and drain. In the SCRM model, the channel is synonymous with the c-Si substrate and the gate

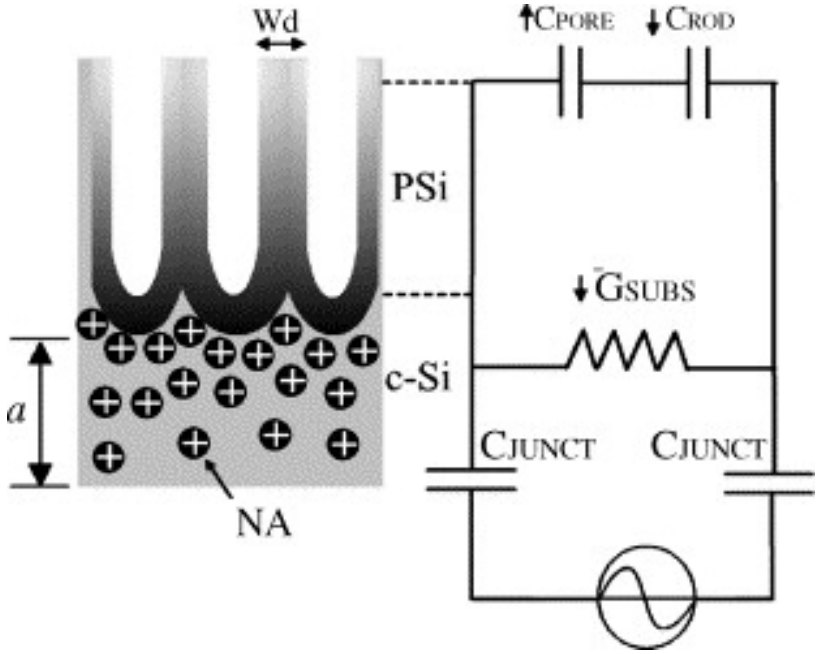

Figure 2.27: Schematic and equivalent circuit model of a PSi layer composed of pores and crystalline silicon (c-Si) rods supported on a c-Si substrate. The PSi layer is represented by capacitors in series. The c-Si substrate is represented by a resistor, G_{SUBS} and the metal-silicon junction for the sensor contacts are represented by C_{JUNCT}. In the presence of of a positive charge on the PSi surface, the space charge width (W_{d}) of the PSi layer increases, the charge carrier density (N_{A}) redistributes, and the width of the conductance channel (a) is reduced. The arrows on the equivalent circuit model indicate the changes to each element corresponding to the changes in the schematic. Reprinted from Sensors and Actuators B, 106, M. Archer et al., Electrical porous silicon chemical sensor for detection of organic solvents, 347-357, Copyright 2005, with permission from Elsevier.

electrode is represented by the PSi layer. Upon interaction with liquid analytes, the PSi layer acting as a charged layer, can modulate the field in the c-Si substrate. This modulation is represented as a change in the space charge region by charge redistribution and a change in the width of the conductive channel (Figure 2.27).

Archer et al. [8] suggest the equivalent circuit, shown in Figure 2.27, with circuit elements corresponding to physical features of the PSi interface. Changes to the conductance and capacitance of the sensor upon absorption of the various organic solvents into the PSi layer, were correlated with the equivalent circuit elements and SCRM model. Demonstrated in Figure 2.28, the impedance-based PSi sensor was able to selectively detect chloroform, acetone, ethanol and acetonitrile [8]. The organic solvents induced different magnitudes of conductance and capacitance change, which appeared to correlate with the varying dielectric constants of each solvent. However, as will be discussed in Chapter 7, careful investigation of changes to the equivalent circuit upon exposure liquid organic solvents requires a comparison of complex impedance plots (Nyquist plots). By correlating experimental complex impedance plots with an equivalent circuit model, the changes to each individual equivalent circuit element can be precisely characterized [123]. While presenting a unique equivalent circuit model and explanation of changes in carrier concentration (SCRM model), the discussion by Archer et al. [8] focuses on changes to conductance and capacitance corresponding to a parallel C-G circuit only at a single frequency. A study comparing the response of both p-type and n-type PSi sensors presents results suggesting instead that the dipole moment is instead responsible for the changes to the complex impedance plots (Chapter 7).

Liyanage and Blackwood [167] have achieved enhanced selectivity between ethanol and acetone by attaching functional organic groups onto a porous silicon impedance sensor. Here, different chemical modifications were used. Modification with 1-decane yielded a hydrophobic non-functionalized hydrocarbon surface and modification with

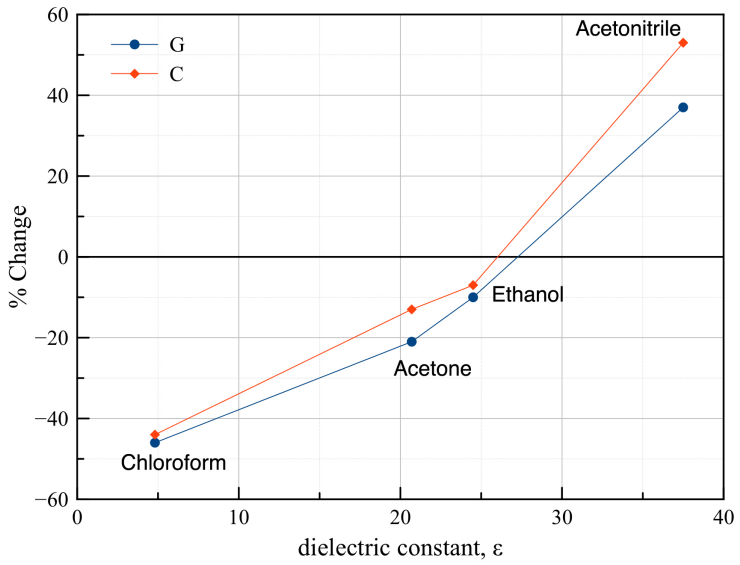

Figure 2.28: Measured change in capacitance (% C) and conductance (%G) with respect to the reference value as a function of the dielectric constant for chloroform, acetone, ethanol and acetonitrile. Adapted from Sensors and Actuators B, 106, M. Archer et al., Electrical porous silicon chemical sensor for detection of organic solvents, 347-357, Copyright 2005, with permission from Elsevier.

undecylenic acid produced an amphipathic (having both hydrophobic and hydrophilic areas) carboxylic acid surface. The authors proposed that these two differently prepared PSi interfaces would undergo distinctly different interactions with the organic solvents [167]. The PSi was formed by an electrochemical etch of p-type Si wafer ($10\,\Omega\,\mathrm{cm}$) in a 1:2:1 solution of HF, ethanol, and deionized water for 20 min with a current density of $22\,\mathrm{mA/cm^2}$ under backside 200 W halogen lamp illumination. After freeze-drying to prevent cracking, the PSi was functionalized with either 1-decene or undecylenic acid [167]. The functionalization method involved exposing the PSi layer to a heated mixture of paraffin oil and organic molecules for 24 h. The paraffin was then removed by immersion in pentane for 1 h. The impedance of both the 1-decane- and undecylenic acid-functionalized PSi sensors decreased with increasing ethanol-in-acetone concentration. However, the linearity of the response was not the same for both types of prepared PSi sensors. The sensor functionalized with 1-decane displayed

a linear response increase for an increasing concentration of ethanol in acetone. However, the undecylenic acid functionalized sensor did not produce a continuous linear response. The authors suggest that this is due to a difference of interactions available to the functionalized surfaces. The 1-decane treated surface can only undergo weak van der Waals interaction, but the undecylenic acid can undergo strong H-bonding. Therefore, the undecylenic acid interacts more strongly with ethanol than acetone leading to a non-linear response pattern as a function of the changing concentration [167]. This suggests that functionalization the PSi surface with undecylenic acid, creating an amphipathic surface capable of strong H-bonding, represents a step towards developing an array of selective PSi sensors. In this case, each sensor of an array is treated with different functional groups providing individualized interacting surfaces targeted to different analytes [167].

2.5 Extension to Porous Silicon Microreactors

Chemical synthesis, analysis of chemical kinetics, and process development all benefit from the many advantages offered by microreactors [130]. Microreactors are particularly useful for surface-supported heterogeneous catalytic reactions, as only small volumes of catalyst are necessary, the catalyst is inherently separated from the reaction products, and essential thermal conditions are easily managed [36, 171, 225]. These conditions allow for swift, consistent, and reliable screening of catalytic materials and optimal reaction conditions [252]. Low reaction volumes are ideal not only for laboratory use but also for on-site and on-demand production of fine chemicals [168]. Examples include hydrogen fuel production through steam reforming, membrane reactor hydrogenation and dehydrogenation, and catalytic oxidation and reduction for gas purification, [166, 168, 238, 282]. Biosensing and glucose monitoring microreactors have been fabricated by the immobilization of enzymes or glucose oxidizing catalysts [66, 154].

Heterogeneous catalysts are those that are in a different phase than the reactants. Most commonly, the catalyst is a solid upon which the gas or liquid phase reactants absorb. Once the catalyzed reaction is complete, the products then desorb from the catalyst. A great advantage of heterogeneous catalysis over homogeneous catalysis is the ease of separating the catalyst from the reaction products. Immobilization of a catalyst onto a support can facilitate this separation process in both traditional batch reactions and in the context of microreactors [225].

The effectiveness of heterogeneous catalysts supported on microreactor surfaces is highly dependent on the active surface area. In order to increase the catalytic performance of microreactors, various modifications have been developed to further enhance the surface area to volume ratio. This was conventionally accomplished using a fixed bed of microchannels packed with catalyst pellets [170, 203], by introducing flow obstacles such as pillars [225], or by depositing a high-surface area catalyst coating such as a zeolite [218]. Porous silicon offers a ideal alternative to these surface enhancing methods. Firstly, silicon is a particularly favorable material for microreactors. Robust micromachining processes, due to the extensive use of silicon in the electronics and semiconductor industry, offer a high level of precision to create a variety of structures with small feature size [206]. Silicon is chemically inert, thermally stable, mechanically rigid, and has beneficial electronic properties. Additionally, silicon micromachining allows for facile integration of sensors, actuators, and heating elements [282]. PSi, which is completely integratable with silicon technology, can be utilized to both enhance surface area and uniquely support catalyst materials.

2.5.1 PSi layer enhancement microreactors

Roumanie et al. [225] used deep reactive ion etching (DRIE) to create a high aspect ratio nanostructuration on the silicon microreactor surface called black silicon. Black

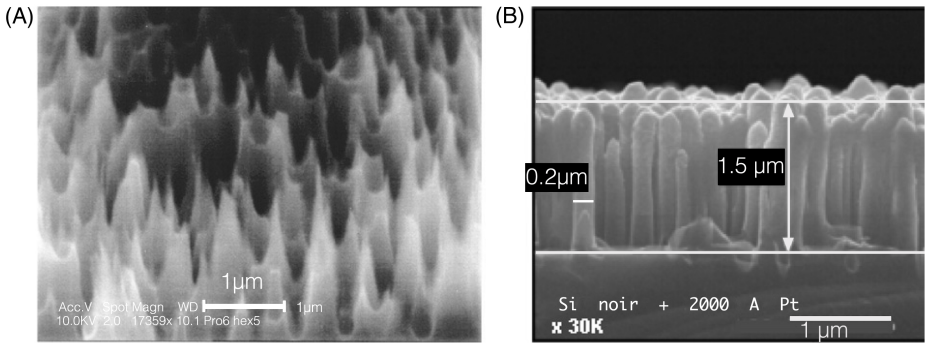

Figure 2.29: Black silicon (a) formed by DRIE and after Pd catalyst deposition (b). Reprinted from Chem. Eng. J. 135, Roumanie M., Delattre C., Mittler F., et al Enhancing surface activity in silicon microreactors: Use of black silicon and alumina as catalyst supports for chemical and biological applications, S317-S326, Copyright 2008, with permission from Elsevier.

silicon, a type of porous silicon named for its light absorbing property, can be fabricated via DRIE, laser chemical etching, pulsed electrochemical etching, fast atom beam etching, or recently by metal-assisted chemical etching [172]. The needle-like structure of black silicon, shown in Figure 2.29, has been described as an "inverted" porous silicon structure [242].

Black silicon was prepared on planar silicon, which was then diced and fitted into a fixed bed microreactor [225]. Pt nanoparticles were deposited on both the planar silicon and black silicon (Figure 2.29b) surface by cathodic sputtering. Catalytic activity enhancement was measured by comparing the conversion of CO to CO_2 for Pt deposited surfaces with and without the black silicon nanostructuration. Roumanie et al. [225] reported a factor of 10 increase in surface activity in the microreactors with the black silicon. For comparison, a porous alumina layer deposited on the planar silicon, requiring a several step washcoating procedure, exhibited an even greater increase in catalytic activity. However, black silicon fabrication is comparatively much simpler to use as it is produced by standard silicon micromachining fabrication methods [225].

To enhance the performance of the catalytic oxidation of rosalva to costenal within

a microstructured reactor, Cao et al. [36] supported a silver catalyst on PSi etched into the reactor surface. The overall structure of the microreactor was formed in three main steps, shown in Figure 2.30. First, a 6 mm wide reaction channel was formed by DRIE with a depth of 0.12 mm. This was followed by Ag metal-assisted HF chemical etching to form a 1 µm to 2 µm deep PSi layer on the reaction channel, increasing the surface area by a factor of 40 000. Finally, Ag catalyst was deposited by a sputter coater and the entire microreactor was anodically bonded with a glass wafer to contain the chemical reaction within the reactor. For comparison, a microreactor was fabricated without porous silicon. Catalytic activity was monitored by measuring the reaction products using gas chromatography. Rosalva oxidation required a lower activation energy and experienced six times more reactivity on the PSi supported silver catalyst versus a thin film silver catalyst [36].

In a manner similar to the above-described deposition of metal catalysts on porous silicon for enhanced catalysis, much research is being conducted on the functionalization of PSi microreactors with enzymes such as Glucose oxidase (GOx) or trypsin for glucose oxidation and other biochemical processes [24, 63, 201]. High aspect ratio Si microreactor channels about 70 µm wide were anodically etched in an HF and ethanol solution to create a PSi surface [24,63]. Drott et al. [63] created various depths of PSi layer on the microreactor surface, shown in Figure 2.31, by increasing etch duration. Enzymes were immobilized on the PSi surface in three steps: silanisation, glutaraldehyde activation, and finally coupling of the GOx or trypsin enzymes to the prepared PSi surface [24, 63]. Compared to a similarly prepared non-porous microreactor, the PSi surface increased catalytic efficiency by 170-fold for GOx enzyme activated glucose turnover [63]. In all studies, increasing the etch duration to increase the PSi layer depth and thus increase the active surface area resulted in an increase in catalytic activity. In particular, the trypsin microreactor experienced an increase in catalytic turnover of more than 200 % [24].

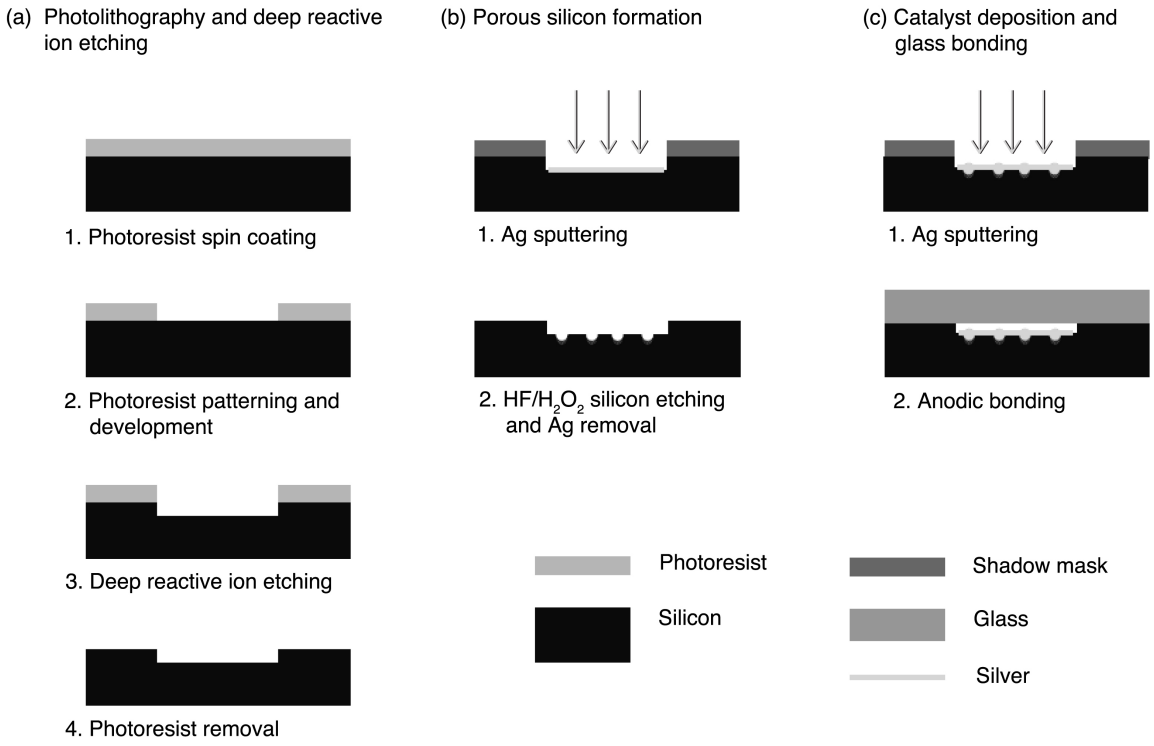

Figure 2.30: Schematic illustration of the microreactor fabrication process: (a) photolithography and deep reactive ion etching, (b) porous silicon formation and (c) catalyst deposition and glass bonding. Reprinted with permission from Cao E., Zuburtikudis I., Al-Rifai N., Roydhouse M., and Gavriilidis A. (2014) Enhanced performance of oxidation of rosalva (9-decen-1-ol) to costenal (9-decenal) on porous silicon-supported silver catalyst in a microstructured reactor. Processes 2 (1), 141-157, Creative Commons License.

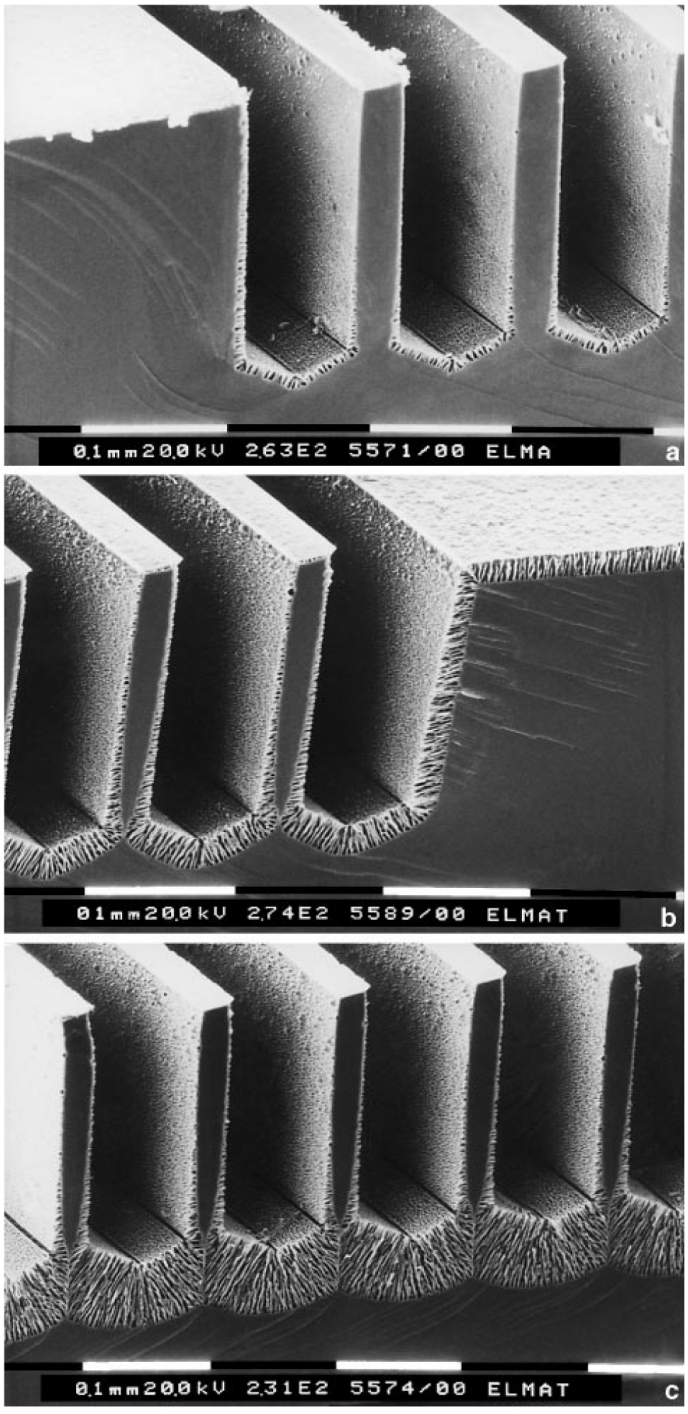

Figure 2.31: SEM of the reactors anodized at $10\,\mathrm{mA/cm^2}$ (a) 10 min, (b) 25 min, and (c) 50 min. Reprinted from Springer and Microchim. Acta, 131, 1999, 117, Porous Silicon Carrier Matrices in Micro Enzyme Reactors-Influence of Matrix Depth, Drott J., Rosengren L., Lindstrm K., and Laurell T., Figure 4, with kind permission from Springer Science and Business Media.

Heterogeneous photocatalysis is the process where a semiconducting catalyst absorbs photons and generates an electron-hole pair, which catalyzes redox reactions. The photocatalytic mechanism depends on various aspects of the semiconductor band structure. The band gap determines the effective range of radiation wavelengths; a photon must be absorbed to excite an electron from the valence to the conduction band. Reduction by the excited electron requires the base of the conduction band to be at a more negative potential than the reaction potential. Similarly, oxidation by electron holes requires that the top of the valence band must be at a more positive potential [5]. Additionally, a slow rate of electron-hole recombination ensures a higher probability for the electron-hole pair to participate in redox reactions, and thus creates a more effective photocatalyst [247]. A primary application of photocatalysis is in environmental remediation, which includes oxidation of organic species for cleaning wastewater, removal of volatile organic compounds and smog from the air, and creating active self-cleaning surfaces [5]. Photocatalysts are particularly well suited for environmental remediation because they operate at or below room temperature [5].

Gole et al. [92] discuss the use of the IHSAB principle (see section 2.4.2) as a general approach to the design of PSi microreactors. Through the deposition of carefully selected metal oxide nanostructures, the PSi interface can be directed to operate in a physisorptive mode, optimal for reversible chemical sensing, or chemisorptive mode, optimal for microreactors [92]. Additionally, by incorporating the UV-light absorbing TiO_2 or its visible-light sensitive oxynitride form, $TiO_{2-x}N_x$ into the PSi framework, PSi photocatalytic microreactors can be produced [93, 149]. The TiO_2 nanoparticles were converted to the oxynitride by application of triethylamine. The TiO_2 was converted both in the form of its nanocolloid or *in-situ* within the PSi interface [93, 149]. The visible-light photocatalytic property of oxynitride formed through direct nitridation was demonstrated by comparing a reflectance spectra of the TiO_2 and $TiO_{2-x}N_x$ nanoparticles. While the TiO_2 nanoparticles demonstrated a

clear onset of reflectance at approximately 350 nm, the oxynitride reflectance onset was red-shifted to 450 nm [93].

2.5.2 PSi membrane microreactors

Taking advantage of the channel structure of PSi, bulk silicon can be removed to expose the backside of a PSi layer to create a flow-through PSi membrane reactor [168, 214, 238]. Due to the ease of etching, device fabrication, and microelectronic integration, PSi had already been recognized as an ideal candidate for devices requiring membrane functionalities. Examples include a PSi membrane filled with Nafion® [56, 210] or sulfuric acid [84] as a proton exchange membrane fuel cell (PEMFC) or as a PEMFC integrated hydrogen gas diffusion layer [82]. As a microreactor, the PSi membranes have been evaluated as hydrocarbon steam reformers [168] and CO preferential oxidation reactors [59, 238]. However, this approach requires many steps of fabrication including pre-defining pore locations, carefully etching the pores, and finally opening the backside of the pores.

For the purpose of enhancing the selectivity of resistive gas sensors to special gases in the presence of CO, Splinter et al. [238] created a flow-through PSi micro membrane reactor coated with a palladium catalyst to convert CO into non-detectable CO_2. Shown in Figure 2.32, the micro membrane reactor featured a 70 µm thick PSi layer that serves as both the membrane, opened from the backside by advanced silicon etching (ASE), and as a thermal insulator between an on-chip heating element and bulk silicon. The on-chip heating element raised the temperature of the reactor to 140 °C to assist the reaction. Palladium was introduced into the pores by submersing the entire silicon reactor into a palladium acetylacetonate solution with a toluene solvent. Catalytic activity of the micro membrane reactor was then measured as a drop in detection signal of an in-series resistive gas sensor, as the CO was converted to the non-detectable CO_2.

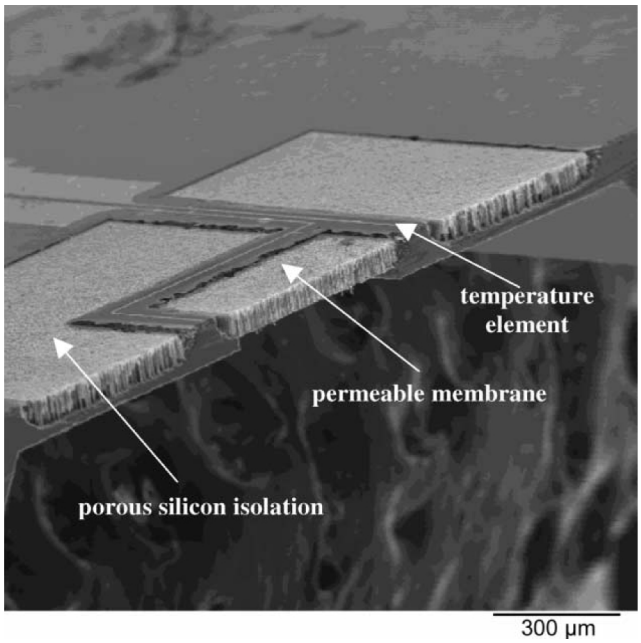

Figure 2.32: SEM of PSi permeable micro membrane with PSi thermal isolation and integrated heating element. Reprinted from Sens. Actuators, B, 83, Splinter A., Strmann J., Bartels O., and Benecke W., Micro membrane reactor: a flow-through membrane for gas pre-combustion, 169-174, Copyright 2002, with permission from Elsevier.

Due to the difficulties and hazards of storing and handling hydrogen for fuel cells, Llorca et al. [168] created a macroporous silicon microreformer for onsite production of hydrogen via the catalytic steam reforming of ethanol. Although ethanol requires a higher reforming temperature than the more extensively studied methanol steam reformers, ethanol yields more hydrogen on a molar basis and is also a renewable bio-fuel. Macroporous silicon was used for the first time as a catalyst support structure to assist in the chemical reaction to produce hydrogen as a parallel channel flow-through microdevice [168]. This represents a good choice as silicon is stable to oxidation at the higher temperatures required for ethanol reforming [84].

The macroporous silicon microreformer was fabricated in two stages: an elegant electrochemical etching process to create the array of microchannels (described earlier in section 2.3.2 and shown in Figure 2.13), followed by a deposition of Co_3O_4−ZnO

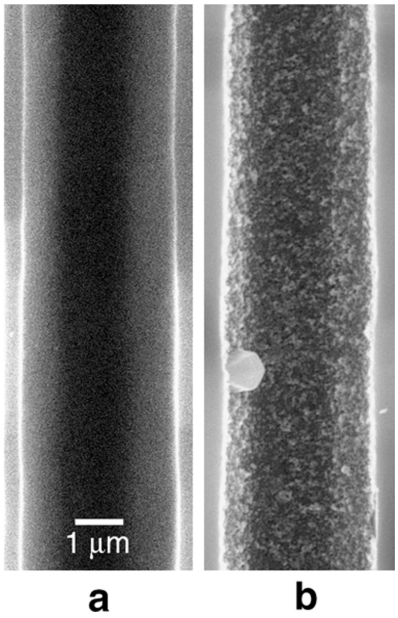

Figure 2.33: Microchannel (a) before and (b) after deposition of zinc and cobalt oxide catalyst layer. Reprinted from Journal of Catalysis, 255, Llorca J., Casanovas A., Trifonov T., Rodrguez A., and Alcubilla R., First use of macroporous silicon loaded with catalyst film for a chemical reaction: A microreformer for producing hydrogen from ethanol steam reforming, 228-233, Copyright 2008, with permission from Elsevier.

catalyst onto the pore walls [168]. Traditional methods of deposition were not sufficient to produce a continuous and even catalyst layer in the newly created high aspect ratio microchannels. Thus, catalyst deposition of zinc and cobalt oxides in a consistent layer approximately 100 nm thick to the walls of the macroporous silicon membrane (Figure 2.33) was completed through a novel complexation-decomposition route.

The microreformer was constructed by gluing steel washers to the catalyst coated microporous membrane with epoxy and then integrating these into a steel housing. Catalytic experiments were carried out inside a furnace as varying molar ratios of ethanol and water diluted in He were passed through the microreformer at atmospheric pressure. Reaction products were measured continuously by online mass spectrometry and compared against a non-catalyst loaded macroporous silicon microreformer. An optimal operation temperature of 773 K and steam-to-carbon ratio

$S/C = 3$ produced a high conversion rate of ethanol and selectivity for H_2 (73.4 vol%). Only minimal amounts of CH_4, an undesirable product of ethanol thermal decomposition, were produced by the catalyst-loaded microreformer. Additionally, the residence time per microchannel was less than 5 ms. Llorca et al. [168] suggest that the produced microreformer could theoretically produce enough H_2 to power a small device requiring several watts.

CHAPTER III

EXPERIMENTAL

This chapter will describe the PSi sensor fabrication process, the gas and liquid chemical detection experiments, and details of the characterization studies used in this work.

3.1 Sensor Design

The PSi sensors were created using microfabrication methods, applied at the Institute for Electronics and Nanotechnology cleanrooms at Georgia Institute of Technology (Georgia Tech IEN). Figure 3.1 illustrates the process flow for sensor fabrication. The process can be summarized as SiC deposition (steps 1–2), photolithography (steps 3–5), reactive ion etching (step 6), electrochemical anodization (step 8), and deposition of metal contacts (step 9). This process creates 12 sensors on each 2" Si wafer, which are then diced into individual sensors (step 10). The PSi sensors were fabricated from 2" p-type and n-type silicon wafers grown using the Czochralski process [65] and purchased from Siltronix. The p-type (100) silicon wafers are single-side polished, boron doped, and have a resistivity of 7 Ω cm to 13 Ω cm. The n-type (100) silicon wafers are single-side polished, phosphorous doped, and have a resistivity of 7 Ω cm to 13 Ω cm.

3.1.1 Silicon carbide deposition

As discussed earlier (Chapter 2), the PSi morphology depends on precise etch conditions, one of which is current density. To achieve an accurate current density, a chemical mask that is resistant to HF-etching is used to create a clearly defined exposed surface area of Si, which is then used to calculate, approximately, the current

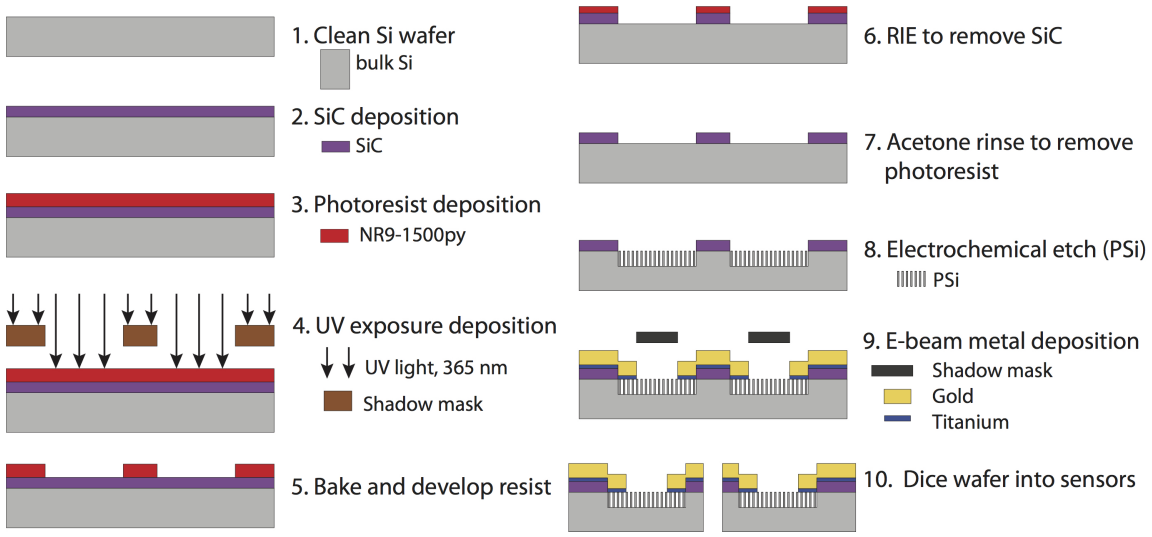

Figure 3.1: Process flow diagram for fabrication of PSi sensors.

that should be applied. The etching mask also allows for precisely patterned local PSi formations on the Si wafer (Figure 3.2). The choice of material for an etching mask depends on the selectivity of the etchant to the masking material. While Si_3N_4 is commonly used as a HF-etching mask [154,238,282], we use a masking layer of SiC. SiC is highly resistant to HF and has a reported etch rate of only a few angstroms per hour in contrast to Si_3N_4, which has an etch rate of several nanometers per minute [240, 248].

As shown in Figure 3.1, the Si wafers are first cleaned using the *Standard Operation Procedure for Substrate Clean* recommended by the Georgia Tech IEN [4], in which the wafer is rinsed with acetone, followed by methanol and isopropanol. The SiC deposition was performed on an Oxford Plasma Enhanced Chemical Vapor Depositor (PECVD) in the Georgia Tech IEN [3]. A layer of SiC was deposited to a thickness of approximately 2000 Å, which was measured on a NanoSpec 3000 Nanospec Reflectometer. This thickness was chosen to optimize the robustness of the mask during the HF-etch and to ensure that the coating is thin enough to ensure continuity of a later deposited metal contact layer across the PSi and SiC border. The PECVD reacts with the precursor gases in a radio frequency (RF) induced plasma to enhance the

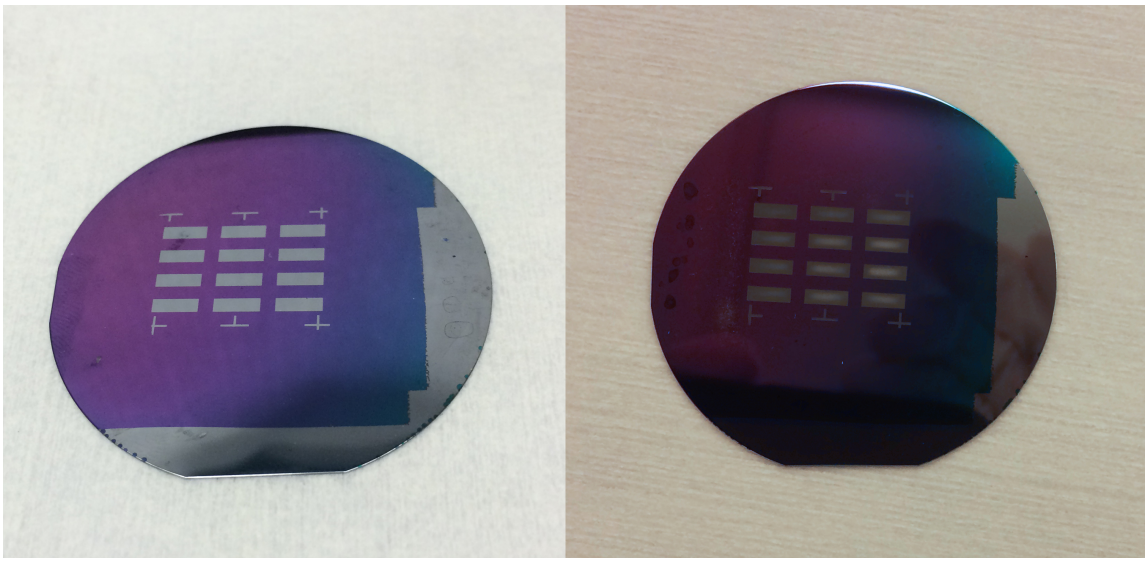

Figure 3.2: Before (left) and after (right) electrochemical anodization of p-type Si. The PSi formation is restricted to the rectangles of exposed Si pattered into the SiC layer. After PSi formation, the surface becomes a dull gray in contrast to the mirror finish of the Si wafer.

reaction and deposition process. The recipe for SiC deposition process requires the precursor gases silane (SH_4, 13 sccm), methane (CH_4, 100 sccm), and nitrogen (N_2, 185 sccm) [4]. The process is carried out at a temperature of 250 °C, a platen power of 50 W, and total pressure of 1000 mtorr. Each process run can deposit SiC onto four 2" wafers.

3.1.2 Photolithography

To pattern the SiC layer for use as an HF-etch mask, a set of photolithographic steps are completed, shown in Figure 3.1 as steps 3–5. During these processing steps, photoresist, a light sensitive polymer, is used to create a patterned mask that will protect specific areas of the SiC from etching during the reactive ion etching step. First, a negative photoresist, Futurrex NR9-1500py, is deposited onto the wafer surface using an SCS G3 Spin Coater in the Georgia Tech IEN [3]. During the spin coating process, approximately 5 ml of photoresist is pipetted onto the wafer surface, then the wafer is accelerated at 500 rpm/s and then held spinning at 3000 rpm for 30 s.

This creates an even layer of the photoresist on the wafer. The photoresist-coated wafer is then soft baked at 150 °C for 2 min. The soft bake toughens the photoresist layer in preparation for UV exposure. The photoresist-coated wafer is then exposed to the final SiC pattern through the use of a Karl Suss MA-6 Mask Aligner [3]. When using negative photoresist, areas that are exposed to UV light are rendered insoluble to the developer solution (areas that are not exposed to UV light will be removed). Therefore, a shadow mask, shown in Figure 3.3, was created where the chrome areas prevent UV light from reaching the photoresist-covered wafer. During exposure, the mask is held in soft contact mode, with an alignment gap of 40 µm. The Karl Suss MA-6 Mask Aligner uses a 350 W mercury lamp to provide UV light for exposure, which is calibrated at 5 mW/cm^2 at 365 nm. The photoresist-covered wafer is exposed for 30 s. After UV exposure, the wafer is hard baked at 100 °C for 5 min prior to developing. To develop the photoresist pattern, the wafer is submerged in Futurrex Resist Developer RD6 for 10 s, cleaned with DI water, and then baked for 20 min at 120 °C to remove any remaining water or developer from the wafer [4].

3.1.3 Reactive ion etching

The pattern of SiC that is not protected by photoresist (step 6 in Figure 3.1), is removed by reactive ion etching (RIE) to reveal the 2 mm by 5 mm windows to the Si surface, shown in Figure 3.2. The Oxford Endpoint RIE (Reactive Ion Etcher) in the Georgia Tech IEN was used to perform the SiC etch. The recipe used for RIE of SiC requires the process gases tetrafluoromethane (CHF_3, 13 sccm), argon (Ar, 10 sccm), and oxygen (O_2, 7 sccm). The process is run at a total pressure of 80 mtorr and a platen power of 200 W. The total process time is calculated for each individual run due to variance in etching rates. The etch rate is measured by recording the SiC layer thickness before and after a short ($\sim$ 40 s) RIE process on the NanoSpec 3000 Nanospec Reflectometer. After the complete RIE process to remove the entire layer of

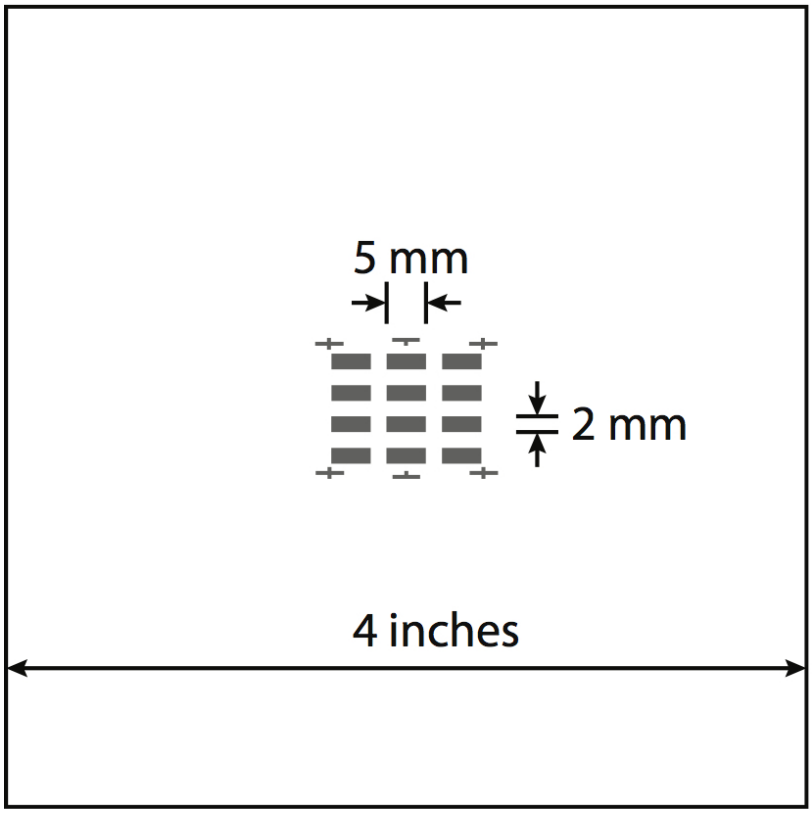

Figure 3.3: Schematic of 4" shadow mask used for exposure of UV light onto a photoresist layer. Gray areas represent areas of a chrome layer that block UV light.

SiC from the patterned windows, a final check is done on the Nanospec Reflectometer to verify that the Si surface has been exposed. A final wash with acetone removes any residual photoresist (step 7, Figure 3.1).

3.1.4 Electrochemical anodization

As shown in step 8 of Figure 3.1, the SiC layer acts as a chemical mask during the electrochemical etching to create a PSi layer (this effect is shown in Figure 3.2). The PSi etching process is unique for the p-type and n-type Si wafers (for further discussion, see section 2.3.1). The p-type wafers are electrochemically etched in a vertical single etch cell (Figure 2.7a) in a solution containing a 1:25 ratio of 49 % HF and acetonitrile (0.8 ml HF and 20 ml acetonitrile), with 0.69 mg of tetrabutylammonium-perchlorate (TBAP). The applied current density is 3 mA/cm^2 and the etch duration is 40 min.

The resulting porous structure is a hybrid structure featuring ∼1.5 µm to 2 µm diameter pores with ∼10 nm diameter porous walls (Figures 2.1a and 2.18). The n-type wafers are electrochemically etched in a horizontal single etch cell (Figure 2.7a) in a solution containing a 1:1 ratio of 49 % HF and ethanol. The anodization is done under topside illumination using a Black-Ray mercury lamp. The applied current density is 14 mA/cm^2 and the etch duration is 10 min. The resulting n-type PSi has pore diameters of 0.5 µm to 0.7 µm and pore depths of 50 µm to 75 µm (Figure 2.1b) [150].

3.1.5 Metalization

Electrical contacts are deposited to the PSi sensor array through e-beam evaporation (step 9, Figure 3.1), using the Denton Explorer in the Georgia Tech IEN [3]. During the e-beam evaporation process, the metal for deposition is held in a crucible and then heated to the point of vaporization by a beam of electrons. The evaporation chamber is evacuated to a pressure of approximately 10^{-7} torr to increase the mean free path of the evaporated metal molecules, thus minimizing contamination and interruption of the evaporated metal. The evaporated metal travels in a straight path from the crucible upwards in a conical spray. The Si wafer is placed in a sample holder above the crucible facing the evaporated metal spray. Therefore, a shadow mask can be used to pattern the metal condensation onto the Si wafer, shown in Figure 3.4. To create metal contacts for the PSi sensors, first a 100 Å layer of Ti is applied at a rate of 1 Å s^{-1} to act as an adhesion layer for the subsequent layer of gold. A 3000 Å layer of Au is deposited at a rate of 1.5 Å s^{-1}. The shadow mask was fabricated from a 0.125" thick aluminum sheet using the water jet in the Invention Studio at Georgia Tech. As a final step in the fabrication, the wafer is diced into individual PSi sensors using a diamond scribe. Figure 3.5 shows a schematic and photo of the completed PSi sensor.

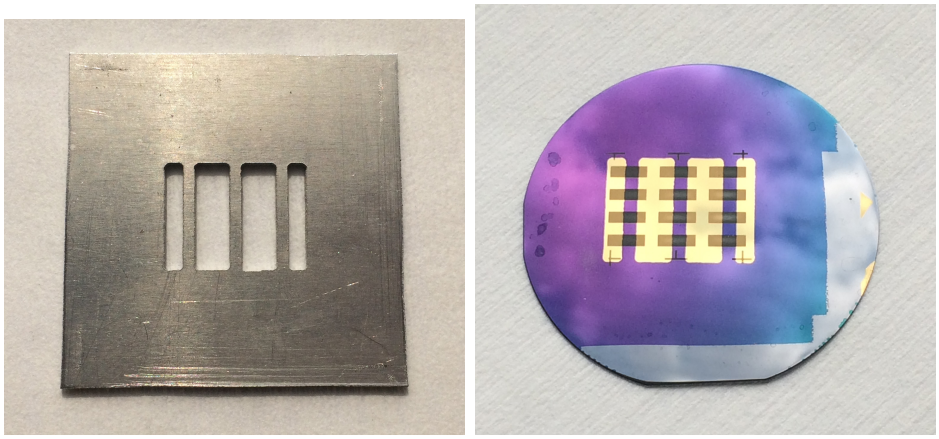

(a) (b)

Figure 3.4: (a) Shadow mask used for depositing the Ti and Au layers for the electrical contacts; (b) Si wafer after deposition of metal electrical contacts.

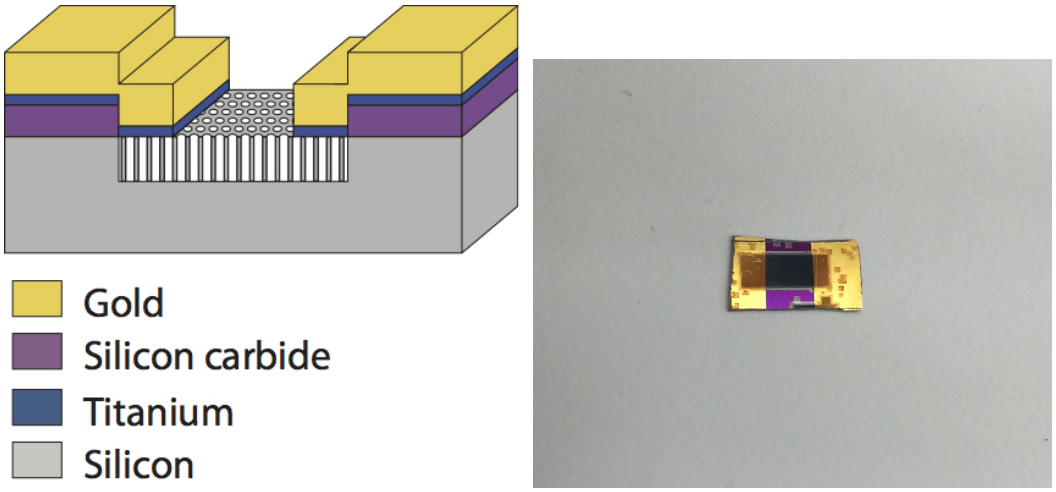

(a) (b)

Figure 3.5: (a) Schematic of completed PSi sensor and (b) photo of a complete n-type PSi sensor.

3.1.6 Nanomaterials depostion

In the interest of enhancing the sensitivity and selectivity of the PSi sensors, metal oxide nanostructures are deposited to the PSi interface. Due to the unique hybrid surface structure of the PSi, the formation of the metal oxide nanoparticles is a simple room temperature process that does not require any time-consuming self-assembly processes or the use of traditional film technology. The resulting metal oxide nanostructures are deposited fractionally to form nanostructured island sites, in stark contrast to interconnected nanostructures or thin films. As such, the metal oxide nanostructures direct the interaction of the PSi interface with chemical gas analytes [86, 92, 92, 100, 146, 150]. For additional discussion, see section 2.4.2 and Chapter 5. Metal oxide depositions utilized in the studies in this thesis include TiO_2, SnO_x, NiO, Cu_xO, and Au_xO.

Figure 3.6 shows an SEM micrograph of TiO_2 nanostructures deposited onto the hybrid nanoporous covered micropores of a p-type PSi sensor. The deposited metal oxide nanostructures are on the order of 10 nm to 50 nm in diameter. To create the nanostructured metal oxide islands on the PSi sensors, the individual PSi sensors are submerged into precursor metal solutions for 15 s, then dipped into deionized (DI) water and then methanol for consecutive 120 s periods. The decorated sensors were then dried over night in a fume hood and heated to at least 100 °C on a hot plate to evaporate any remaining water or methanol from the pores.

A nanoparticle colloidal solution of TiO_2 (anatase phase) [43,98,149] was prepared as follows. First 500 ml of deionized (DI) water is combined with 160 ml acetic acid in an Erlenmeyer flask, which is then placed in an ice bath on a stir plate. The solution is cooled to 0 °C while under constant stirring with a magnetic stir bar and constant N_2 flow. Once the solution is cooled to 0 °C, 20 ml of 2-propanol is combined with 75 ml titanium isopropoxide in a cylindrical separatory funnel with a dropping tube. The combined 2-propanol and titanium isopropoxide solution is then slowly dripped

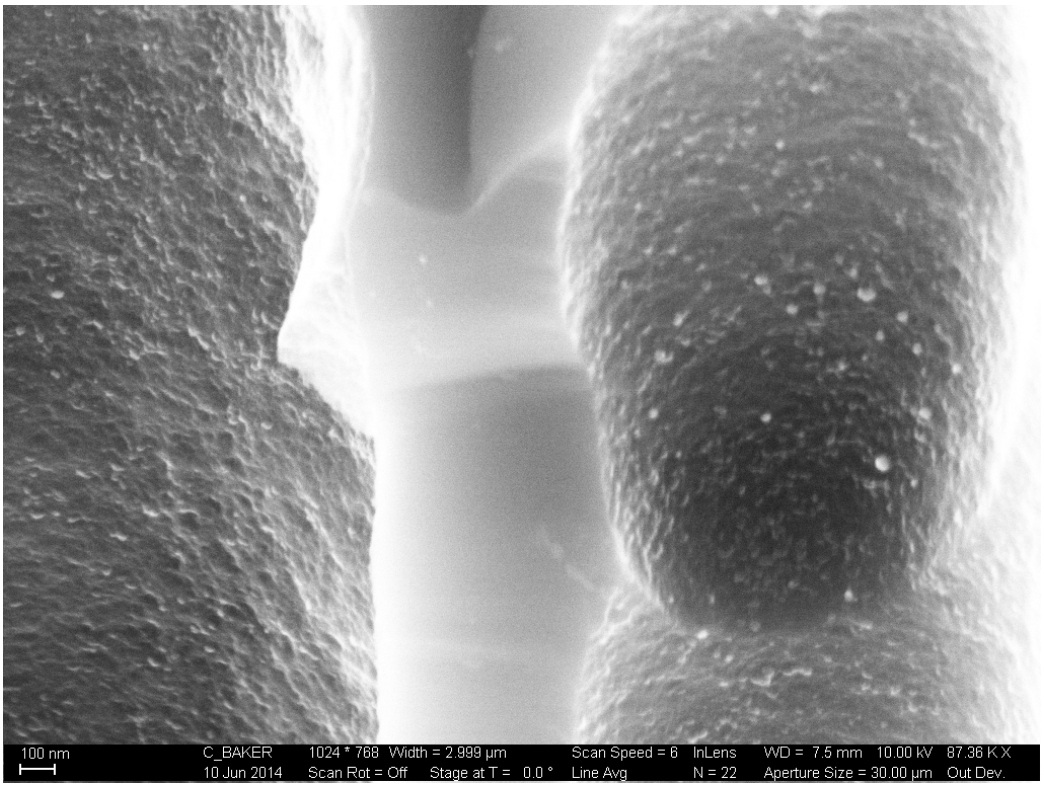

(a)

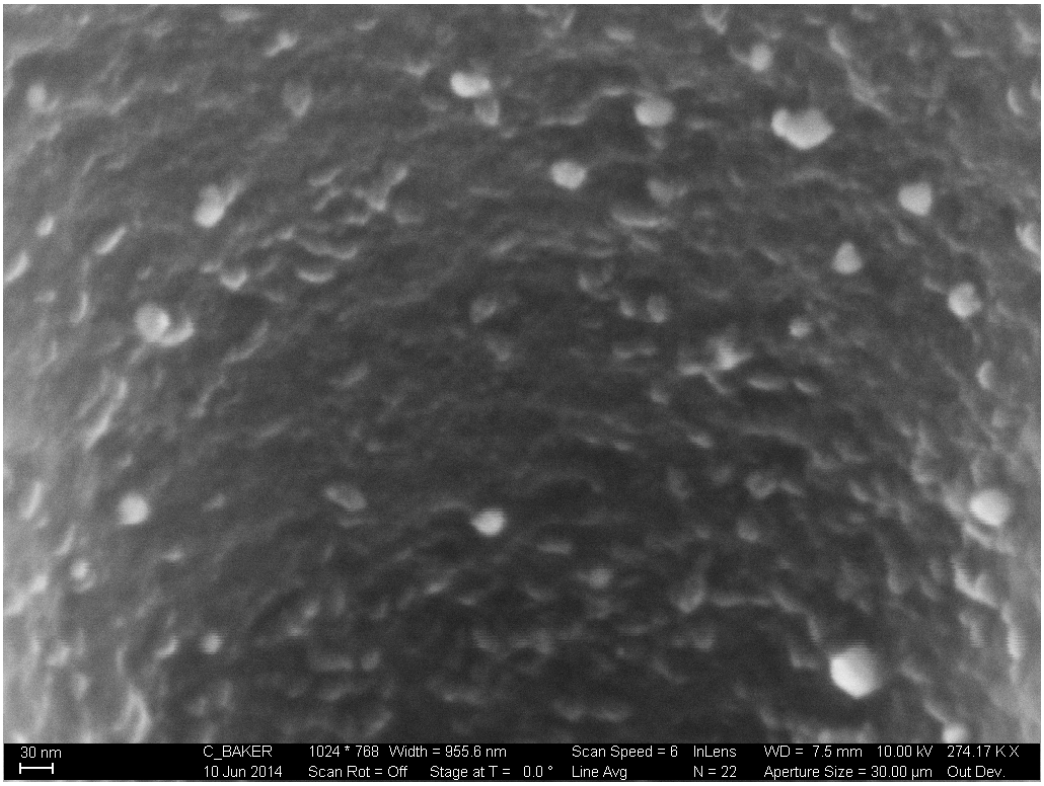

(b)

Figure 3.6: SEM micrograph of a p-type PSi sensor with TiO_2 nanoparticles shown at (a) 87 kX magnification and (b) 274 kX magnification.

into the DI water and acetic acid solution, under constant stirring and N_2 flow. Once all of the 2-propanol and titanium isopropoxide solution has been added, the complete mixture is allowed to stir over night. The resulting TiO_2 colloidal solution is stored under refrigeration [43, 98]. For deposition of the TiO_2 on to the PSi interface, the solution is diluted with methanol in a 1:1 ratio.

SnO_2 was fabricated by combining 0.33 M tin chloride ($SnCl_2$), 1.92 M sodium hydroxide (NaOH), and 0.33 M sodium citrate at 70 °C. The resulting solution was allowed to cool to room temperature and kept under constant stirring with a magnetic stir bar. This procedure was adapted from van Noort et al. [195] by L. Seals and J. L. Gole. An electroless nickel solution was prepared by combining 20 g/l nickel chloride with 40 g/l sodium hydroxide (complexing agent), 0.67 g/l sodium borohydride (reducing agent) and 44 g/l ethylene diamine (stabilizer) [199]. A commercially available electroless gold metallization solution (Transene) is used as the precursor for the Au_xO metal oxide nanostructured depositions. In Chapter 6, alternative materials including cobalt oxide, iron oxide nanoparticles, and metal chlorides are explored. The deposition solutions are discussed in detail in Chapter 6; however, the deposition process follows the same procedure as that for the metal oxides described in this section.

3.2 Gas Sensing Experiments

As shown in Figure 3.7a, the various analyte gases were entrained in ultra high purity (UHP) nitrogen (99.999+ % Matheson) and then brought to the PSi sensor interfaces. The analyte gases were purchased from Matheson Gas as 1000 ppm mixtures with an N_2 balance gas. The gas flow through 1/8" stainless steel tubing for the analyte and the entraining UHP nitrogen gases are controlled by MKS type 1179A (N_2, NO_x, NH_3) and 1159A (H_2S, SO_2) mass flow controllers (MFCs). In order to characterize the sensitivities of the PSi sensors to inorganic analytes in the presence of volatile

organic chemicals (VOCs), the gas testing setup was modified as shown in Figure 3.7b. The MKS type 1479A MFC was used for directing the flow of nitrogen through the bubble flow configuration to entrain the aromatics. The MFCs are controlled by either a single-channel MKS 246 or a four-channel MKS 247 power supply/read out system. The MKS power supply/read out systems are controlled by LabVIEW through a National Instruments (NI) USB-6353.

The resistance of each PSi sensor is measured in 0.05 s intervals at 10 samples per interval using a DC current. The voltage bias used in these experiments is 3 V to obtain an optimum signal to noise ratio. This corresponds to the typical voltage supplied by a lithium battery. The LabVIEW program that controls the MKS power supply/read out systems also controls the supplied DC current and data collection through the NI USB-6353. The LabVIEW block diagram is included in Appendix D. Python and MATLAB were used in the analysis of the data.

Electrical connection to the PSi sensors was originally accomplished by precision probes (Figure 3.8a), which were connected to the NI USB-6353 via a simple voltage divider. However, in the interest of measuring the response of multiple PSi sensors simultaneously, a new sensor contact apparatus was developed (Figure 3.8b). The new contact apparatus features a clear plastic lid fabricated from 3D printed UV curable resin on the Objet Eden 250 3D printer in the Invention Studio at Georgia Tech. The lid supports the spring pin connectors that electrically connect the PSi sensors to the base, which, in this design, directly integrates with a breadboard for subsequent connection to the voltage divider and NI USB-6353. The new sensor contact apparatus can also be directly connected to a mobile microprocessor (shown in the background of Figure 3.8b) for mobile sensing. The microprocessor can send the collected gas sensor data to a computer via bluetooth. Figure 3.9 demonstrates an initial "proof of concept" test of the mobile sensor connector, microprocessor system, and bluetooth connection. A key feature of the sensor connector apparatus is

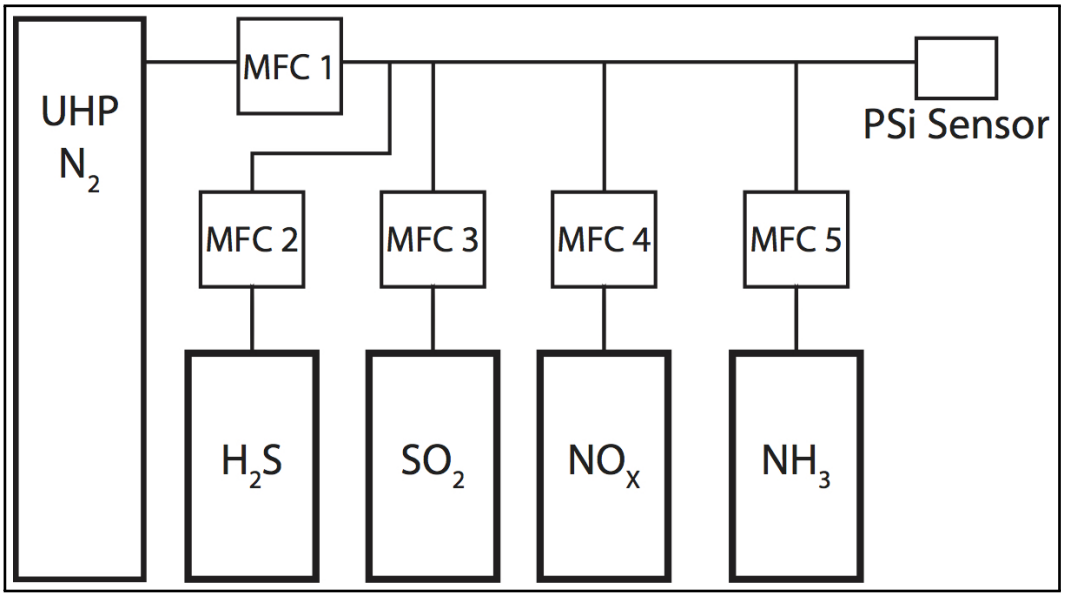

(a)

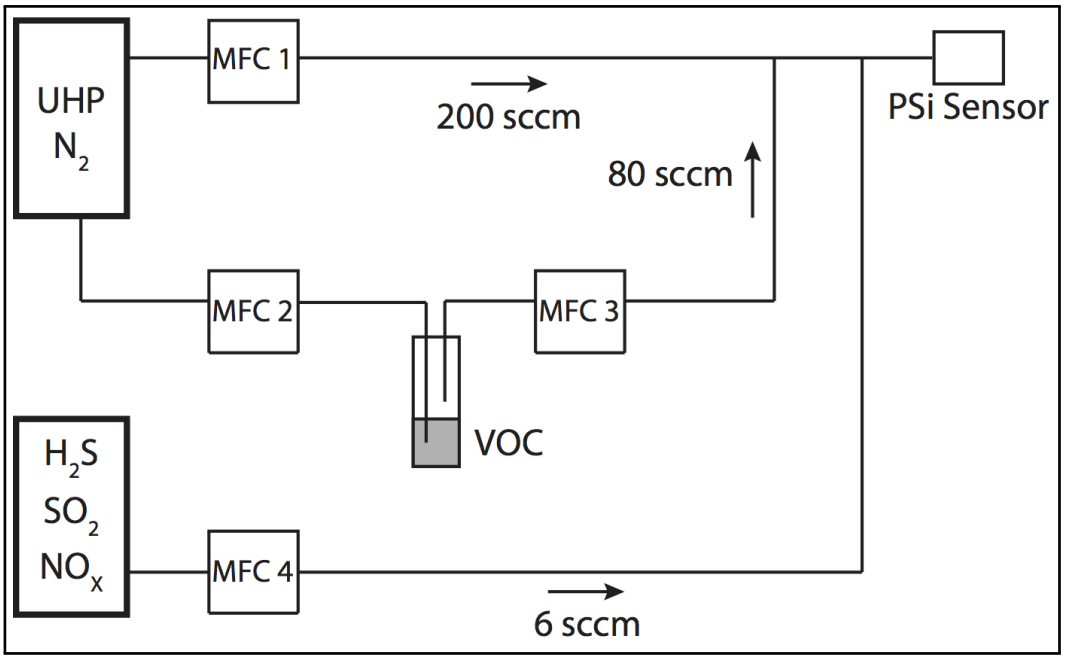

(b)

Figure 3.7: Schematic of gas testing setup for (a) standard testing of inorganic pollutants and (b) the modification of the testing setup for selectivity testing in the presence of volatile organic chemicals (VOCs). 1/8" stainless steel tubing connects the gas tanks and mass flow controllers (MFCs).

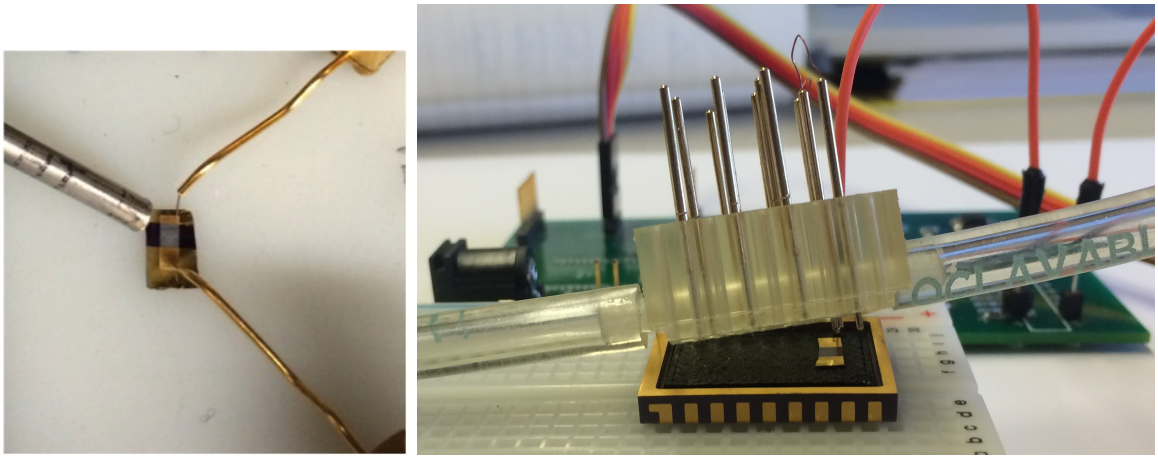

(a) (b)

Figure 3.8: (a) Picture of electrical connection to a PSi sensor using precision probes with the stainless steel tube directing the gas flow onto the PSi sensor interface. (b) Picture of 3D printed contact and gas flow apparatus using spring pin connectors. The apparatus can be directly integrated into a gas flow line and connect up to nine sensors.

not only the ability to simultaneously test multiple sensors, but the ability to easily switch out individual sensors for testing, as each sensor is non-permanently held in place. The spring pin connectors create a sufficient electrical contact without the need for permanent wire-bonding.

For each gas detection experiment run, the PSi sensor is first purged with a minimum of 30 min of nitrogen to establish a baseline resistance. Then the analyte mixture is introduced at various concentrations for 120 s followed by a nitrogen purge for 240 s. An example of a complete gas sensing experiment is given in Table 3.1. The nitrogen purge facilitates desorption of the analyte gas from the PSi surface as well as its diffusion back out of the pores. All sensors are evaluated in an unsaturated mode to allow for a shorter time scale of experiments. A full cycle of saturation and complete desorption is unnecessary as the onset of the sensor response (within 2 s) is clearly detectable [85, 95, 199]. The time to return to the baseline resistance for particularly sticky gases such as NH_3 and H_2S can be longer that the 240 s nitrogen purge time, suggesting that the interaction of the inorganic gas analytes with the

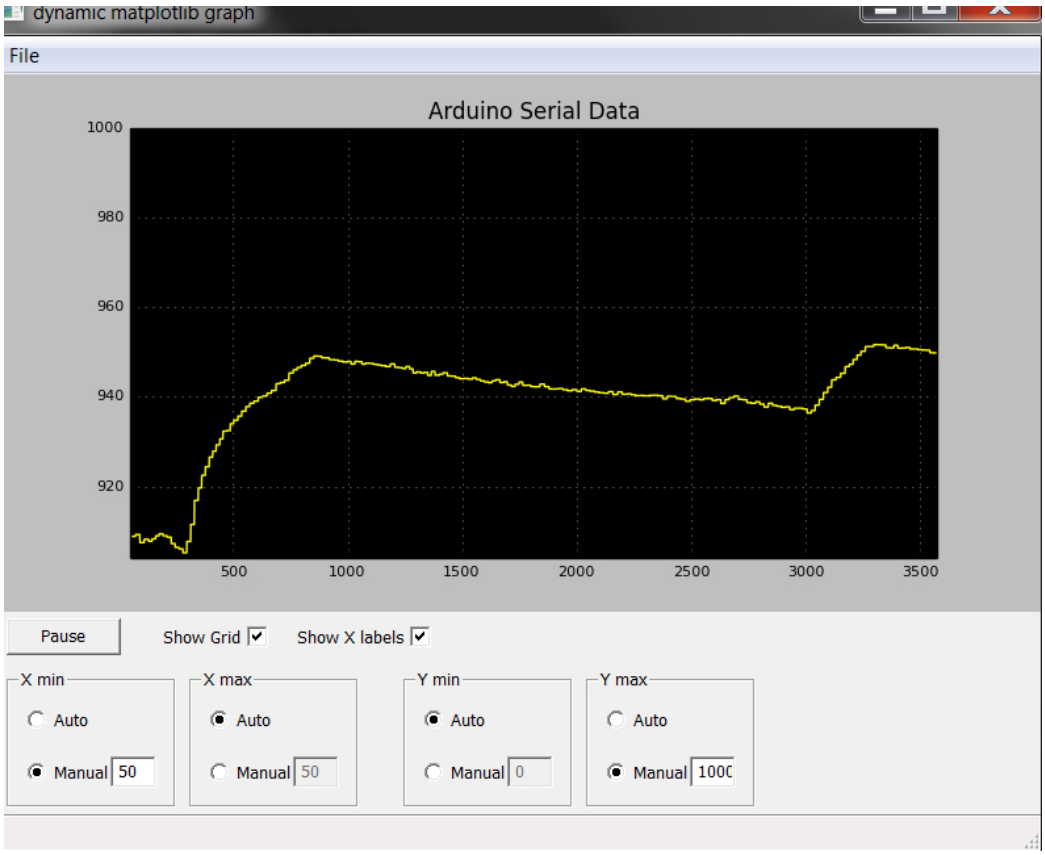

Figure 3.9: Demonstration of realtime bluetooth data from mobile PSi sensor connector and microprocessor unit. In this demonstration, 20 ppm of NH_3 was pulsed through the PSi connection apparatus from approximately 400 s to 900 s and 3000 s to 3300 s.

PSi interface is dominated by physisorption, but also displays weak chemisorption. A long purge with UHP nitrogen will produce a return to baseline resistance and sensors that have been rejuvenated by a short soak in dilute HF return to baseline faster [86]. *Sensor rejuvenation* refers to the cleaning of contaminants and general surface regeneration of the PSi interface. The rejuvenation process was developed to return poisoned sensors to their original level of performance [86]. When considering the effect of nanostructured materials depositions, each PSi sensor is tested before and after materials deposition to control for variance from sensor to sensor and isolate only those changes due to the deposition process.

Table 3.1: Typical gas sensing experiment testing the response of a PSi sensor to 1 ppm to 5 ppm and 10 ppm of an analyte gas, where the standard cubic centimeters per minute (sccm) and the corresponding concentrations of analyte gas are shown. The supplied analyte gas is at a concentration of 1000 ppm in N_2 and is then mixed with a flow of UHP N_2 according to the given sccm values.

Step Number	N_2 flow (Q_{N_2}/sccm)	Analyte flow (Q_{analyte}/sccm)	Analyte concentration (C/ppm)	Time per step (t/s)
1	200	0	0	1800
2	200	0.2	1	120
3	200	0	0	240
4	200	0.4	2	120
5	200	0	0	240
6	200	0.6	3	120
7	200	0	0	240
8	200	0.8	4	120
9	200	0	0	240
10	200	1.0	5	120
11	200	0	0	240
12	200	2.0	10	120
13	200	0	0	240

3.3 Organic Solvent Detection Experiments

Impedance measurements of the PSi sensors in the presence of organic solvents were performed using a Solartron 1260 Impedance Analyzer controlled with ZPlot software. The data was then analyzed with ZView software. For each sensor, the complete impedance, Z, was measured for a frequency sweep from 100 Hz to 100 000 Hz under dry conditions in a chemical hood. The impedance was collected every 100 Hz. Electrical connections were made with the precision probes depicted in Figure 3.8a. A dc bias of 0 V and an ac signal of 90 mVrms was used following studies reporting ideal conditions for minimizing noise and optimizing reproducibility of PSi impedance sensors [8]. From the impedance data gathered from 100 Hz to 100 000 Hz, a Nyquist plot ($\mathrm{Re}\, Z$ versus $\mathrm{Im}\, Z$) was generated both to serve as a basis for generating an equivalent circuit model and as a baseline to compare to sensor response in the presence of organic solvents. Equivalent circuit models were created within the ZView software and simulated using the internal fitting program. Figure 3.10 illustrates the equivalent circuit models used for p-type and n-type PSi sensors. The differences in the equivalent circuit models are due to the distinctly different porous structure of p-type and n-type PSi. For further discussion, see Chapter 7.

To test for the PSi sensor impedance response to various organic solvents, first the impedance was measured at 100 000 Hz, 90 mVrms, and a bias of 0 V for 20 min. At this frequency, the sensors were operating in a capacitance-dominated mode. At approximately 1 min to 2 min into the 20 min data collection period, 10 µl of the solvent was deposited to the PSi interface. This allowed for monitoring how the solvent affected the various aspects of the PSi sensor as a function of absorption of the solvent into the pores and its subsequent evaporation. Also, the impedance spectra was collected over a frequency range of 100 Hz to 100 000 Hz during exposure to the organic solvents. Due to the quick evaporation time of some solvents, only 8 data points were collected at logarithmically-equal intervals. This allows a comparison of

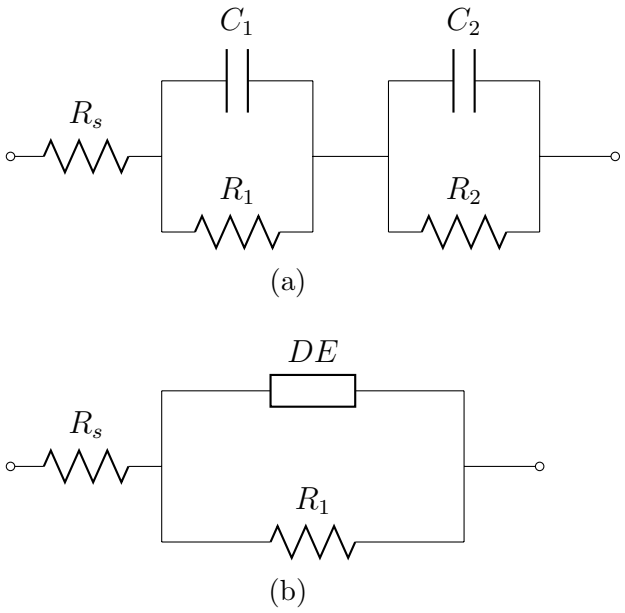

Figure 3.10: Equivalent circuit models for (a) p-type and (b) n-type PSi sensors where R_s represents the resistance of the metal contacts and R_1 and R_2 represent the internal resistance through the sensor. For p-type PSi sensors, the hybrid nanoporous-covered microporous structure is represented by the two capacitances, C_1 and C_2. For n-type PSi, the pores are represented by the distributed capacitance element (DE).

Nyquist plots under dry and solvent-exposed conditions. By simulating the equivalent circuit model to each Nyquist plot, a change in the values of the equivalent circuit elements can then be calculated. Each corresponding dry and solvent data collection was performed within ∼1 h and compared to repeated tests on different days at different times. The sensors were gently heated to 100 °C to remove any remaining solvent before subsequent tests.

3.4 Characterization Studies

All characterization studies were completed at the Georgia Tech IEN Microscopy Laboratory. X-ray photoelectron spectroscopy (XPS) data of the binding energies of C, Au, O, and the relevant metals (see Chapter 6) was collected on a Thermo K-alpha XPS and analyzed using Thermo Avantage software [3]. The X-ray source was Al Kα with a spot size of 400 µm^2. An electron flood gun was used for charge compensation.

The C and Au scans were repeated 4 times and the O and relevant metal scans were repeated 8 times. All XPS experiments were conducted at 10^{-8} mbar. Deposition time of the nanostructured materials was increased to 10 min to 40 min for XPS analysis, as these experiments require a much higher concentration than that required for conductometric analysis. Scanning electron microscope (SEM) images were obtained on a Zeiss Ultra60 FE-SEM using SmartSEM software [3]. A high efficiency In-lens SE detector was used with an accelerating voltage of 10 kV and an aperture size of 30 mm.

CHAPTER IV

RESPONSE MECHANISMS OF PSI SENSORS

This chapter presents developments of a simulated sensor Diffusion-Interaction model that allows for an exploration of interaction mechanisms between the analyte gas and a nanostructure decorated porous silicon sensor interface. This model sequentially explores linear, Langmuir adsorption, and a new response model based on the Fermi Distribution function. This modeling provides insight regarding the diffusion mechanics of the porous structure and the adsorption characteristics of the analyte gases, and gives credence to the dominance of electronic interactions. This model is now extended to simultaneously incorporate diffusion, adsorption, the nature of the Fermi-distribution, as well as explore the effect of nanostructure depositions. The agglomerative *combined diffusion-adsorption-interaction* model endeavors to describe the dynamics of the PSi interface with a focus on the first few seconds of interaction with a target analyte. The development of the sensor model is as follows:

- The first stage of the development of the sensor simulation model focuses solely on the diffusion mechanics of the analyte gas into and out from the porous structure of the interface. A numerical simulation of Fick's second law was created to simulate the diffusion and dictate the average concentration within the pores at every time step. The transduction of the interaction of this average concentration into a simulated sensor response was accomplished through a simple *linear response mechanism*.

- The impetus behind the second stage of model development was concerning the nonlinearity of the magnitude of PSi sensor response even at concentrations as low as 10 ppm. Therefore, the transduction of the interaction between the PSi

sensor and analyte gas was updated to an *adsorption response mechanism*. This version of the model translates only the fraction of the concentration of analyte gas within the porous structure actively adsorbed to the PSi interface into a simulated sensor response.

- The third stage of model development considered the effectiveness of the simulated sensor model to describe long time scale saturation conditions at higher concentration levels. Here, a derivation of the response from a consideration of charge carrier density led to the development of a *Fermi-Distribution response mechanism*. Where the adsorption response mechanism struggled to describe the sensor response for a progression of high concentration saturation conditions, the Fermi-Distribution response mechanism excelled. This stage of the model was also able to handle the intricacies of switching from simulated acidic to basic gas analytes as well as switching from n-type to p-type systems, without the use of empirical modeling.

- The final stage of the model development returned the focus of the sensor simulation model to the low concentration unsaturated mode interactions and established a combined *adsorption-Fermi-Distribution response mechanism*. In this version of the model, the transduction of analyte-interface interactions were represented by the as-derived Fermi-Distribution function responding to the fraction of the analyte concentration that is adsorbed onto the surface within the porous structure. The observed weak chemisorption of some gas analyte species, which effectively slowed down the desorption out of the porous structure, was represented by a stickiness parameter incorporated into the time-dependent diffusion portion of the sensor model. The complete sensor simulation model is presented in Appendix D.

For this analysis, the quality of fit of each stage of the model is evaluated through a non-linear regression model, where the parameters are estimated and optimized using the method of least squares. In the method of least squares, the sum of squares criterion, Q, given by,

$$Q = \sum_{i=1}^{n} \left[y_i - f(x_i, \hat{\vec{\beta}}) \right]^2 , \tag{4.1}$$

is minimized. Here, y_i is the experimentally measured dependent variable (sensor response), x_i are the predictor or input values (concentration as a function of time) and $\hat{\vec{\beta}} = \left\{ \hat{\beta}_0, \hat{\beta}_1, \ldots \right\}$ are the estimated parameters or variables for optimization. In this particular model, the parameters can include sensitivity factors (S, χ), the Fermi level and charge carrier mobility constants (β_0), and the adsorption coefficient (K).

A significant disadvantage of nonlinear least squares regression is the necessity of iterative optimization of the parameters. This is accomplished with the Python code, *simulation.py*, provided in Appendix D, which first performs an iterative search on the diffusion constant, then estimates the remaining parameters by performing a non-linear least squares curve fit with the algorithm `scipy.optimize.curve_fit`. Iterative optimization requires user-provided starting values or initial guesses for the parameters. These initial values must be reasonably close to the true value; otherwise, the iterative search may converge to a local minimum instead of the true global minimum. A general method for estimating good starting values is by taking partial derivatives of Q with respect to each parameter, setting each derivative equal to zero, and then solving the system of equations. Even in the simplest models, the parameters are not independent of each other, which must be kept in mind when adjusting initial guesses. As an additional parameter to compare the quality of fit for a particular model, the standard deviation of error is calculated by,

$$\sigma = \sqrt{\frac{Q}{n-p}} , \tag{4.2}$$

where n is the number of data points and p is the number of parameters.

4.1 Diffusion-Interaction Model

For the purpose of exploring the interactions of target gas analytes with nanostructure-modified PSi interfaces, a *diffusion-interaction* model of the sensor response was created [147, 163, 199]. Although an empirical model for the interaction, such as the Freundlich adsorption isotherm [7], could provide a better fit to the experimental data, a mechanistic model was chosen to provide insights into the physics of the interactions. While the dominant diffusion mechanics can be analytically solved for the one dimensional approximations used in this analysis, we seek to model the dynamic interactions under changing atmospheric conditions. Therefore, a numerical simulation following the process summarized in Figure 4.1 is used. The simulated sensor is given an input of atmospheric conditions that are identical to the experimental gas concentrations supplied to the real sensor. The sensor model first simulates diffusion of the gas analyte into the porous structure. The model then calculates the sensor response to the average concentration in the pores for a particular interaction response mechanism. In general, the sensor response mechanism is given by,

$$R(t) = R_0 + \Delta R(C(t), \vec{\beta}) \tag{4.3}$$

where $R(t)$ is the sensor response due to interactions with an analyte gas and R_0 is the baseline response (established in the absence of the analyte). The change in response, $\Delta R(C(t), \vec{\beta})$, is a function of both the average concentration of the analyte gas inside the pores ($C(t)$) and a set of variable optimization parameters ($\vec{\beta} = \{\beta_0, \beta_1, \ldots\}$).

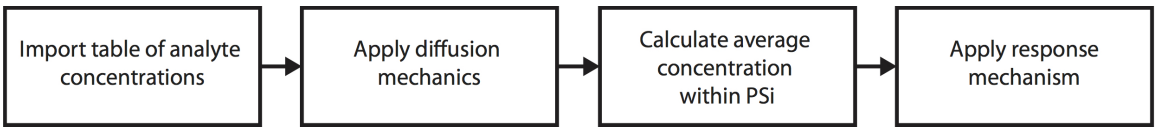

Figure 4.1: Flow diagram of numerical simulation of the PSi sensor model.

4.1.1 Linear response mechanism

A first-pass simulated sensor model, designed to explore the diffusion mechanics of the PSi sensors, assumes the change in response is a linear function described by,

$$\Delta R(t) = S \cdot C(t) \tag{4.4}$$

where the average concentration of the analyte in the pores, $C(t)$, is scaled by a sensitivity factor, S. As the dimension of R and C are Ω and ppm respectively, the dimensions of the sensitivty factor are Ω/ppm.

Modeling the diffusion of the analyte gas into the pores of the sensor interface requires approximating the porous silicon as a collection of one-dimensional wells of length L [54, 147, 163, 199, 274]. The concentration of the ambient analyte gas at the open end of each well was assumed to be a constant source: the diffusion of the analyte molecules into the pores does not deplete the concentration at the open end of the well. Fick's second law governs the diffusion of the analyte gas molecules into the wells through the equation,

$$\frac{\partial C(z,t)}{\partial t} = D_{\mathrm{PSi}} \frac{\partial^2 C(z,t)}{\partial z^2}\,, \tag{4.5}$$

where D_{PSi} is the diffusion constant for porous silicon (PSi) [42,163,199]. The boundary conditions for a pore of finite depth from a continuous source are,

$$C(z,t)\big|_{t=0} = 0 \tag{4.6}$$

$$C(z,t)\big|_{z=0} = C_0 \tag{4.7}$$

$$\left.\frac{\partial C(z,t)}{\partial z}\right|_{z=L} = 0\,, \tag{4.8}$$

where C_0 is the concentration of the analyte gas at the surface of the sensor. The explicit Euler method was used to solve the differential equation and a time step of $dt = 0.05\,\mathrm{s}$ was used. The time step was sufficiently small to achieve a convergence of error within tolerance. Figure 4.2a demonstrates a visualization of the diffusion

of 1 ppm of an arbitrary analyte gas into and out from a one-dimensional pore with a length of 10 units and a plot of the average concentration within the pore (Figure 4.2b). Here, the porous interface is simplified to a single one dimensional pore that is closed at one end. For the initial exploration of the diffusion mechanics of the PSi sensor interface, the following assumptions were used:

- Pores are uniform in width throughout their entire length.
- The diffusion constant is constant throughout the pores.
- No significant adsorption occurs at the bottom of the pore.
- The response is linear with the average concentration of the analyte gas within the pore.

Figure 4.3 demonstrates the reasonably good fit of the diffusion simulation with experimental data. NH_3 acts as a base, donating electrons to a p-type interface, which combine with electronic holes. This represents a reduction in the majority charge carrier concentration of the p-type sensor and, therefore, an increase in the measured resistance. To illustrate the development of the simulated sensor model, the same data set will be shown compared to a best fit for each subsequent modification of the model. Here, the sum of squares for the best fit model is $Q = 677$. As this model includes two parameters, D_{PSi} and S, and the data set has 45 100 data points that are compared with the simulation, the standard deviation of error is $\sigma = 0.123$. The first derivative of the data and simulation is also shown. The first derivative is useful for operation as a sensor; the peak amplitude of the derivative, which can be determined within seconds of exposure to a particular concentration, can be correlated to ambient concentration for development of a fast acting sensor.

The experimental supply of analyte gas is slightly delayed reaching the sensor interface from the time at which a mass flow controller (MFC) controlling the gas

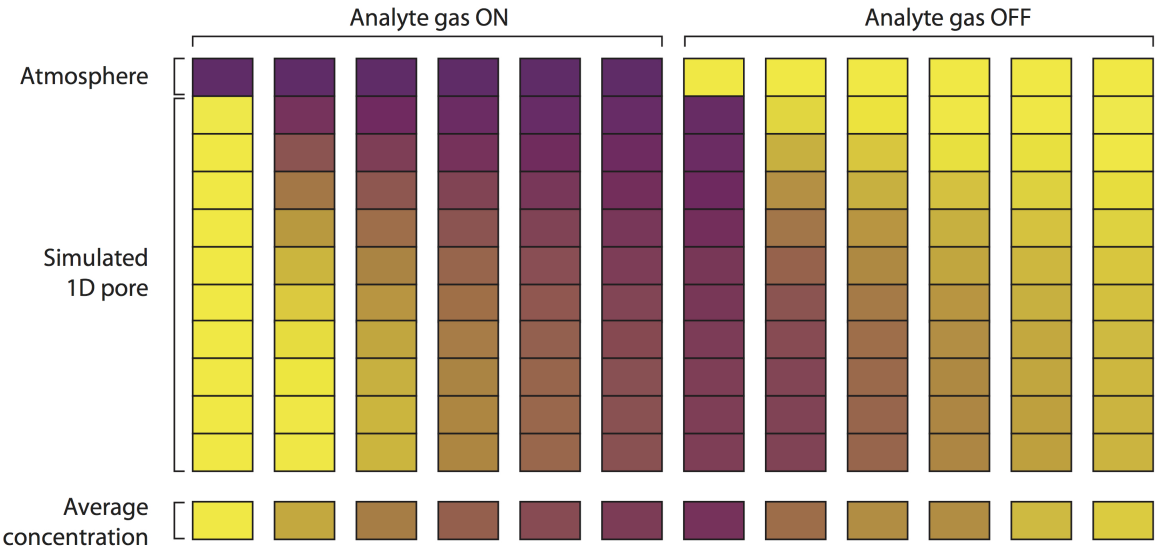

(a)

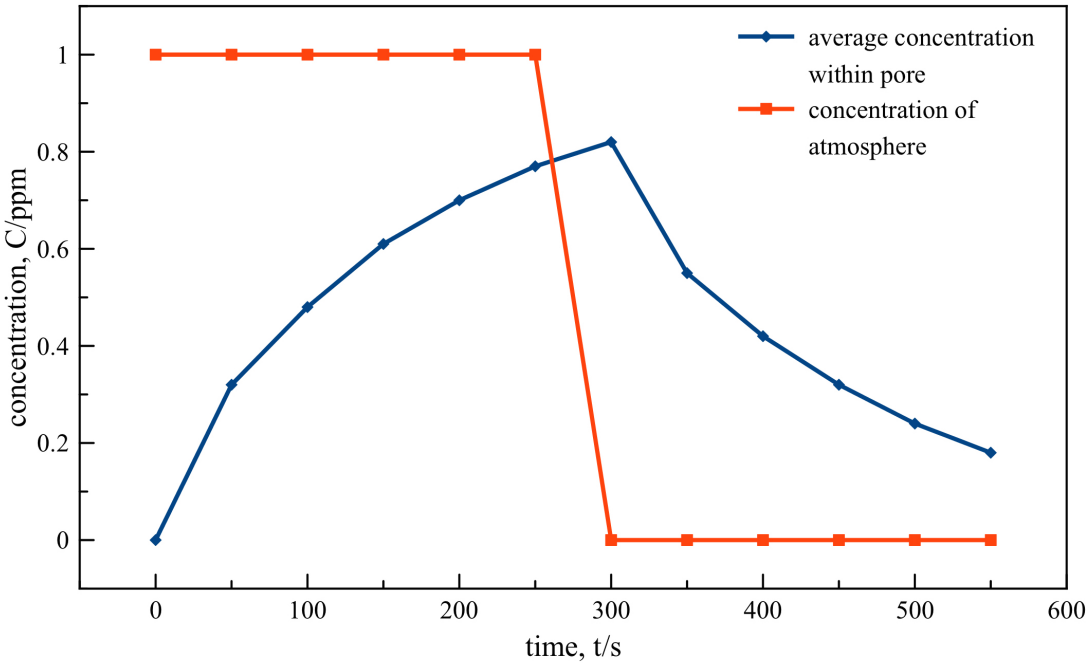

(b)

Figure 4.2: Simulated diffusion of 1 ppm of an arbitrary analyte gas into and out from a 1D pore. (a) Visual representation where yellow indicates pure nitrogen and purple represents 1 ppm of the analyte gas. (b) Plot of the average concentration within the pore compared with the supplied atmospheric concentration. The selected points correspond to the illustrated concentrations. A table of the calculated values used to generate the image are provided in Appendix A and the program for generating the values is provided in Appendix D.

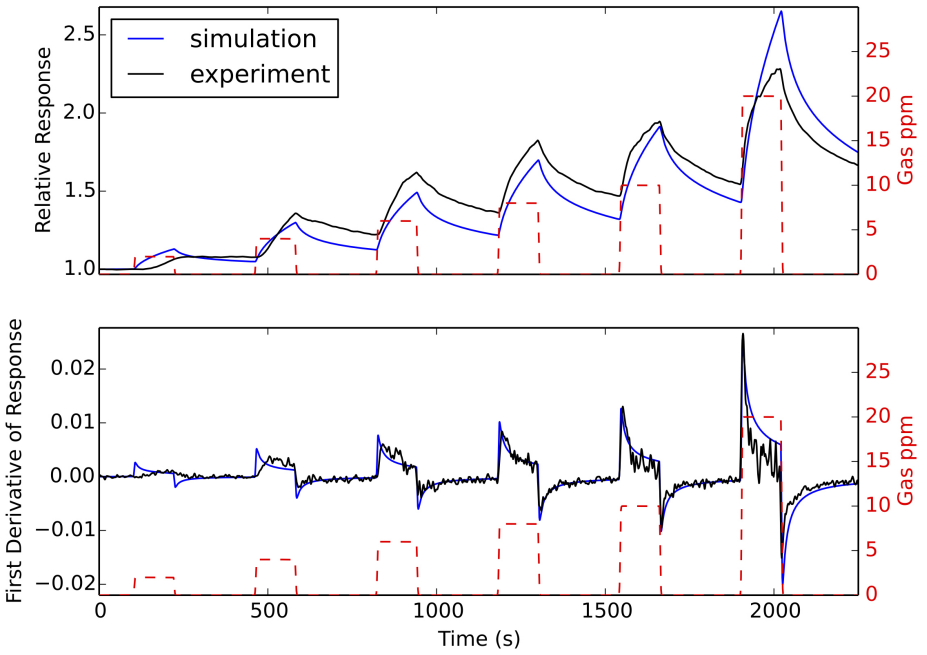

Figure 4.3: Comparison of diffusion simulation with experimental data collected for the response of a p-type PSi sensor in the presence of 2 ppm to 20 ppm NH_3 (red dashed lines). The relative response defined as R/R_0 (top) and the first derivative of the response (bottom) are shown. $Q = 677$ and $\sigma = 0.123$.

supply (Figure 3.7) switches open. Initially, this was compensated for by applying a linear ramp of the atmospheric conditions supplied to the PSi sensor model [147]. As seen in Figure 4.4, this adjustment improves the fit of the model to the experimental data. In particular, the first derivative of the response highlights the necessity of more realistically modeling the atmospheric conditions experienced by the actual PSi sensor. Figure 4.4c demonstrates that the model can be further improved by applying an exponential ramp. The ramp function is also used for simulating turning off the supplied concentrations.

While the diffusion model with a linear response mechanism is a simplistic first-pass representation of the interactions of the analyte-PSi interface, the model provides insight into the overall diffusion mechanics. The diffusion constant for the simulated PSi sensors is on the order of $10^{-12}\,\mathrm{m}^2$ /s to $10^{-9}\,\mathrm{m}^2$ /s, which is characteristic of Knudsen diffusion. Knudsen diffusion describes the diffusion of gas molecules through

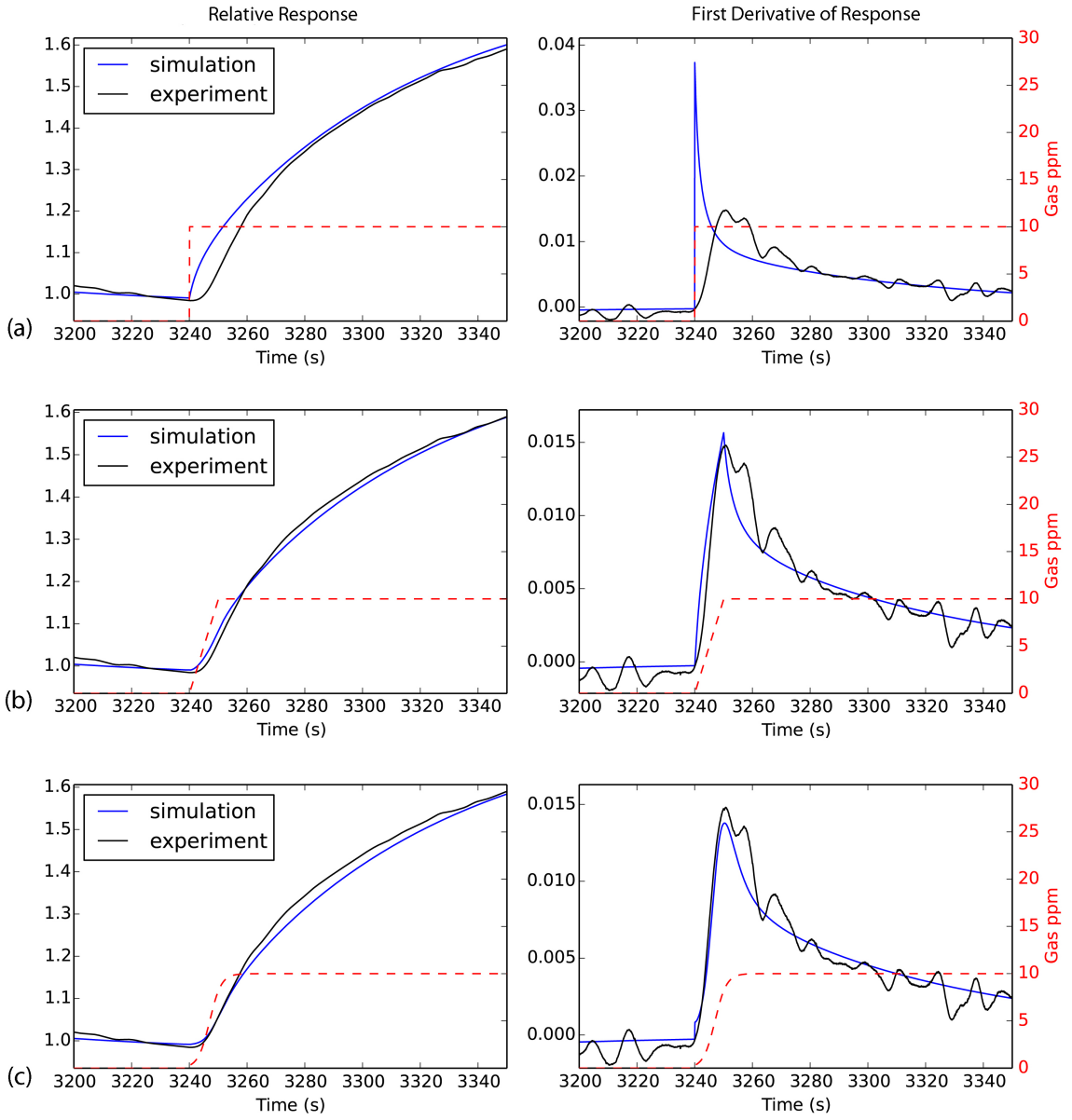

Figure 4.4: Comparison of diffusion simulation with experimental data collected for the response of a p-type PSi sensor in the presence of 10 ppm NH_3. The atmospheric conditions supplied to the simulated PSi sensor model are created as (a) a step function, (b) a linear ramp, or (c) exponential function.

nanometer scale pores [177]. This indicates that, while fast Fickian diffusion describes the diffusion of the analyte gas into the micrometer-diameter porous structures, the gas must also diffuse into the nanoporous features of the hybrid PSi, and these pores are limiting.

4.1.2 Adsorption response mechanism

During our investigations to extract analyte concentrations from the experimental data, we determined that the sensor response was not simply linearly related to concentration. To improve the quality of fit of the sensor model, the Langmuir adsorption isotherm was incorporated to simulate adsorption/desorption effects [152]. The change in response, ΔR, is now defined as a non-linear function of concentration and includes an adjustable adsorption coefficient, K,

$$\Delta R(t) = S \cdot \frac{KC(t)}{1 + KC(t)}\,, \tag{4.9}$$

where $K = K_a/K_b$ is the rate of adsorption divided by the rate of desorption. Here, S is again the sensitivity factor, now with the dimensions of Ω. Figure 4.5 demonstrates the drastic improvement of the quality of the fit of the simulated sensor model by incorporating adsorption/desorption effects. The sum of squares of the best fit is $Q = 163$ and the standard deviation of error, now calculated with a total of three parameters (D_{PSi}, K, and S), is $\sigma = 0.0601$.

For the analysis of the adsorption response mechanism model, we focused on the analytes NH_3 and NO, which act as a base (electron donor) and an acid (electron acceptor), respectively. Figure 4.6 demonstrates the application of the simulated sensor model to a p-type PSi sensor exposed to 1 ppm to 10 ppm NO. The sum of squares for this fit is $Q = 31$ and the standard deviation of error is $\sigma = 0.0262$.

Comparing the adsorption response mechanism model for NH_3 and NO provides insight into the behavior of various gas analytes with the PSi interface. Table 4.1

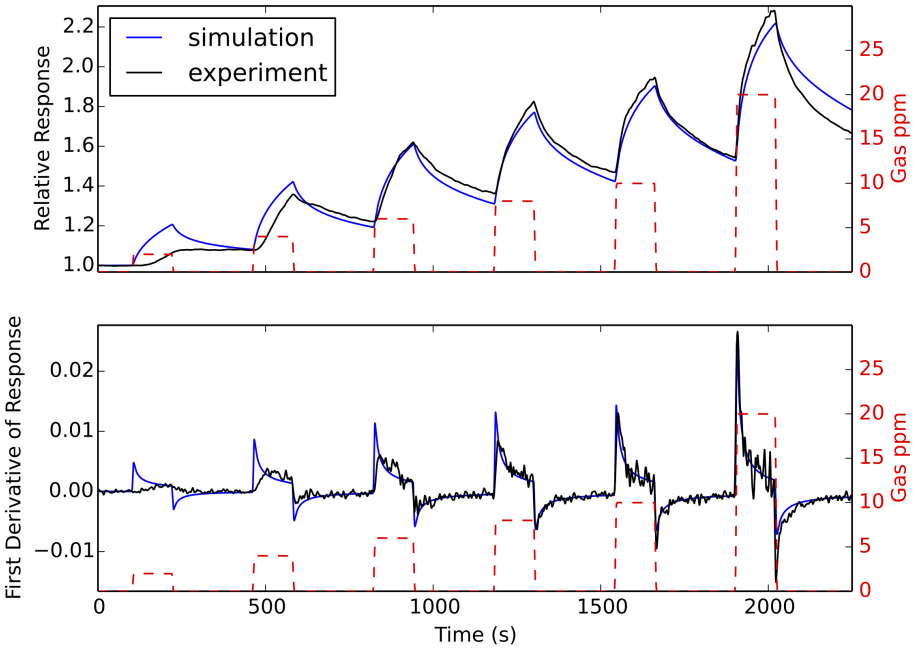

Figure 4.5: Comparison of adsorption response mechanism simulation with experimental data collected for the response of a p-type PSi sensor in the presence of 2 ppm to 20 ppm NH_3. The relative response defined as R/R_0 (top) and the first derivative of the response (bottom) are shown. $Q = 163$ and $\sigma = 0.0601$.

lists the estimated values of the simulation parameters, D_{PSi}, K, and S for the p-type PSi sensor used as an illustrative example in this chapter, as well as parameter values calculated for p-type PSi sensors with a range of nanostructured depositions. These values were calculated from a study of the PSi sensor in multiple-analyte gas experiments, where NH_3 and NO were pulsed onto the sensor both separately and simultaneously during the experiment [147]. For simulating the response to multiple analytes, the response mechanism was expanded to account for the competing processes of the two analyte gases, given by:

$$\Delta R(t) = \begin{cases} 1 - \frac{1}{1-\left(\Delta R_{\text{NH}_3} - \Delta R_{\text{NO}}\right)} & \text{if } \Delta R_{\text{NH}_3} - \Delta R_{\text{NO}} < 0 \\ \Delta R_{\text{NH}_3} - \Delta R_{\text{NO}} & \text{if } \Delta R_{\text{NH}_3} - \Delta R_{\text{NO}} > 0\,. \end{cases} \tag{4.10}$$

The individual response changes due to the analyte gases are given by the Langmuir

adsorption isotherm for the case of multiple adsorbing species:

$$\Delta R_{\mathrm{NH_3}}(t) = S_{\mathrm{NH_3}} \cdot \frac{K_{\mathrm{NH_3}} C_{\mathrm{NH_3}}(t)}{1 + K_{\mathrm{NH_3}} C_{\mathrm{NH_3}}(t) + K_{\mathrm{NO}} C_{\mathrm{NO}}(t)} \tag{4.11}$$

$$\Delta R_{\mathrm{NO}}(t) = S_{\mathrm{NO}} \cdot \frac{K_{\mathrm{NO}} C_{\mathrm{NO}}(t)}{1 + K_{\mathrm{NH_3}} C_{\mathrm{NH_3}}(t) + K_{\mathrm{NO}} C_{\mathrm{NO}}(t)} \,. \tag{4.12}$$

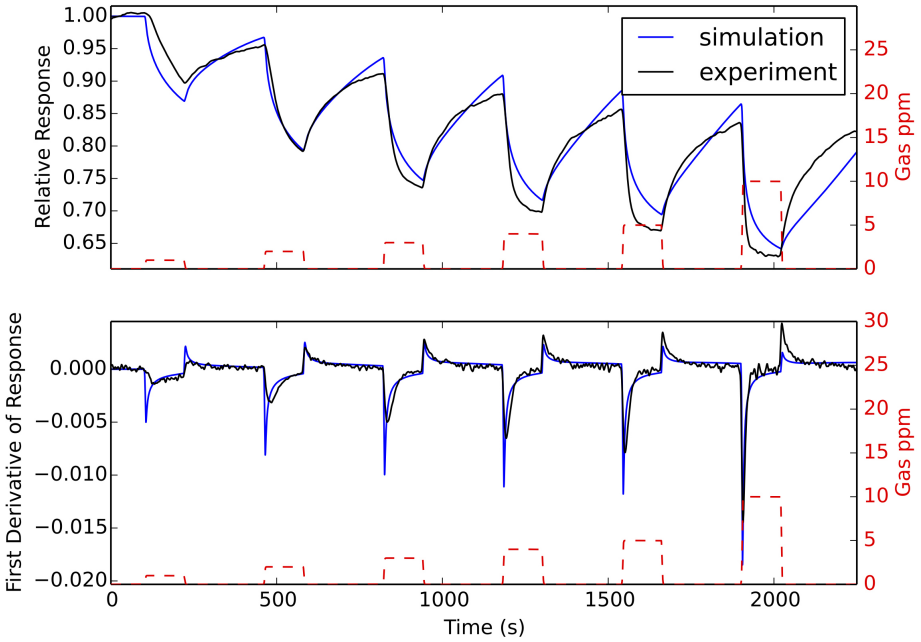

Figure 4.6: Comparison of adsorption response mechanism simulation with experimental data collected for the response of a p-type PSi sensor in the presence of 1 ppm to 10 ppm NO. The relative response defined as R/R_0 (top) and the first derivative of the response (bottom) are shown. $Q = 31$ and $\sigma = 0.0262$.

The comparative sensitivities and adsorption coefficients reported in Table 4.1 are consistent with the expected behavior of NH_3 versus NO. The response for NH_3 is stronger than that for NO. Additionally, NH_3 is a "sticky" gas, which desorbs more slowly than it absorbs, especially when compared with other gas analytes. As $K = K_a/K_d$, an adsorption constant of $K > 1$ indicates that the adsorption process dominates the deposition process (and vice versa). In general, the adsorption constant for "sticky" NH_3 is smaller than NO for a particular PSi interface.

Table 4.1: Sensitivity (S/ohm), adsorption coefficient (K) and diffusion constant ($D_{\mathrm{PSi}}/\mathrm{m^2s^{-1}}$) for adsorption response mechanism model of NH_3 and NO interacting with p-type PSi sensors.

Sensor	sensitivity		adsorption constant		diffusion constant	
	NO	NH_3	NO	NH_3	NO	NH_3
blank PSi	-0.44	2.12	0.75	0.18	1.3×10^{-11}	3.7×10^{-12}
PSi + Au_xO	-0.27	24.8	14.4	0.47	4.9×10^{-9}	4.9×10^{-9}
PSi + TiO_2	-0.73	69.8	0.93	0.41	4.9×10^{-9}	4.9×10^{-9}
PSi + MgO	-0.21	0.527	0.21	0.377	4.9×10^{-9}	4.9×10^{-9}
PSi + CaO	-0.40	13.8	4.82	0.28	4.9×10^{-12}	4.9×10^{-12}
PSi + BaO	-0.44	2.24	0.38	0.12	4.9×10^{-11}	4.9×10^{-11}

Values for metal oxide nanostructure decorated sensors are reprinted from [147].

4.1.3 Fermi-Distribution response mechanism

While the diffusion focused linear response mechanism model and the adsorption response mechanism model were useful for providing insights into the diffusion and adsorption processes of the analyte gas-PSi interface, an analysis at saturation time scales, up to concentrations of 50 ppm, revealed the necessity for improvements to the model. Figure 4.7 demonstrates a comparison of a saturation curve for the experimental data with the adsorption response mechanism model and a newly proposed Fermi-distribution response mechanism [148]. Here, a p-type PSi sensor decorated with Au_xO nanoparticles is exposed to sequentially increasing concentrations of NH_3 and NO. The response, ΔR, versus concentration, or *saturation curve*, is compared with a log-log plot of the saturation curve and a derivative of the saturation curve. This comparison magnifies the inability of the adsorption isotherm response mechanism to fit the saturation curve, as the adsorption isotherm model only marginally fits the experimental data for the log-log and derivative plots. In contrast, the Fermi-Distribution response mechanism model adequately fits the experimental data for all cases in an extended time saturation environment [148].

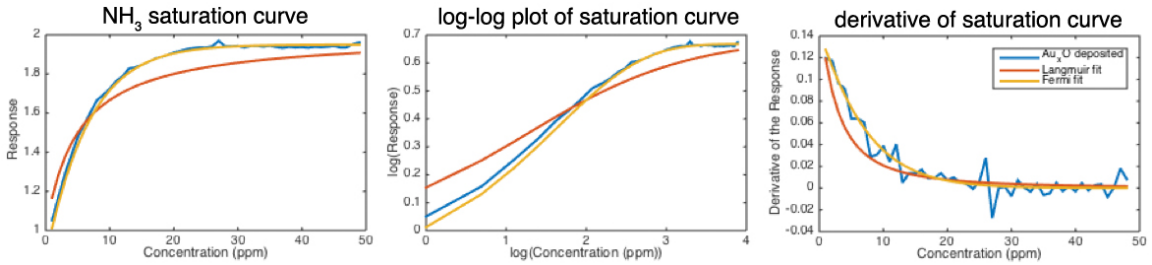

(a)

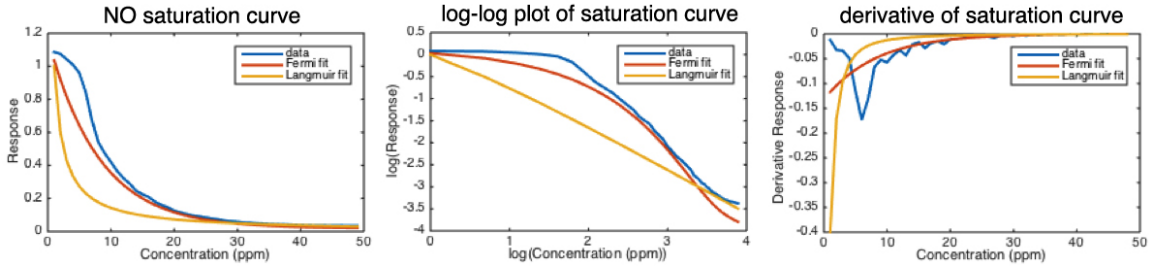

(b)

Figure 4.7: A comparison of the adsorption and Fermi-Distribution models with experimental data collected for a saturation response curve (right) for an Au_xO nanostructure decorated p-type PSi sensor for exposure to (a) NH_3 and (b) NO concentrations up to 50 ppm. The experimentally measured sensor response to NH_3 or NO is in blue. The log-log plot (middle) and the derivative of the saturation response curve (right) illustrate the notably better fit of the Fermi-Distribution response mechanism model. Reprinted with permission from [148].

The Fermi-Distribution response mechanism model was derived from the consideration of the charge carrier concentration of n-type and p-type semiconductors. The measured resistance of the PSi sensor is proportional to the resistivity, ρ, by:

$$R = \frac{\rho L}{A}\,, \tag{4.13}$$

where L is the length and A is the cross-sectional area of the resistor (PSi sensor). Therefore, the resistance response of the PSi sensor can be written in terms of the conductivity through the relation,

$$\rho = \frac{1}{\sigma}\,. \tag{4.14}$$

The conductivity of an extrinsic semiconductor of arbitrary doping concentration is derived in section 2.2.1 as,

$$\sigma_{\text{extrinsic}} = n_i e \left(\mu_c \mathrm{e}^{e\phi_F/k_BT} + \mu_v \mathrm{e}^{-e\phi_F/k_BT}\right)\,, \tag{4.15}$$

where ϕ_F is the potential difference between the midband and the Fermi level (chemical potential), which is dependent on the impurity doping density by,

$$N_d - N_a = 2n_i(T)\sinh\frac{e\phi_F}{k_BT}\,, \tag{4.16}$$

where μ_c and μ_v are the electron and hole mobilities in the conduction and valence band, respectively. Therefore, it is clear that the resistance of the PSi sensor is related to both the mobility and density of the charge carriers. It is assumed that the analyte gas does not change the mobility of the charge carriers, but instead adjusts the density of charge carriers by shifting the location of the Fermi level at constant temperature [148]. The resistivity of the PSi sensors is given by,

$$\rho = \frac{1}{\sigma} = \frac{1}{n_i e \left(\mu_c \mathrm{e}^{e\phi_F/k_BT} + \mu_v \mathrm{e}^{-e\phi_F/k_BT}\right)} \tag{4.17}$$

For the p-type semiconductor systems used in this chapter, $N_a > N_d$. Therefore, for the purposes of the simulation, the resistivity of the PSi sensor can be approximated as,

$$\rho_p \approx \frac{1}{n_i e \left(1 + \frac{\mu_v}{\mu_c}\mathrm{e}^{-e\phi_F/k_BT}\right)}\,. \tag{4.18}$$

Similarly, for n-type semiconductor systems, $N_d > N_a$ and the resistivity can be written as,

$$\rho_n \approx \frac{1}{n_i e \left(\frac{\mu_c}{\mu_v} \mathrm{e}^{e\phi_F/k_B T} + 1\right)} . \tag{4.19}$$

In the presence of an analyte gas, the Fermi level is shifted up or down by a factor, $\Delta\phi$. Here, $\phi_F + \Delta\phi$ represents the electronic chemical potential of the atmosphere at the sensor interface (within the pores of the PSi sensor) when the analyte gas is introduced [147]. In the absence of any gas analyte (an atmosphere of UHP nitrogen), the system is assumed to be in equilibrium and $\Delta\phi$ is set equal to zero and the chemical potential of the surrounding atmosphere is equal to ϕ_F. When gas analytes are introduced to the atmosphere, $\Delta\phi$ is given by,

$$\Delta\phi = \sum \chi_i C_i \tag{4.20}$$

where C_i is the concentration of each individual chemical species and χ_i is a sensitivity factor that scales the influence of a particular chemical species on the chemical potential of the atmosphere. Here, the dimensions of χ_i are V/ppm. For example, the p-type semiconductor resistivity becomes,

$$\rho_p \approx \frac{1}{n_i e \left(1 + \frac{\mu_v}{\mu_c} \mathrm{e}^{-e(\phi_F + \Delta\phi)/k_B T}\right)} . \tag{4.21}$$

This is consistent with the discussion of the analyte gas acting as an acid or base. An acid with an electrochemical potential lower than that of the PSi sensor will adjust the Fermi level down, decreasing the electron density in the conduction band and increasing the number of holes in the valence band; this represents an increase in resistance for n-type semiconductor systems and a decrease in resistance for p-type semiconductor systems. The opposite will occur with a base having an electrochemical potential higher than that of the PSi sensor.

For the purpose of the simulated sensor model, the sensor response mechanism for

a p-type PSi sensor is now given by,

$$R^p(t) = \frac{L/A}{n_i e\left(1 + \frac{\mu_v}{\mu_c}\mathrm{e}^{-e(\phi_F+\Delta\phi)/k_BT}\right)}\,, \tag{4.22}$$

where L and A are the length and cross-sectional area of the sensor and $R(t)$ is again the resistance of the sensor. For simplicity, the constants are collected, giving,

$$R^p(t) = \frac{\beta_1}{1 + \beta_0\mathrm{e}^{-e\Delta\phi/k_BT}}\,, \tag{4.23}$$

where $\beta_0 = (\mu_v/\mu_c)\mathrm{e}^{-e\phi_F}$ and $\beta_1 = L/Aen_i$. The baseline resistance, R_0, in the absence of any gas analytes is thus given by,

$$R_0^p = \frac{\beta_1}{1 + \beta_0}\,. \tag{4.24}$$

For comparison with experimental data, the relative resistance response, $\Omega(t)$, is given by,

$$\Omega(t) = \frac{R^p(t)}{R_0^p} \tag{4.25}$$

$$= \frac{\beta_1}{1 + \beta_0\mathrm{e}^{-e\Delta\phi/k_BT}} \cdot \frac{1 + \beta_0}{\beta_1} \tag{4.26}$$

$$= \frac{1 + \beta_0}{1 + \beta_0\mathrm{e}^{-e\Delta\phi/k_BT}}\,, \tag{4.27}$$

where $\Delta\phi = \sum \chi_i C_i(t)$.

Shown in Figure 4.7, the Fermi-Distribution model can easily handle both increases and decreases in resistance in response to gas analytes acting as bases or acids. This should be compared to the more cumbersome conditional change in response, which was necessary when using the Langmuir adsorption interaction model (Equation 4.10). For the Fermi-Distribution response function, modeling the addition of electrons (in the case of NH_3) versus the removal of electrons (in the case of NO) is simply a matter of switching the coefficient of the analyte chemical potential sensitivity factor, χ_i, from positive to negative.

The Fermi-Distribution response mechanism model also explains the observed dependence of the response on temperature [13, 148]. In an experiment where sensor

response to NH_3 was collected at gradually increasing temperature, the sensor signal showed an exponential decay in amplitude [13]. This is in agreement with the thermal exponential decay term in the Fermi-Distribution response mechanism model. While this temperature dependence of the sensor response could potentially be explained by an increase in chemisorption reaction rate, the ease of returning to baseline invalidates this conclusion. Therefore, we suggest that the Fermi-Distribution response mechanism model is a viable method of explaining the mechanisms occurring between the analyte gas and the porous silicon interface, especially under saturation conditions.

To properly model the full range of analyte concentrations at saturation levels, Figure 4.7 clearly indicates that a Fermi-Distribution response mechanism is required. This reveals that the limit to the response of a particular sensor is a matter of electronic band structure saturation, rather than adsorption saturation. However, the Fermi-Distribution response mechanism model has existing limitations in simulating the PSi sensor response at low concentrations when operating in an unsaturated mode.

Figure 4.8 illustrates the best fit, minimizing the sum of squares, for the p-type PSi sensor exposed to 2 ppm to 20 ppm NH_3 used as an example throughout this chapter. Here, the sum of squares was $Q = 256$ and the standard deviation of error was $\sigma = 0.0753$. While this represents a better fit than the simple linear response mechanism outlined in section 4.1.1 ($Q = 677$), the fit is not as good as the adsorption isotherm response mechanism model described in section 4.1.2 ($Q = 163$). In particular, the Fermi-Distribution response mechanism model struggles to properly model the diffusion out of the pores, as can be seen in Figure 4.8 (note in particular the fit of diffusion after exposure to 20 ppm). This suggests that while the Fermi-Distribution response mechanism dominates at high concentrations and saturation conditions, the limiting effects of adsorption are necessary to describe the dynamics at low concentration and unsaturated conditions. In other words, at low concentrations,

the response of the PSi sensors are likely limited by Langmuir adsorption, where adsorbed analyte molecules only cover a fraction of a monolayer of the interface; the changes due to the adsorbed analyte molecules are well below the limitations governed by the Fermi-Distribution function. The following section will describe two key modifications to the sensor model: incorporation of adsorption effects into the Fermi-Distribution response mechanism, as well as introducing a parameter to address the stickiness, or weak chemisorption, of some gases [85, 198].

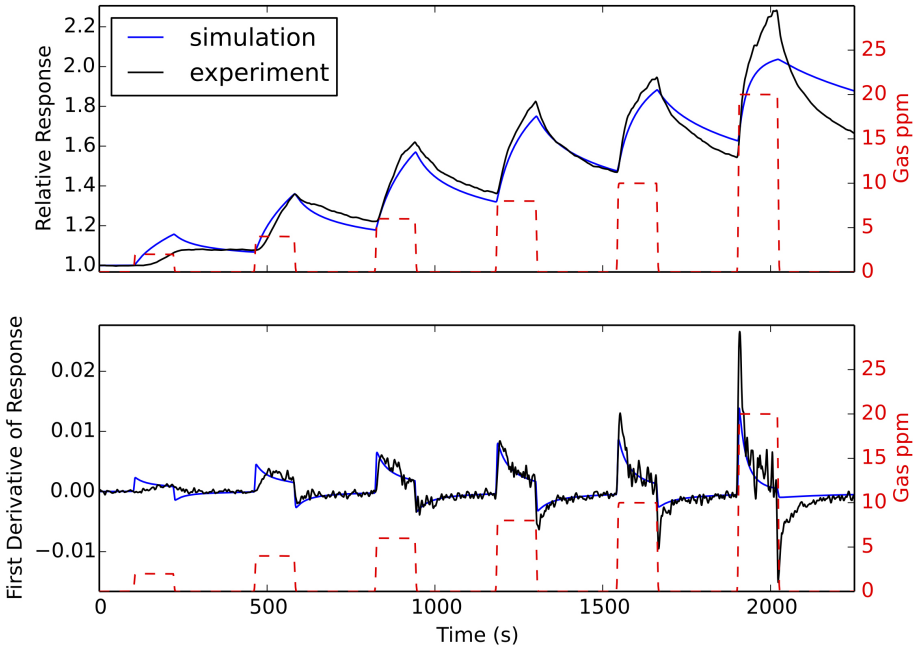

Figure 4.8: Comparison of Fermi-Distribution response mechanism simulation with experimental data collected for the response of a p-type PSi sensor in the presence of 2 ppm to 20 ppm NH_3. The relative response defined as R/R_0 (top) and the first derivative of the response (bottom) are shown. $Q = 256$ and $\sigma = 0.0753$.

4.1.4 Combined adsorption-Fermi-Distribution model

The adsorption effects were introduced to the Fermi-Distribution model by adjusting the change in Fermi level due to the presence of an analyte gas, $\Delta\phi$ in Equation 4.27. Rather than assuming that the shift in Fermi level, $\Delta\phi$, is linear with concentration, the shift was instead set to be linear with the *fraction* of gas analyte molecules

adsorbed to the PSi interface:

$$\Delta\phi(t) = \chi \cdot \theta(t)\,, \tag{4.28}$$

where $\theta(t)$ is fraction of the maximum amount of possible gas analyte adsorption and χ is the chemical potential of the particular chemical species with dimensions of V (volt). This value is described by the generalized treatment of the Langmuir isotherm, known as BET theory, which incorporates multilayer adsorption, given by:

$$\theta(t) = \frac{K_{\mathrm{BET}} C(t)}{(C_0 - C(t))\left(1 + (K_{\mathrm{BET}} - 1)\frac{C(t)}{C_0}\right)}\,, \tag{4.29}$$

where, K_{BET} is a dimensionless adsorption constant and C_0 is the saturation concentration of the analyte. The adsorption constant, K_{BET}, is given by:

$$K_{\mathrm{BET}} \propto \mathrm{e}^{\frac{q_1 - q_L}{RT}}\,, \tag{4.30}$$

where q_1 is the heat of adsorption of the first layer, q_L is the heat of liquefaction of the adsorptive species (or also heat of adsorption of the multi-layers), R is the gas constant, and T is the absolute temperature. Typical values of K_{BET} range from 50 to 300. BET theory, named for the surnames of its originators, Brunauer, Emmett, and Teller, is used to describe adsorption dominated by physisorption [273] (in contrast to the Langmuir isotherm, which is usually a better model for describing chemisorption). Therefore, the BET theory based adsorption model is appropriate for these PSi sensor systems.

Figure 4.9 demonstrates the quality of fit of this combination adsorption-Fermi-Distribution model. The least sum of squares is $Q = 161$ and the standard deviation of error is $\sigma = 0.0598$. As predicted, incorporating adsorption effects improves the fit of the simulation compared to the Fermi-Distribution model for the low concentration unsaturated conditions. Table 4.2 presents a comparison of the quality of fitting for each of the response mechanisms. On average, testing a large number of sample PSi response experimental data sets, the *combined* adsorption-Fermi-Distribution

model resulted in the highest quality of fit (lowest sum of squares). The next best fitting model was the Langmuir adsorption response mechanism (section 4.1.2). The BET adsorption model behaves similarly to the Langmuir adsorption isotherm in low concentration conditions ($C(t) \ll C_0$), which can explain the closeness of the quality of fit. However, the combined adsorption-Fermi-Distribution response mechanism model represents a significantly more appropriate model for the PSi sensor system for several reasons beyond a just having slightly better fit. The combined model can handle both acidic and basic gas analyte interactions with a simple sign change, similar to the Fermi-Distribution model. Also similar to the Fermi-Distribution model, the combined model can still explain temperature effects, which are absent from the linear and adsorption models. The temperature effect of exponentially reducing the response is also present in the BET theory adsorption constant (Equation 4.30). Finally, the BET adsorption equation does not limit the response for high concentration saturation conditions, allowing the Fermi-Distribution function to dominate in that regime.

Table 4.2: Sum of squares criterion, Q, and standard deviation of error, σ, for the best fit for each stage of the PSi sensor simulation model for a p-type PSi sensor exposed to 2 ppm to 20 ppm NH_3.

Response mechanism (RM) model	Q	σ
Linear RM	677	0.123
Langmuir adsorption RM	163	0.0601
Fermi-Distribution RM	256	0.0753
Combined BET adsorption-Fermi-Distribution RM	161	0.0598

To account for situations where the analyte gas is particularly sticky and exhibiting weak chemisorption [85, 198], a stickiness parameter, s was incorporated into the diffusion model [139], rather than the response mechanism. The reasoning for this was that the delayed release of the analyte molecules is a time-dependent behavior that then affects the concentrations diffusing among segments of the simulated

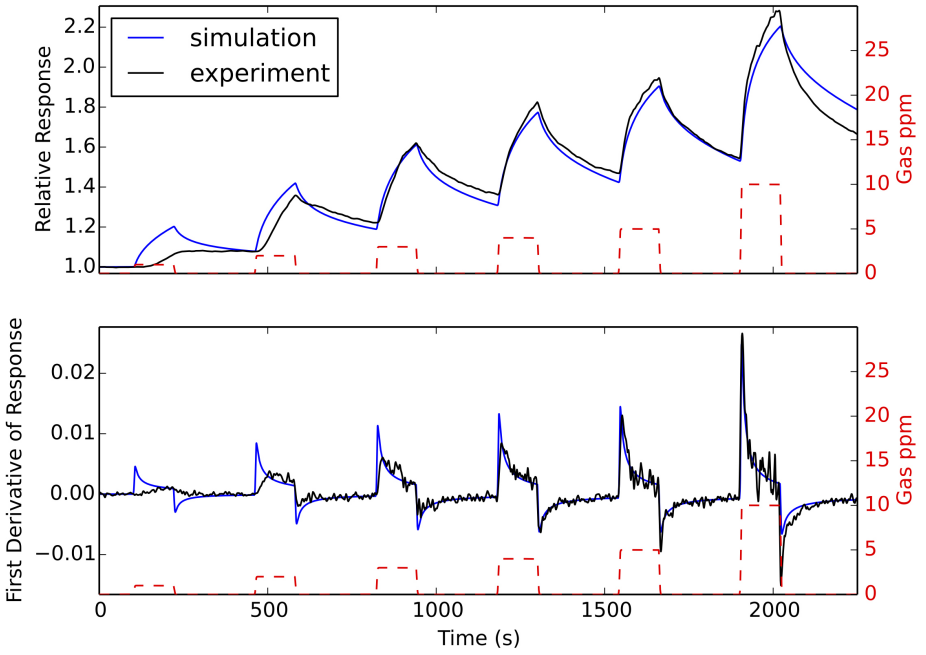

Figure 4.9: Comparison of *combined* adsorption-Fermi-distribution response mechanism simulation with experimental data collected for the response of a p-type PSi sensor in the presence of 2 ppm to 20 ppm NH_3. The relative response defined as R/R_0 (top) and the first derivative of the response (bottom) are shown. $Q = 161$ and $\sigma = 0.0598$.

PSi pore. As the response mechanisms, such as adsorption and adjustments of the carrier density through a shift in Fermi level, were assumed to occur at time scales much shorter than diffusion, only the diffusion mechanics of the simulation remained time-dependent. The response mechanisms were thus calculated from the average concentration dictated by the diffusion model at each time step.

The stickiness parameter, s was incorporated into the diffusion mechanism component of the sensor model as a lag in the diffusion out of a particular pore segment. Shown in the Python code, *simulation.py* within the function, `Cavg_calc_new` (Appendix D), the concentration of each segment of the simulated one dimensional pore is updated at each time step by an *evolution matrix*, which applies the diffusion mechanics equation described in section 4.1.1. For every term in the evolution matrix

that is negative, representing gas diffusing out of a segment and into another, a stickiness lag parameter is applied. Figure 4.10 demonstrates the effect of adjusting the stickiness parameter for a p-type PSi sensor exposed to 100 ppm H_2S. An increase in stickiness or chemisorptive effects of an analyte gas represents a decrease in the ability for that gas to desorb and then diffuse from any particular location within each pore. Therefore, as s is used in the simulation code, *simulation.py* (Appendix D), as a scaling factor for the desorption, a lower value of s signifies a greater stickiness or weak-chemisorption effect [139]. The least sum of squares, Q is shown for each subsequent adjustment of the stickiness parameter to illustrate the improvement of the model.

4.2 Conclusions

The PSi sensor simulation model provides a fundamental understanding of the mechanisms of analyte gas and porous silicon sensor interface interactions. Through a systematic exploration of the PSi sensor response to gas analytes and comparison with a range of simulated response mechanisms, the characteristics of various chemical and physical parameters of the interface interactions were brought to light. The linear response mechanism model provided an initial understanding of the diffusion mechanics and highlighted the dominance of Knudsen diffusion of the gas analyte into the nanometer diameter pores. The adsorption model allowed for a comparison of interactions of the PSi sensors with gas analytes with different energies of adsorption. The derived Fermi-Distribution model provided a high quality fit at high concentrations and saturation conditions. The Fermi-Distribution model also offered insight into the representation of changing atmospheric chemical composition by a change in chemical potential. A combined adsorption-Fermi-Distribution model was developed to include adsorption effects into the Fermi-Distribution model to improve the quality

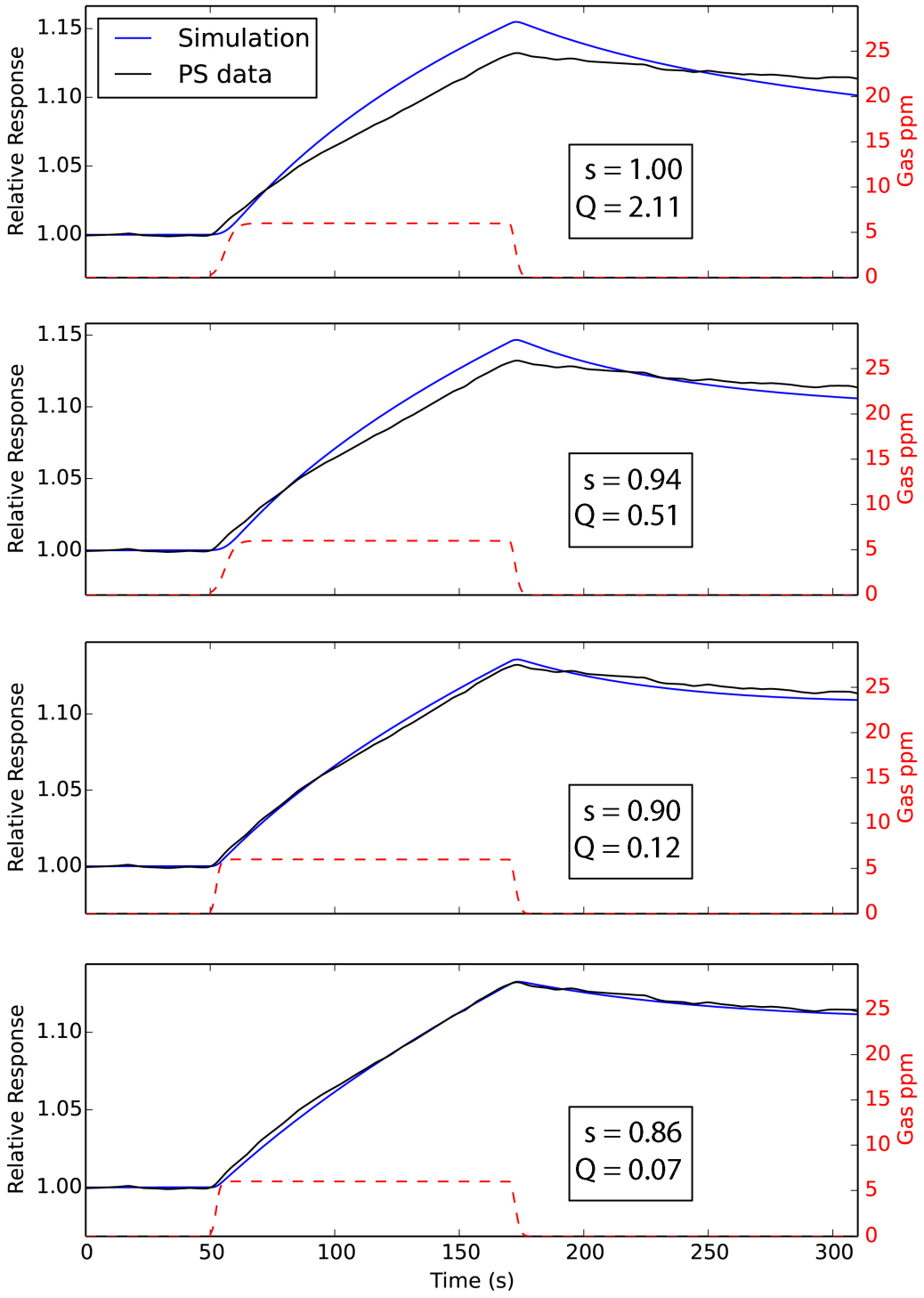

Figure 4.10: Comparison of simulation with experimental data collected for the response of a p-type PSi sensor in the presence of 100 ppm H_2S for increasing degrees of simulated *stickiness*, s and the corresponding best fit sum of squares, Q.

of fit at low concentrations in unsaturated conditions. Finally, a stickiness parameter is introduced into the model to better represent situations where the analyte gas exemplifies weak chemisorption.

As an extended consideration, the model was applied to PSi sensor experimental data before and after metal oxide nanostructure depositions. For example, Figure 4.11 illustrates a best fit for the same p-type PSi sensor used throughout this chapter, with a metal oxide nanostructured deposition (MgO), exposed to 2 ppm to 20 ppm NH_3. This represents a step towards developing a quantifiable model of the IHSAB principle and illustrating how the sensor response to various gas analytes change upon nanostructure decoration. However, the current PSi sensor simulation is no longer a simple linear model with just a single adjustable sensor sensitivity parameter, but instead includes multiple dependent parameters. For example, the estimated parameters for the PSi sensor treated with MgO were changed from the untreated PSi sensor as follows: the adsorption constant, K_{BET} was slightly increased, the influence of the chemical potential of NH_3, $\chi_{\mathrm{NH_3}}$, was slightly decreased, and β_0, the collection of constants describing the Fermi level and carrier mobilities, was greatly increased. Further development of a simulation fitting program, and comparison with a much larger data set of similarly prepared and tested sensors, will allow for a more defined correlation between sensor response and interface modifications.

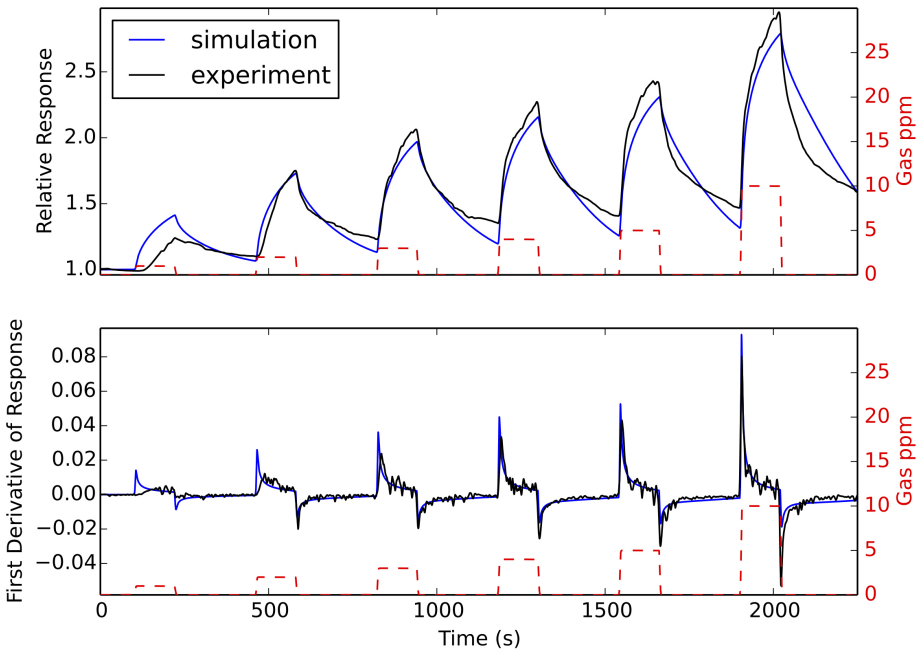

Figure 4.11: Comparison of *combined* adsorption-Fermi-distribution response mechanism simulation with experimental data collected for the response of a p-type PSi sensor decorated with MgO, in the presence of 2 ppm to 20 ppm NH_3. The relative response defined as R/R_0 (top) and the first derivative of the response (bottom) are shown.

CHAPTER V

IHSAB: ENHANCED SENSITIVITY AND SELECTIVITY

Nanostructure modified PSi interfaces have been demonstrated as effective chemical gas sensors for low levels of inorganic analytes such as NH_3, NO_x, SO_2, and PH_3 [86, 92, 94, 95, 145, 163, 164, 197, 197]. The sensors are rapidly responding, as demonstrated in Chapter 4 by monitoring the first derivative of the response, reversible, returning to the baseline resistance value within reasonable timescales, and repeatable [162,163,197,233]. Observed sensitivities and the sensor system reversibility can be predicted from the recently developing Inverse Hard/Soft Acid/Base IHSAB model [86, 92, 94, 95, 145, 163, 164, 197], which provides a means of linking chemical selectivity and the mechanism of sensor response. This model combines the basic tenants of acid/base chemistry (the ability of bases to donate electrons and acids to seek electrons) and semiconductor physics. The materials selected for nanostructured islands serve the role of guiding gateways to force a dominant electron transduction (versus chemisorption) at the decorated extrinsic semiconductor interface. The selection of these nanostructures and the variable and controllable reversible interaction they introduce for sensor applications is well predicted by the IHSAB model as it dictates the coupling of analyte/interface acid-base interactions with the properties of the majority carriers in an extrinsic semiconductor [86,92,94,95,145,163,164,197]. The inverse hard and soft acid and base (IHSAB) concept complements the tenants of HSAB interactions [207, 208]. Based on the reversible interaction of hard acids and bases with soft bases and acids, the IHSAB principle enables the selection of interacting materials that do not form strong covalent or ionic chemical bonds, thus it represents the inverse of the HSAB model for significant bond formation based

on strong ionic (hard acid/base) or covalent (soft acid/base) interactions and chemical bond formation. The selection of the nanostructures that are deposited to the nanopore-covered microchannels can be predicated based on a clearly designed procedure and established materials properties [86, 92, 94, 95, 145, 163, 164, 197].

5.1 Sensitivity: Enhanced Detection of H_2S and CO

Here, we apply the principles that we have outlined above to the reversible detection of the H_2S and CO analytes. The energy efficient and simple sensor platforms that we develop demonstrate a superior sensitivity to H_2S, display a very slow degradation due to the H_2S gas, and can be readily rejuvenated both from extensive use and excessive water contamination [86]. The nanostructure modified PSi sensors are demonstrated as sensitive *at room temperature* to CO at concentrations well below previously reported levels [28, 113, 119, 175, 188, 228]. Table 5.1 summarizes recent advances in the detection of CO utilizing nanostructured metal oxides. Earlier work with the nanostructure modified PSi sensors featured in this thesis demonstrated the ability of a SnO_x nanostructured deposition to greatly enhance the PSi response to CO (Table 5.1) [163]. Using the IHSAB principle as a guide for the selection of nanostructured deposition, here, an additional enhancement of the PSi sensor response to CO is explored.

The placement of H_2S and CO on the IHSAB scale [86, 92, 94, 95, 145, 163, 164, 197] is shown in Figure 5.1. These particular placements will be discussed in section 5.1.3. Selected nanostructured metal oxides are deposited to the nanopore-covered micropores of the PSi sensors, as described in Chapter 3, to provide for distinct and variable sensitivities. The variable sensitivities of each sensor can be used in combination as a basis to develop a matrix of selectivity. In this study, nanostructured deposits generated from electroless gold, tin, and nickel [92, 198], as well as nanotitania [43, 98] provide for a variable matrix for the detection of H_2S on a p-type PSi interface. For

Table 5.1: Lower exposure limit of CO gas sensor materials and methods.

Reported LEL*	Operating Temperature	Material	Method	Reference
50 ppm	350 °C	0.2 wt% Pt/SnO_2	FSP (nanopowders); Thermophoresis (sensor)	[175]
500 ppm	200 °C to 400 °C	SnO_2	FSP (nanopowders); drop coating (sensor)	[228]
10 ppm	150 °C	CuO	soft chemistry (nanospheres); thick film screen printing (sensor)	[119]
< 5 ppm	300 °C	SnO_2	single nanowire	[113]
1 ppm	25 °C	SnO_2 treated PSi	Sn electroless solution	[163]

*Lower Exposure Limit

sensitivity studies of the PSi response to small concentrations of CO, the PSi sensors are decorated with nanotitania and tin oxide nanostructures. The PSi sensors are tested as described in Chapter 3. After a purge in UHP nitrogen for a minimum of 30 min to establish a baseline for sensor response, the PSi sensor is exposed to various concentrations of H_2S or CO in cycles of 120 s followed by an UHP nitrogen purge for 240 s.

5.1.1 Sensor response to H_2S

Figure 5.2 indicates the response to H_2S for an untreated p-type porous silicon interface at concentrations of 0.6 ppm to 6.0 ppm and demonstrates the repeatability of experimental tests. Here, relative resistance is the measured resistance, R, divided by the baseline resistance, R_0. It is to be noted that running the sensor at 4 V does little to improve the response at 3 V. A rapid response is observed at each concentration, but the time frame for the H_2S to desorb from the sensor surface clearly exceeds the time scale for adsorption.

Figure 5.3a demonstrates the response to H_2S for an untreated p-type PSi interface

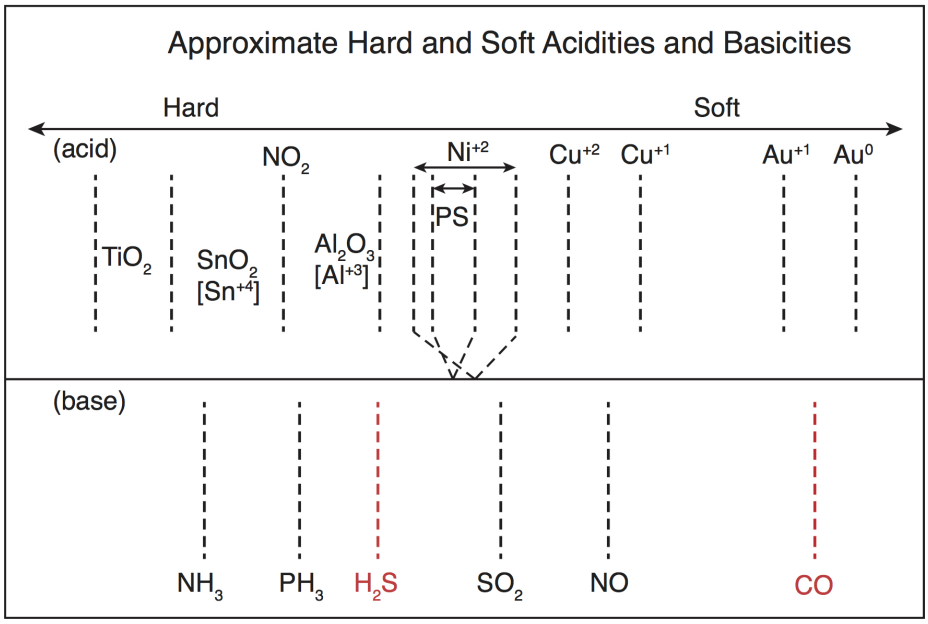

Figure 5.1: Approximate IHSAB scale showing the positioning of H_2S and CO (red).

at concentrations of 6 ppm to 60 ppm and Figure 5.3b corresponds to H_2S at 100 ppm. The data in Figures 5.2 and 5.3 demonstrate a range of concentrations with which we can assess the degree of consistent dependence on concentration and the nature of signal quenching at higher concentration. These data indicate some evidence for quenching at analyte concentrations in excess of 60 ppm. As shown in the figures, the return to baseline, or "recovery", takes longer than the 240 s UHP nitrogen purge. However, the recovery time can be improved, as will be demonstrated, by using select metal oxide depositions and the rejuvenation techniques that we have developed [86].

The effectiveness of the IHSAB model, as it predicts the changes in sensor sensitivity as a function of the choice of metal oxide nanostructure deposition, is shown in Figures 5.4 through 5.7. Figure 5.4 indicates the response to H_2S for an SnO_x nanostructure decorated p-type PSi interface, compared to the response for the undecorated p-type PSi interface at concentrations of 6 ppm, 12 ppm, 18 ppm, 24 ppm, 30 ppm and 60 ppm. We observe a considerable enhancement of the response versus an untreated PSi sensor after SnO_x decoration. In view of the hard acid character of SnO_x resulting in a significant molecular orbital mismatch with H_2S (Figure 5.1),

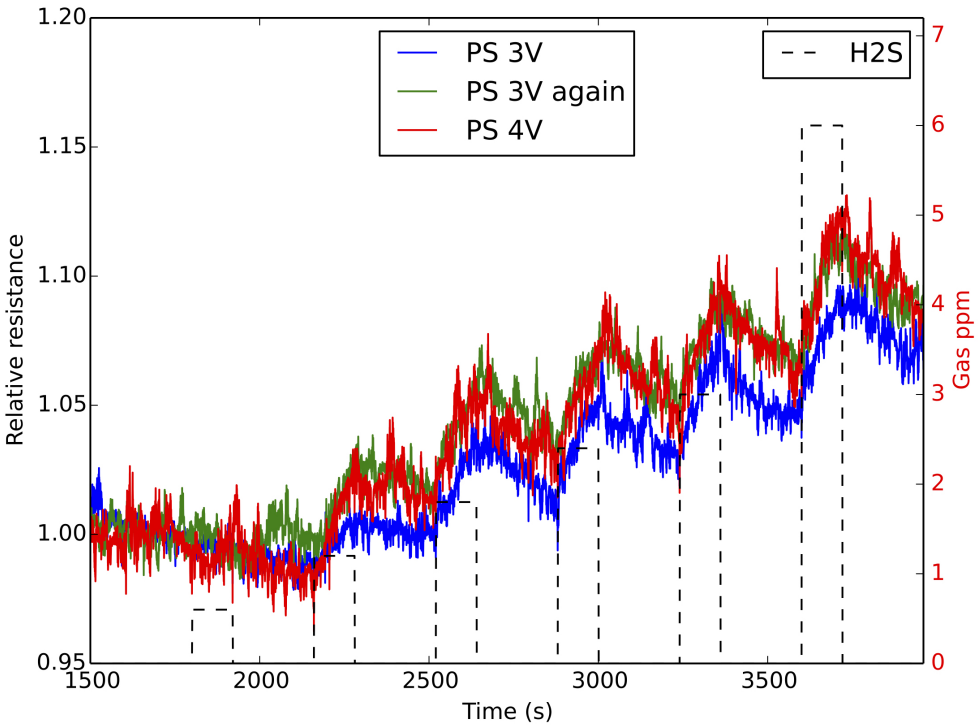

Figure 5.2: Responses to H_2S for an untreated p-type porous silicon interface at concentrations of 0.6 ppm, 1.2 ppm, 1.8 ppm, 2.4 ppm, 3.0 ppm and 6.0 ppm at 3 V and 4 V bias voltage. The boxes (black dashed) denote the analyte concentration over the time of analyte gas exposure to the sensors.

this is not surprising.

Figure 5.5 indicates the response to H_2S for a TiO_2 decorated p-type PSi interface, comparing this to the response for the undecorated p-type PSi interface at concentrations of 6 ppm, 12 ppm, 18 ppm, 24 ppm, 30 ppm and 60 ppm. We observe a considerable enhancement of the response after TiO_2 nanostructure decoration. Noting the scales for Figures 5.4 and 5.5, it is apparent that the enhancement exceeds that induced with SnO_x decoration. This is consistent with the positioning in Figure 5.1 and is, again, not surprising in view of the hard acid character of TiO_2 . The result is also consistent with previous observations [86, 92].

Figure 5.6 indicates the response of H_2S to an NiO decorated p-type PSi interface, comparing this to the response for the undecorated p-type PSi interface at concentrations of 6 ppm, 12 ppm, 18 ppm, 24 ppm, 30 ppm and 60 ppm. We observe a

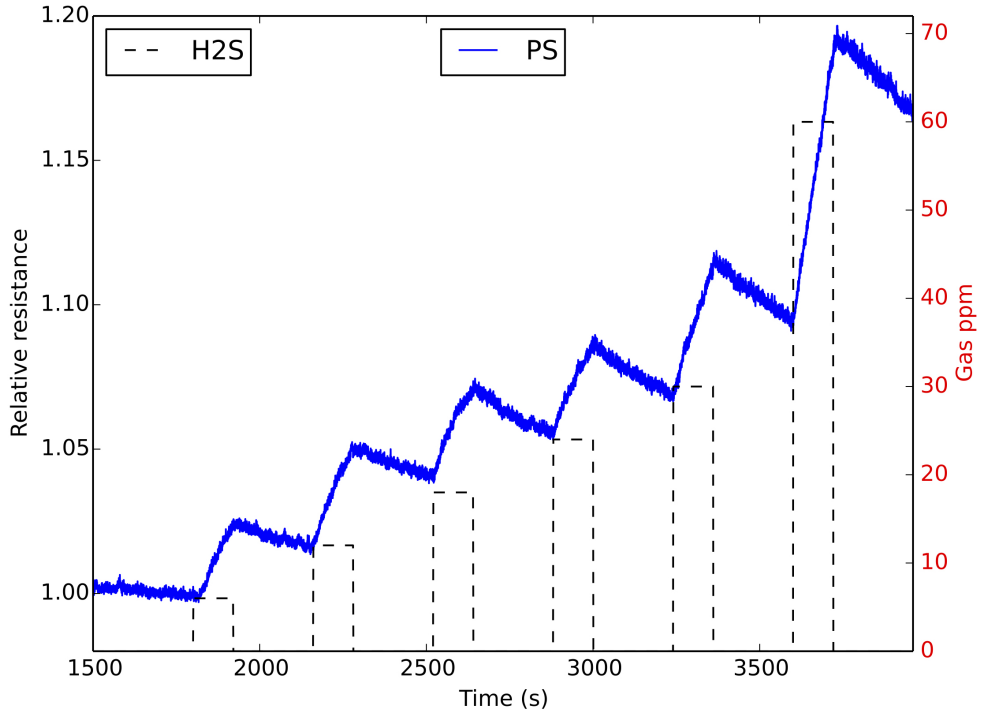

(a)

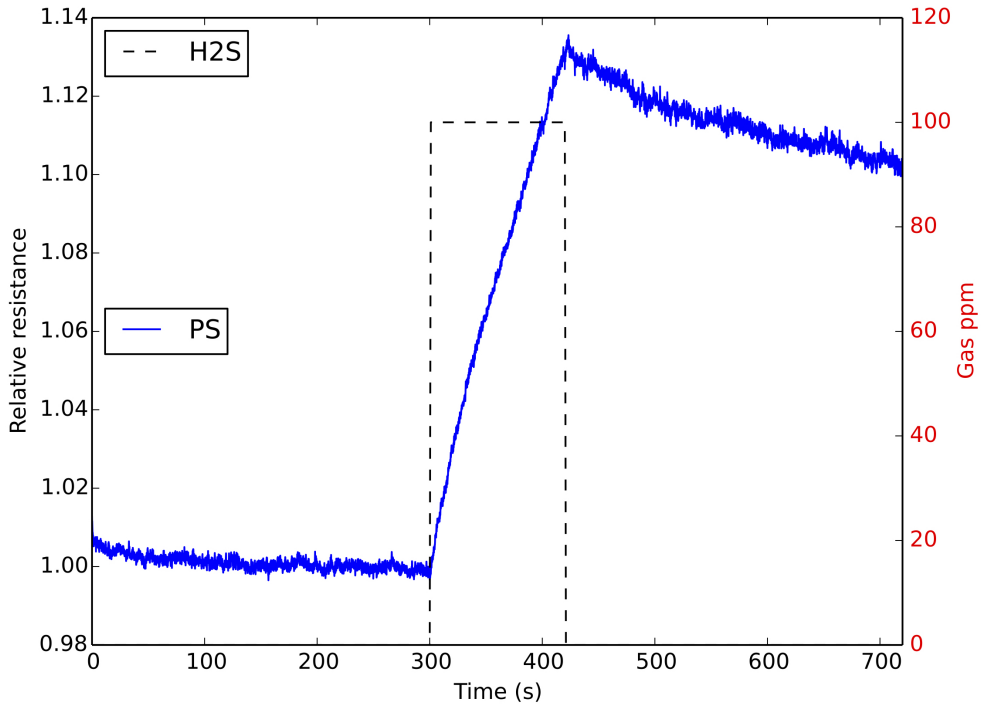

(b)

Figure 5.3: (a) Responses to H_2S for an untreated p-type PSi interface at concentrations of 6 ppm, 12 ppm, 18 ppm, 24 ppm, 30 ppm and 60 ppm. (b) Response to H_2S of an untreated p-type PSi interface at a concentration of 100 ppm. The dashed boxes denote the analyte concentration over the time of analyte gas exposure to the sensor.

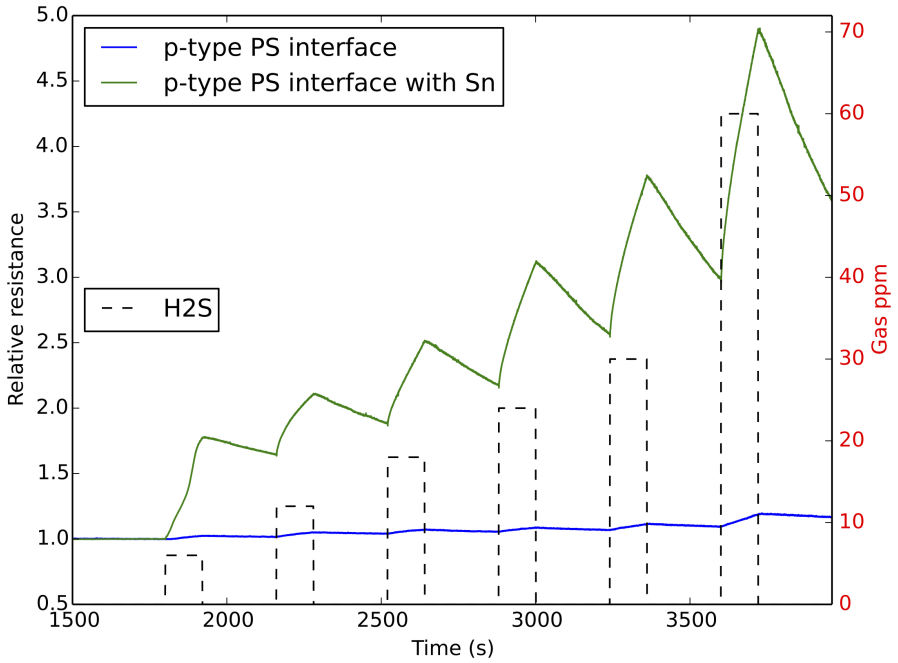

Figure 5.4: Response of SnO_x treated PSi interface (green) to H_2S and comparison to untreated PSi interface (blue). The boxes (black dashed) denote the analyte concentration over a range from 6 ppm to 60 ppm.

notable enhancement of the response after NiO nanostructure decoration. However, this enhancement is notably less than that induced with SnO_x or TiO_2 decoration. As Figure 5.1 demonstrates, NiO is a much weaker acid and is much closer in orbital makeup to H_2S.

Figure 5.7 indicates the response of H_2S to a Au_xO ($x \gg 1$) decorated p-type PSi interface, comparing this to the response for the undecorated p-type PSi interface at concentrations of 6 ppm, 12 ppm, 18 ppm, 24 ppm, 30 ppm and 60 ppm. We observe a very substantial enhancement of the response after Au_xO decoration, which well exceeds that induced with SnO_x or TiO_2 decoration. Figure 5.1 demonstrates that Au_xO lies far to the weak acid side of H_2S and displays a significant orbital mismatch with this sulfurous base. The reversible Au_xO interaction leads to a strong reversible response. The onset of the sensor response is quite rapid and clearly visible and, as

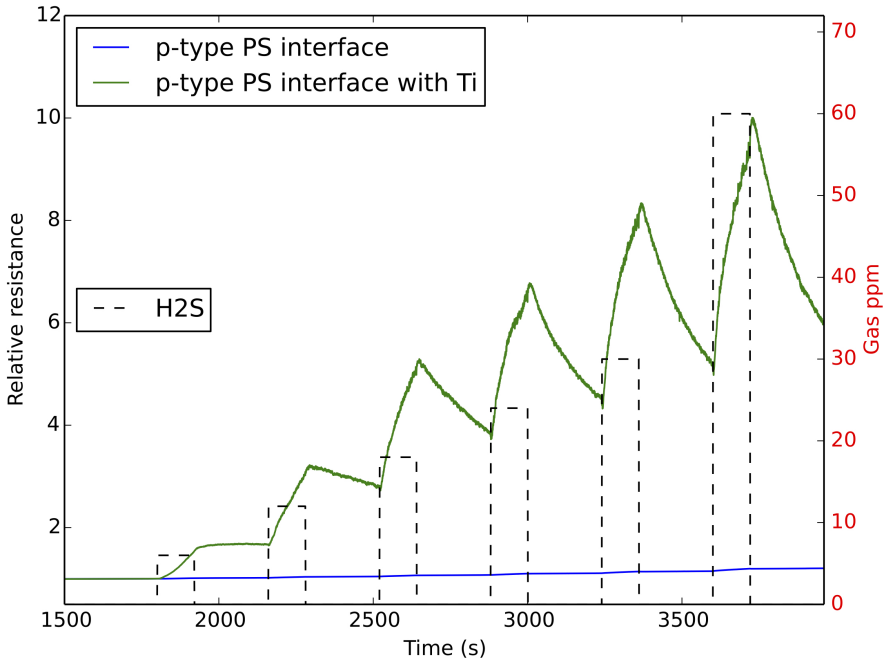

Figure 5.5: Response of TiO_2 treated PSi interface (green) to H_2S and comparison to untreated PSi interface (blue). The boxes (black dashed) denote the analyte concentration over a range from 6 ppm to 60 ppm.

well, the recovery of the sensor is sufficiently rapid that a clear baseline is maintained.

Table 5.2 demonstrates the relative responses for metal oxide nanostructure decorated surfaces formed from nanotitania, electroless tin, copper, nickel, and gold treatments for forming Ti^{4+}, $Sn^{2+,4+}$, $Cu^{1+,2+}$, Ni^{2+} oxides, and $Au^{1+,0}$ clustered oxide nanostructured coatings, respectively. The relative responses in Table 5.2 for the nanostructure decorated interfaces substantially exceed those for the untreated porous silicon interface and represent multiplicative factors that exceed those of all other analytes studied thus far. The PSi sensor response enhancement due to a particular nanostructured metal oxide, $M_{\text{treatment}}$ is given by,

$$M_{\text{treatment}} = \frac{S_{\text{treated}}}{S_{\text{untreated}}} \tag{5.1}$$

where Streated is the sensitivity of the treated sensor and $S_{\text{untreated}}$ is the sensitivity

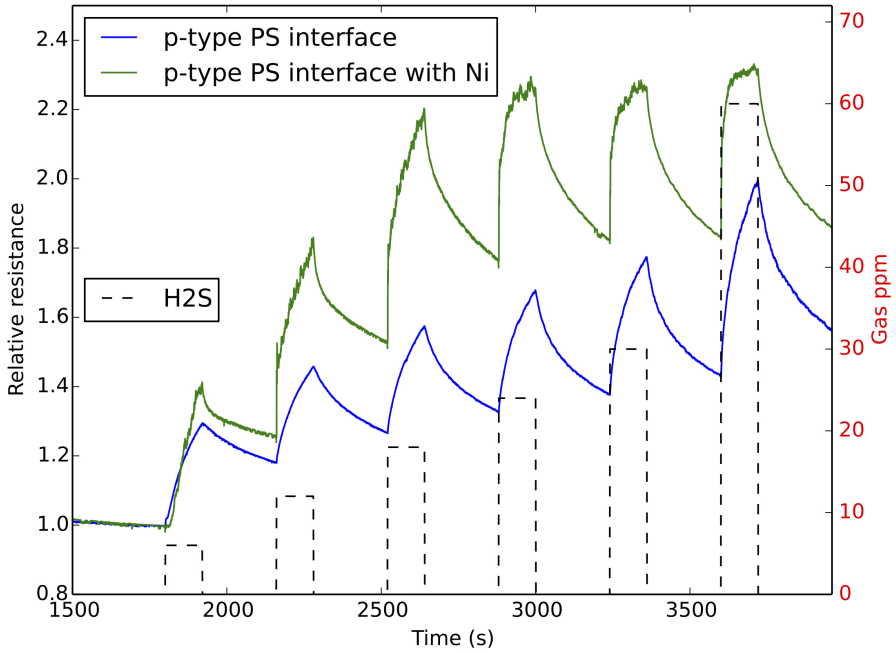

Figure 5.6: Response of TiO_2 treated PSi interface (green) to H_2S and comparison to untreated PSi interface (blue). The boxes (black dashed) denote the analyte concentration over a range from 6 ppm to 60 ppm.

of the untreated sensor. Sensitivity is defined as,

$$S = \frac{R - R_0}{R_0} = \frac{\Delta R}{R_0} \tag{5.2}$$

where R_0 is the baseline resistance, R is the resistance in the presence of a given analyte, and ΔR will be referred to as the sensor response.

5.1.2 Sensor response to CO

Figure 5.8 demonstrates the response to CO for a SnO_x decorated p-type PSi interface, comparing with the response for the undecorated p-type PSi interface at concentrations of 2 ppm, 4 ppm, 6 ppm, 8 ppm, 10 ppm and 20 ppm. Here, the amphoteric CO is acting as a weak acid, much like NO [86, 92]. The CO extracts electrons from the PSi interface, which increases concentration of electronic holes, the majority charge carriers in p-type semiconductors. Therefore, a decrease in resistance is observed for

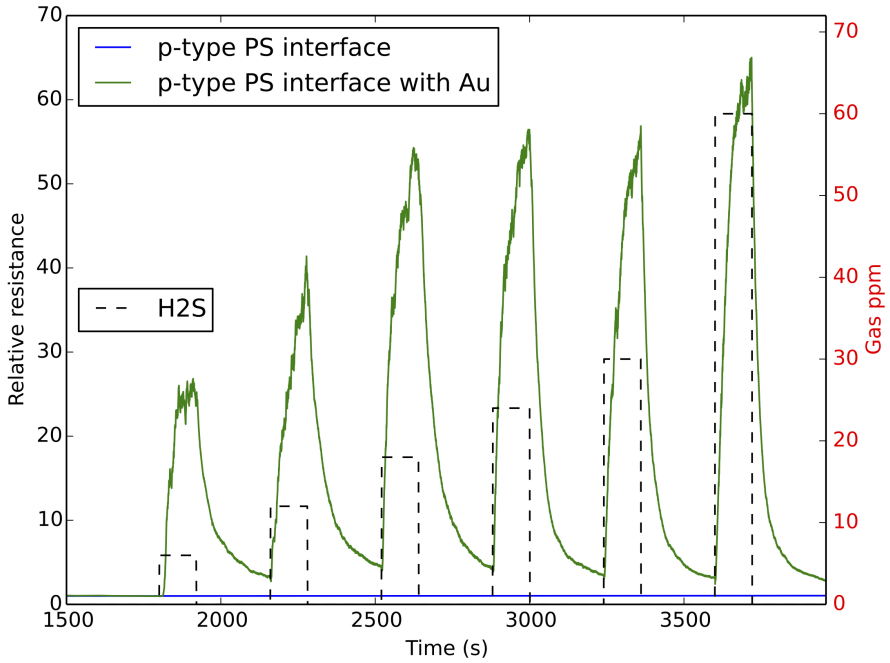

Figure 5.7: Response of TiO_2 treated PSi interface (green) to H_2S and comparison to untreated PSi interface (blue). The boxes (black dashed) denote the analyte concentration over a range from 6 ppm to 60 ppm.

the p-type PSi sensor in the presence of CO. We observe a considerable enhancement of the response after SnO_x nanostructure decoration. This result is consistent with the positioning in Figure 5.1 as a SnO_x nanostructure modification will increase the orbital mismatch between the interface and the CO analyte gas. The result is also consistent with previous observations [163].

Figure 5.9 indicates the response to CO for a TiO_2 decorated p-type PSi interface, comparing this to the response for the undecorated p-type PSi interface at concentrations of 2 ppm, 4 ppm, 6 ppm, 8 ppm, 10 ppm and 20 ppm. We observe a considerable enhancement of the response after TiO_2 nanostructure decoration. Again, the amphoteric CO is shown to act as a weak acid, extracting elections and thus decreasing the resistance of the p-type PSi sensor. Similar to the interaction of H_2S with a SnO_x versus TiO_2 decorated PSi interface, the TiO_2 appears to enhance the sensor response

Table 5.2: Resistance response enhancement, $M_{\text{treatment}}$ (Equation 5.1), for various nanostructured metal oxide depositions on a p-type PSi sensor. The baseline resistance values for these experiments were on the order of 300 Ω to 600 Ω.

Metal oxide deposition	Change in response
TiO_2	60
SnO_x	22
NiO	2
Au_xO ($x \gg 1$)	60

to CO to a greater degree than SnO_x. This is consistent with the fact that TiO_2 is farther away from CO than SnO_x on the IHSAB scale (Figure 5.1), representing a larger orbital mismatch. The result is expected and also consistent with previous observations [86, 92].

5.1.3 Discussion

Figure 5.1 demonstrates that the strong acids TiO_2 and SnO_x represent ideal metal oxide nanostructures to direct electron transduction with the amphoteric analyte CO. Lewis et al. [163] demonstrated that treating the PSi sensor with gold clustered oxide, Au_xO ($x \gg 1$), decreased the sensor response to CO. Therefore, CO can be reasonably positioned close to Au_xO on the IHSAB scale. As expected, and illustrated by a comparison of Figures 5.8 and 5.9, TiO_2 provides a larger increase in sensor response (as the separation between CO and TiO_2 is greater than CO and SnO_x).

The basis for the positioning of H_2S in Figure 5.1 was originally based on the comparison of the relative responses for 1 ppm H_2S with an Au_xO ($x \gg 1$) deposited PSi surface versus an untreated PSi surface and to data obtained for NH_3, PH_3, and NO [94]. Based on ionization potential, as well as proton affinity data, we suggested that H_2S lies close to, but probably to the soft acid side of PH_3. The results presented in Figures 5.4 through 5.7 support this suggestion. However, the comparison of those results obtained for TiO_2, SnO_x, and Au_xO ($x \gg 1$) suggest that H_2S acts as a harder

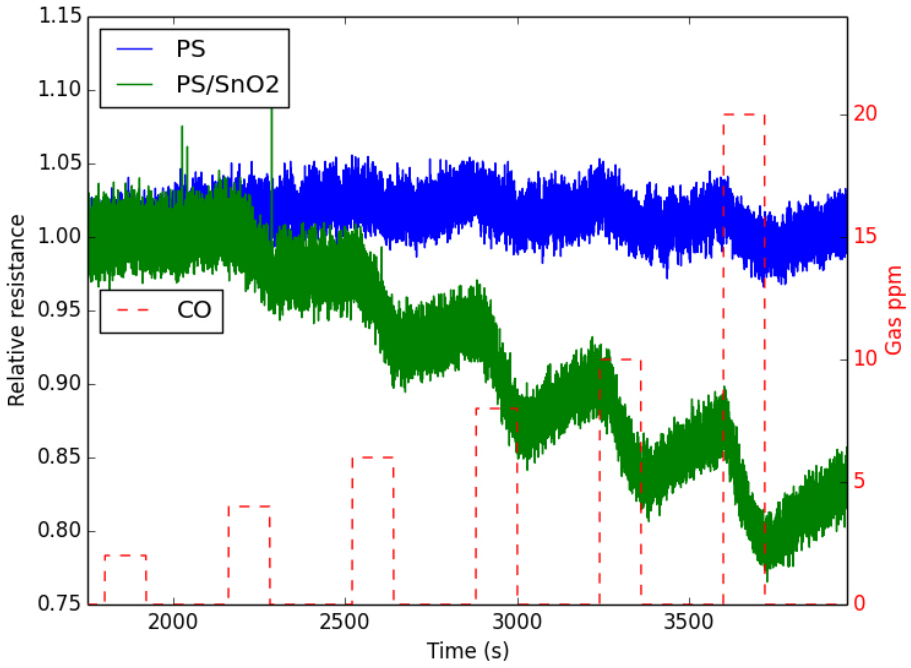

Figure 5.8: Response of SnO_x treated p-type PSi interface (green) to CO and comparison to untreated p-type PSi interface (blue). The boxes (black dashed) denote the analyte concentration over a range from 2 ppm to 20 ppm.

acid than previously suggested. This adjustment has been made to Figure 5.1.

The responses reported for H_2S in Figures 5.4 through 5.7 and CO in Figures 5.8 and 5.9 can be explained within the concept of the IHSAB principle [86, 92, 94, 95, 145, 163, 164, 197]. The underlying IHSAB principle dictates the physisorption directed response (electron transduction) to a number of basic, acidic, and amphoteric analytes as they interact with the nanostructure decorated p- or n-type PSi extrinsic semiconductor interface [86, 92, 94]. The dominant factor is the HOMO-LUMO energy increment. If the donor orbital energy (highest occupied molecular orbital, HOMO) is not well matched with the acceptor (lowest unoccupied molecular orbital, LUMO), then the interaction will be weak and feature only minimal chemical bonding. In the context of IHSAB, this mismatch occurs in cases where a hard acid

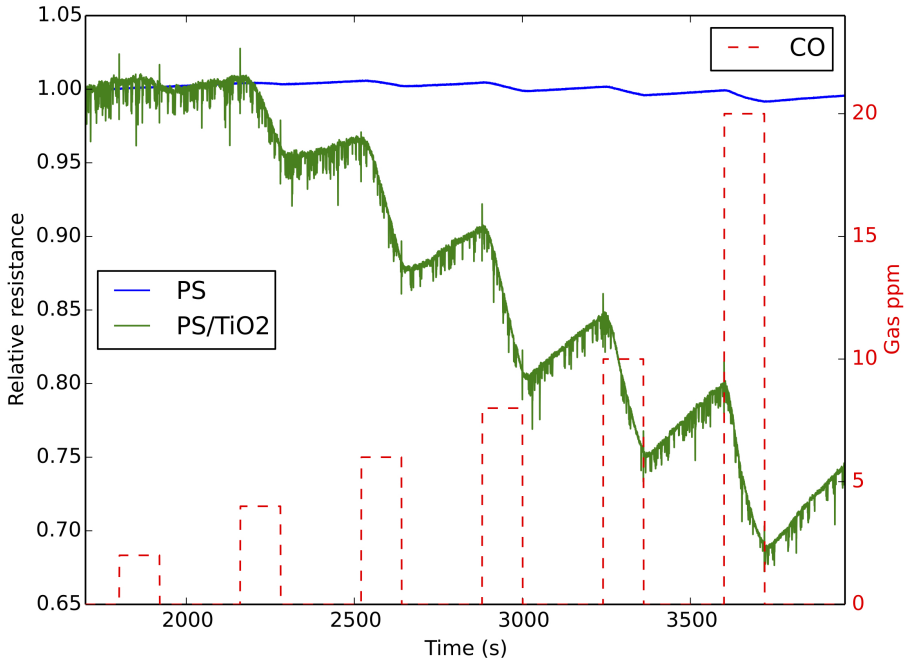

Figure 5.9: Response of TiO_2 treated p-type PSi interface (green) to CO and comparison to untreated p-type PSi interface (blue). The boxes (black dashed) denote the analyte concentration over a range from 2 ppm to 20 ppm.

interacts with a soft base (or a soft acid with a hard base). As the HOMO(donor)-LUMO(acceptor) energy gap decreases, there can be more charge transfer between the analyte gas molecule and the sensor interface. This leads to a stronger Lewis acid-base interaction, resulting in a chemisorption dominated interaction and a decreased sensor response. In the case of Lewis acid-base bonds, the donor retains the electron pair [60]. At the other extreme is the interaction of an anion and a cation forming an ionic bond with a much larger bond dissociation energy (BDE). A large BDE will also result if the electrons are fully shared forming a covalent bond. The IHSAB principle is, in large part, based on controlling the size of the Lewis acid-base bond dissociation energy through appropriate choices of nanostructured decoration for each target analyte.

A first order comparison of the response data for H_2S with an exemplary list of

hard, borderline, and soft acids and bases allows the positioning of this base. By monitoring the trends in hard and soft acid and base behavior, first order selections can be made for the modification of the PSi hybrid interface (or any extrinsic semiconductor interface onto which a nanopore-coated microporous structure can be formed) with nanostructured metal oxide deposits to create a range of sensitivities (responses) for the target analyte. The change in Lewis acidity is the primary factor that affects the interactions of the metal oxides TiO_2, SnO_x, NiO, and Au_xO ($x \gg 1$) with H_2S. As demonstrated in Figures 5.4 and 5.5, the significant orbital mismatch of the hard acids SnO_x and TiO_2 interact similarly with the effectively moderate base H_2S. Additionally, as expected from Figure 5.1, the mismatch of H_2S with TiO_2, which greater than that for SnO_x, produces a larger response enhancement (Table 5.2). Concomitantly, Au_xO represents a very weak acid and whose molecular orbital makeup is, again, strongly mismatched with H_2S (Figure 5.1). This leads to a weak interaction, as opposed to strong chemical bonding, and a substantial electron transduction. The Au_xO decorated surface shows a stronger response than do the comparable TiO_2 and SnO_x decorated interfaces. Therefore, H_2S should be positioned closer TiO_2 and SnO_x than Au_xO on the IHSAB scale. The observed change in sensor response upon decoration of the PSi surface with NiO is consistent with the fact that it lies further to the soft acid side of H_2S than the undecorated PSi, representing a slight increase in orbital mismatch.

Molecular data needed to address the orbital energy arguments is available in terms of molecular proton affinities, acidities, and ionization potentials [122, 165]. However, these data are not broadly available for surfaces or nanoclusters. While our measurements now provide semi- quantitative data about the doped metal oxide surface sites, further experiments will help to quantify that data.

5.2 Selectivity: Inorganic Detection in the Presence of Organic Vapor

In this section, we demonstrate the highly selective detection the inorganic pollutants NO_x (NO, NO_2), SO_2, and H_2S in the presence of the volatile organic chemicals (VOCs) toluene, benzene, and xylene using nanostructure metal oxide decorated interfaces. This selectivity can be obtained for sensors with sensitivities that are varied for a diversity of nanostructured metal oxides applied to a PSi interface. In all cases, the response to these inorganic analytes strongly dominates that for toluene, benzene, and xylene. The responses are also consistent with the recently developing IHSAB concept. The nanostructure metal oxide decorated PSi conductometric sensors are found to have selectivity ratios well in excess of $10^4 : 1$ for toluene and benzene, and well in excess of $10^3 : 1$ for xylene. The dominance of the response of these small inorganic sulfur and nitrogen compounds has important implications for the monitoring of significant contaminants in the vicinity of oil and natural gas formations.

The reversible interaction of NO_x, SO_2, and H_2S with a PSi interface is well represented by the recently developing IHSAB model. Our studies of these small inorganics takes advantage of the fact that the sensitivity of our nanostructure decorated PSi conductometric sensor configurations to small inorganic analytes far exceeds the sensitivity to VOCs, including the aromatics toluene, benzene, and xylene. P-type PSi sensors with SnO_x, NiO, and Au_xO nanostructure-directing depositions were used to characterize the relative sensitivities of the sensor interface to the considered analytes in the presence of these VOCs.

5.2.1 Propagation of Error Calculations

In view of the significant selective response observed for the described sensor systems, standard deviations for the changes in the conductometric resistance (conductance), the concentrations of inorganic analyte gases, and the relative sensitivities to these

gases (NO_x , SO_2, and H_2S) compared to volatile organic chemicals (benzene, toluene, and xylene) were calculated to assess a complete propagation of error [144]. The changes in resistance (ΔR) are described by

$$\Delta R = R - R_0 \tag{5.3}$$

where R is the conductometric response resistance and R_0 is the baseline resistance. The error of the change in resistance is then given by

$$\sigma_{\Delta R} = \sqrt{\sigma_R^2 + \sigma_{R_0}^2} \tag{5.4}$$

where σ_R and σ_{R_0} are the uncertainty of the response resistance and baseline resistance.

The concentration of the inorganic analyte gases supplied to the sensor, C_{analyte}, is given by

$$C_{\text{analyte}} = \frac{Q_{\text{analyte}}}{Q_{\text{analyte}} + Q_{\text{N}_2}} \times C_{\text{tank}} \tag{5.5}$$

where Q_{analyte} and Q_{N_2} are the volume flow rates provided by the mass flow controllers (MFCs) in standard cubic centimeters per minute (SCCM) and C_{tank} is the concentration supply inorganic gas tanks. The error of this concentration is found by using the equation

$$\sigma_{C_{\text{analyte}}} = C_{\text{analyte}} \times \sqrt{\left(\frac{\sigma_{Q_{\text{analyte}}}}{Q_{\text{analyte}}}\right)^2 + \frac{\sigma_{Q_{\text{analyte}}}^2 + \sigma_{Q_{\text{N}_2}}^2}{\left(Q_{\text{analyte}} + Q_{\text{N}_2}\right)^2} + \left(\frac{\sigma_{C_{\text{tank}}}}{C_{\text{tank}}}\right)^2} \tag{5.6}$$

where the uncertainty of the volume flow rates due to the calibration of the MFCs are estimated at 1 % based on a realistic assessment of the manufacturer specifications, and the uncertainty of the concentration of the supplied inorganic gas tanks is measured at 2 %. Finally, the relative sensitivities (S) are given by

$$S = \frac{\Delta R_{\text{analyte}}/\Delta R_{\text{VOC}}}{C_{\text{analyte}}/C_{\text{VOC}}} \tag{5.7}$$

where the concentration of the volatile organic chemicals are extrapolated from the analysis provided for a similar experimental setup [127]. The uncertainty is found

using the relationship

$$\sigma_S = S \times \sqrt{\left(\frac{\sigma_{\Delta R_{\text{analyte}}}}{\Delta R_{\text{analyte}}}\right)^2 + \left(\frac{\sigma_{\Delta R_{\text{VOC}}}}{\Delta R_{\text{VOC}}}\right)^2 + \left(\frac{\sigma_{C_{\text{analyte}}}}{C_{\text{analyte}}}\right)^2} \tag{5.8}$$

where the uncertainty of the concentration of the volatile organic chemicals is estimated at 10 %.

5.2.2 Selective response to inorganic analytes

Figure 5.10 exemplifies the extremely weak response of a SnO_x decorated p-type porous silicon interface to toluene, which is only $\sim 2\,\Omega$. This response is exceeded slightly by the aromatics benzene and xylene, but, as we will demonstrate, their response is greatly exceeded by all of the tested inorganic analytes.

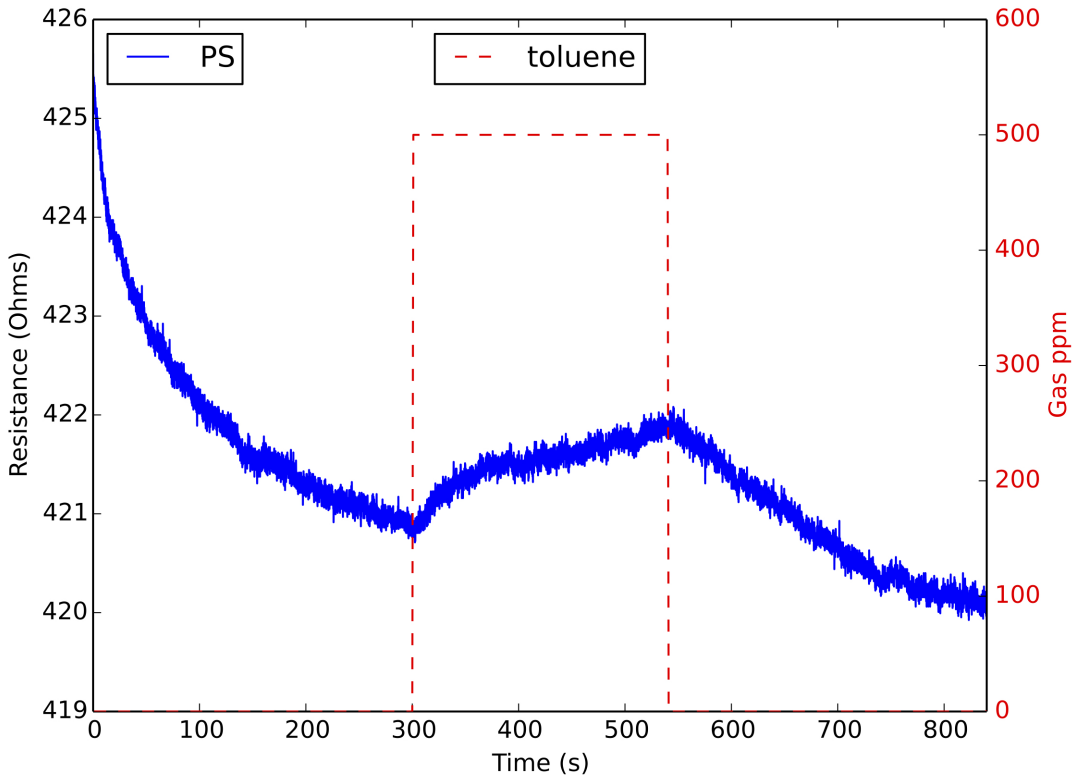

Figure 5.10: Observed response for toluene for a SnO_x decorated p-type PSi sensor. The observed conductance change is $(1.10 \pm 0.28)\,\Omega$.

Figure 5.11 corresponds to a scan of the conductometric response, at room temperature, for benzene in comparison to H_2S. The scan is taken as a function of time. Initially, ultra-high-purity (UHP) nitrogen flows over the sensor for a period of 1200 s. This is followed by a 120 s exposure to a benzene gas flow, obtained from a bubbler, that is subsequently passed through a Mass Flow Controller (MFC) (see Chapter 3 for a schematic of the experimental setup). Here benzene, whose vapor pressure considerably exceeds toluene, is mixed with the UHP nitrogen flow beginning at 1200 s. The initial small rise in the response (resistance) to benzene (counter to a small increase in conductance (decrease in resistance) due to benzene in the absence of H_2S)) is most likely due to the initial cooling of the sensor. H_2S is brought into the nitrogen/benzene flow at 1320 s. For this reason, the slight rise preceding the H_2S signal can also not be due to interaction with H_2S.

Figure 5.11 presents the response for H_2S in the presence of a benzene concentration that is estimated to be $(23\,400 \pm 2340)$ ppm. It should be apparent that the benzene signal is barely visible over the time (abscissa) from 1200 s to 1320 s. Based on these results, the ratio of the H_2S to benzene response is in excess of 100 000, shown by

$$\frac{\Delta R_{\mathrm{H_2S}}}{\Delta R_{\mathrm{benzene}}} \times \frac{C_{\mathrm{benzene}}}{C_{\mathrm{H_2S}}} \cong \frac{(7277 \pm 11)\,\Omega}{(11 \pm 6)\,\Omega} \times \frac{(23\,400 \pm 2340)\,\mathrm{ppm}}{(20.98 \pm 0.51)\,\mathrm{ppm}} = 738\,000 \pm 398\,000 \tag{5.9}$$

which corresponds to a response ratio of approximately 340 000–1 136 000 to 1. Similar data for H_2S versus toluene [15] and xylene are given in Appendix B (Figures B.1 and B.2) and summarized in Table 5.3.

Figure 5.12 corresponds to a comparison of the relative sensor sensitivities for SO_2 versus xylene. The PSi interface is decorated with an Au_xO ($x \gg 1$) deposit, which also increases the response relative to PSi [86, 94]. Here the signal for xylene at (200 ± 20) ppm is barely visible versus that for SO_2 at (16.85 ± 0.41) ppm. SO_2 is a moderate acid and withdraws electrons from the decorated porous silicon interface.

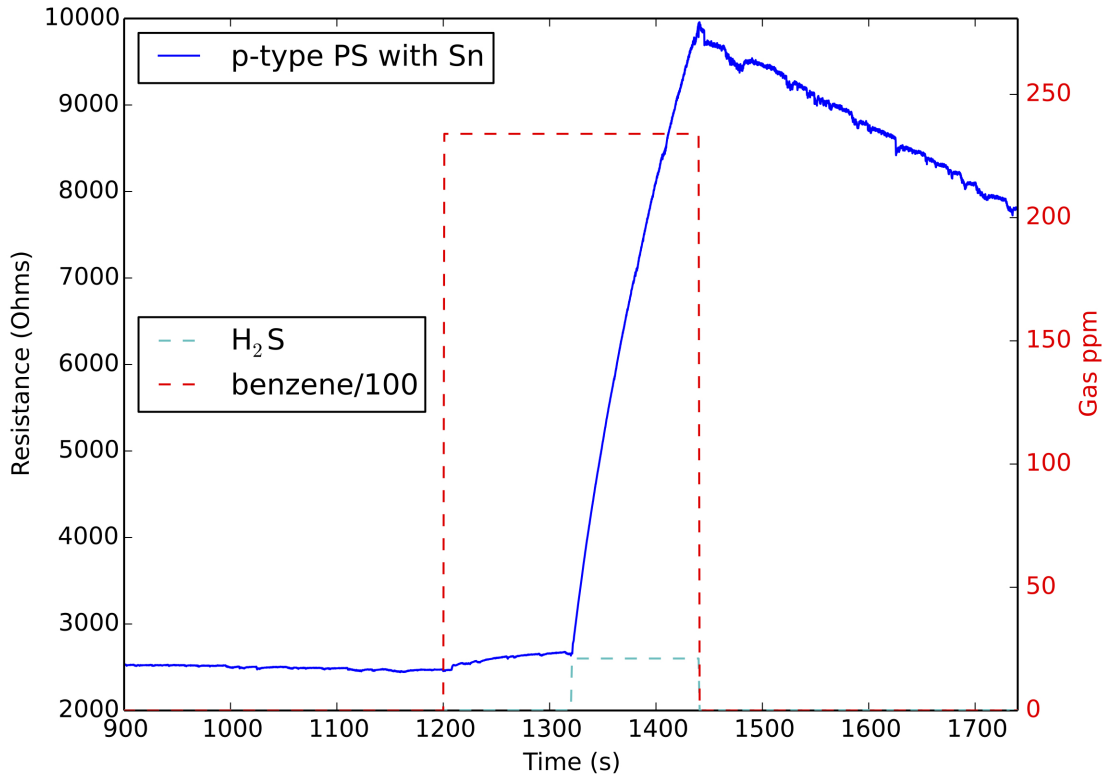

Figure 5.11: Comparison of response for $\sim 20\,000$ ppm benzene over the range denoted by the red box and (20.98 ± 0.51) ppm H_2S over the range denoted by the aqua box for a SnO_x decorated p-type PSi sensor.

This increases the majority charge carriers, holes, and increases the conductance of the porous silicon interface [86, 92, 94]. The first dominant minimum corresponds to SO_2 with xylene while the second minimum generated after a much shorter time scale corresponds to SO_2 alone. The recovery with the significant xylene concentration, whose response appears to be barely observable, is slower than with toluene. The dominant minimum corresponds to a conductance increase of $(138 \pm 7)\,\Omega$ for the etch conditions used in this experiment. Similar data for SO_2 versus toluene and benzene are given in Appendix B (Figures B.3 and B.4) and summarized in Table A.3.

Figure 5.13 corresponds to a comparison of the relative sensor sensitivities for NO_2 versus toluene. Here the signal for toluene at (500 ± 50) ppm is barely visible

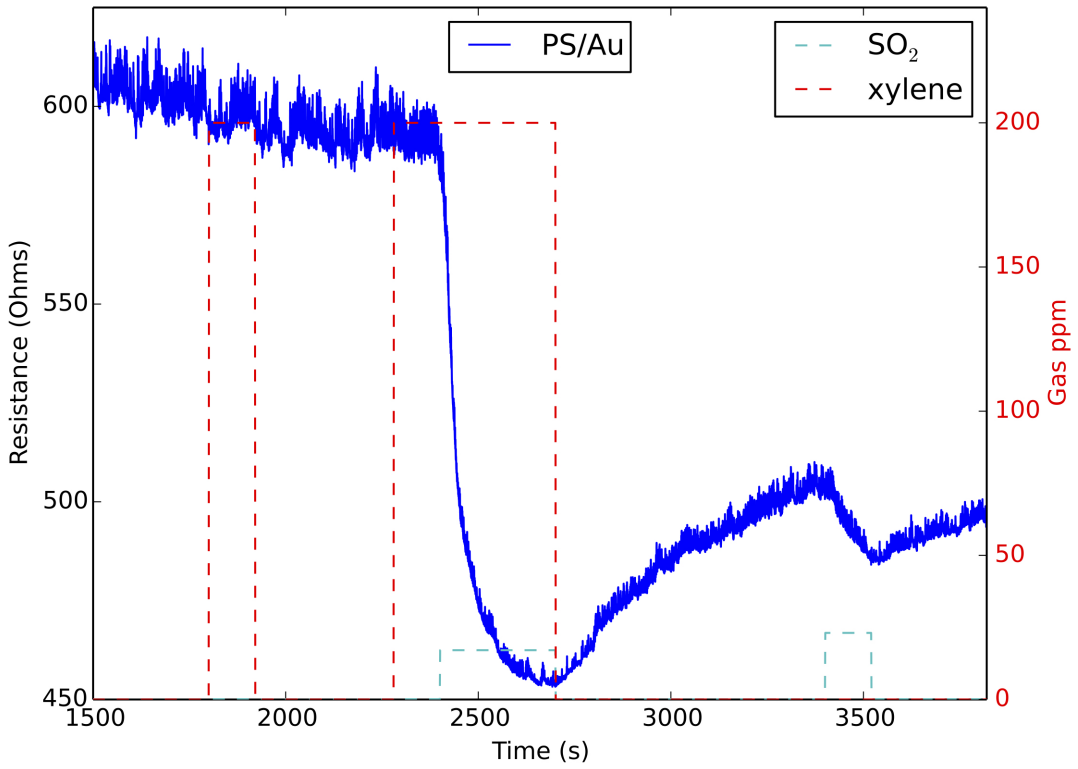

Figure 5.12: P-type, Au_xO decorated, PSi sensor response to (200 ± 20) ppm xylene over the range denoted by the red dashed boxes and (16.85 ± 0.41) ppm SO_2 over the range denoted by the black dashed boxes.

versus that for NO_2 at (27.78 ± 0.68) ppm. NO_2 is a moderate acid and withdraws electrons from the porous silicon interface. This increases the majority charge carriers, holes, and increases the conductance of the porous silicon interface [86, 92, 94]. The first dominant minimum corresponds to NO_2 with toluene while the while the second minimum generated over a much shorter time scale corresponds to NO_2 alone. These minima are very similar and correspond to a conductance increase of $(110 \pm 1)\,\Omega$.

Figure 5.14 corresponds to a comparison of the relative sensor sensitivities for NO versus toluene. Here the signal for toluene at (500 ± 50) ppm is again barely visible versus that for NO at (27.78 ± 0.68) ppm. NO is amphoteric and in this case acts as a weak acid withdrawing electrons from the porous silicon interface but not to the

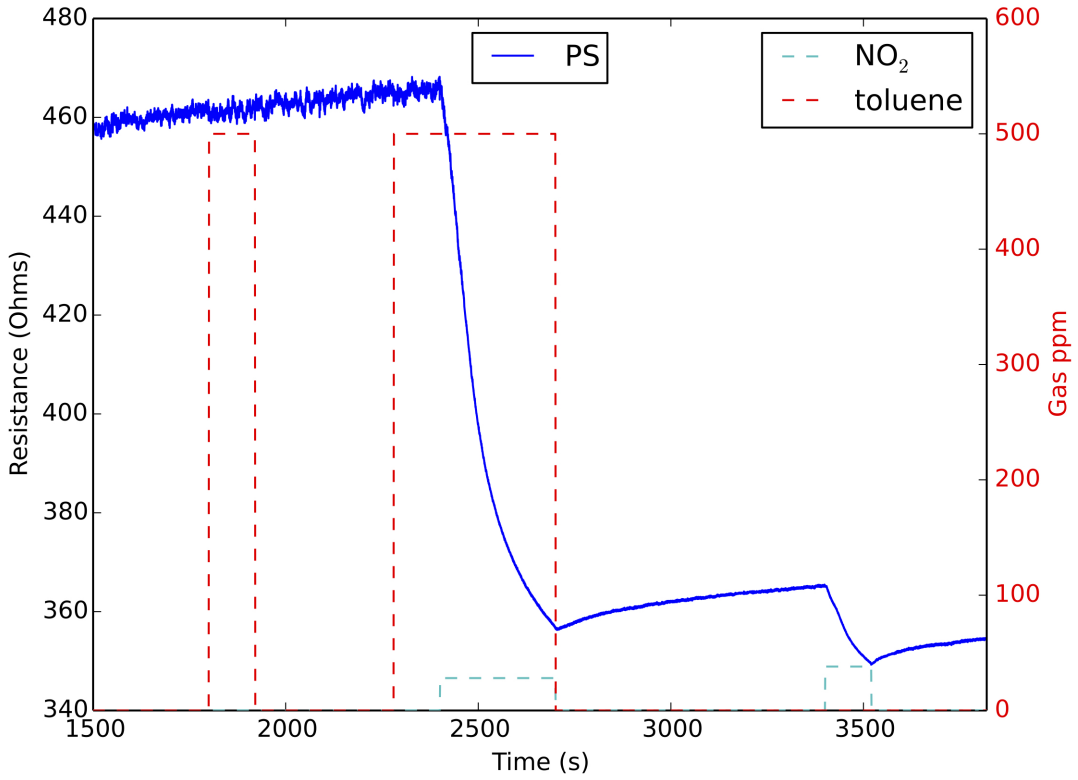

Figure 5.13: P-type PSi sensor response to (500 ± 50) ppm toluene over the range denoted by the red dashed boxes and (27.78 ± 0.68) ppm NO_2 (first zone with 280 sccm N_2 with the aromatics) and (38.46 ± 0.95) ppm (second zone with 200 sccm without the aromatics) over the range denoted by the aqua dashed boxes.

extent of NO_2. This increases the majority charge carriers, holes, and increases the conductance of the porous silicon interface [86, 92, 94]. The first dominant minimum corresponds to NO with toluene while the while the second minimum generated over a much shorter time scale corresponds to NO alone. These minima are very similar and correspond to a conductance increase of $(11.8 \pm 0.1)\,\Omega$.

Figure 5.15 corresponds to a comparison of the relative sensor sensitivities for NO versus NO_2 and toluene. Here the signal for toluene at (500 ± 50) ppm is again barely visible versus that for NO and NO_2 at (27.78 ± 0.68) ppm. The weaker acidic nature of NO versus NO_2 is emphasized in the figure. Similar data for NO and NO_2 versus benzene and xylene are given in Appendix B (Figures B.5 through B.9) and

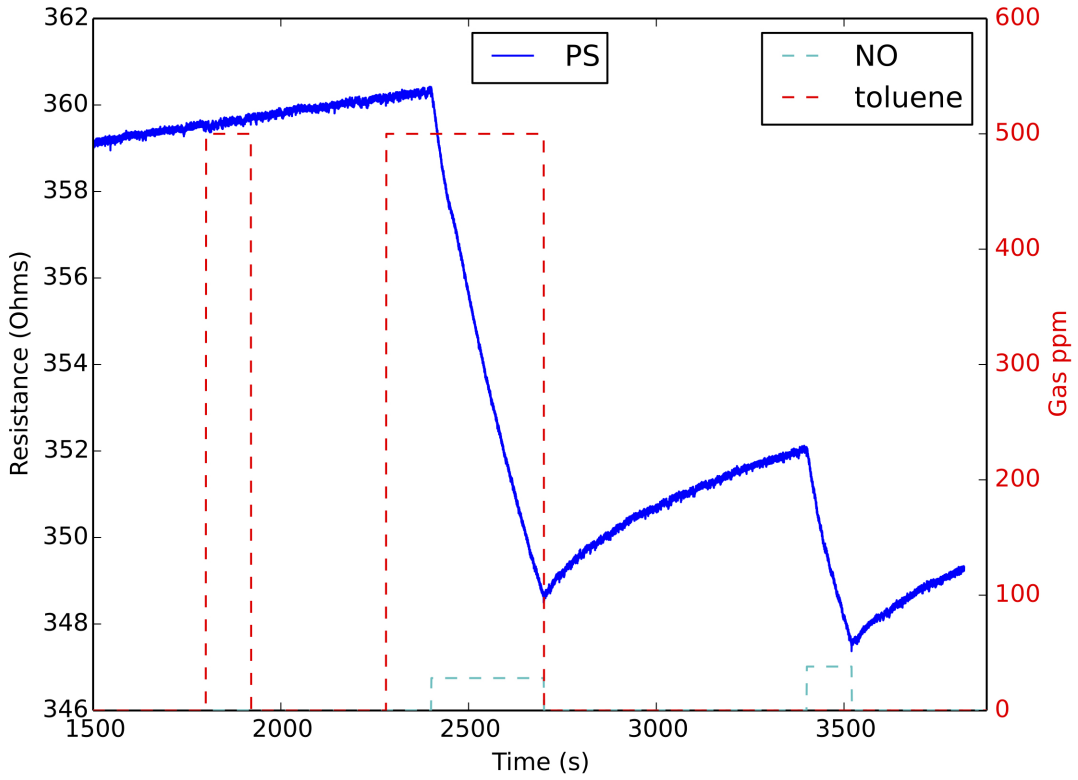

Figure 5.14: P-type PSi sensor response to (500 ± 50) ppm toluene over the range denoted by the red dashed boxes and (27.78 ± 0.68) ppm NO (first zone with 280 sccm N_2 with the aromatics) and (38.46 ± 0.94) ppm (second zone with 200 sccm without the aromatics) over the range denoted by the aqua dashed boxes.

summarized in Table A.3.

5.2.3 Discussion and Conclusions

The most important result demonstrated in these studies is the strong dominance of the response of the studied sensor interfaces to NO_x, H_2S, SO_2, and H_2S verses the BTEX molecules toluene, benzene, and xylene. The observed behavior of the dominant analytes also follows that expected from the recently developing IHSAB concept [86,92,94]. The dominance of H_2S, SO_2, and NO_x is apparent despite some small differences in the nanopore-covered microporous arrays that support the nanostructure directing metal oxides and significant differences in the nanostructured oxides,

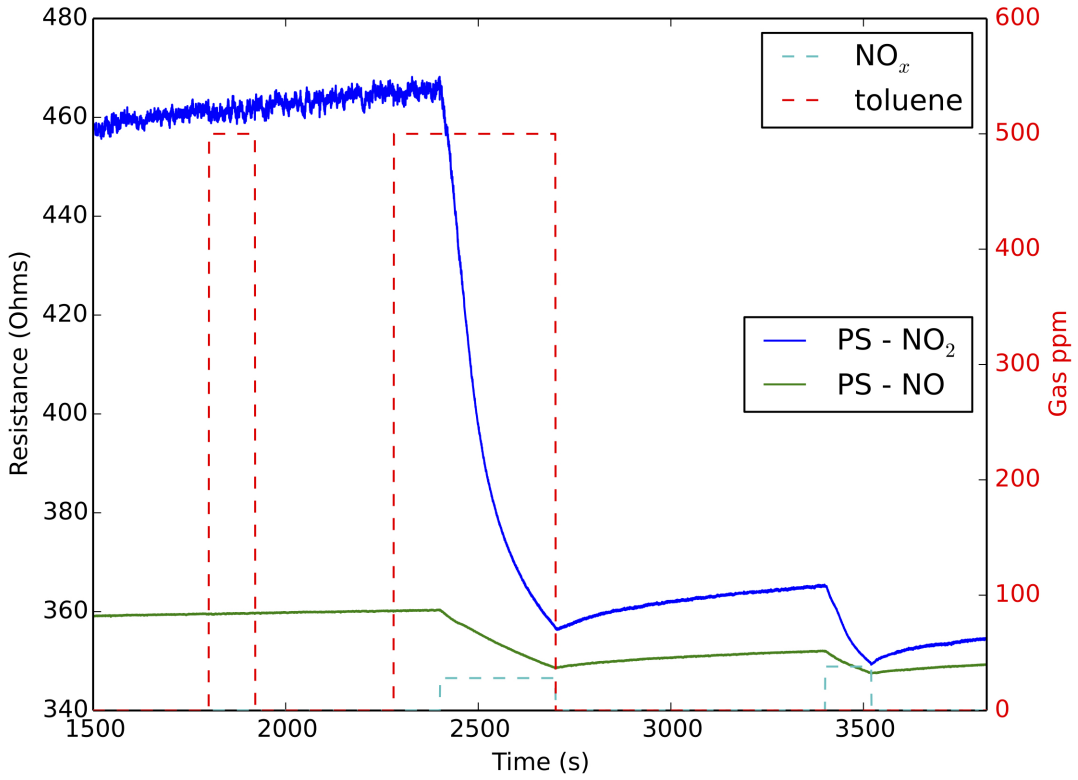

Figure 5.15: Comparison of NO and NO_2 p-type PSi sensor response to (500 ± 50) ppm toluene over the range denoted by the red dashed boxes and (27.78 ± 0.68) ppm NO or NO_2 (first zone with 280 sccm N_2 with the aromatics) and (38.46 ± 0.94) ppm (second zone with 200 sccm without the aromatics) over the range denoted by the black dashed boxes.

which decorate the systems.

Further improvements in the sensitivity for the analytes can be made. However, of greatest importance is that in all the cases tested, the sensitivity to the analytes greatly exceeds that of the BTEX (benzene, toluene, ethylbenzene, xylene) molecules. We summarize these ratios for the particular interfaces studied in Table 5.3 where we separate the sulfur and nitrogen based compounds considering first those analyte surface interactions with the highest selectivity. First note that the ratios all greatly exceed 20/1, an industry benchmark. As described in Section 5.2.1, the error propagated in Table 5.3 is obtained with conservative estimates of the potential system

Table 5.3: Relative sensitivity ratios of H_2S, SO_2, NO_2, and NO to the BTEX molecules toluene, benzene, and xylene for particular nanostructure decorated nanopore-coated microporous structures used in this study.

Inorg.	toluene	benzene	xylene	Nanostructure deposition
H_2S	$(186\,000 \pm 27\,000)$	$(738\,000 \pm 398\,000)$	(1630 ± 790)	SnO_x
SO_2	(641 ± 369)	$(15\,800 \pm 5300)$	(418 ± 154)	SnO_x and Au_xO
NO_2	(1950 ± 340)	$(198\,000 \pm 91\,000)$	(308 ± 63)	untreated
	(1150 ± 560)			NiO
NO	(4140 ± 1240)	$(27\,900 \pm 9400)$	(247 ± 31)	TiO_2, SnO_x, and Au_xO

uncertainties in order to obtain a definite upper bound estimate on the propagated error bounds. These bounds have purposely been somewhat inflated. However, in virtually all cases, especially for benzene, the ratios well exceed 500/1.

CHAPTER VI

EXPANDED MATERIALS DEPOSITION STUDIES

This chapter will highlight two initial studies for using the porous silicon (PSi) sensor system to explore interface interactions: an analysis of magnetic materials depositions and the potential for magnetically enhanced sensing [16], and a discussion on the properties of Group IIA metal depositions and their effects on chemical sensing [254].

6.1 Magnetic Sensor Enhancement

In this study, small magnetic fields are found to greatly enhance the reversible room temperature conductometric responses of n- and p- type PSi interfaces, treated with nanostructured island sites containing paramagnetic Co(II) and Fe(II) [16]. At concentrations sufficiently low so as to avoid cross talk between the nanostructured island sites, the response to NO concentrations demonstrates the significant effect that the Co(II) and Fe(II) have on the decorated extrinsic semiconductor majority charge carriers. Co(II) and Fe(II) oxide sites enhance the PSi sensor response and provide a means for small magnetic fields to interact with and enhance the sensor interface response. For p-type systems, the interaction is small with virtually constant thermal electron populations lying above the Fermi energy at 0 K. The electron removal rate increases with magnetic field strength. At the highest magnetic fields and NO analyte concentrations, the available electron population is depleted, and the response to the analyte decreases at higher concentrations. At lower magnetic fields (< 1000 G) the response faithfully follows concentration. For n-type systems, the magnetic field interaction increases resistance, which may be attributed to the interaction with donor levels ≈ 0.025 eV below the conduction band. A substantial enhancement of sensor response relative to that for the Co(II) and Fe(II) treated PSi interfaces is observed

with the introduction of a small magnetic field [16].

6.1.1 Magnetic materials and methods

In this study we treat the micro-/nanoporous framework with $CoCl_2 \cdot 6\,H_2O$ at various initial concentrations and degrees of water removal, measuring the effect of a magnetic field on the sensor response of the decorated interface [16]. For comparison, we also treat the interface with nanotitania [43, 98]. We are not applying a coating technique that requires an exacting structural film arrangement but a much simpler process. In order to maintain a sensor response consistent with the IHSAB principle, the nanostructure deposition must be maintained at a sufficiently low level to avoid cross-talk between the nanostructures [92]. Selected nanostructured metals, metal oxides, and nanoparticle catalysts can be deposited to the nanopore-covered micropores to provide for distinct and variable sensitivities [92]. Following this procedure, we have also treated the micro-/nanoporous PSi interface with 10 nm iron oxide particles functionalized with NH_3. The iron oxide particles were provided by Dr. Jie Xu, Senior Research Scientist for the Food Processing Technology Division of Georgia Tech Research Institute.

Based on previous results [96, 97], nanostructured deposits of cobalt(II) chloride hexahydrate are partially oxidized as the prepared sensor interfaces are subsequently cleaned and as the sensors are tested at atmospheric pressure. The initially introduced titania (anatase) may be crystalline, but we cannot be certain of this crystallinity after deposition to the PSi surface. The untreated PSi hybrid structures are exposed for 30 s to the $CoCl_2 \cdot 6\,H_2O$ at varying concentrations, or to nanotitania solutions, and are subsequently placed in deionized (DI) H_2O and MeOH for consecutive 120 s periods. At the lower cobalt concentrations, the conductometric response agrees well with that expected from a well-behaved conductometric sensor response. However, the introduction of a magnetic field diminishes this response. As the cobalt concentration

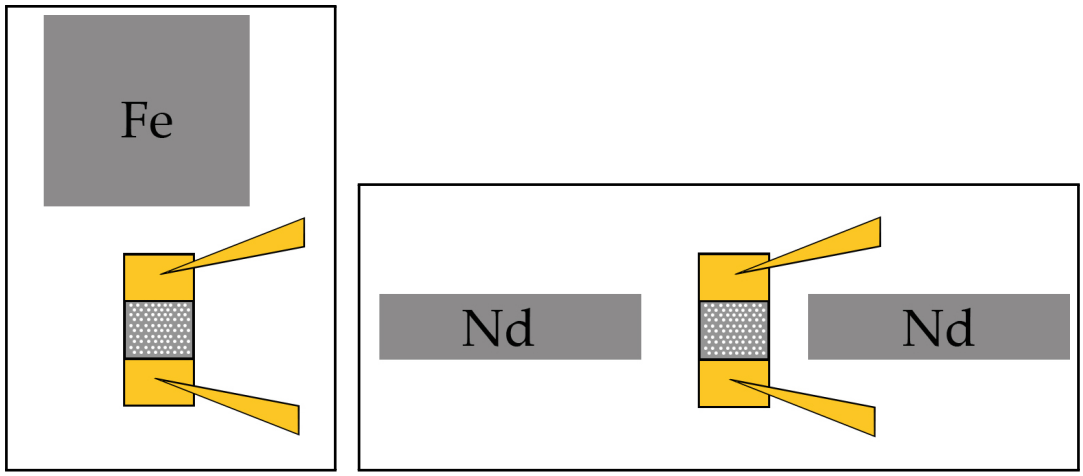

Figure 6.1: (a) Classical iron magnet configuration. The iron magnet can be rotated in the direction of the sensor, which is monitored with two precision microprobes as a gas flow of entrained NO intersects the sensor. (b) Neodymium rare earth magnet configuration interacting from below and corresponding to $\sim 2000\,\mathrm{G}$. Reprinted with permission from Journal of Applied Physics, C. Baker et al., Magnetically induced enhancement of reversibly responding conductometric sensors, 115, 164312. Copyright 2014, AIP Publishing LLC.

is increased, the sensor response decreases from that of the untreated PSi interface, but can be enhanced substantially through introduction of a magnetic field [80, 81, 160, 178, 184, 185, 222, 265].

The magnetic fields used in these experiments vary from 80 G to 2000 G (0.008 T to 0.2 T). They are generated using the two configurations pictured in Figures 6.1a and 6.1b. In the first configuration, a classical iron magnet creates a field of 80 G at the sensor interface. The second configuration uses a neodymium rare earth (nickel coated) magnet placed so as to create a magnetic field of ∼2000 G at the sensor interface. The magnitudes of these fields are measured with a Lakeshore Model 421 Gaussmeter at the location of the sensor.

In all cases, low ppm concentrations of NO are brought to the hybrid surface after entrainment in UHP nitrogen (Matheson 99.999+%) at room temperature. The system is purged for a minimum of 30 min before use with UHP nitrogen, which

provides for the removal of residual water, and establishment of a baseline resistance [198]. The typical resistances for the base PSi structures range between 300 Ω and 10 000 Ω at room temperature.

6.1.2 Results

For comparison, Figure 6.2 reveals no effect by the magnetic field on untreated porous silicon. Figure 6.3 indicates the response after TiO_2 nanostructures, at a concentration limited to a value to avoid cross-talk between the nanostructures, is deposited to an n-type PS interface. Amphoteric NO in the range 1 ppm to 10 ppm, entrained in UHP N_2 and brought to the PSi interface produces a conductometric signal corresponding to an increase in resistance with analyte concentration. This is indicative of the interaction of an acid gas with an interface that has been mildly treated with TiO_2 [86, 92]. Treatment after the TiO_2 deposition to the PSi interface produces a surface, which does not overcome the weak acidity of NO. Of greater importance is the fact that the signal observed with a magnetic field (up to 2000 G) for this non-magnetic material is virtually identical to that of the untreated interface. While there is clear concentration dependence with analyte, the non-magnetic nanostructured TiO_2 deposition is clearly not affected by the presence of the magnetic field.

6.1.2.1 Cobalt decorated interfaces

Figure 6.4 depicts results obtained as $CoCl_2 \cdot 6\,H_2O$ from a solution at a concentration of 0.5 M ($1.19\,g\,ml^{-1}$) is deposited to an n-type PSi interface and dried in air. Amphoteric NO in the range 1 ppm to 10 ppm, entrained in UHP N_2 and brought to the PSi interface produces a conductometric signal corresponding to an increase in resistance and is indicative of the interaction of an acid gas [86, 92]. Treatment with the $CoCl_2 \cdot 6\,H_2O$, produces a surface that overcomes the weak acidity of NO leading to the extraction of electrons from this gas and a decrease in resistance as a function of analyte concentration. Here, the Co(II) compound, deposited at a concentration to

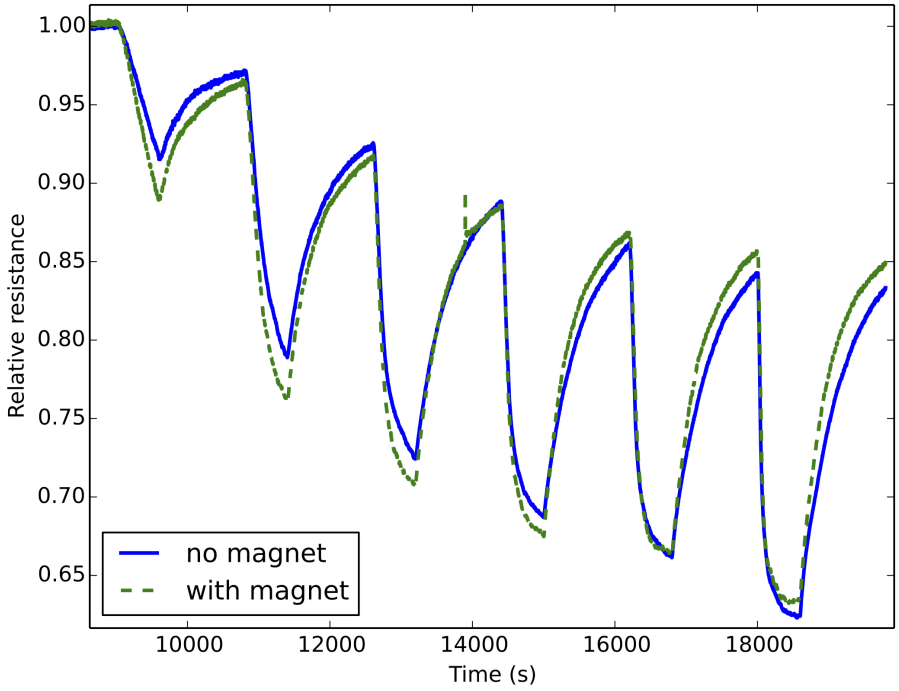

Figure 6.2: A comparison of the resistance response to 1 ppm–5 ppm and 10 ppm of NO of untreated n-type PSi without any magnetic field (blue) and in the presence of a 435 G magnetic field (green). Reprinted with permission from Journal of Applied Physics, C. Baker et al., Magnetically induced enhancement of reversibly responding conductometric sensors, 115, 164312. Copyright 2014, AIP Publishing LLC.

avoid cross-talk between the nanostructures, acts as a stronger acid than NO so as to extract electrons. At this cobalt concentration, the introduction of an 80 G magnetic field produces an enhanced conductometric response, which is a function of analyte concentration and corresponds to a decrease in resistance with magnetic field.

Figure 6.5 depicts results obtained as $CoCl_2 \cdot 6\,H_2O$, from a solution at a concentration of 0.5 M, is deposited to an n-type PSi interface and heated to a temperature of 50 °C to remove a significant component of water and form a $Co(II)Cl_2$ chain, accompanied by a decreased water concentration [266]. This leads to a water depleted long chain of $CoCl_2$ molecules surrounded on top and bottom by water molcules [266]. Amphoteric NO in the range 1 ppm to 10 ppm, entrained in UHP N_2 and brought to the PSi interface produces a conductometric signal corresponding to an increase in

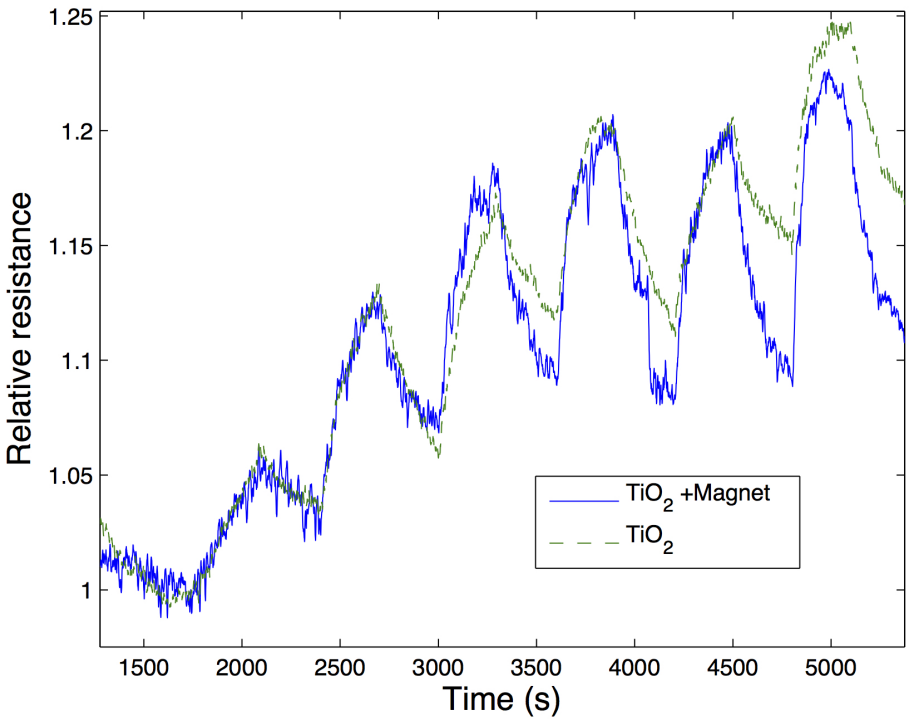

Figure 6.3: A comparison of the resistance response to 1 ppm–5 ppm and 10 ppm of NO of TiO_2 n-type PSi without any magnetic field (blue) and in the presence of a 80 G magnetic field (green). Reprinted with permission from Journal of Applied Physics, C. Baker et al., Magnetically induced enhancement of reversibly responding conductometric sensors, 115, 164312. Copyright 2014, AIP Publishing LLC.

resistance and indicative of the interaction of an acid gas [86,92]. Now treatment with the resulting $CoCl_2$ hydrated polymer produces a surface that does not overcome the weak acidity of NO. The Co(II) deposition leads to a decreased signal corresponding to a considerable decrease in the extraction of electrons by the NO and a decrease in the resistance as a function of NO concentration. Here, the Co(II) compound again counters the extraction of electrons by NO. At this cobalt concentration, the introduction of an 80 G magnetic field produces an enhanced conductometric response relative to the Co(II) deposited surface and corresponding to an increase in resistance with analyte concentration and magnetic field.

Figure 6.6 depicts results obtained as $CoCl_2 \cdot 6\,H_2O$ at a solution concentration of 0.5 M is deposited to a p-type PSi interface. Amphoteric NO in the range 1 10ppm,

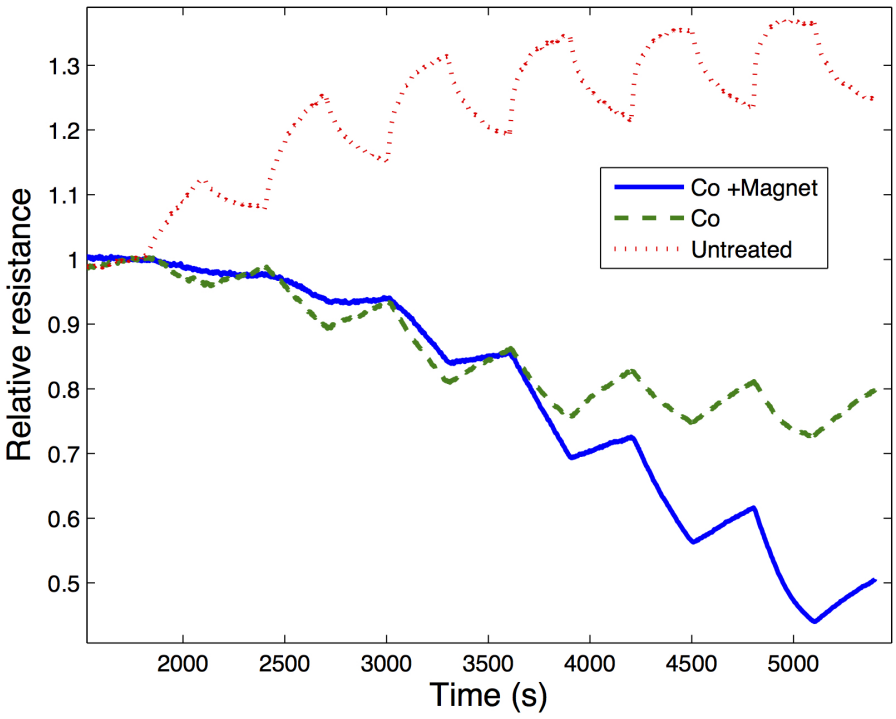

Figure 6.4: A comparison of the resistance response to 1 ppm–5 ppm and 10 ppm of NO of untreated n-type PSi (red), $CoCl_2 \cdot 6\,H_2O$ treated n-type PSi (green), and $CoCl_2 \cdot 6\,H_2O$ treated n-type PSi in the presence of an 80 G magnetic field (blue). Reprinted with permission from Journal of Applied Physics, C. Baker et al., Magnetically induced enhancement of reversibly responding conductometric sensors, 115, 164312. Copyright 2014, AIP Publishing LLC.

entrained in UHP N_2 and brought to the PSi interface produces a conductometric signal corresponding to a decrease in resistance and indicative of the interaction of an acid gas as it removes electrons from a p-type PS surface [86, 92]. Treatment with the $CoCl_2 \cdot 6\,H_2O$ produces a surface, which quenches the effect of the weak acidity of NO leading to a decrease in the extraction of electrons by this gas and a decrease in the conductance as a function of analyte concentration. This change likely results as the concentration of $CoCl_2 \cdot 6\,H_2O$ is sufficient to force crosstalk between the nanostructures, hence a decrease in conductance change. At this cobalt concentration, the introduction of an 80 G magnetic field produces an enhanced conductometric response corresponding to a decrease in resistance (increase in conductance) with

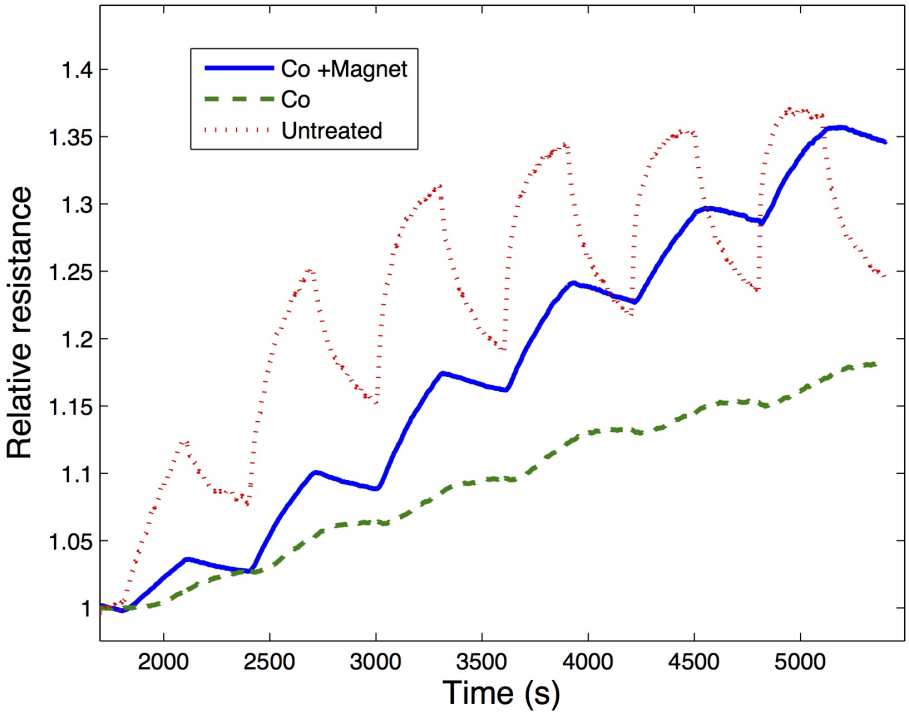

Figure 6.5: A comparison of the resistance response to 1 ppm–5 ppm and 10 ppm of NO of untreated n-type PSi (red), $CoCl_2{\cdot}(6-x)H_2O$ $(x > 2)$ treated n-type PSi (green), and $CoCl_2{\cdot}(6-x)H_2O$ $(x > 2)$ treated n-type PSi in the presence of an 80 G magnetic field (blue). Reprinted with permission from Journal of Applied Physics, C. Baker et al., Magnetically induced enhancement of reversibly responding conductometric sensors, 115, 164312. Copyright 2014, AIP Publishing LLC.

magnetic field and analyte concentration.

Figure 6.7 depicts results obtained as $CoCl_2 \cdot 6\,H_2O$ at a solution concentration of 0.25 M, half that of Figure 6.6, is deposited to a p-type PSi interface. Amphoteric NO in the range 1 ppm to 10 ppm, entrained in UHP N_2 and brought to the PSi interface produces a conductometric signal corresponding to an increase in conductance with analyte concentration and indicative of the interaction of an acid gas as it removes electrons from a p-type PSi surface [86,92]. Treatment with the $CoCl_2 \cdot 6\,H_2O$ produces a surface that enhances the effect of the weak acidity of NO leading to an increase in the extraction of electrons by this gas and an increase in the conductance

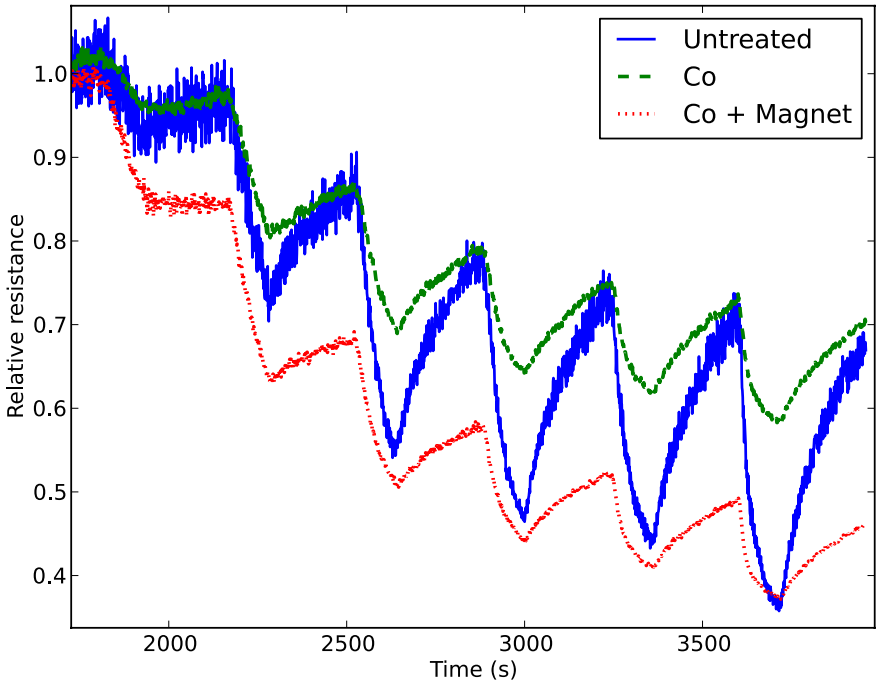

Figure 6.6: A comparison of the resistance response to 1 ppm–5 ppm and 10 ppm of NO of untreated p-type PSi (blue), $CoCl_2 \cdot 6\,H_2O$ treated p-type PSi (green), and $CoCl_2 \cdot 6\,H_2O$ treated p-type PSi in the presence of an 80 G magnetic field (red). Reprinted with permission from Journal of Applied Physics, C. Baker et al., Magnetically induced enhancement of reversibly responding conductometric sensors, 115, 164312. Copyright 2014, AIP Publishing LLC.

as a function of concentration. This result is consistent with the expected enhancement of the conductometric conductance due to $CoCl_2 \cdot 6\,H_2O$ at a concentration sufficiently low so as to prevent crosstalk between the decorated nanostructures and hence an increase in the conductance. The result is in agreement with the recently developed IHSAB principle. At this cobalt concentration, the introduction of a $\sim$2000 G magnetic field does not interact so as to increase the conductometric response. While there appears to be some increase relative to the PSi interface at 1 ppm to 3 ppm, this increase does not match that observed for the Co(II) deposition. The signal is also constant at pressures over the range 3 ppm to 10 ppm where the magnetic field no longer appears to follow the analyte concentration increase.

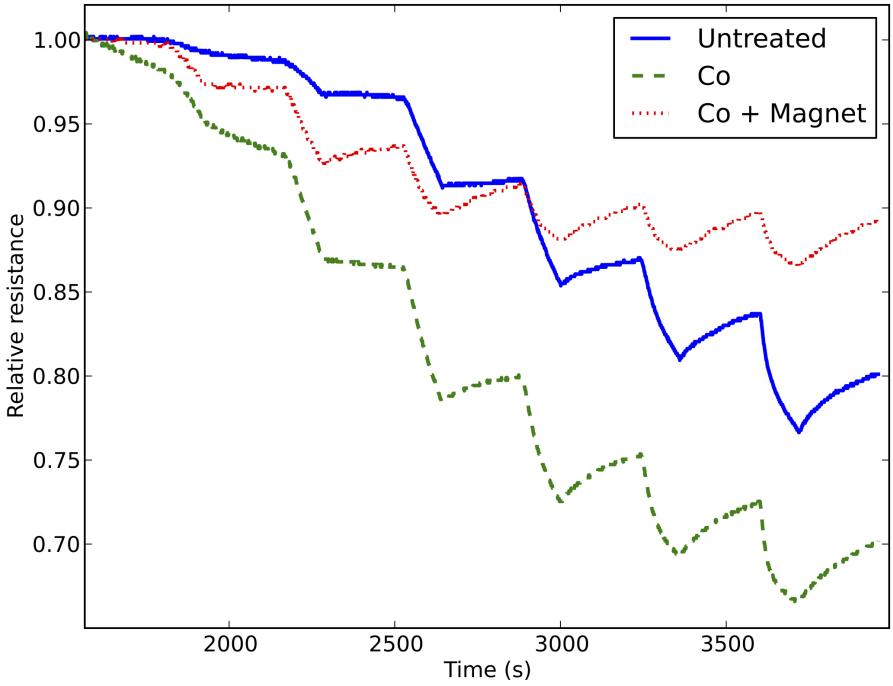

Figure 6.7: A comparison of the resistance response to 1 ppm–5 ppm and 10 ppm of NO of untreated p-type PSi (blue), 0.25 M $CoCl_2 \cdot 6\,H_2O$ treated p-type PSi (green), and 0.25 M $CoCl_2 \cdot 6\,H_2O$ treated p-type PSi in the presence of an 80 G magnetic field (red). Reprinted with permission from Journal of Applied Physics, C. Baker et al., Magnetically induced enhancement of reversibly responding conductometric sensors, 115, 164312. Copyright 2014, AIP Publishing LLC.

6.1.2.2 Iron oxide decorated interfaces

Figure 6.8 depicts results obtained after 10 nm iron oxide (Fe(II)) nanoparticles functionalized with NH_3 are deposited to a p-type PSi interface at a concentration of 0.05 M. Amphoteric NO in the range 1 ppm to 10 ppm, entrained in UHP N_2 and brought to the PSi interface produces a conductometric signal corresponding to a decrease in resistance with analyte concentration and indicative of the interaction of an acid gas as it removes electrons from a p-type PSi surface [86,92]. Treatment with the iron oxide nanostructures produces a surface that greatly quenches the response due to the weak acidity of NO, leading to a decrease in the extraction of electrons by this gas and, hence, to a decrease in the conductance change as a function of concentration.

This change likely results as the concentration of iron oxide nanostructures facilitates cross talk between the nanostructures and hence to a drop in conductance [86, 92]. Further, it is apparent that the ratio of intensities at NO concentrations greater than 3 ppm is severely curtailed (quenched in intensity). At these Fe(II) concentrations, the introduction of a $\sim$ 2000 G magnetic field produces an enhanced conductometric response relative to that obtained from the Fe(II) deposition, corresponding to a decrease in resistance (increase in conductance) with magnetic field. However, this response is still considerably less than that for the PSi interface.

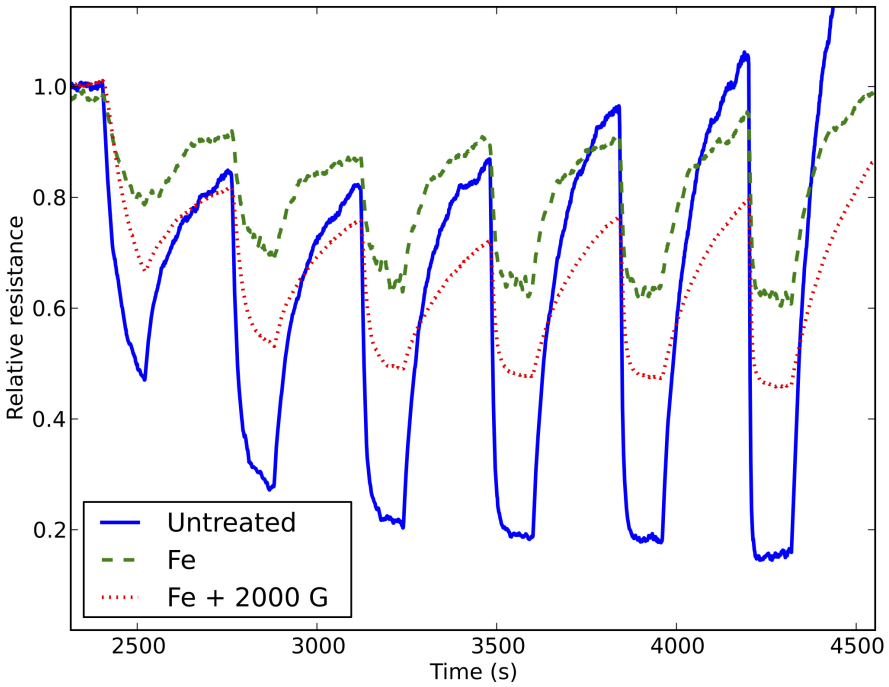

Figure 6.8: A comparison of the resistance response to 1 ppm–5 ppm and 10 ppm of NO of untreated p-type PSi (blue), 0.05 M iron oxide nanostructure treated p-type PSi (green), and 0.05 M iron oxide nanostructure treated p-type PSi in the presence of a $\sim$ 2000 G magnetic field (red). Reprinted with permission from Journal of Applied Physics, C. Baker et al., Magnetically induced enhancement of reversibly responding conductometric sensors, 115, 164312. Copyright 2014, AIP Publishing LLC.

Figure 6.9 depicts results obtained as 10nm iron oxide Fe(II) nanoparticles functionalized with NH_3 at a lowered concentration (0.045 M) relative to Figure 6.8 are

deposited to a p-type PSi interface. Amphoteric NO in the range 1 ppm to 10 ppm, entrained in UHP N_2 and brought to the PSi interface produces a conductometric signal corresponding to a decrease in resistance with analyte concentration and indicative of the interaction of an acid gas as it removes electrons from a p-type PSi surface and thus increases conductance [86,92]. Treatment with the iron oxide nanostructures produces a surface that greatly enhances the response of the PSi interface to the weakly acidic NO, leading to an increased extraction of electrons by this gas and, hence, an increase in the conductance (hole carriers) as a function of analyte concentration. This change results as the concentration of iron oxide nanostructures is sufficiently low so as to avoid crosstalk between the nanostructures. The substantial increase in conductance is expected from the IHSAB principle. Further, the response follows the concentration up to levels of 4 ppm NO, but begins to quench at NO concentrations in excess of 5 ppm. The response, is not only considerably greater than that in Figure 6.8, but far less noisy. At the deposited Fe(II) concentrations, the introduction of a $\sim$ 2000 G magnetic field produces a response that parallels that of Fe(II) at the lowest concentrations but then shows a considerable quenching relative to both the response of the PSi interface and the Fe(II) decorated interface. This degree of quenching suggests that limited available electron concentration (above the 0 K Fermi level - additional discussion in section 6.1.3), at the temperature of the experiment, is being depleted at a significantly enhanced rate from the decorated PSi interface through magnetic field interaction. This distinguishing characteristic is at 2000 G, which suggests a comparison with lower magnetic fields.

Figure6.10 depicts results obtained as 10 nm iron oxide Fe(II) nanoparticles functionalized with NH_3, again at a lowered concentration (0.045 M) relative to Figure 6.8, are deposited to a p-type PSi interface. Again, amphoteric NO in the range 1 10ppm, entrained in UHP N_2 and brought to the PSi interface to produce a conductometric

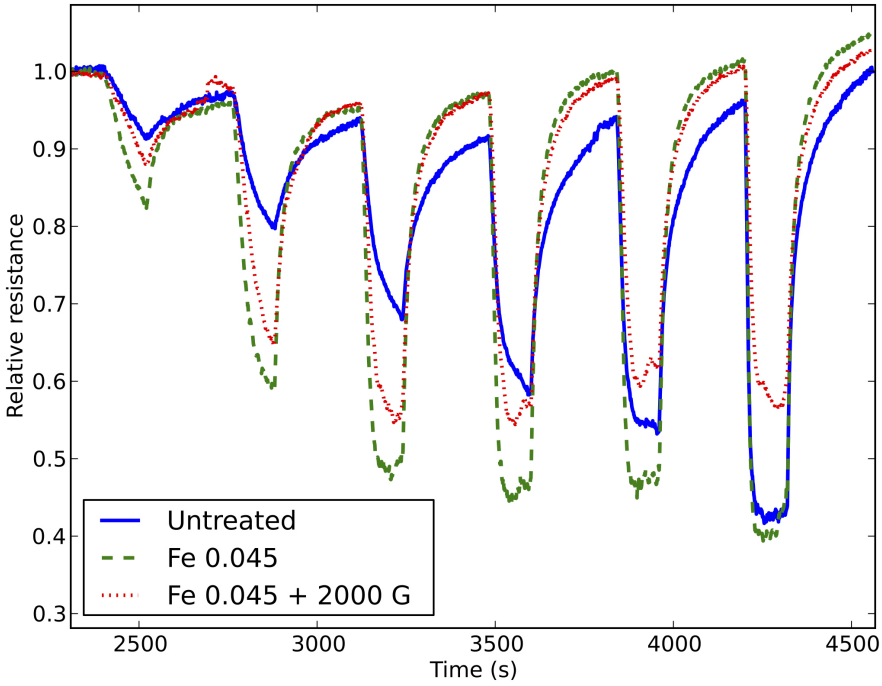

Figure 6.9: A comparison of the resistance response to 1 ppm–5 ppm and 10 ppm of NO of untreated p-type PSi (blue), 0.045 M iron oxide nanostructure treated p-type PSi (green), and 0.045 M iron oxide nanostructure treated p-type PSi in the presence of a $\sim$ 2000 G magnetic field (red). Reprinted with permission from Journal of Applied Physics, C. Baker et al., Magnetically induced enhancement of reversibly responding conductometric sensors, 115, 164312. Copyright 2014, AIP Publishing LLC.

signal corresponding to a decrease in resistance with analyte concentration and indicative of the interaction of an acid gas as it removes electrons from a p-type PSi surface [86, 92]. Treatment with the iron oxide nanostructures produces a surface which greatly enhances the response due to the weak acidity of NO and leads to an increase in the extraction of electrons by this gas and, hence, an increase in the conductance as a function of analyte concentration. Again, the concentration of iron oxide nanostructures is sufficiently low so as to avoid crosstalk between the nanostructures, leading to a substantial increase in conductance as expected from the IHSAB principle. However, in sharp contrast to Figure 6.9, at the deposited Fe(II) concentrations, the introduction of a $\sim$ 1000 G magnetic field produces a response that, while

somewhat weaker, faithfully follows concentration through 5 ppm, and is comparable to that at 10 ppm to that of both the Fe(II) decorated and untreated PSi interface. It is apparent that the electron concentration at the PSi surface is depleted at a much slower rate than that characteristic of the response recorded for the 2000 G field. The response variation as a function of analyte concentration suggests that the thermally populated electrons with which the magnetic field interacts are being depleted at a significantly slower rate from the decorated PSi interface through magnetic field interaction. This suggests an inherent limit to the electron population with which the magnetic field is interacting dictated by thermal excitation above the Fermi level, $\mathcal{E}_F$. These loosely bound electrons interact with the magnetic field and are depleted at a rate proportional to the magnetic field thus increasing the concentration of holes and p-type interface conductance.

Figure 6.11 depicts results obtained as 10 nm iron oxide Fe(II) nanoparticles functionalized with NH_3 at a lowered concentration (0.040 M) are deposited to an n-type PSi interface. Amphoteric NO in the range 1 ppm to 10 ppm, entrained in UHP N_2 and brought to the PSi interface to produce a conductometric signal corresponding to an increase in resistance as a function of analyte concentration and indicative of the interaction of an acid gas as it removes electrons from the n-type PSi surface [86, 92]. Treatment with the iron oxide nanostructures produces a surface that greatly enhances the response due to NO and leads to an increase in the extraction of electrons by this gas and, hence, an increase in the resistance as a function of concentration. This change results as the concentration of iron oxide nanostructures is sufficiently low so as to avoid crosstalk between the nanostructures. We again observe a substantial increase in resistance as expected from the IHSAB principle. Further, one notes that the response follows concentration up to concentrations of 4 ppm NO, beginning to quench at 5 ppm. At the deposited Fe(II) concentrations, the introduction of a $\sim$ 2000 G magnetic field produces a response that closely parallels that of Fe(II) at the

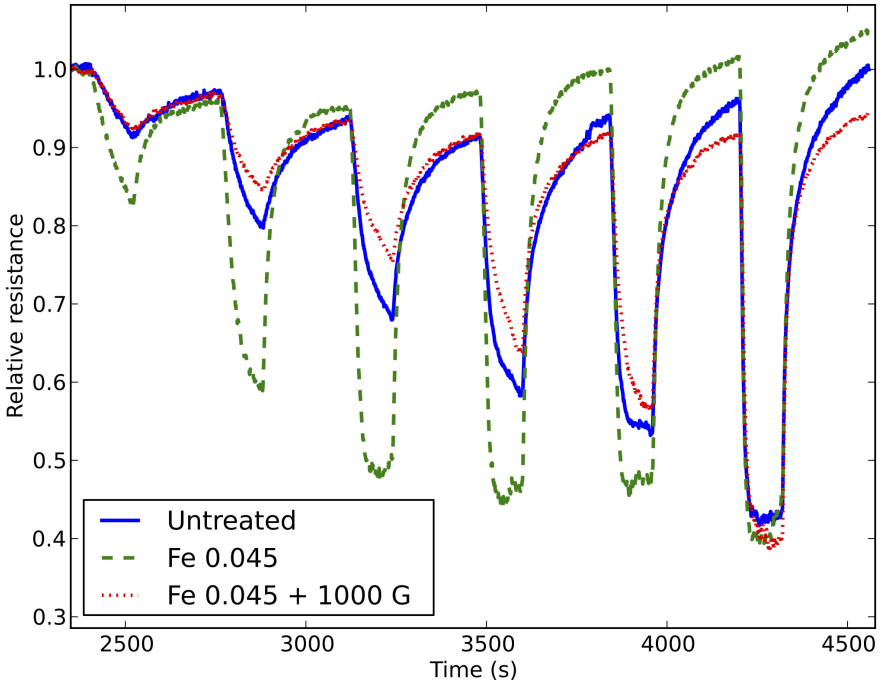

Figure 6.10: A comparison of the resistance response to 1 ppm–5 ppm and 10 ppm of NO of untreated p-type PSi (blue), 0.045 M iron oxide nanostructure treated p-type PSi (green), and 0.045 M iron oxide nanostructure treated p-type PSi in the presence of a $\sim$ 1000 G magnetic field (red). Reprinted with permission from Journal of Applied Physics, C. Baker et al., Magnetically induced enhancement of reversibly responding conductometric sensors, 115, 164312. Copyright 2014, AIP Publishing LLC.

lowest concentrations but then shows a considerable increase relative to both the response of the PSi interface and the Fe(II) decorated interface. This increase suggests the possibility that the electrons with which the magnetic field interacts are being removed from the donor levels at an increased rate. The electron removal will be suggested to go through the conduction band for the n-type semiconductor. There is a considerable increase in the response of the decorated PSi interface through magnetic field interaction. This behavior is again significant.

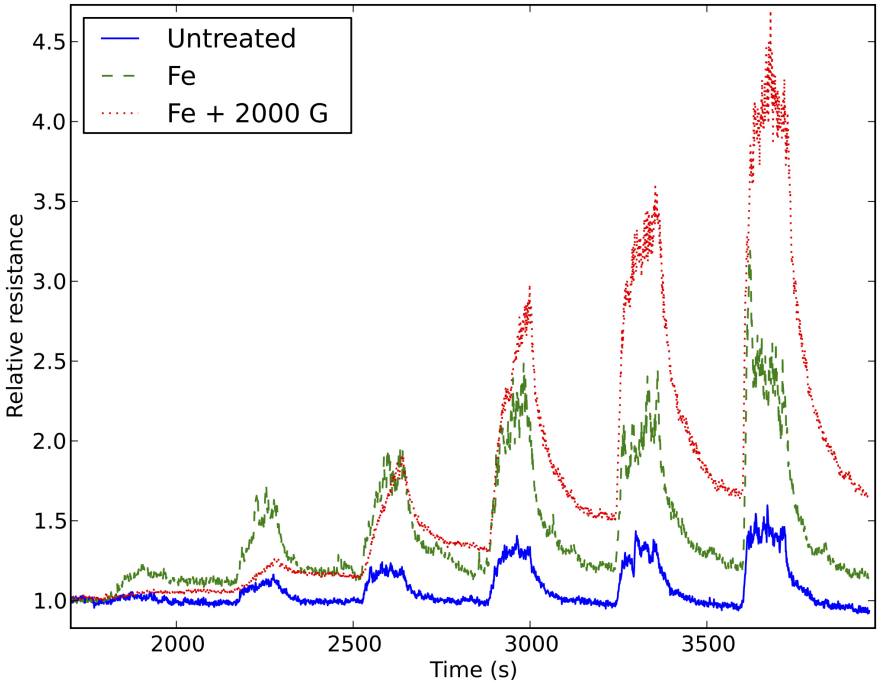

Figure 6.11: A comparison of the resistance response to 1 ppm–5 ppm and 10 ppm of NO of untreated n-type PSi (blue), 0.04 M iron oxide nanostructure treated n-type PSi (green), and 0.04 M iron oxide nanostructure treated n-type PSi in the presence of a $\sim$ 2000 G magnetic field (red). Reprinted with permission from Journal of Applied Physics, C. Baker et al., Magnetically induced enhancement of reversibly responding conductometric sensors, 115, 164312. Copyright 2014, AIP Publishing LLC.

6.1.3 Discussion

The discussion of these systems should begin with the consideration of the Fermi-Dirac level distribution and its correlation with the energy levels of extrinsic semiconductors depicted in Figure 6.12 [226]. Both p- and n-type semiconductors have similar thermal distributions. We are concerned with the deviation of this distribution at temperatures greater than 0 K as those electrons at energies above $\mathcal{E}_F$ in Figure 6.12 can readily interact with a magnetic field. These electrons have thermal energies $k_BT = (8.6173 \times 10^{-5}\,\mathrm{eV\,K^{-1}})(300\,\mathrm{K}) = 0.025\,\mathrm{eV}$ at room temperature. It is unlikely that an electron will be excited at room temperature if it lies more than 0.1 eV below the Fermi level, as the states within an energy range of k_BT are almost entirely

filled [226]. This suggests that in a p-type semiconductor (see section 2.2), the easily accessed electron population is small and virtually at a constant value at a given temperature. As a magnetic field interacts with those electrons that are easily accessible, the rate of interaction and electron removal increases with magnetic field. This should produce a signal at the lowest NO concentrations that becomes muted at the higher NO concentrations as the electron population is depleted. The effect should be more pronounced the higher the magnetic field and lead to a notable quenching at higher NO concentrations. We suggest that this effect is manifest in the response to the 2000 G magnetic field in Figure 6.9. At lower magnetic field strengths, the available electron population should be depleted more slowly. The response to the 1000 G magnetic field in Figure 6.10, that is initially weaker, follows the NO concentration dutifully through 5 ppm and displays a significant intensity at 10 ppm. We suggest that this results as the virtually constant electron population above $\mathcal{E}_F$ at a given temperature is not as rapidly depleted. The results we observe for the iron oxide system in Figure 6.9 also appear to be manifest in the Co(II) results of Figure 6.7.

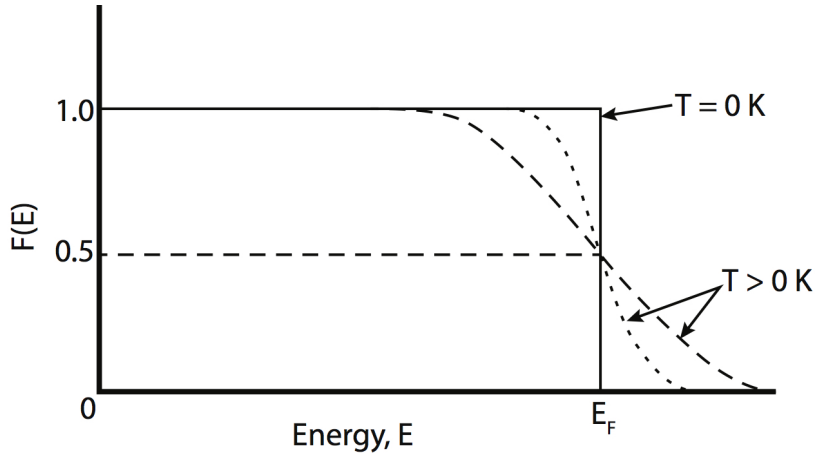

Figure 6.12: The Fermi-Dirac probability function at $T = 0$ K and $T > 0$ K. Reprinted with permission from Journal of Applied Physics, C. Baker et al., Magnetically induced enhancement of reversibly responding conductometric sensors, 115, 164312. Copyright 2014, AIP Publishing LLC.

In contrast, the n-type semiconductor framework, with free electrons readily accessible from the donor levels, within $\mathcal{E}_d \sim 0.025\,\text{eV}$ of the conduction band, furnishes a significant population over and above the thermal level population (Figure 6.13). This is in contrast to the acceptor level population lying within 0.01 eV of the valance band and more than 1 eV below the conduction band for a p-type system.

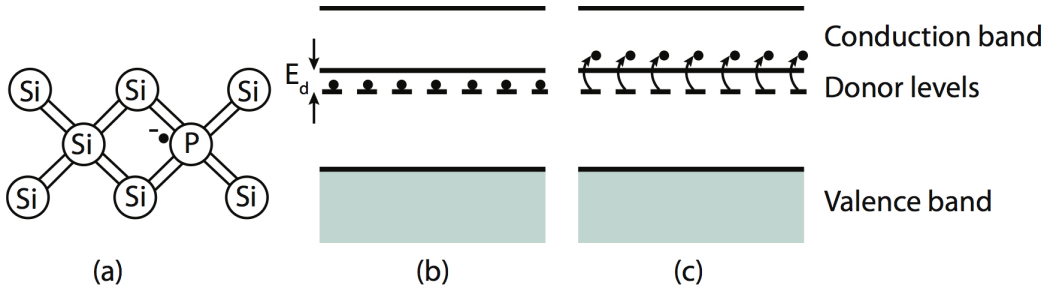

Figure 6.13: (a) Schematic lattice for an n-type semiconductor; (b) donor levels at absolute zero and (c) above absolute zero. Reprinted with permission from Journal of Applied Physics, C. Baker et al., Magnetically induced enhancement of reversibly responding conductometric sensors, 115, 164312. Copyright 2014, AIP Publishing LLC.

The data in Figure 6.11 demonstrates the significant affect which the fractional Fe(II) population has as it leads to an increase in sensitivity as dictated by the IHSAB principle. Figure 6.11 demonstrates that the introduction of a small magnetic field leads to a further considerable increase in the response of the interface. This increase might be explained with the use of Figure 6.13. The excess electrons in the n-type system are less tightly bound and should be more accessible to the magnetic field than are other sites in the lattice. Calculations demonstrate that the applied magnetic fields correspond to an energy increment that is of same order of magnitude or slightly larger than the 0.025 eV donor level-conduction band separation. Alternatively, the introduction of these magnetic fields should allow one to further remove electrons from the donor level to the conduction band thus decreasing the donor charge carriers and increasing the response of the system to NO (resistance increase). This equivalent electric field, with energy 0.01 eV to 0.025 eV, exceeds by several orders of magnitude

that which would be obtained from E_{perp} associated with the Hall effect [262, 263]. The magnitude of the Hall effect in these systems is sufficiently small that it must be measured in an AC mode and is not accessible to DC measurement.

The small magnetic fields necessary to significantly enhance the sensor response for the Co(II) and Fe(II) systems we have studied make use of the fundamental properties of an extrinsic semiconductor as they are coupled to an easily deposited and controllable interface. These results suggest the viability of small devices in which the analog of small coils placed in close proximity to the Co(II) and Fe(II) decorated interfaces will be amenable to the readily measurable enhancement of sensor response.

We have obtained response data for several metal oxides which we have found to be predicted by the IHSAB concept forming "materials sensitivity matrices" for a given analyte as outlined in Figure 6.14 [86, 92, 146, 150, 151]. This will enhance the capability to sense analytes and their mixtures. In Figure 6.14, the analyte scale is fixed in terms of acid/base properties, as determined by the energy of the lone pair (lone electron) donating to the positive metal site. The analyte lone pair energies can be evaluated from their ionization potentials or proton affinities (gas phase basicity). Co(II) and Fe(II) are paramagnetic transition metal sites which fall in the region close to Ni(II) in Figure 6.14. These ions respond to a magnetic field in contrast to the Ti(IV) sites present in TiO_2 (Figure 6.3). The cobalt and iron ion sites represent borderline acid sites and both respond similarly to NO. The IHSAB principle would predict that the presence of these sites would enhance the response of a sensor system.

6.2 Group IIA deposition

This study focuses on the oxides and hydroxides of the hard acids of the Group IIA metals. In strong contrast to the remaining elements of the periodic table, the Group IIA metals form hydroxides, which are decidedly of comparable or greater stability than the corresponding metal oxides. $Mg(OH)_2$ represents a weak base, whereas

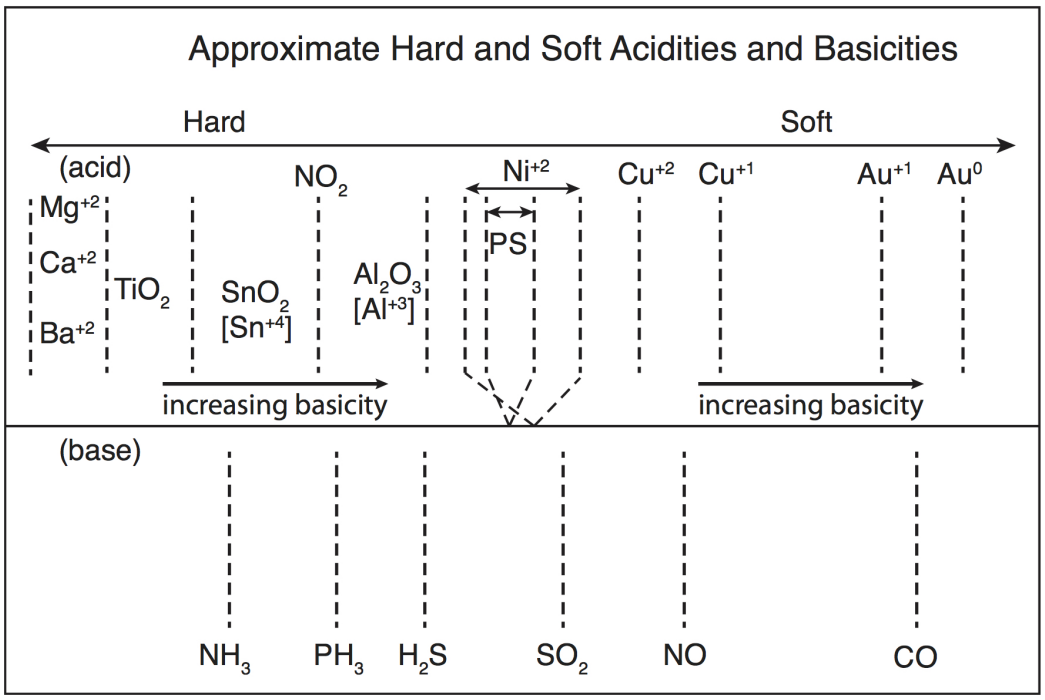

Figure 6.14: Estimated hard and soft acidities and basicities based on resistance changes relative to a p- and n-type porous silicon interface.

the heavier metal hydroxides of Ca, Sr, and Ba are known to form strong bases [116]. However, since the dihydroxides can donate a hydrogen they are classified as Brönsted acids. Based on the conductometric responses with respect to decorated p-type PSi, the Mg^{2+} sites appear to act as oxide-based Lewis acids. This conductometric interaction is modified for the heavier Group IIA compounds indicating a virtual reversal in the interaction of a decorated PSi interface to NH_3. This process causes a much more significant change than *in-situ* nitridation [98, 151]. Within this study an important observation is that the changes in conductometric reversible response and acid/base interaction are easily monitored for very small M^{2+} deposition concentrations. This is in sharp contrast to the corresponding changes associated with the transformation of the Group IIA oxides to their hydroxides as measured by X-ray photoelectron spectroscopy (XPS), energy dispersive X-ray analysis (EDAX), infrared (IR) spectroscopy, and nuclear magnetic resonance (NMR) measurements.

6.2.1 Materials and Methods

Untreated PS hybrid structures, with an exposed PS area of 4 mm^2, are fully submerged in 0.02 M to 0.05 M Group IIA metal-based aqueous solutions, in which the metal dichlorides are fully dissolved. These preparations are expected to initially produce the hydrated Group IIA ions, M^{2+} and Cl^- and subsequently the metal oxides and hydroxides ($MgCl_2$, $K_{sp} = 738$; $CaCl_2$, $K_{sp} = 1210$; $Mg(OH)_2$, $K_{sp} = 5.6 \times 10^{-12}$; $Ca(OH)_2$, $K_{sp} = 5 \times 10^{-6}$; $Ba(OH)_2$, $K_{sp} = 5 \times 10^{-3}$) or combinations thereof. The solubility in water of the metal hydroxides increases with increasing atomic number but is notably lower than the chlorides. The PSi interface is exposed to these solutions for 15 s. After the 15 s exposure they are subsequently placed in deionized (DI) H_2O for a 120 s period and rinsed in MeOH for 120 s. The nanostructure sites studied with X-ray diffraction (XRD) appear to correspond to amorphous structures, which display no diffraction pattern [198]. However, this might be attributed to the extremely small amount of deposited material. It is unlikely that crystallization occurred during the short deposition and subsequent surface cleaning process, as the deposition solutions were prepared from the metal dichloride dissolved in DI H_2O. The concentrations of the Group IIA metals Mg, Ca, and Ba optimum deposition concentrations are approximately an order of magnitude lower than the metal oxide sites we have previously studied [92, 94, 95, 151].

X-ray photoelectron spectroscopy (XPS) data of the binding energies of C, Au, O, and the relevant Group IIA metal was collected on a Thermo K-alpha XPS and analyzed using Thermo Avantage software. The X-ray source is Al Kα with a spot size of 400 μm^2 and an electron flood gun was used for charge compensation. The C and Au scans were repeated 4 times and the O and relevant metal scans were repeated 8 times. All XPS experiments were conducted at 10^{-8} mbar. Deposition time of the Group IIA metals was increased to 10 min to 40 min for XPS analysis, as these experiments require a much higher concentration than that required for conductometric analysis.

Scanning electron microscopy (SEM) studies [85, 95, 100, 151, 163, 164] demonstrate that the nanostructure deposits are physically well separated.

6.2.2 Results

This section will outline the responses of Mg, Ca, and Ba treated PSi interfaces. In all cases, these responses are compared to that for the untreated PSi interface. We find that the Mg decorated PSi interfaces are consistent with the formation of an acidic metal oxide surface whereas the Ca and Ba treated interfaces demonstrate a very different behavior, correlating with a distinctly different reversible interaction with NH_3. This result is consistent with a greater bond strength for the M−OH bond relative to both the M−Cl and M=O bond strengths for the majority of the Group IIA metals of Mg, Ca, and Ba [264]. Table 6.1 presents a comparison of relative responses for future reference.

Table 6.1: Average change in signal for p-type PSi interface for the average response to 1 ppm and 2 ppm of NH_3 and NO after decorating with the Group IIA metals, relative to an undecorated PSi interface.

	Mg			Ca			Ba		
	0.03 M	0.04 M	0.05 M	0.02 M	0.03 M	0.04 M	0.03 M	0.04 M	0.05 M
NH_3	1	2.9	0.5	0.8	0.5	0.2	0.075	0.45	1.6
NO	0.55	0.5	1	0.75	0.45	0.3	1.4	0.65	0.5

6.2.2.1 Mg decorated interfaces

A response from interfaces created with Mg^{2+} deposition, a hard metal oxide based Lewis acid, requires a much lower deposition concentration than the other metal oxide directed systems studied previously [94, 151]. For this discussion, response, ΔR, is defined as the resistance of the sensor in the presence of the analyte, R, divided by the baseline resistance, R_0. The results given in Figures 6.15 demonstrate that the

deposited Mg^{2+}-based decoration of a p-type PSi interface, to which ammonia readily contributes electrons. This process decreases the semiconductor majority charge carriers, which are holes, and thus increases the system resistance. This is consistent with the formation of a metal oxide. Figure 6.15a demonstrates the response to NH_3 observed as Mg^{2+} is deposited at a concentration of only 0.03 M. At this concentration, the Mg^{2+} deposition increases the response at the highest NH_3, concentrations of 8 ppm, 10 ppm and 20 ppm. At 0.04 M, Figure 6.15b demonstrates that the response to the Mg^{2+} deposited interface is greatly enhanced as a larger resistance change is recorded for the treated PSi interface at 2 ppm–10 ppm and 20 ppm. Mg^{2+} is a very strong Lewis acid, which, at an Mg^{2+} deposition of only 0.04 M, strongly enhances the ability of NH_3 to contribute electrons to the porous silicon interface. The NH_3 analyte donates electrons to a p-type PSi interface. These electrons combine with holes, thus reducing the number of majority charge carriers and increasing resistance. Mg^{2+} is a hard acid [94] acceptor atom of small size, which is not easily polarized. These characteristics account for the considerably lower concentration range over which the Mg^{2+} Lewis acid influences and enhances the NH_3 interaction [86, 92, 94]. At 0.05 M, the Mg^{2+} concentration the sensor response decreases (Figure 6.16). The acidic shift of the interface, created by the Mg^{2+} deposition is found to have an optimal solution deposition concentration between 0.03 M and 0.05 M. At concentrations of 0.05 M or higher the Mg^{2+} centers begin to strongly interact, cross-talking with each other [100], and decreasing effectiveness.

Figure 6.17 demonstrates the response of an Mg^{2+} treated PSi sensor to NO. When interacting with the undecorated PSi interface, NO, appears to act as a weak acid, attempts to withdraw electrons from the PSi interface, thus increasing the majority charge carrier concentration (holes). Figure B.10 demonstrates the response to NO for an interface decorated with Mg^{2+} at a concentration of 0.03 M. The Mg^{2+} deposition produces a response, similar to that shown in Figure 6.17, that appears

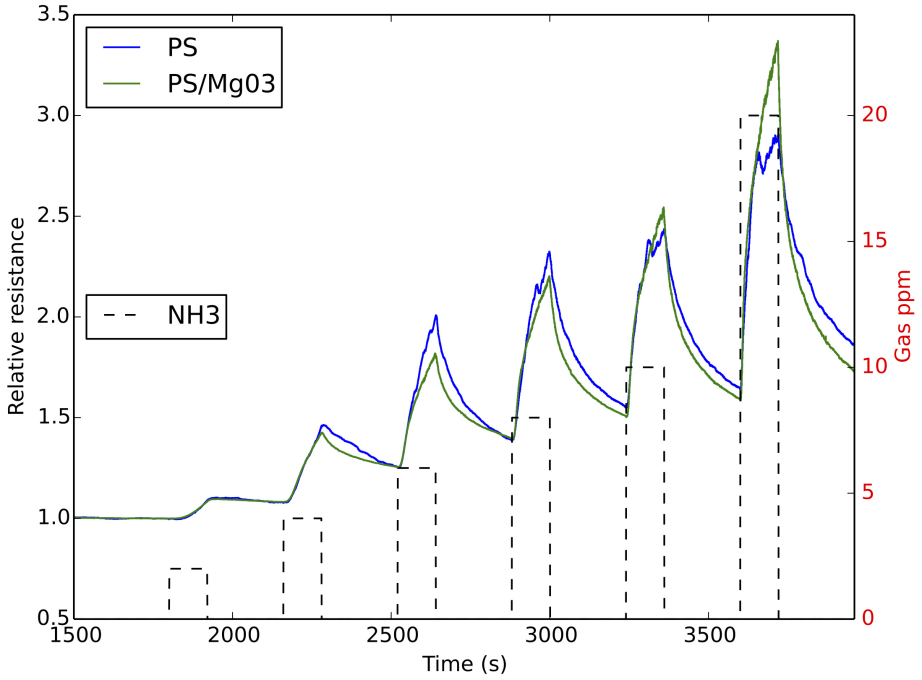

(a)

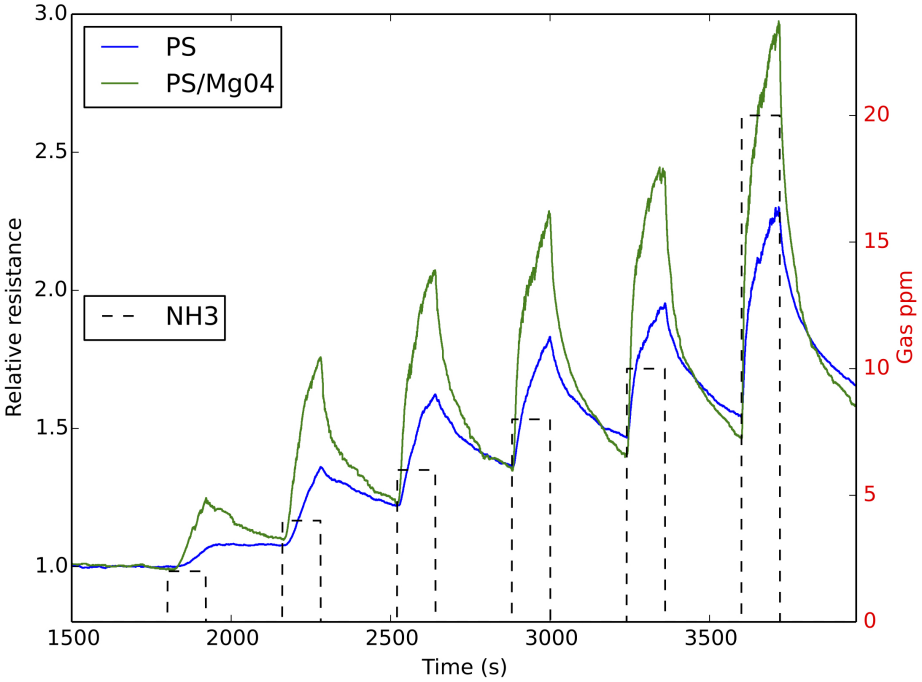

(b)

Figure 6.15: Response to NH_3 of an Mg^{2+} decorated p-type PSi interface before (solid blue) and after (green) treatment of the surface for 15 s with a (a) 0.03 M and (b) 0.04 M solution. The boxes (black dashed) denote the analyte concentration from 2 ppm to 20 ppm over the time of analyte gas exposure to the sensors. Reprinted from Applied Surface Science, 337, T.C. Tune, C. Baker, N. Hardy, A. Lin, T.J. Widing, J.L.Gole, Formation of nanostructured Group IIA metal activated sensors: The transformation of Group IIA metal compound sites, 216-223, Copyright 2015, with permission from Elsevier.

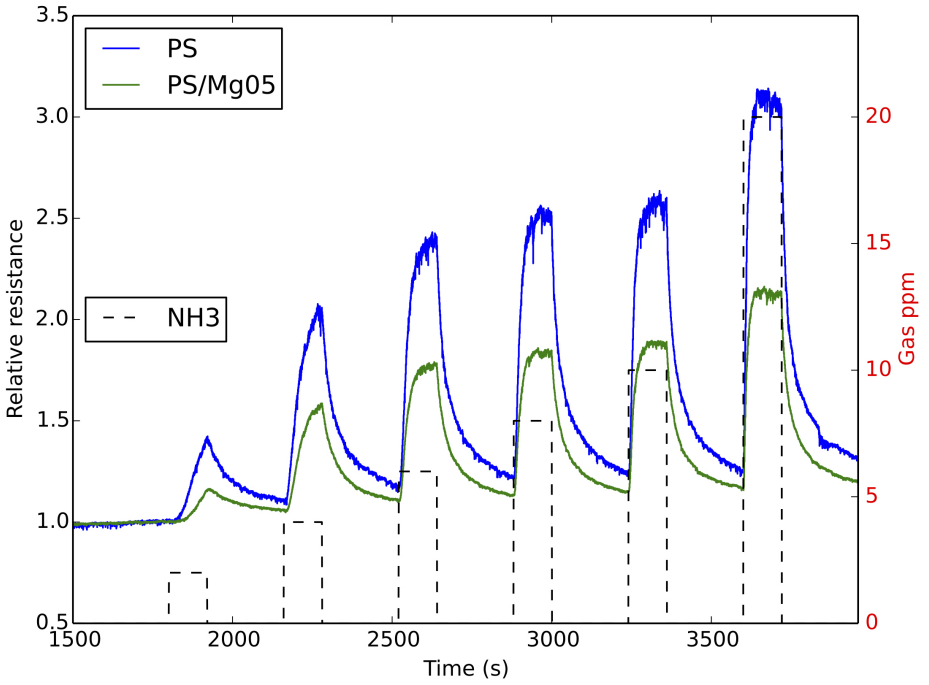

Figure 6.16: Response to NH_3 of an Mg^{2+} decorated p-type PSi interface before (solid blue) and after (green) treatment of the surface for 15 s with a (a) 0.05 M solution. The boxes (black dashed) denote the analyte concentration from 2 ppm to 20 ppm over the time of analyte gas exposure to the sensors. Reprinted from Applied Surface Science, 337, T.C. Tune, C. Baker, N. Hardy, A. Lin, T.J. Widing, J.L.Gole, Formation of nanostructured Group IIA metal activated sensors: The transformation of Group IIA metal compound sites, 216-223, Copyright 2015, with permission from Elsevier.

weaker in the analyte concentration range 1 ppm to 3 ppm, increasing to a comparable (4 ppm and 5 ppm) and slightly greater strength at 10 ppm. At 0.04 M, Figure 6.17 demonstrates that the response of the Mg^{2+} deposited interface greatly decreases, as a smaller conductance change is recorded for the treated PSi interface at 1 ppm to 5 ppm and 10 ppm. Mg^{2+} easily competes with NO for the available electrons at an Mg^{2+} deposition concentration of only 0.04 M as the decorated PSi interface overcomes the weak acid character of NO. The Mg^{2+} sites force NO to contribute electrons to the decorated interface, which combine with holes. The total number of majority charge carriers is still increased in the presence of NO, but however, the change in majority charge carriers is decreased. At $0 \cdot 05$ M, the Mg^{2+} does not affect the interaction of NO and the sensor response (Figure B.11). The acidic shift of the

interface is found to have an optimal deposition concentration between 0.03 M and 0.05 M. At concentrations of 0.05 M or higher the Mg^{2+} centers appear to strongly interact, cross-talking and decreasing their effectiveness.

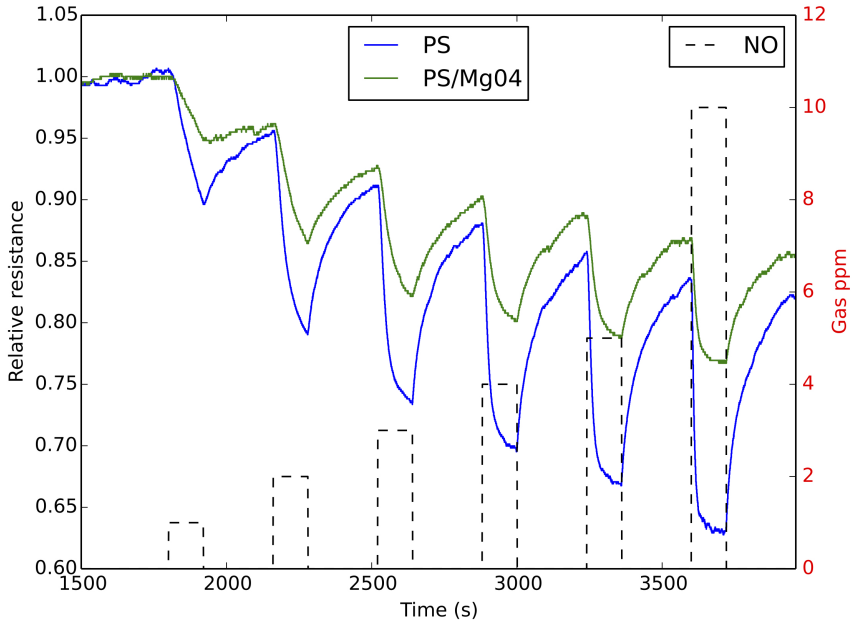

Figure 6.17: Response to NO of an Mg^{2+} decorated p-type PSi interface before (solid blue) and after (green) treatment of the surface for 15 s with a 0.04 M solution. The boxes (black dashed) denote the analyte concentration from 1 ppm to 10 ppm over the time of analyte gas exposure to the sensors. Reprinted from Applied Surface Science, 337, T.C. Tune, C. Baker, N. Hardy, A. Lin, T.J. Widing, J.L.Gole, Formation of nanostructured Group IIA metal activated sensors: The transformation of Group IIA metal compound sites, 216-223, Copyright 2015, with permission from Elsevier.

6.2.2.2 Ca decorated interfaces

Figure 6.18 demonstrates the response of a Ca^{2+} treated PSi sensor to NH_3 and NO. NH_3 contributes electrons to an untreated p-type PSi interface, increasing the sensor resistance response by decreasing the majority charge carriers (holes) and NO attempts to extract electrons, increasing the majority charge carriers and the sensor conductance. As Ca^{2+}-based nanostructures are deposited to a PSi interface at a concentration of 0.02 M, the Ca^{2+} deposition, only slightly affects the response to

NH_3, which shows a consistent slight decrease relative to the untreated PS interface (Figure B.12). NO shows a slight decrease in response at 1 ppm to 3 ppm, virtually the same response at 4 ppm, and a slightly increased conductance change at 5 ppm and 10 ppm (Figure B.13).

Figures 6.18 and B.14 demonstrate the responses to NH_3 and NO as Ca^{2+}-based nanostructures were deposited to PSi interfaces from a solution at concentrations of 0.03 M and 0.04 M, respectively. At both concentrations a clear change in the response for both NH_3 and NO is observed. The Ca^{2+} deposition decreases the resistance response to NH_3. This is in stark contrast to the response of the Mg^{2+} decorated interface. The response to NO decreases substantially relative to that for the undecorated PSi interface for all concentrations 1 ppm to 10 ppm. The ability of NO to extract electrons decreases substantially, as would be expected on the basis of a metal oxide decorated interface. These results suggest that the Ca^{2+}-based nanostructure sites do not correspond precisely to sites that extract electrons but rather to an interface dominated by inverse interactions relative to the PSi surface. In other words, the decrease in response for NH_3 is consistent with an interface with decreased ability to attract electrons. The similar behavior with respect to NO is puzzling and suggests several possibilities. The response to NO may be due to an enhanced chemisorption, impeding the reversible response of NO. NO, an amphoteric free radical, behaves as both an acid and a base. If the decorated interface attracts electrons from NO to form the more stable NO^+ this will produce a decrease in response. The decrease in response might also result as the alkali hydroxides are known to etch silicon and this phenomenon may extend to the Group IIA hydroxides.

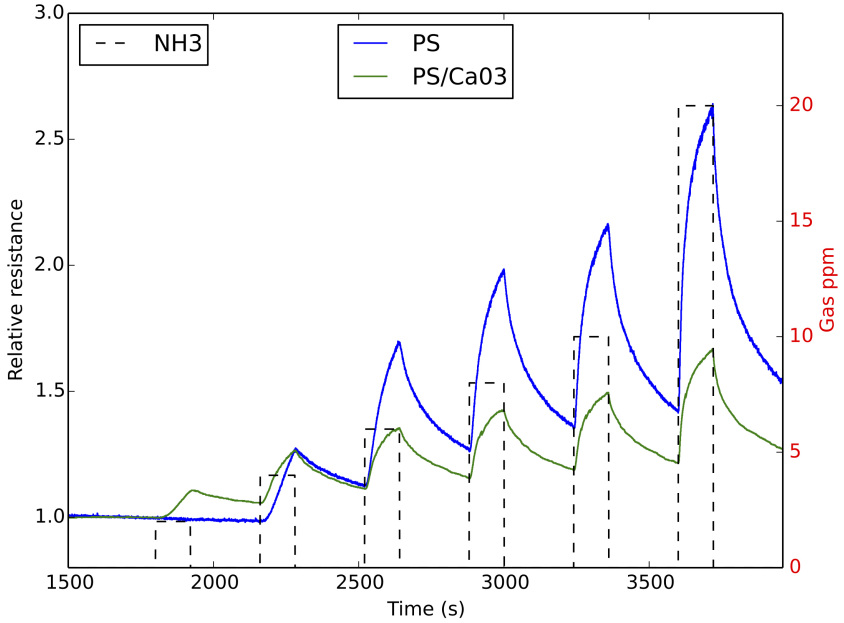

(a)

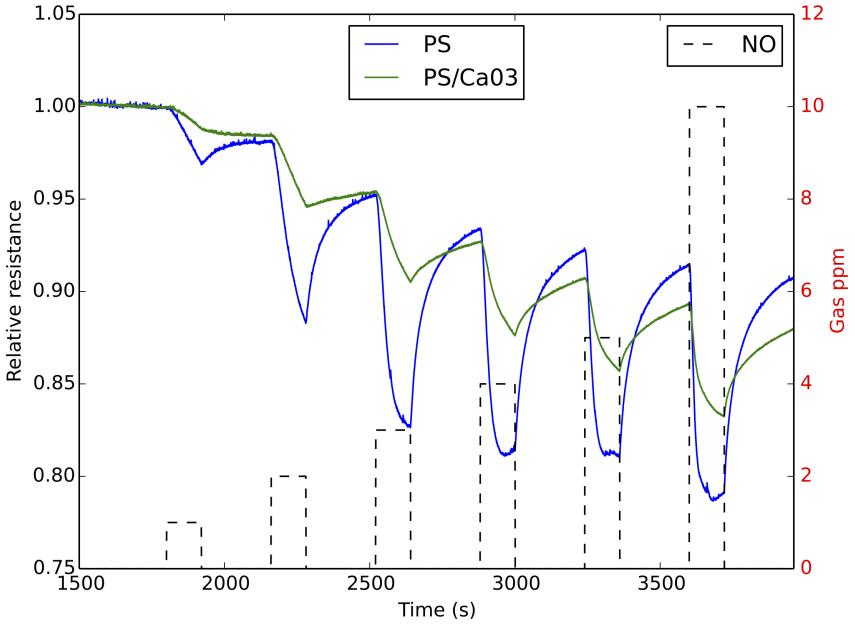

(b)

Figure 6.18: Response to (a) NH_3 and (b) NO of a Ca^{2+} decorated p-type PSi interface before (solid blue) and after (green) treatment of the surface for 15 s with a 0.03 M solution. The boxes (black dashed) denote the analyte concentration from (a) 2 ppm to 20 ppm (NH_3) or (b) 1 ppm to 10 ppm (NO) over the time of analyte gas exposure to the sensors. Reprinted from Applied Surface Science, 337, T.C. Tune, C. Baker, N. Hardy, A. Lin, T.J. Widing, J.L.Gole, Formation of nanostructured Group IIA metal activated sensors: The transformation of Group IIA metal compound sites, 216-223, Copyright 2015, with permission from Elsevier.

6.2.2.3 Ba decorated interfaces

At a concentration of 0.03 M, the Ba^{2+} deposition leads to a greatly muted sensor response for NH_3 corresponding to a substantial decrease in resistance change (Figure 6.19a), similar to the change in response shown in Figure 6.18a due to the Ca^{2+} deposition. This is counter to the observed behavior for Mg^{2+}. The NO response for the Ba^{2+} treated PSi interface increases relative to that for the untreated PSi interface as the analyte concentration increases from 1 ppm to 10 ppm (Figure 6.19a). This is counter to that expected for a Lewis acid-based interface, suggesting the influence of hydroxyl bonding. The relative behaviors of the NH_3 and NO systems are therefore consistent. Figure B.15 indicates that, while the Ba^{2+} treated interface at first shows a notable increase in response to NO, this signal degrades as a function of time. This could result from the presence of hydroxyl groups. However, the initial response is in complete contrast to the Mg^{2+} system and also differs from the Ca^{2+}-based deposited interface.

The Ba^{2+} deposition at a concentration of 0.04 M leads to a muted sensor response for NH_3 (Figure B.16a), although not to the degree observed at 0.03 M. This result is counter to the observed behavior for Mg^{2+}. The response to NO corresponds to a decrease in resistance (increase in conductance). However, the relative change in response for the treated interface at 0.04 M (Figure B.16b) is notably less than that at 0.03 M. This might also result from the much larger size of the Ba^{2+} site as it shields active sites from the analytes at the higher concentration leading to a decrease of the response to NH_3 and NO at 0.04 M.

Figures B.17a and B.17b demonstrate the response to NH_3 and NO observed as Ba^{2+}-based nanostructures are deposited to PSi interfaces from a solution at a concentration of 0.05 M. The response to the Ba^{2+} decorated interface exceeds that for the untreated PSi interface in a manner similar to that for Mg^{2+}. The response to NO is notably weaker compared to the untreated interface for all concentrations

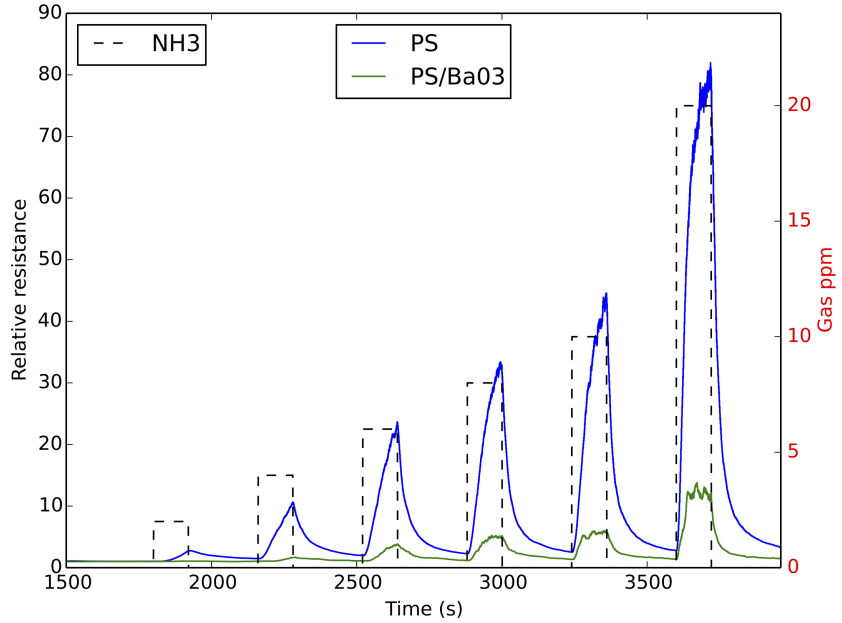

(a)

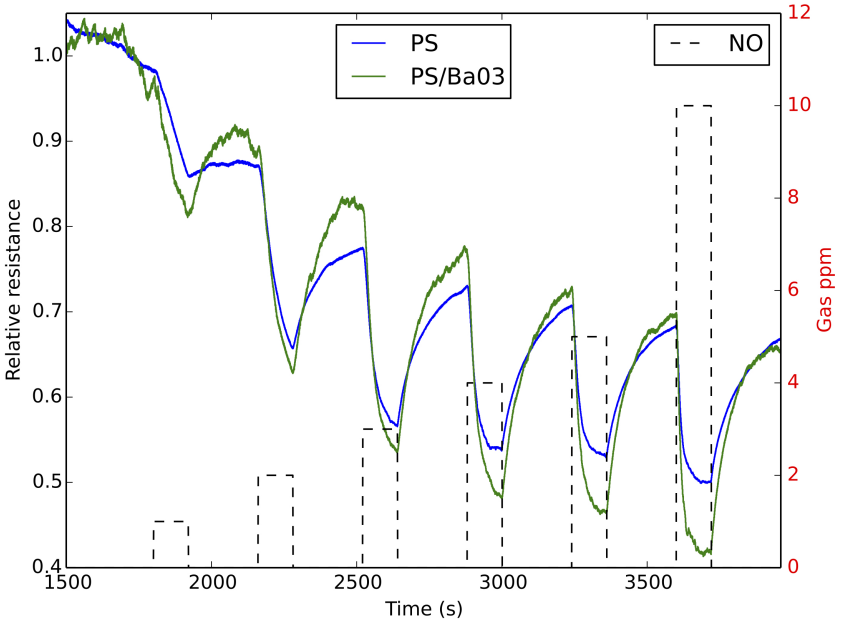

(b)

Figure 6.19: Response to (a) NH_3 and (b) NO of a Ba^{2+} decorated p-type PSi interface before (solid blue) and after (green) treatment of the surface for 15 s with a 0.03 M solution. The boxes (black dashed) denote the analyte concentration from (a) 2 ppm to 20 ppm (NH_3) or (b) 1 ppm to 10 ppm (NO) over the time of analyte gas exposure to the sensors. Reprinted from Applied Surface Science, 337, T.C. Tune, C. Baker, N. Hardy, A. Lin, T.J. Widing, J.L.Gole, Formation of nanostructured Group IIA metal activated sensors: The transformation of Group IIA metal compound sites, 216-223, Copyright 2015, with permission from Elsevier.

1 ppm to 10 ppm, again similar to Mg^{2+}, although this effect is more likely due to the size of the Ba^{2+}-based nanostructures.

6.2.2.4 XPS results

XPS results are shown for Ca^{2+} and Ba^{2+} decorated PSi interfaces in Figures 6.20 and 6.21, respectively. It is of note that deposition time for detection of these Group IIA metals by XPS was required to be in excess of 10 min. The spectral plotting and peak fitting was done using Igor software (http://www.wavemetrics.com/index.html). The peaks were found using the "multi-peak fit 2" analysis package with Gaussian functions. Adventitious carbon is present in all air exposed materials and dependent on the machine usage prior to the runs discussed in this monograph. Thus, the C1s peak of adventitious carbon, present on both treated and untreated samples, was used as a reference to correct peak offset due to sample charging. The C1s scans also show evidence of a higher binding energy shoulder suggesting the presence of C−O bonds (Figure 6.22). This is consistent with samples treated with MeOH throughout the sensor fabrication process [198].

Ciston et al. [47, 48] explain that the presence of OH bonds will present as a shoulder of higher binding energy on the O1s spectrum. We have investigated the O1s spectra for the magnesium, calcium, and barium systems and have been unable to detect a clear asymmetry in any of the O1s peaks. However, this may not be surprising due to the much larger concentration of silicon oxide sites whose total intensity dwarfs the deposited Group IIA metal bonds to oxygen and hydroxyl groups. All previous studies of the decorated PSi interfaces demonstrate that the observed character of the interface is dominated by the nanostructure deposition [85]. The cross section for magnesium is sufficiently low and the XPS spectrum is quite noisy making definitive peak observation and identification tenuous.

The C1s peak of the Ca^{2+} decorated PSi interface is ~ 0.16 eV lower than that

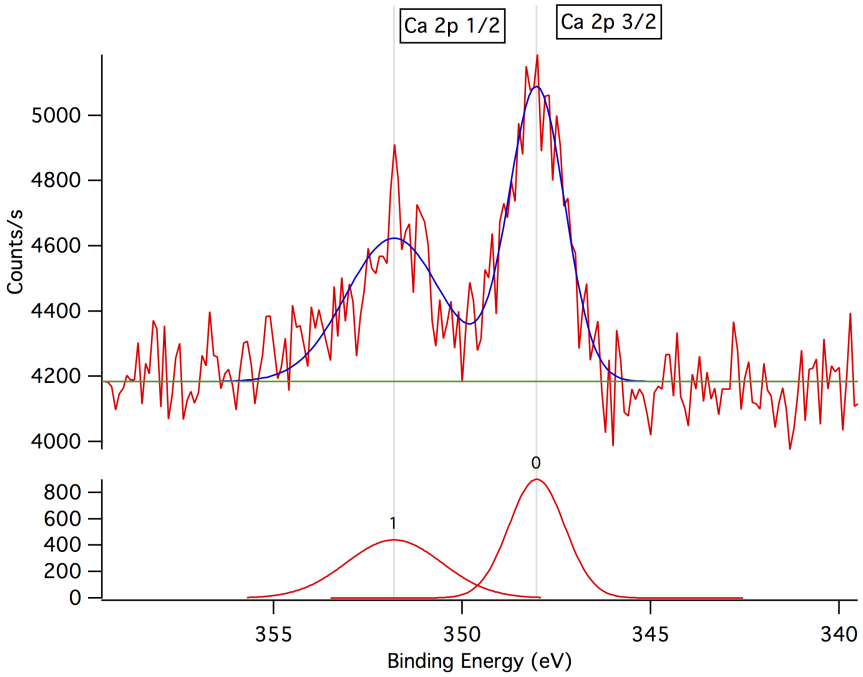

Figure 6.20: Calcium 2p XPS spectrum of PSi interface with a 10 min deposition of Ca^{2+}. Reprinted from Applied Surface Science, 337, T.C. Tune, C. Baker, N. Hardy, A. Lin, T.J. Widing, J.L.Gole, Formation of nanostructured Group IIA metal activated sensors: The transformation of Group IIA metal compound sites, 216-223, Copyright 2015, with permission from Elsevier.

for adventitious carbon at 284.8 eV. Adjusting for the offset gives calcium peaks at 351.64 eV and 347.68 eV. According to Selvam et al. [234] and correlated with the NIST data compilation [2], $Ca(OH)_2$ has a Ca2 $p_{1/2}$ peak at 351.5 eV and a Ca2 $p_{3/2}$ peak at 347.6 eV. In contrast, the NIST data compilation has values for CaO Ca2 $p_{1/2}$ peaks at 351.1 eV and Ca2 $p_{3/2}$ at 347.0 eV. These data are obtained for air-exposed samples. Sosulnikov and Teterin [237] report for CaO a Ca2 $p_{1/2}$ peak at 349.7 eV and Ca2 $p_{3/2}$ peak at 346.0 eV. For $CaCO_3$, which Selvam et al. [234] suggest will have a similar XPS spectrum to $Ca(OH)_2$, Sosulnikov and Teterin [237] provide a Ca2 $p_{1/2}$ peak at 351.0 eV and Ca2 $p_{3/2}$ at 247.3 eV. Both studies suggest that the Ca^{2+} on the PSi interface is that of the hydroxide.

Fukuda et al. [77] studied the difference in XPS spectra for BaO and $Ba(OH)_2$. Fukuda et al. [77] worked with data uncorrected for sample charging and so compared

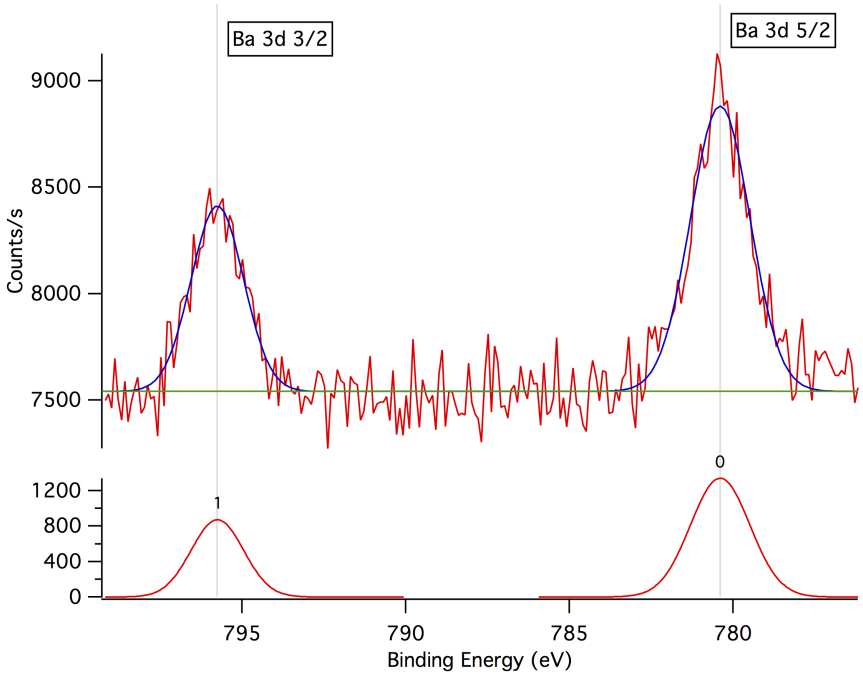

Figure 6.21: Barium 3d XPS spectrum of PSi interface with a 40 min deposition of Ba^{2+}. Reprinted from Applied Surface Science, 337, T.C. Tune, C. Baker, N. Hardy, A. Lin, T.J. Widing, J.L.Gole, Formation of nanostructured Group IIA metal activated sensors: The transformation of Group IIA metal compound sites, 216-223, Copyright 2015, with permission from Elsevier.

the difference between Ba3 $d_{5/2}$ and O1 s peaks for BaO and $Ba(OH)_2$, which were 250.9 eV and 249.0 eV respectively. For the Ba^{2+} decorated PSi interface, the Ba3 $d_{5/2}$ peak was at 780.39 eV and the O1 s at 533.04 eV (Figure 6.23). This gives a difference of 247.35 eV, which is closer to the $Ba(OH)_2$ results of Fukuda et al. [77].

6.2.3 Discussion

The most significant result obtained in this study is the observation of the conversion of the decorated sensor interface interaction with NH_3 for the Ca^{2+} and Ba^{2+} treated interfaces versus the Mg^{2+} interface. Figure 6.14 demonstrates that the oxides of the Group IIA metals are expected to be among the hardest acids. The data that we have obtained for magnesium (surface preparation solution pH 5–7) clearly demonstrates this trend as the concentration range over which changes in response occur

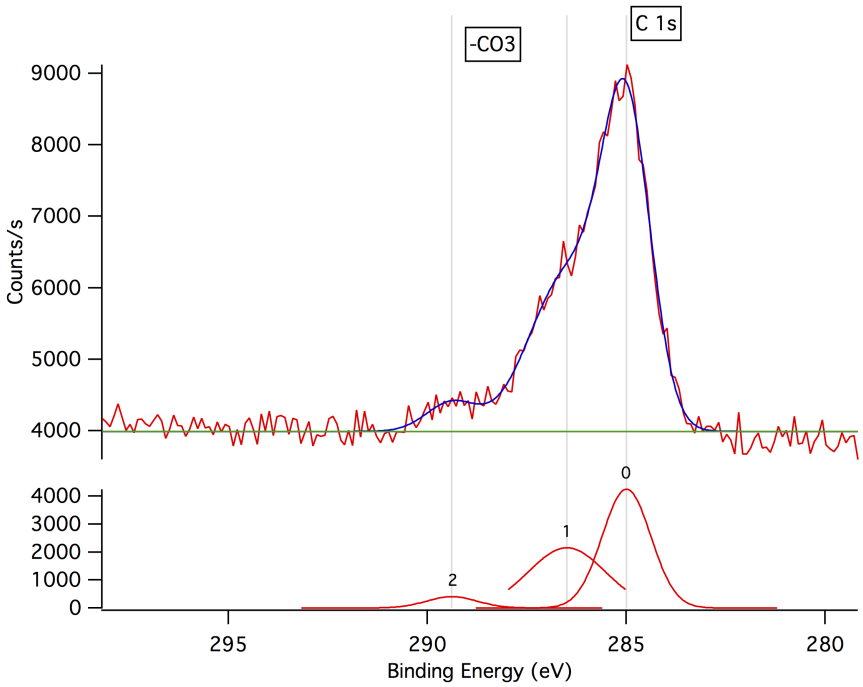

Figure 6.22: XPS spectrum of adventitious carbon on PSi interface with 40 min deposition of Ba^{2+}. Reprinted from Applied Surface Science, 337, T.C. Tune, C. Baker, N. Hardy, A. Lin, T.J. Widing, J.L.Gole, Formation of nanostructured Group IIA metal activated sensors: The transformation of Group IIA metal compound sites, 216-223, Copyright 2015, with permission from Elsevier.

is approximately an order of magnitude lower than that observed in previous studies involving the nanostructured metal oxides. The depositions in the present study, especially those involving Mg^{2+} form well separated nanostructured islands, 30 nm or smaller [85]. However, the depositions formed by the heavier Group IIA metals (also pH 5–7) modify the character of the interface as it changes from a strongly acidic character. The primary indicator is the change in response observed for NH_3 for the Ca^{2+} and Ba^{2+} decorated surfaces. This must represent a complex interaction involving the deposited products of the heavier Group IIA metal-based solutions, which renders a response that appears to be the inverse of that for the Mg^{2+} deposited solutions. This manifestation is easily observed but must be the subject of further study before this trend will be useful in sensor development.

The results in Table 6.1 may provide further insight. The maximum change for

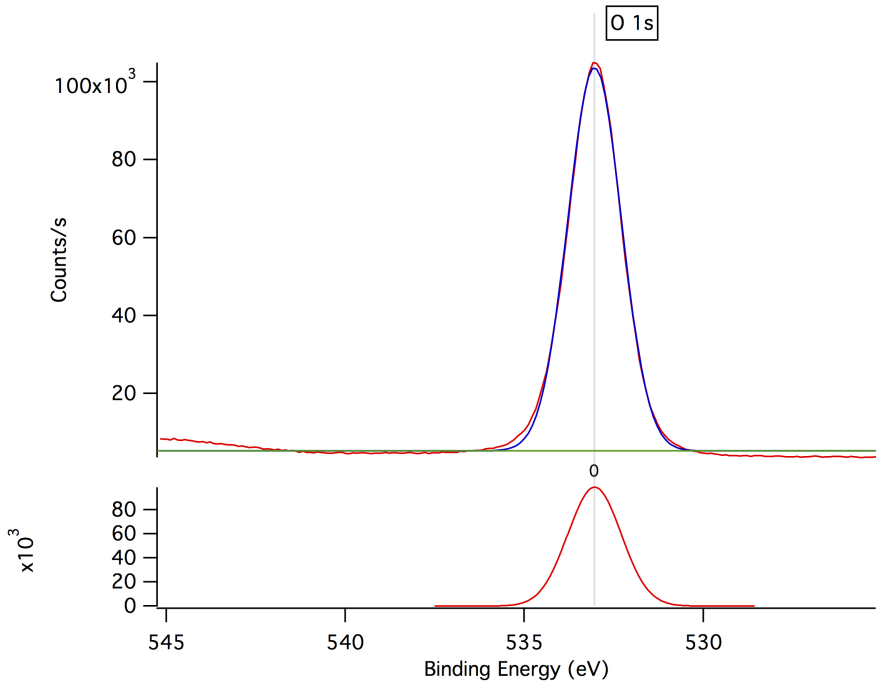

Figure 6.23: XPS spectrum of oxygen on PSi interface with 40 min deposition of Ba^{2+}. Reprinted from Applied Surface Science, 337, T.C. Tune, C. Baker, N. Hardy, A. Lin, T.J. Widing, J.L.Gole, Formation of nanostructured Group IIA metal activated sensors: The transformation of Group IIA metal compound sites, 216-223, Copyright 2015, with permission from Elsevier.

the NH_3 signal response is approximately 0.1 to 3 corresponding to a factor of 30. The maximum change for NO is 0.3 to 1.5, corresponding to a factor of approximately 5. If we relate these changes to a free energy difference, the factor of 30 corresponds to an energy change of 2 kcal/mol. A factor of 5 corresponds to an energy difference of about 1 kcal/mol. Although the signal differences are clearly real, they represent energy range changes of less than 2 kcal/mol, which is quite small. Thus, the conductometric response associated with IHSAB behavior would appear to monitor very small energies.

The nature of the interactions observed for metal oxide deposited interfaces can be described by the recently developing IHSAB model. By depositing metal oxide nanostructure islands to the PSi interface, the response of a sensor can be enhanced or diminished [92]. The IHSAB model explains this phenomenon by linking chemical

selectivity and the balance of electron transduction (electron transfer) and chemisorption [86, 92, 150, 151] with the sensor response mechanisms. This model predicts the interaction of acidic, basic, and amphoteric gas analytes with nanostructure treated PSi sensor interfaces. A hard acid will form a strong ionic bond with a hard base and a soft acid will form a strong covalent bond with a soft base. For the purposes of chemical sensing, we wish to minimize this bond formation [205, 280, 281]. The IHSAB model guides the fabrication of a nanostructure-treated PSi gas sensor to stimulate an electron transduction-physisorption-dominated mode as an inorganic gas analyte interacts with a decorated interface. Electron transduction (transfer) dominates chemisorption through the interaction of a hard acid and soft base or soft acid and hard base. Figure 6.14 indicates that the Group IIA metal oxides are among the hardest acids and we expect that, if they decorate a PSi interface, they will interact reversibly with several basic analytes. The dominant factor is the HOMO-LUMO energy increment. If the donor orbital energy (HOMO) is not well matched with the acceptor (LUMO), then the interaction will be weak. As the HOMO (donor)-LUMO (acceptor) energy gap decreases, there can be more charge transfer between the molecule (analyte) and the created interface, leading to a stronger Lewis acid-base interaction. Conversely, the greater the HOMO-LUMO energy gap, the greater the orbital mismatch, enhancing the electron transduction mode. The IHSAB principle is in large part based on controlling the size of the Lewis acid-base bond dissociation energy.

The trends which we observe in the present study suggest that while the IHSAB model is appropriate to describe the interaction with an Mg^{2+} decorated interface, the character of the interfaces generated from the heavier alkaline earths appear to follow the known trends in basicity associated with the Ca^{2+} and Ba^{2+} hydroxides [116]. As described within the IHSAB model, the Brönsted acid character should facilitate a more significant HOMO-LUMO mismatch than the M^{2+} sites [150]. It seems apparent

that the weak interactions associated with the IHSAB effect (see above), while they apply to Mg^{2+}, are dominated by the formation of basic interfaces for Ca^{2+} and Ba^{2+}.

The significant changes in the conductometric signals observed in these studies as we traverse from magnesium to calcium and barium decorating solutions are easily monitored. The XPS studies on calcium and barium suggest that metal-hydroxide bonds are present but the changes observed much smaller than the manifest effects observed in the conductometric responses. EDAX, with its extremely low cross section for hydrogen cannot be used to distinguish the presence of hydroxide bonds vs. the oxides. IR studies, while indicating the formation of the hydroxide, are difficult to correlate. Finally, NMR studies for the Group IIA systems produce very broad signals, which may be indicative of the presence of hydroxide sites but this requires extensive calibration for not only the Group IIA centers but also for porous silicon.

The results that we have obtained for the Group IIA metals demonstrate a limit of the periodic acid strength of what one can use with porous silicon. It is quite significant that the PS interface can be converted from acidic to basic character and that the resulting conductometric response is then the inverse of that predicted by the IHSAB model. The data in Figure B.15 indicate that the Ba^{2+}-based solutions will degrade the PSi interface with time. This is not surprising in view of results that have been observed in the etching of PS with the alkali hydroxides KOH and NaOH [74, 161]. This implies that the use of alkaline-based nanostructures, which would be expected to form stronger hydroxides than oxides, while they might facilitate the formation of basic interfaces, may also be deleterious to the interaction of the decorated PSi interface in a manner similar to the alkali hydroxides. Thus, their use for sensor devices may be tenuous.

6.3 Conclusions

We have demonstrated the efficacy of a relatively small magnetic field to enhance the performance of a conductometric sensor interface. The effect, which is manifest for those transition metals that possess magnetic moments, may have potential significant implications for the development of small-scale sensor devices employing paramagnetic ion distributions to enhance sensor response in small magnetic fields. Future experiments will more closely analyze the effect of magnetic field strength on sensor response.

We have demonstrated that the conductometric measurement of the sensor response to interfaces decorated from Group IIA metal ion solutions. The observations suggest that we have observed a response consistent with Group IIA oxide formation for magnesium. However, we observe a change in conductometric character for calcium and barium depositions following an easily monitored change in the decorated PSi interface that appears to correspond to a decrease in acid character. While the hydroxides give up a hydrogen and are Brönsted acids their behavior when deposited to a PSi interface is not commensurate with an acid site and the IHSAB model. This is consistent with the known increase in base strength for the hydroxides of calcium through barium relative to magnesium. The data suggest that differing Group IIA compounds are formed from the deposition of the metal chlorides in aqueous solution and that a pattern suggestive of the known increase in basic character from magnesium to calcium and barium is manifest in the conductive response observed for these systems. The data that we have obtained demonstrate the readily monitored conversion of the decorated PSi interface commensurate with a reversal of reversible sensor behavior and consistent with XPS monitoring of the decorated interfaces. The effects observed are easily monitored in contrast to the corresponding changes associated with the transformation of the Group IIA oxide to hydroxide bonds observed in XPS, EDAX, IR, and NMR measurements.

These studies represent an initial demonstration of the capacity for the PSi sensor systems, combined with an understanding of the developing IHSAB concept, to provide a tool for exploring a variety of interface interactions.

CHAPTER VII

IMPEDANCE LIQUID SOLVENT DETECTION

This chapter will discuss extending the use of PSi sensor technology to the detection and selective identification of a range of organic solvents with applications in many industries including pharmaceuticals, consumer goods (cleaning products and personal care products), ground water quality monitoring, and phytoremediation of the environment [37,108,239,246]. Expanding the PSi sensor system to include liquid solvent detection represents an additional step towards creating a complete electronic nose or environment analysis system.

Table 7.1 lists the organic solvents that were tested with their various physical properties. The solvents were selected so that a range of the different properties could be explored and correlated with the observed changes in the impedance of the sensors. Archer et al. [8] specifically considered the dielectric constant, dipole moment, electronic polarizability, and bond character (polar versus non-polar) of organic solvents. The surface tension and vapor pressure are included to correlate with response and evaporation times of the various organic solvents.

Many different geometries of electrical contacts have been used for conductometric sensors. While PSi impedance sensors featuring backside electrical contacts have been used extensively [8, 167], we chose to use the simple sensor design outlined in Chapter 3. Frontside contacts can be expected to display a faster response time, as the solvents initially interacts with the pore openings before infiltration [111]. The design and fabrication process, including electrical contact deposition, is fully integrated with standard microfabrication methods. Additionally, we wish to correlate our findings in this study with the already established and robust gas-phase sensor model outlined

Table 7.1: Chemical properties of various organic solvents.

Solvent	dielectric constant, $\varepsilon/\varepsilon_0$	dipole moment, μ/D	polarizability, $\alpha/10^{-24}\,\mathrm{cm}^3$	bond character	surface tension γ/dyn cm^{-1}	vapor pressure p/kPa
Acetone	20.7	2.85	6.33	Polar	18.8	46.4
Water	80.1	1.82	1.45	Polar	72.75	3.27
Methanol	32.7	1.7	3.3	Polar	18.9	35.3
Ethanol	24.5	1.69	5.13	Polar	22.39	11
Isopropanol	17.9	1.66	6.9	Polar	21.7	10.8
Chloroform	4.81	1.15	8.4	Polar	29.0	26.7
Toluene	2.38	0.43	12.26	Non-polar	28.52	3.69
Isoprene	2.1	0.25	9.7	Non-polar	16.9	73.19

Reported values at 25 °C from [196] and the CRC Handbook of Chemistry and Physics (85th Edition).

in Chapters 5 and 6.

N-type and p-type PSi sensors were fabricated according to the description in Chapter 3. Impedance measurements were performed with a Solartron 1260 Impedance Analyzer and controlled with ZPlot software. The data was then analyzed with ZView software. For each sensor, the complete impedance was measured for a frequency sweep from 100 Hz to 100 000 Hz. A dc bias of 0 V and an ac signal of 90 mVrms was used based on studies reporting ideal conditions for minimizing noise and optimizing the reproducibility of PSi impedance sensors [8]. The impedance response of the PSi sensors in the presence of organic solvents was tested both as a function of time (at 100 kHz) and as a function of frequency, for comparison of complex impedance plots (Nyquist plots). For each response test, 10 µl of an organic solvent was placed on the PSi interface. The volume was chosen to balance optimizing both ease of handling and time of evaporation (corresponding to the duration of sensor response). To collect a complete complex impedance spectra across the entire frequency range of interest before evaporation of the solvent, the impedance was collected at 8 equally logarithmically spaced increments of frequency. This allows for a complete picture of the the complex impedance to be collected in under 10 s, which is less than the time of evaporation for the organic solvents used in this study. The surface morphology of the PSi sensors used in this study were characterized by SEM (Zeiss Ultra60 FE-SEM) using an In-lens SE detector.

7.1 Equivalent circuit model

The response mechanism of PSi sensors to liquid organic solvents is a combination of several mechanisms. At a surface/liquid interface, electrostatic equilibrium must be reached. This is accomplished through the formation of an electrical double layer consisting of the space-charge region of the semiconductor and the Gouy layer in the electrolyte solution [123]. Within the Gouy layer, the adsorbed species on the

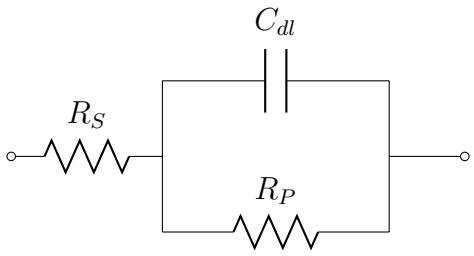

Figure 7.1: Schematic diagram of a Simplified Randles Cell.

semiconductor surface form the Stern layer and nearby ions form the Diffuse layer [123]. As a result of the adsorbed molecules forming a double layer, the space-charge region of the semiconductor must compensate the charge to reach equilibrium [8,123]. The changes to the space-charge region then modulate the carrier concentration within the PSi sensor as well as the width of the conducting channel. In order to study the impedance response of the PSi sensors to organic solvents, these physical features can be explored through the correlation with an equivalent circuit model.

The development of equivalent circuit models for the PSi sensors began with a consideration of the Simplified Randles Cell equivalent circuit, shown in Figure 7.1. The Randles equivalent circuit, which is a commonly used equivalent circuit for describing electrochemical cells, produces a simple semicircle Nyquist plot similar to that of the PSi sensors [73,123,153]. When used to describe electrochemical cells, R_S is the solution resistance, R_P is the charge transfer/polarization resistance, and C_{dl} describes the double layer capacitance [73,153]. For the PSi sensors, R_S is considered the resistance of the electrical contacts, R_P represents the charge-transfer resistance to move carriers through the PSi sensor, and C_{dl} is still considered a double-layer capacitance [123]. While the Simplified Randles cell equivalent circuit is a convenient first-pass model due to its simplicity and the clear physical interpretation of circuit elements, the limited parameters are unable to accurately model the experimental data.

Figure 7.2a shows the Nyquist plot ($\mathrm{Re}\, Z$ versus $\mathrm{Im}\, Z$) of the impedance spectra

for an n-type PSi sensor in dry air at atmospheric temperature and pressure and the equivalent circuit model used to simulate the experimental data collected for n-type PSi sensors. The total impedance of the equivalent circuit model, which features a distributed capacitance element (DE), is given by,

$$Z_{\mathrm{n-type}} = R_S + \left(\frac{1}{R_1} + C(j\omega)^P\right)^{-1} . \tag{7.1}$$

$Z_{DE} = 1/[C(j\omega)^P]$ is the impedance across the distributed capacitance element of where P is an empirical factor that can range from 0 to 1 and $\omega = 2\pi f$ is the angular frequency, where f, the linear frequency, is measured in Hz. Here, the distributed capacitance element is a constant phase element (CPE), where the impedance Z_{DE} has a constant phase angle in the complex plane and the exponent, P, determines this angle. Physically, the empirical factor, P, describes the deviation from an ideal perfectly smooth electrode ($P = 0.5$ for an ideal porous electrode and $P = 1$ for a perfectly smooth electrode) [123]. Table 7.2 lists the values of the equivalent circuit model that provides the simulated data shown in Figure 7.2a. The simulated equivalent circuit model was fit to the experimental data by a non-linear regression model using the method of least squares. The minimized sum of squares value, Q, for the n-type equivalent circuit model is 1.1636. For comparison with other models, the standard deviation of error is $\sigma = \sqrt{Q/(n-p)} = 0.037$, where the number of data points is $n = 1000$, and the number of parameters is $p = 4$.

In contrast, Figure 7.2b shows the Nyquist plot of the impedance spectra for a p-type PSi sensor in dry air at atmospheric temperature and pressure and the equivalent circuit used to simulate the experimental data collected for p-type PSi sensors. The total impedance of the equivalent circuit model, which features a series of two parallel capacitor and resistor elements, is given by,

$$\widetilde{Z}_{\mathrm{p-type}} = R_S + \left(\frac{1}{R_1} + j\omega C_1\right)^{-1} + \left(\frac{1}{R_2} + j\omega C_2\right)^{-1} . \tag{7.2}$$

Table 7.3 lists the values of the equivalent circuit model that provides the simulated

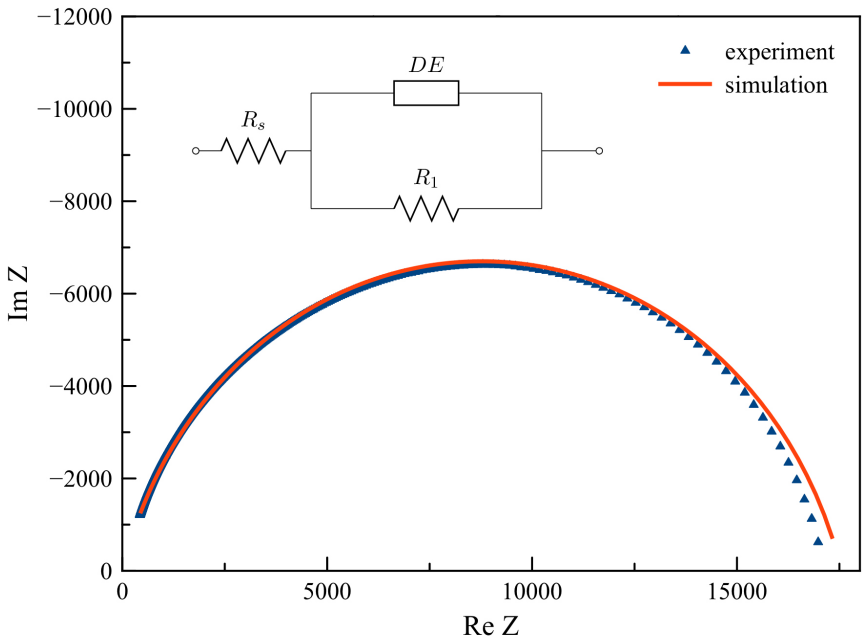

(a)

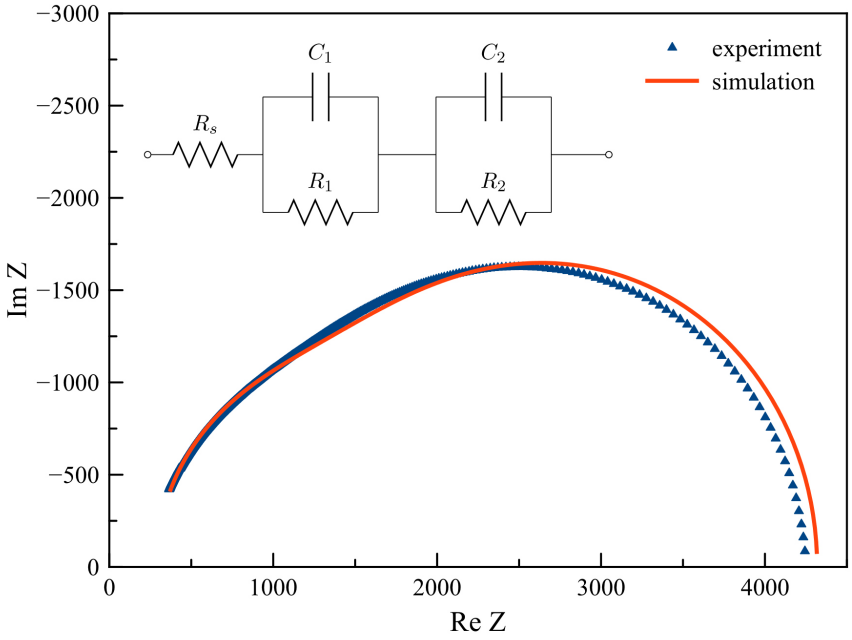

(b)

Figure 7.2: Nyquist plot of (a) an n-type PSi sensor and (b) a p-type PSi sensor in dry air at atmospheric temperature and pressure comparing experimental data (blue) to simulated data (red).The equivalent circuit model shown was used to provide the simulated data (red).

Table 7.2: Parameter values for the equivalent circuit model describing an n-type PSi sensor in dry air at atmospheric temperature and pressure. The minimized sum of squares for this model is $Q = 1.1636$ and the standard deviation of error is $\sigma = 0.037$.

Element	Value	Unit
R_S	1×10^{-7}	Ω
DE	CPE type 1	
DE-C	1.138×10^{-8}	F
DE-P	0.83016	
R_1	17 554	Ω

Table 7.3: Parameter values for the equivalent circuit model describing a p-type PSi sensor in dry air at atmospheric temperature and pressure. The minimized sum of squares for this model is $Q = 0.6844$ and the standard deviation of error is $\sigma = 0.022$.

Element	Value	Unit
R_S	287.4	Ω
C_1	5.2961×10^{-9}	F
R_1	1103	Ω
C_2	1.2377×10^{-8}	F
R_2	2928	Ω

data shown in Figure 7.2b, with a minimized sum of squares value of $Q = 0.6844$ and the standard deviation of error is $\sigma = 0.022$.

The equivalent circuit models for the PSi sensors, and in particular the differences between the n-type and p-type models, can be explained through an analysis of the porous structure. Figure 7.3 shows the differences in the porous structure of the n-type and p-type PSi sensors used in this study. The n-type PSi sensors feature densely packed pores with diameters of approximately 0.4 µm (Figure 7.3a). The distributed capacitance element in the n-type equivalent circuit model could, therefore, represent the distribution of slightly varying micropores across the PSi interface. In contrast, the p-type PSi structure has widely spaced micrometer-diameter pores and a nanoporous coating (Figure 7.3b). Correlating with the proposed equivalent circuit, each of the parallel capacitance and resistance elements could represent each of the

hybrid-porous structure regimes; one component set represents the parallel capacitance and resistance of the nanoporous coating in series with the parallel capacitance and resistance of the microporous structure.

7.2 Signatures of organic solvents

7.2.1 Complex impedance behavior

Organic solvents have a clear effect on the impedance spectra of the PSi sensors. Figure 7.4 illustrates typical changes to the Nyquist plots of n-type sensors in the presence of various *polar* organic solvents. A simulation of the equivalent circuit for the n-type PSi sensors was fit to the experimentally collected impedance data in both dry conditions and upon application of the organic solvents. To control for small variations in temperature and humidity, the sensor was tested in dry conditions and then under solvent conditions within 1 h for comparison for each solvent test.

Figure 7.5 demonstrates the typical changes in both the real and imaginary impedance after exposure to non-polar organic solvents. Again, the equivalent circuit was fit to the experimentally collected impedance data in dry conditions and in the presence of organic solvents. Table 7.4 lists the changes to each circuit element of the equivalent circuit model due to each liquid chemical species. Of particular note is the clear trend in the diameter of the complex Nyquist curve semicircle to decrease upon exposure to organic molecules with dipole moments above 1.66 D or decrease upon exposure to organic molecules with dipole moments of 1.15 D and less.

The increase or decrease in the complex Nyquist plot semicircle corresponds to an increase or decrease in the value for the charge transfer or polarization resistance, R_1, as shown in Table 7.4. The empirical factor, P, experiences very little change with changing environments and the contact resistance. R_S is completely unaffected by the presence of the organic solvents. This is consistent with the results of other impedance studies of PSi organic solvent sensors [8, 123]. Often, the assumption is

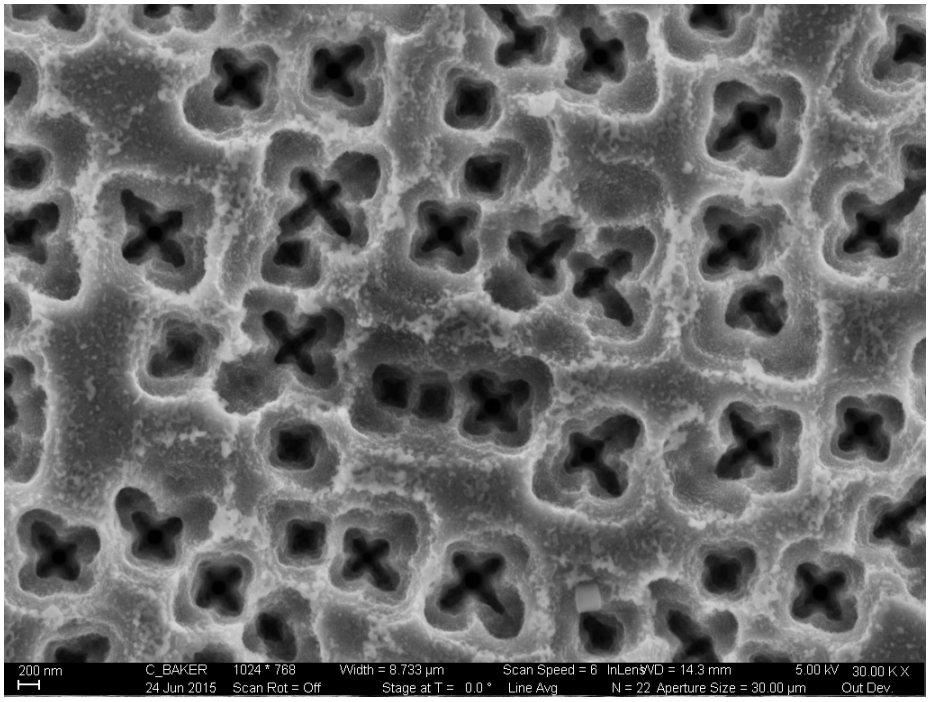

(a)

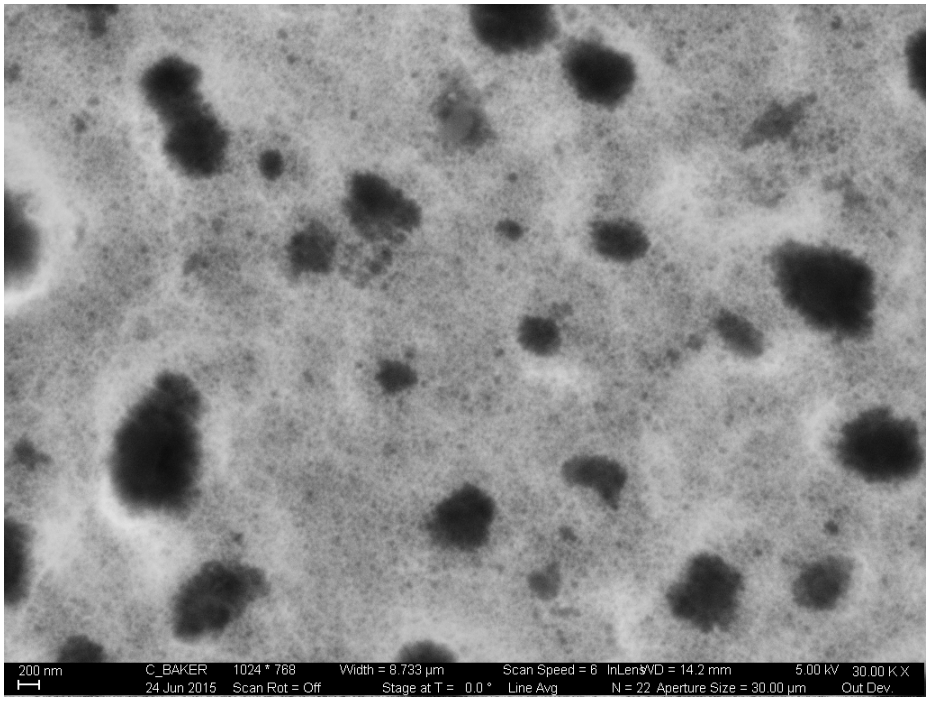

(b)

Figure 7.3: SEM micrographs of a top view of (a) n-type and (b) p-type PSi sensors used in this study at 30 kX magnification.

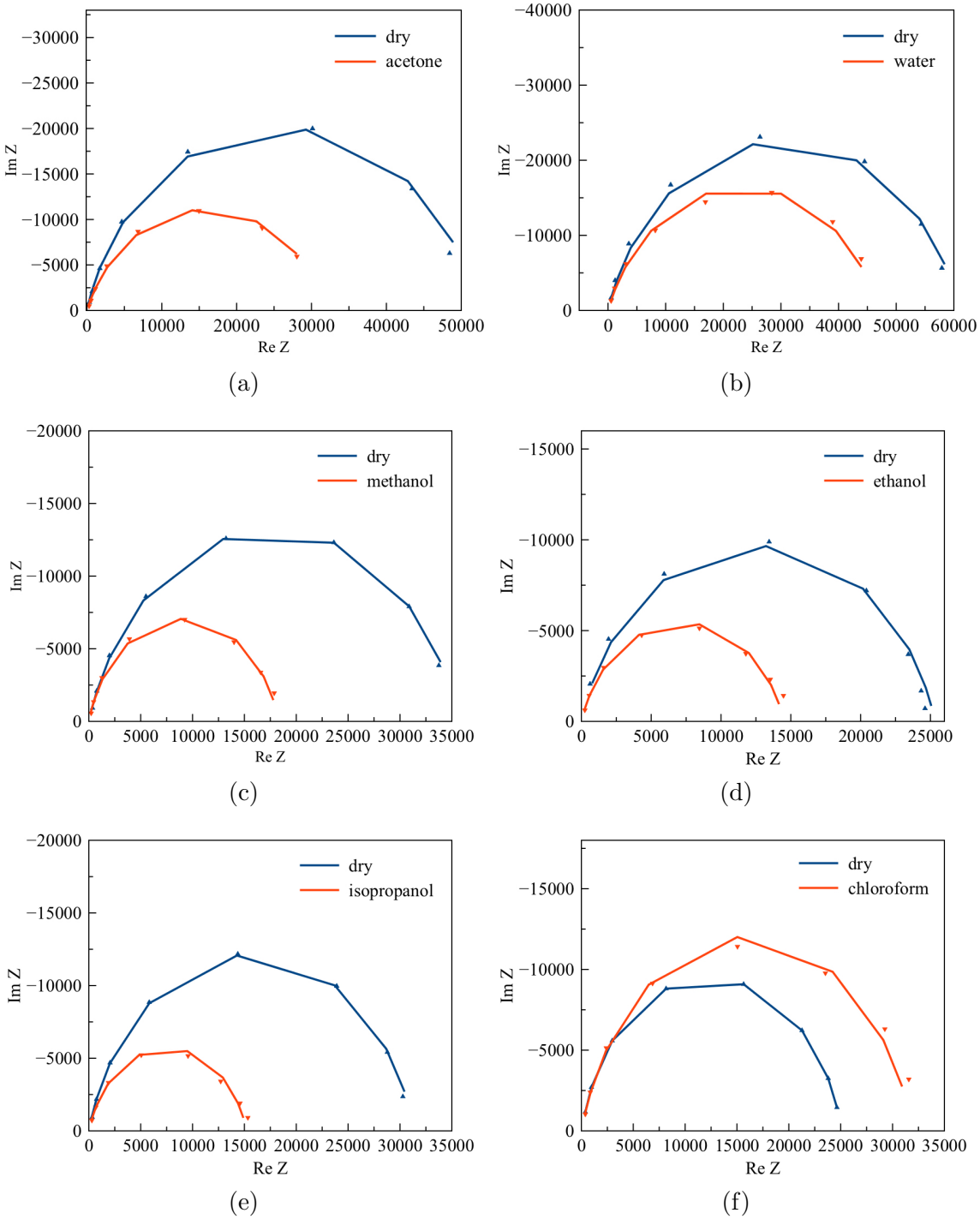

Figure 7.4: Complex impedance plots (Nyquist plots) of n-type PSi sensors comparing dry conditions (blue) and upon exposure to various *polar* organic solvents (orange). The experimental data is shown as triangle markers and the fitted equivalent circuit simulation is shown as a solid line.

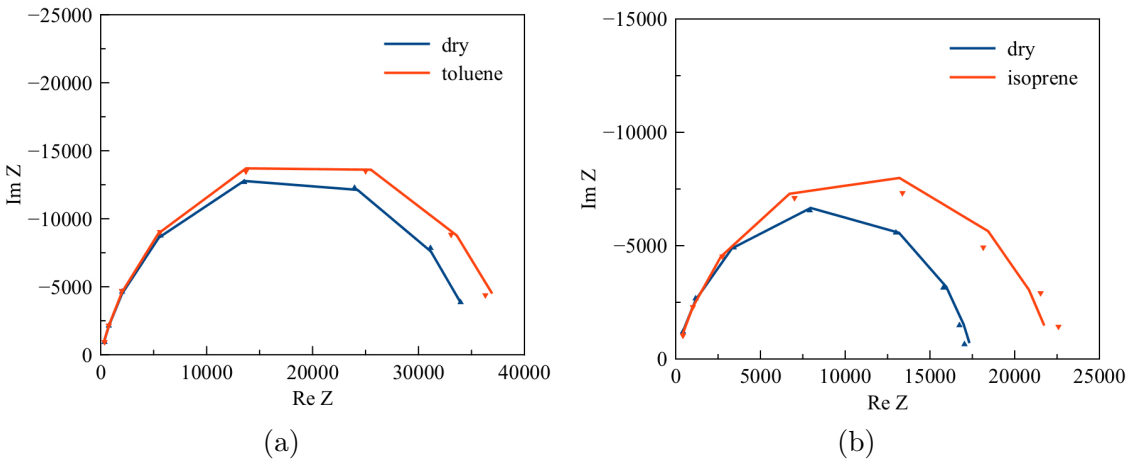

Figure 7.5: Complex impedance plots (Nyquist plots) of n-type PSi sensors comparing dry conditions (blue) and upon exposure to various *non-polar* organic solvents (orange). The experimental data is shown as triangle markers and the fitted equivalent circuit simulation is shown as a solid line.

made that the metal-semiconductor contact junction does not affect the PSi sensor response and remains constant [8]. With the exception of the interaction with toluene, the capacitance of the distributed capacitance constant phase element is increased upon exposure to the organic solvents. A table of the values of the equivalent circuit elements corresponding to the complex Nyquist curves for the PSi sensors is provided in Appendix A.

In complement to the study of the effects on n-type systems, the typical interactions of polar and non-polar organic solvents on p-type PSi interfaces are presented in Figures 7.6 and 7.7 respectively. Here the increase or decrease in the radius of the complex Nyquist diagram is represented by an increase or decrease of the two parallel resistors (Figure 7.2b). The calculated changes of the values for each equivalent circuit element is provided in Table 7.5. For all cases, the simulated parameter values for the parallel equivalent circuit elements R_2 and C_2 were larger than R_1 and C_1 (for example, see Table 7.3). With the exception of toluene, which only minimally affected the equivalent circuit values of the p-type PSi sensor, the magnitude of the change for R_2 and C_2 was also notably larger than the magnitude of the change for

Table 7.4: Changes in equivalent circuit elements for n-type PSi sensors upon application of organic solvents.

Solvent	R_S	DE-C	DE-P	R_1
Acetone	0 %	279 %	−7 %	−39 %
Water	0 %	111 %	−4 %	−23 %
Methanol	0 %	10 %	3 %	−49 %
Ethanol	0 %	273 %	−1 %	−43 %
Isopropanol	0 %	56 %	−2 %	−52 %
Chloroform	0 %	63 %	−3 %	30 %
Toluene	0 %	−14 %	1 %	6 %
Isoprene	0 %	59 %	−3 %	27 %

Table 7.5: Changes in equivalent circuit elements for p-type PSi sensors upon application of organic solvents.

Solvent	R_S	C_1	R_1	C_2	R_2
Acetone	0 %	111 %	−34 %	143 %	42 %
Water	0 %	3 %	−14 %	14 %	−18 %
Methanol	0 %	33 %	4 %	536 %	−65 %
Ethanol	0 %	60 %	−37 %	125 %	−59 %
Isopropanol	0 %	28 %	−25 %	143 %	−51 %
Chloroform	0 %	−1 %	18 %	11 %	26 %
Toluene	0 %	1 %	3 %	8 %	3 %
Isoprene	0 %	−15 %	19 %	−9 %	83 %

R_1 and C_1. Therefore, for the purposes of the present analysis, the focus will lie with the changes to the values of equivalent circuit elements R_2 and C_2.

Interestingly, all of the organic solvents induced changes to the complex Nyquist diagram for the p-type system of equal sign and comparable magnitude to those changes experienced by the n-type PSi sensors. The exception to this trend, however, is acetone. Interaction of the p-type PSi sensor with acetone expanded the Nyquist diagram in the low frequency range (right side of the complex plot) and appeared to shrink the Nyquist diagram in the high frequency range (left side of the complex plot). This phenomenon is shown in Table 7.5, and is explored further in Figure 7.8, which

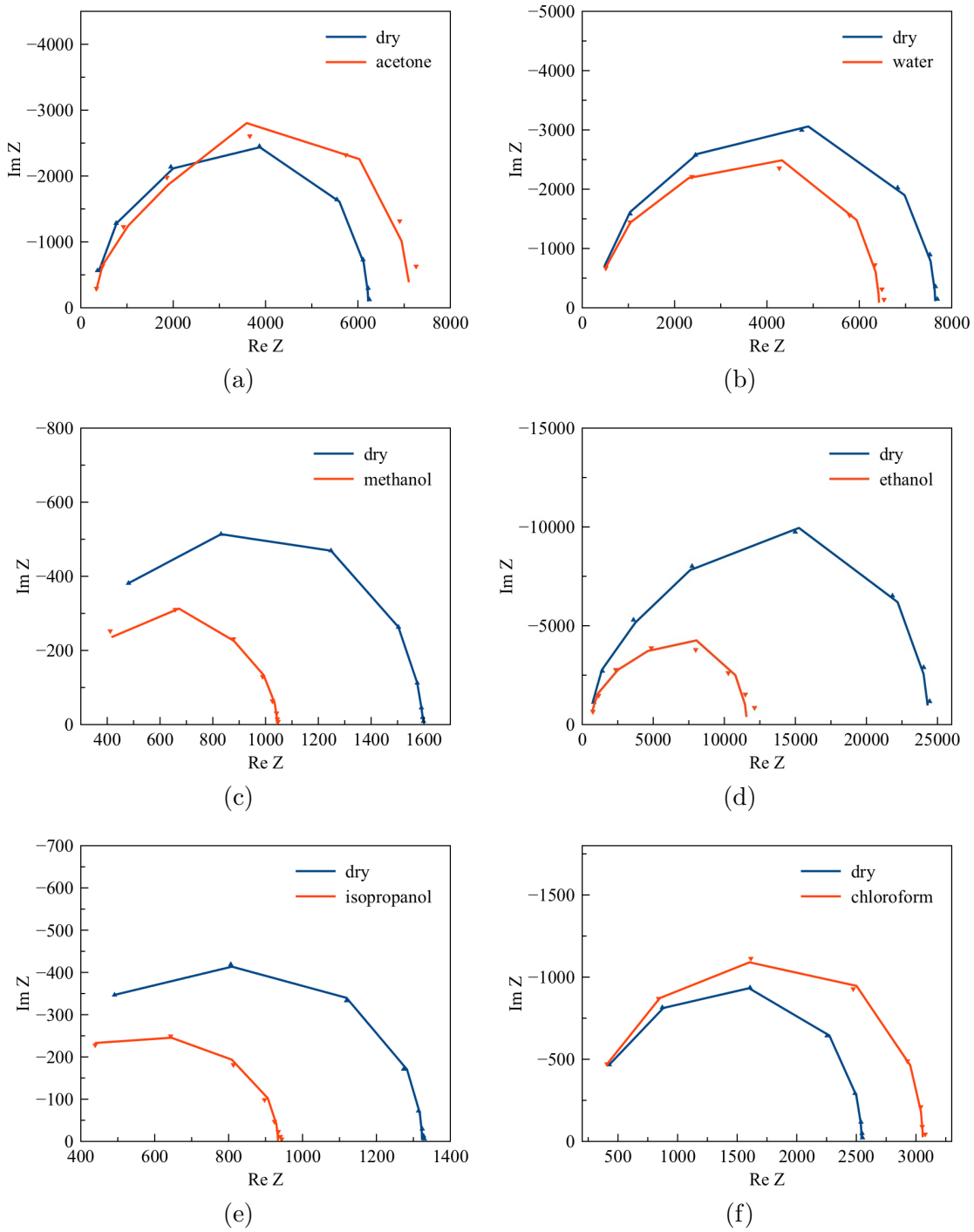

Figure 7.6: Complex impedance plots (Nyquist plots) of p-type PSi sensors comparing dry conditions (blue) and upon exposure to various *polar* organic solvents (orange). The experimental data is shown as triangle markers and the fitted equivalent circuit simulation is shown as a solid line.

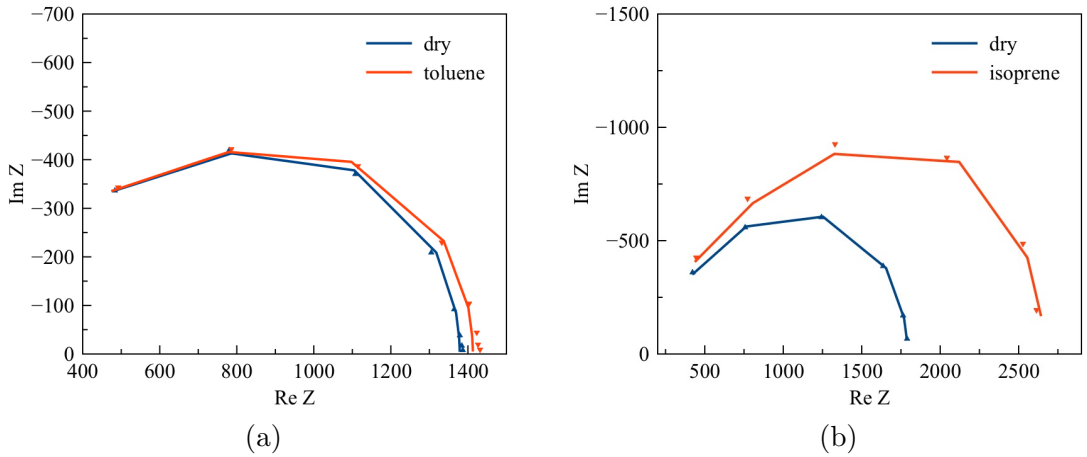

Figure 7.7: Complex impedance plots (Nyquist plots) of p-type PSi sensors comparing dry conditions (blue) and upon exposure to various *non-polar* organic solvents (orange). The experimental data is shown as triangle markers and the fitted equivalent circuit simulation is shown as a solid line.

illustrates the changes to the real and imaginary parts of impedance as a function of time at high and low frequencies. The low frequency data points are heavily influenced by the value of R_2, which increases in the presence of acetone, in contrast to the n-type systems. The high frequency data points are heavily influenced by the value of R_1, which decreases in the presence of acetone, similar to the n-type systems. The unique response to acetone is possibly due to the much larger dipole moment in comparison with the other organic solvents. Here, the strength of the dipole moment of acetone may induce a local field on the PSi layer, leading to an injection of electrons into the conducting channel. As p-type and n-type systems are characterized by their opposite charge carriers (electronic holes versus electrons), this would then represent a decrease in resistance of the n-type PSi sensors, but an increase in resistance for the p-type PSi sensors.

7.2.2 Real-time capacitance and conductance

The real-time changes to the capacitance and conductance of the PSi sensors were calculated from the complex impedance collected as a function of time. Other groups

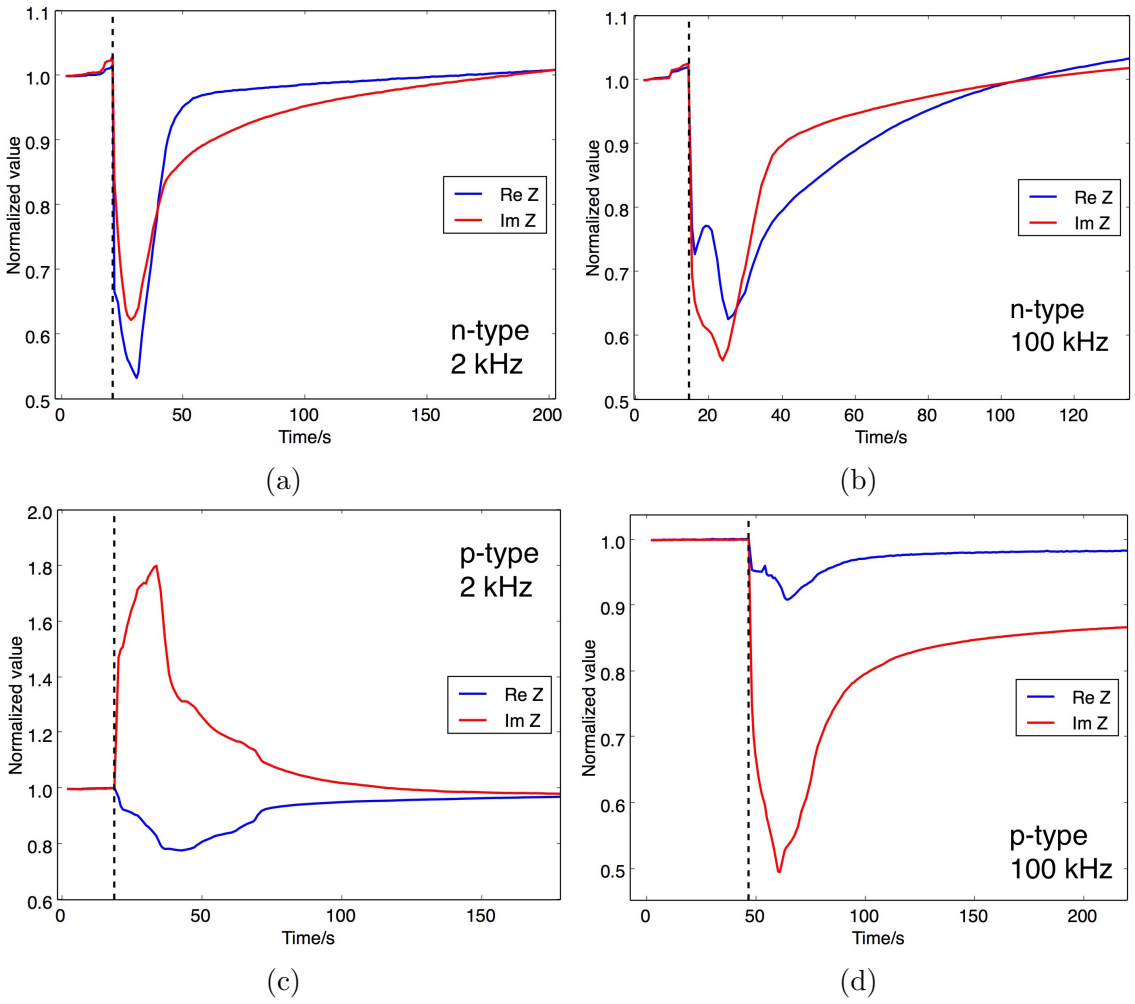

Figure 7.8: The real (blue) and imaginary (red) part of impedance of (a,b) n-type and (c,d) p-type PSi sensors upon exposure to acetone at (a,c) 2 kHz and (b,d) 100 kHz. The vertical dashed line indicated the time at which the solvent was dropped onto the PSi sensor.

have studied the PSi response to liquid organic solvents through an examination of changes to a parallel conductance and capacitance, without correlating their results to an equivalent circuit [8,111]. These studies have reported contrasting results, possibly due to not considering the capacitance and conductance related to actual equivalent circuit elements. This discussion will look at the capacitance and conductance calculated from the equivalent circuit models defined in this chapter.

The complex impedance was collected at 100 kHz, which corresponds to an enhancement of the capacitive behavior of the sensor [8]. This frequency was also chosen in order to compare results to previous studies in the literature [8, 111]. Figures 7.9 and 7.10 illustrate the real-time capacitance and conductance changes for n-type PSi sensors exposed to polar and non-polar organic solvents, respectively. The capacitance and conductance for the n-type system were calculated from the real and imaginary impedance values collected by the impedance analyzer through the relation,

$$Z_{\mathrm{n-type}} = \mathrm{Re}\, Z + j\, \mathrm{Im}\, Z = R_S + \frac{1}{G + C(j\omega)^P}\,, \tag{7.3}$$

where $G = 1/R_1$. Therefore, solving for capacitance and conductance as functions of $\mathrm{Re}\, Z$ and $\mathrm{Im}\, Z$, where $j^P = \cos(\frac{\pi P}{2}) + j\sin(\frac{\pi P}{2})$, provides,

$$C = \frac{-\,\mathrm{Im}\, Z / \left(\sin(\frac{\pi P}{2})\omega^P\right)}{\left(\mathrm{Re}\, Z - R_S\right)^2 + (\mathrm{Im}\, Z)^2} \tag{7.4}$$

$$G = \frac{\mathrm{Re}\, Z - R_S}{\left(\mathrm{Re}\, Z - R_S\right)^2 + (\mathrm{Im}\, Z)^2} - \cos\left(\frac{\pi P}{2}\right) C\,. \tag{7.5}$$

As shown in Table 7.4, R_S is unaffected by the presence of the organic solvents and P is only very slightly affected. Therefore, both R_S and P were treated as constants. As can be seen in Equation 7.8, the conductance can actually be greatly affected by the empirical exponent, P. For example, for a value of $P < 1$, the second term in Equation 7.8 is non-zero and can therefore reduce the calculated value for G and even change its sign. Therefore, the equivalent circuit is critical for properly establishing changes to the conductance and capacitance for analysis.

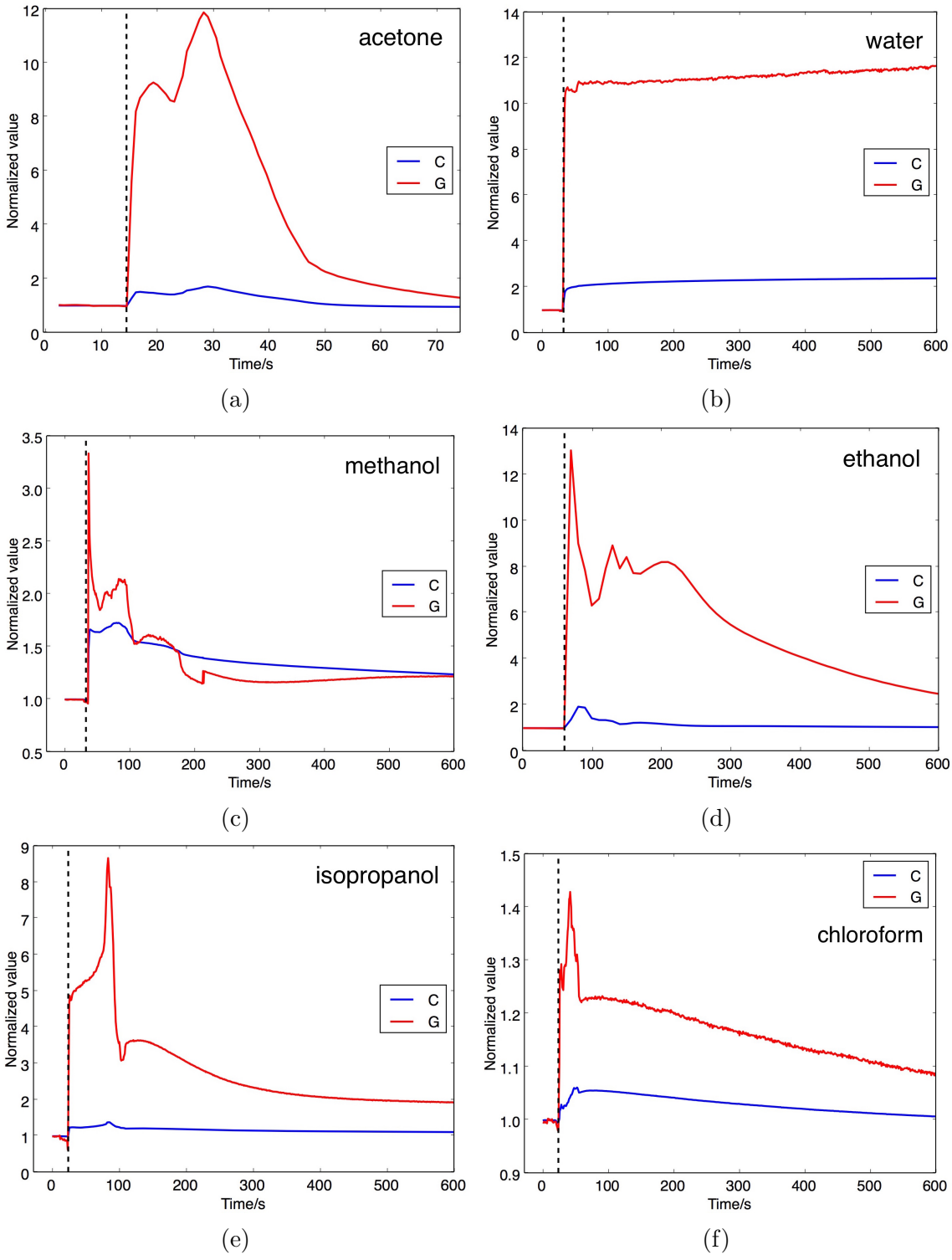

Figure 7.9: Conductance (red) and capacitance (blue) of n-type PSi sensors upon exposure to various polar organic solvents. The vertical dashed line indicated the time at which the solvent was dropped onto the PSi sensor.

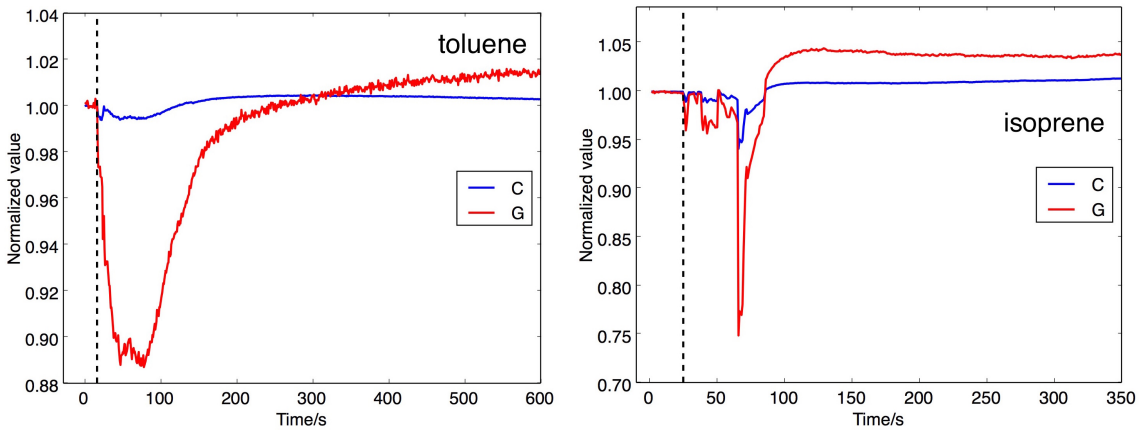

(a) (b)

Figure 7.10: Conductance (red) and capacitance (blue) of n-type PSi sensors upon exposure to various non-polar organic solvents. The vertical dashed line indicated the time at which the solvent was dropped onto the PSi sensor.

In contrast, for the p-type systems, while the changes to the values of one set of parallel resistance and capacitance was larger than the other set, the smaller changes were not negligible (Table 7.5). As a result, the individual changes as a function of time were not separable. Therefore, for the purpose of comparison to the n-type system and the results of previous studies, the conductance and capacitance of the p-type systems were calculated from a simple Randles circuit with a contact resistance, R_S in series with a parallel C-G circuit, where the total impedance is given by,

$$Z_{\mathrm{n-type}} = \mathrm{Re}\, Z + j\, \mathrm{Im}\, Z = R_S + \frac{1}{G + Cj\omega}\,. \tag{7.6}$$

The capacitance and conductance are then given by,

$$C = \frac{-\,\mathrm{Im}\, Z/\omega}{(\mathrm{Re}\, Z - R_S)^2 + (\mathrm{Im}\, Z)^2} \tag{7.7}$$

$$G = \frac{\mathrm{Re}\, Z - R_S}{(\mathrm{Re}\, Z - R_S)^2 + (\mathrm{Im}\, Z)^2}\,. \tag{7.8}$$

Figure 7.11 shows the calculated real-time conductance and capacitance of p-type PSi sensors in the presence of polar organic solvents. Figure 7.12 shows the conductance and capacitance in the presence of non-polar organic solvents.

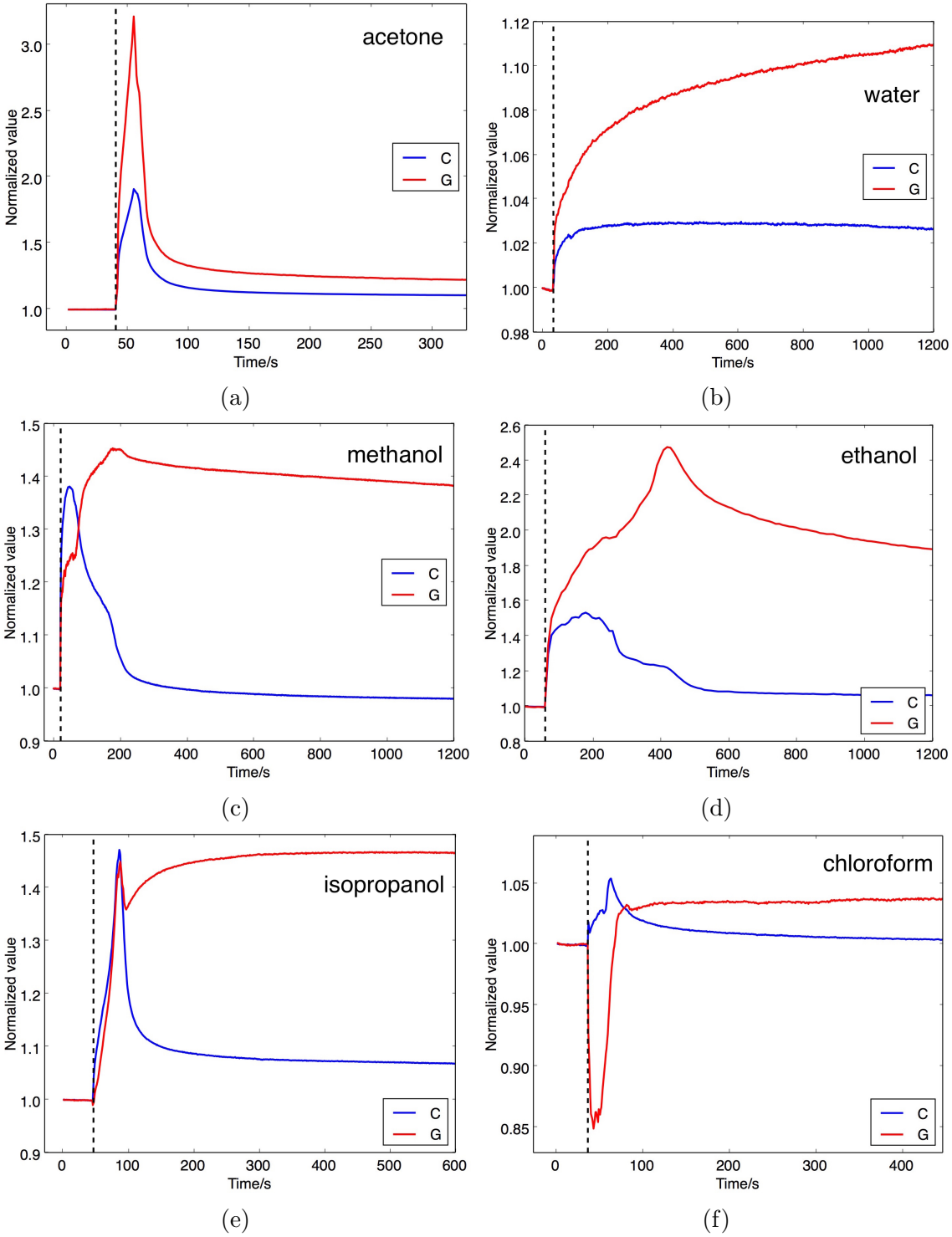

Figure 7.11: Conductance (red) and capacitance (blue) of p-type PSi sensors upon exposure to various polar organic solvents. The vertical dashed line indicated the time at which the solvent was dropped onto the PSi sensor.

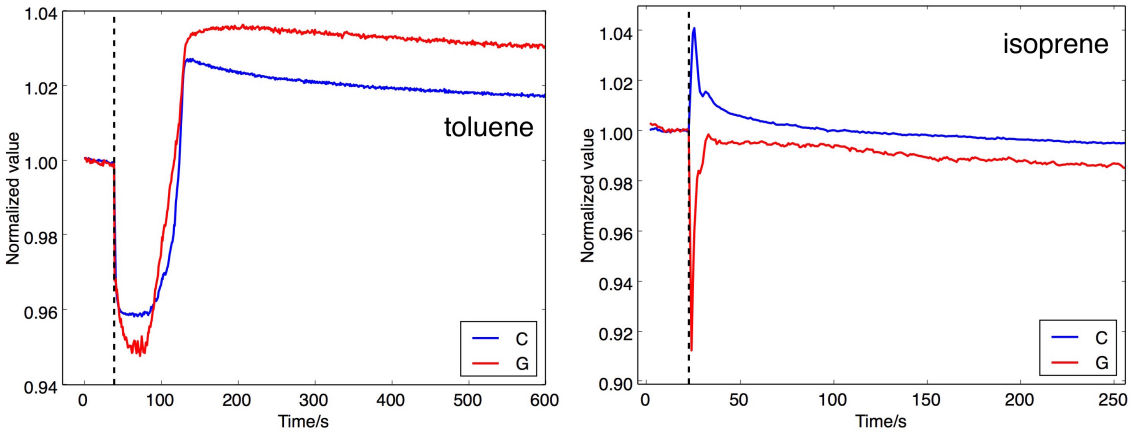

Figure 7.12: Conductance (red) and capacitance (blue) of p-type PSi sensors upon exposure to various non-polar organic solvents. The vertical dashed line indicated the time at which the solvent was dropped onto the PSi sensor.

The conductivity and capacitance of the PSi sensors are influenced by several different parameters, rather than one single effect [231]. While at first a separation of polar versus non-polar effects would seem intuitive, the behavior of chloroform (and acetone for p-type systems) dispels that theory. Instead, an examination of a combination of dipole moment and polarizability provides insight into interface interactions. Depending on the intensity of the dipole moment of the organic solvent analyte, different response mechanisms are dominant. The organic molecule dipole moment produces a local field, which is dependent on the value of the dipole moment, the distance from the interface and the orientation of the molecule [135]. This local field can shift the energy position of the surface states, which subsequently modifies the space-charge region (SCR) of the PSi interface (for full discussion, see Chapter 2, section 2.2.2) [231]. The modification of the space charge region modulates the energy distribution of the density of states of the bulk Si. The Fermi level or chemical potential shifts relative to the conduction band thus shifting the carrier concentration [231], which is transduced as a change in conductance. The modulation of the surface states also produces shifts in the observed double layer capacitance.

For organic solvents of dipole moments of 1.66 D and larger, the dominant effect is the dipole moment. This is seen as an increase of the conductance and capacitance for those organic solvents with moderate to large dipole moments (Figures 7.9 and 7.11). For organic solvents with low dipole moments, the polarizability must also be considered to explain the response. As seen in Table 7.1, the organic solvents with the lowest dipole moments also have the highest polarizability, α. The electric field within the PSi framework can create an induced dipole moment on the organic molecules. This induced dipole moment is then able to affect the PSi interface in the same way as the permanent dipole moment of the other organic solvents. However, the influence of the induced dipole moment is opposite in sign to the permanent dipole moments, as represented by the negative change in the conductance and capacitance. This results as either the induced dipole moment has opposite sign or the orientation is such that produces this effect. Chloroform and isoprene represent borderline cases. For chloroform, the change in capacitance, while positive, is very small for both p-type and n-type systems. However, the affected change in conductance is negative for the p-type systems at 100 kHz. Similarly, the total dipole moment of isoprene (permanent plus induced), which has a similar polarizability to chloroform, is on the border of producing a positive or negative change.

In the case of acetone, which features both a large dipole moment and a large polarizability, this balancing effect of permanent and induced dipole moment may be significant. As shown in Figure 7.8, the direction of change for the imaginary part of the impedance across the p-type sensor is opposite at low and high frequencies. Shown in Figure 7.13, the sign of the conductance change is opposite at 2 kHz versus 100 kHz. Therefore, the electric field at high and low frequencies is different, producing a different magnitude for the induced dipole moment. Thus, the total dipole moment of the acetone molecules could be different enough to produce these opposite effects.

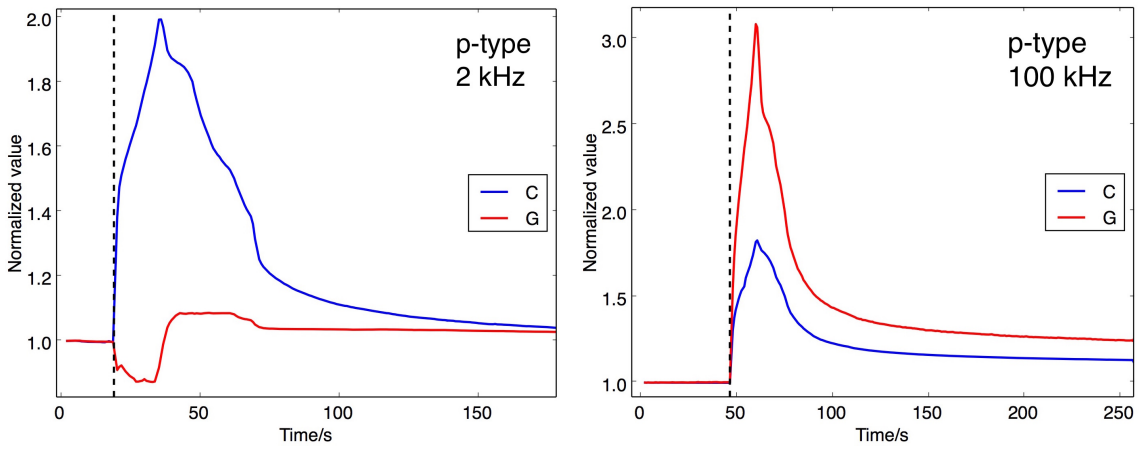

(a) (b)

Figure 7.13: The capacitance (blue) and conductance (red) of a p-type PSi sensor upon exposure to acetone at (a) 2 kHz and (b) 100 kHz. The vertical dashed line indicated the time at which the solvent was dropped onto the PSi sensor.

7.3 Influence of nanostructure metal oxide depositions

Nanostructure modification of PSi interfaces has been shown to be an effective method to adjust the sensor response to a range of chemical analytes for the purpose of developing an array of uniquely interacting interfaces [13, 85, 86, 93, 167, 174, 199, 278]. To further explore the dipole interactions of the PSi sensors with organic solvents, interactions were compared for PSi sensors treated with nanostructured metal oxide depositions. Figure 7.14 illustrates the effect of Au_xO and SnO_x nanostructure depositions on the complex Nyquist diagram for p-type PSi sensors under dry conditions. The nanostructures are prepared and deposited to the PSi interface as described in Chapter 3, section 3.1.6.

Schmeißer et al. [232] explain that nanoscale particles, in contrast to their bulk counterparts, feature unique properties. In particular, nanoparticles with a metallic core and oxide shell have large dipole moments. These metal clusters with oxide coatings can modify the properties of substrates they are in contact with by inducing a dipole moment at the interface [232]. The metal oxide nanoparticles used in this study are not the same core-shell structure as those investigated by Schmeißer et

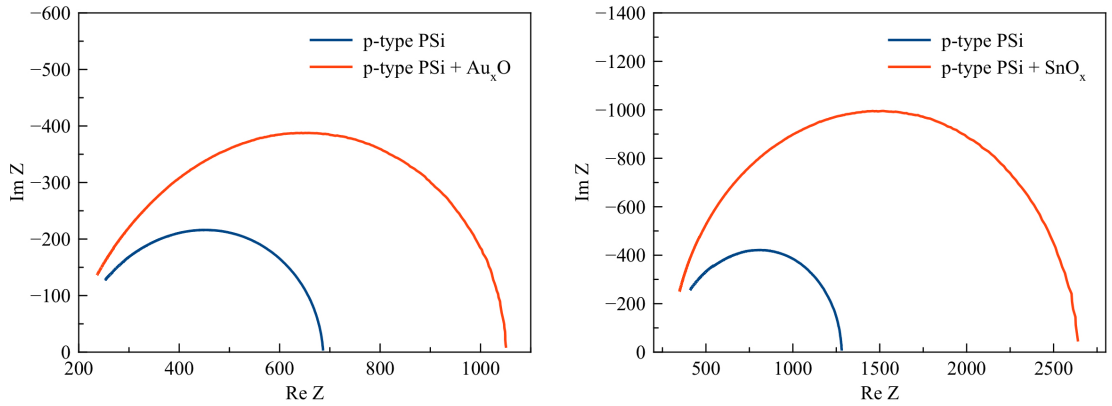

Figure 7.14: Complex impedance plots (Nyquist plots) of p-type PSi sensors in dry conditions comparing before and after decoration with (a) Au_xO nanostructures and (b) SnO_x nanostructures.

al. [232], but may exhibit similar properties.

As shown in Figure 7.14, the metal oxide nanostructures greatly affect the complex impedance. However, it should be noted that this effect is size dependent limited to nanoscale particles [85, 86]. Therefore, the deposition of the metal oxide nanostructures must be at a level low enough to produce such particles. Husairi et al. [123] investigated the influence of a layer of ZnO nanostructures on the interactions of a PSi interface with liquid ethanol. Through an analysis of the complex impedance curves and complementary equivalent circuit elements, Husairi et al. [123] demonstrated that the ZnO nanostructures increased both the real and imaginary parts of the complex impedance. They explain that the ZnO layer acted as an additional capacitive layer storing additional charge and increasing the value of the double-layer capacitance element in the equivalent circuit. The increase in the the real part of impedance was explained as resulting from the oxide layer forming a barrier for charge and mass transfer [123]. They also determined that the effect was dependent on the ZnO layer thickness.

Figure 7.15 demonstrates the effect of Au_xO and SnO_x nanostructure depositions on the interaction with the polar organic molecule ethanol. Here, the significant effect

of the dipole moment interactions of the metal oxide nanostructure depositions can be seen. The treatment of an n-type PSi sensor with Au_xO not only expanded the radius of the complex Nyquist curve but enhanced the response to ethanol: the change in charge transfer/polarization resistance, R_1, upon exposure to ethanol was increased by a factor of 1.5. This effect is even more pronounced with the SnO_x decorated n-type PSi sensor, where the change in charge transfer/polarization resistance, R_1, upon exposure to ethanol was increased by a factor of 3. The ratio of R_1 in the presence of ethanol to R_1 in dry conditions decreased from 0.57 to 0.38 upon treatment with Au_xO and from 0.76 to 0.39 upon treatment with SnO_x. Figure 7.16 demonstrates the effect of Au_xO and SnO_x nanostructure depositions on the interaction with the polar organic molecules isopropanol and acetone. Here, the ratio of R_1 in the presence of the solvent to R_1 in dry conditions was modified upon deposition of metal oxide nanostructures. The enhanced response upon nanostructure decoration can be seen, a greater effect produced by the SnO_x deposition.

In contrast, the metal oxide nanostructure depositions have little effect on the response to organic solvents with small dipole moments, such as toluene. Figure 7.17 illustrates that while the metal oxide nanostructure depositions expanded the complex Nyquist diagrams, the amount by which the equivalent circuit elements changed was virtually the same before and after metal oxide treatment. For example, the ratio of R_1 in the presence of toluene to R_1 in dry conditions changed from 1.06 to 1.07 for upon treatment with Au_xO and from 1.09 to 1.15 upon treatment with SnO_x. Therefore, the dipole interactions of the metal oxide nanostructure depositions appear to enhance the response only to those organic solvents with dipole moments above 1.15 D.

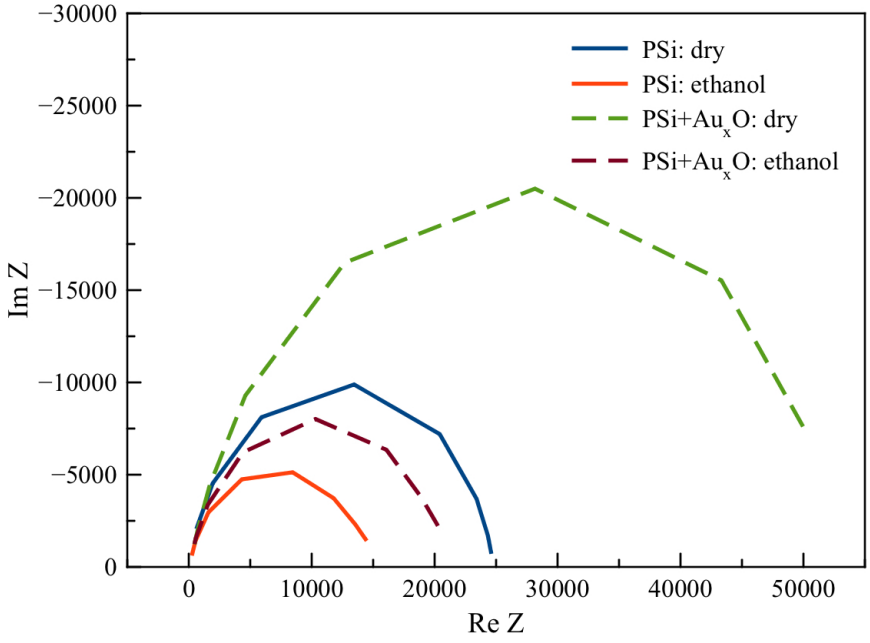

(a)

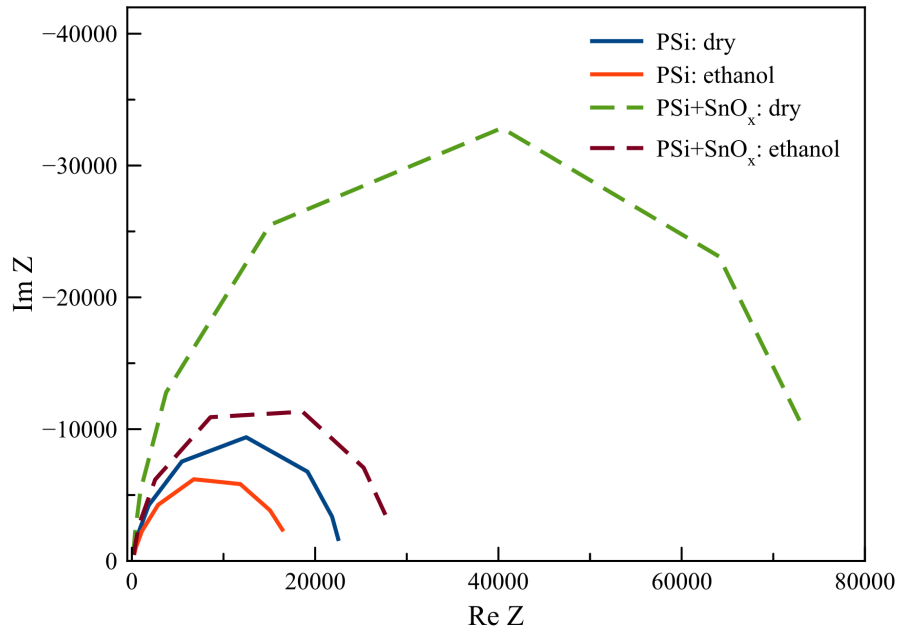

(b)

Figure 7.15: Complex impedance plots (Nyquist plots) of n-type PSi sensors in dry conditions and in the presence of ethanol, comparing before and after decoration with (a) Au_xO nanostructures and (b) SnO_x nanostructures.

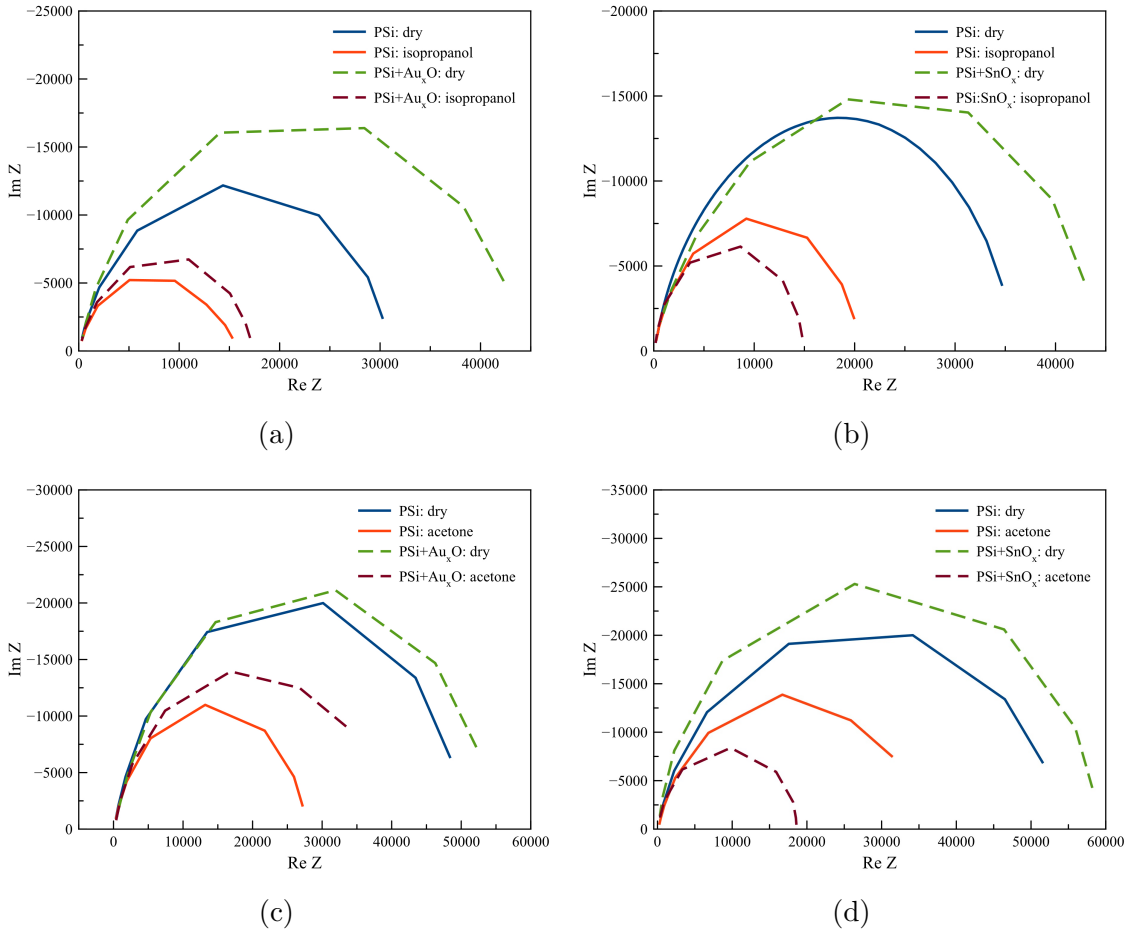

Figure 7.16: Complex impedance plots (Nyquist plots) of n-type PSi sensors in dry conditions and in the presence of (a,b) isopropanol and (c,d) acetone, comparing before and after decoration with (a,c) Au_xO nanostructures and (b,d) SnO_x nanostructures.

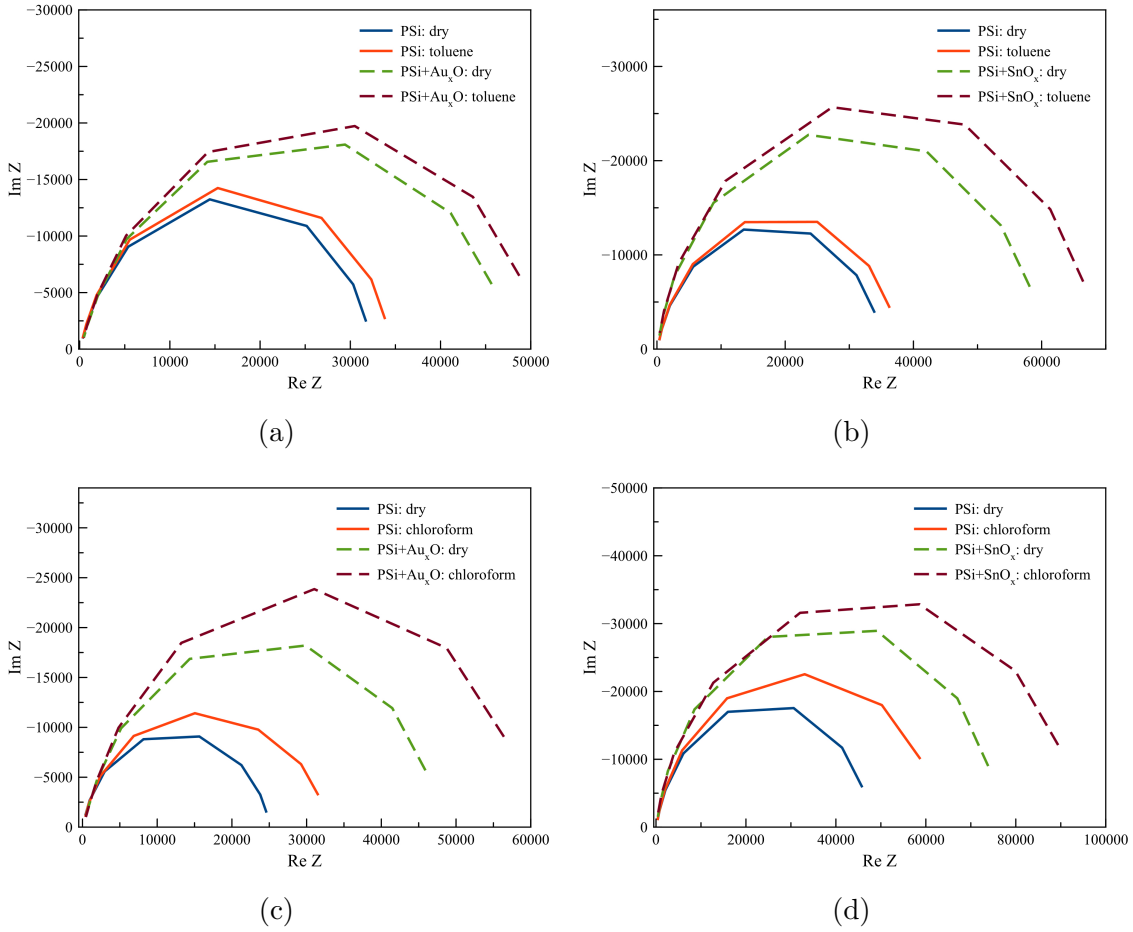

Figure 7.17: Complex impedance plots (Nyquist plots) of n-type PSi sensors in dry conditions and in the presence of (a,b) toluene and (c,d) chloroform, comparing before and after decoration with (a,c) Au_xO nanostructures and (b,d) SnO_x nanostructures.

7.4 Conclusions

In summary, the PSi sensor systems clearly demonstrate the capacity to detect the presence of liquid organic solvents and distinguish between solvents with different chemical properties. The differences in the response to various organic solvents is correlated with the dipole moments of the organic molecules, suggesting the dominance of dipole-dipole interactions at the PSi interface. Deposition of nanostructured metal oxides, which produce large dipole moments, drastically affect the interactions of the PSi interface with organic solvents with dipole moments larger than 1.15 D. These findings suggest that an appropriate focus for future study of the interactions of PSi sensors and liquid organic solvents should revolve around exploring the effects of metal oxide nanostructure deposition of varying dipole moments. Controlling the response to various organic solvents through select nanostructure depositions could allow for the creation of an array of selective and uniquely interacting interfaces. Therefore, identifying the optimal deposition range for the nanostructured metal oxides should be the subject of future work.

APPENDIX A

SUPPLEMENTARY TABLES

Table A.1: Environmental safety standards for select VOC vapors and pollutant gases.

Gas/Vapor	Chemical Formula	PEL/ppm	REL/ppm	IDLH/ppm
Benzene	C_6H_6	1	0.1	500
Ethanol	C_2H_5OH	1000	1000	3300
Isopropanol	C_3H_7OH	400	400	2000
Methanol	CH_3OH	200	200	6000
Toluene	C_7H_8	200	100	500
Xylene	C_8H_{10}	100	100	900
Ammonia	NH_3	50	25	300
Carbon dioxide	CO_2	5000	5000	40000
Carbon monoxide	CO	50	35	1200
Hydrogen sulfide	H_2S	20	10	100
Nitric oxide	NO	25	25	100
Nitrogen dioxide	NO_2	5	1	20
Phosphine	PH_3	0.3	0.3	50
Sulfur dioxide	SO_2	5	2	100

VOC, volatile organic compound; PEL, permissible exposure limit; REL, recommended exposure limit; IDHL, immediately dangerous to life or health.
Safety standards reported by the National Institute for Occupational Safety and Health (NIOSH, http://www.cdc.gov/niosh/).

Table A.2: Simulated diffusion of 1 ppm of an arbitrary analyte gas into and out from a 1D pore.

t/50 s	1	2	3	4	5	6	7	8	9	10	11	12
atmos.	1.00	1.00	1.00	1.00	1.00	1.00	0.00	0.00	0.00	0.00	0.00	0.00
	0.02	0.82	0.88	0.91	0.93	0.95	0.94	0.15	0.10	0.07	0.06	0.04
	0.00	0.65	0.76	0.82	0.86	0.89	0.92	0.28	0.20	0.15	0.11	0.08
	0.00	0.50	0.65	0.73	0.80	0.85	0.88	0.41	0.29	0.21	0.16	0.12
	0.00	0.37	0.55	0.66	0.74	0.80	0.85	0.51	0.37	0.28	0.21	0.16
sim.	0.00	0.27	0.46	0.59	0.69	0.76	0.82	0.60	0.44	0.33	0.25	0.19
pore	0.00	0.19	0.38	0.53	0.64	0.73	0.79	0.66	0.50	0.38	0.29	0.22
	0.00	0.13	0.33	0.49	0.61	0.70	0.77	0.70	0.54	0.41	0.31	0.24
	0.00	0.09	0.29	0.46	0.59	0.69	0.76	0.73	0.57	0.44	0.33	0.25
	0.00	0.07	0.27	0.44	0.58	0.68	0.75	0.74	0.59	0.45	0.34	0.26
	0.00	0.07	0.27	0.44	0.58	0.68	0.75	0.74	0.59	0.45	0.34	0.26
avg.	0.00	0.32	0.48	0.61	0.70	0.77	0.82	0.55	0.42	0.32	0.24	0.18

Table A.3: Sensor response (and percentage change from baseline resistance) to the BTEX molecules toluene, benzene, and xylene to the nanostructure decorated nanopore-coated microporous structures used in this study for each inorganic gas test.

Inorganic analyte	Toluene	Benzene	Xylene
H_2S	$(0.50 \pm 0.07)\,\Omega$ (0.1 %)	$(11 \pm 6)\,\Omega$ (0.4 %)	$(30 \pm 15)\,\Omega$ (1.1 %)
SO_2	$(0.5 \pm 0.3)\,\Omega$ (0.1 %)	$(30 \pm 7)\,\Omega$ (0.9 %)	$(4 \pm 1)\,\Omega$ (0.7 %)
NO_2	$(1.0 \pm 0.1)\,\Omega$ (0.2 %)	$(5 \pm 2)\,\Omega$ (0.3 %)	$(4.0 \pm 0.7)\,\Omega$ (0.6 %)
NO	$(1.0 \pm 0.5)\,\Omega$ (0.2 %)	$(1.0 \pm 0.1)\,\Omega$ (0.2 %)	$(2.0 \pm 0.1)\,\Omega$ (0.5 %)

Table A.4: Values for equivalent circuit elements for n-type PSi sensors in dry conditions and in the presence of various organic solvents.

Sensor	Environment	R_S/Ω	C/F	P	R_1/Ω
PSi	dry	1×10^{-7}	1.46×10^{-8}	0.8345	52182
	acetone	1×10^{-7}	5.54×10^{-8}	0.7722	32075
	dry	1×10^{-7}	1.00×10^{-8}	0.8116	61000
	water	1×10^{-7}	2.11×10^{-8}	0.7762	47000
	dry	1×10^{-7}	1.97×10^{-8}	0.8108	35722
	methanol	1×10^{-7}	2.17×10^{-8}	0.8367	18305
	dry	1×10^{-7}	6.70×10^{-9}	0.8302	25325
	ethanol	1×10^{-7}	2.50×10^{-8}	0.8199	14502
	dry	1×10^{-7}	1.35×10^{-8}	0.8377	31401
	isopropanol	1×10^{-7}	2.11×10^{-8}	0.8209	15215
	dry	1×10^{-7}	9.13×10^{-8}	0.8500	24680
	chloroform	1×10^{-7}	1.49×10^{-8}	0.8215	31981
	dry	1×10^{-7}	1.46×10^{-8}	0.8345	52182
	toluene	1×10^{-7}	1.16×10^{-8}	0.8492	35473
	dry	1×10^{-7}	1.15×10^{-8}	0.8302	17554
	isoprene	1×10^{-7}	1.83×10^{-8}	0.8043	22325
PSi/Au_xO	dry	1×10^{-7}	1.85×10^{-8}	0.8171	54597
	ethanol	1×10^{-7}	2.19×10^{-8}	0.8218	20857
	dry	1×10^{-7}	1.94×10^{-8}	0.8039	49888
	chloroform	1×10^{-7}	1.97×10^{-8}	0.8038	63472
	dry	1×10^{-7}	1.94×10^{-8}	0.8039	49888
	toluene	1×10^{-7}	1.79×10^{-8}	0.8102	53328
PSi/SnO_x	dry	1×10^{-7}	5.18×10^{-9}	0.9220	75352
	ethanol	1×10^{-7}	1.76×10^{-8}	0.8680	29157
	dry	1×10^{-7}	6.11×10^{-9}	0.8637	76477
	chloroform	1×10^{-7}	5.29×10^{-9}	0.8525	90314
	dry	1×10^{-7}	6.66×10^{-9}	0.8610	59546
	toluene	1×10^{-7}	5.91×10^{-8}	0.8566	67844

APPENDIX B

SUPPLEMENTARY FIGURES

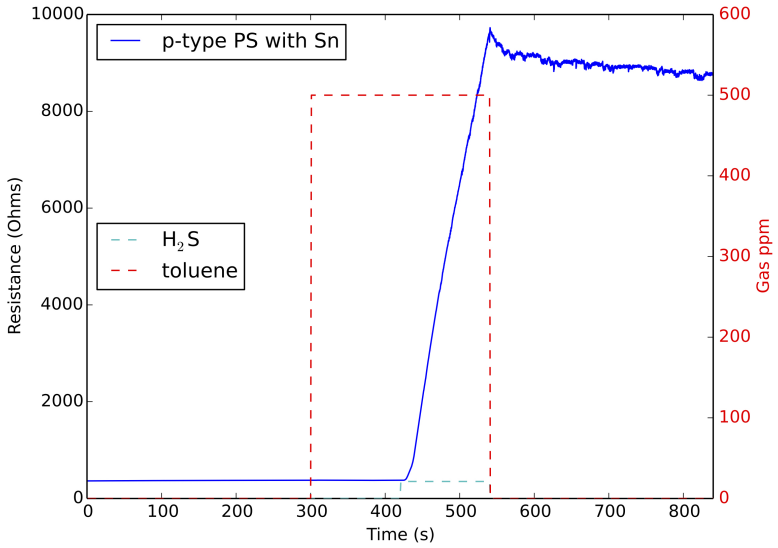

Figure B.1: SnO_x decorated p-type PSi sensor response to (500 ± 50) ppm toluene over the range denoted by the red box and (20.98 ± 0.51) ppm H_2S over the range denoted by the aqua box. A signal from toluene is barely visible. Reprinted from Sensors and Actuators, B, 212, Baker C., Laminack W., and Gole J.L., Sensitive and selective detection of H_2S and application in the presence of toluene, benzene, and xylene, 28-34, Copyright 2015, with permission from Elsevier.

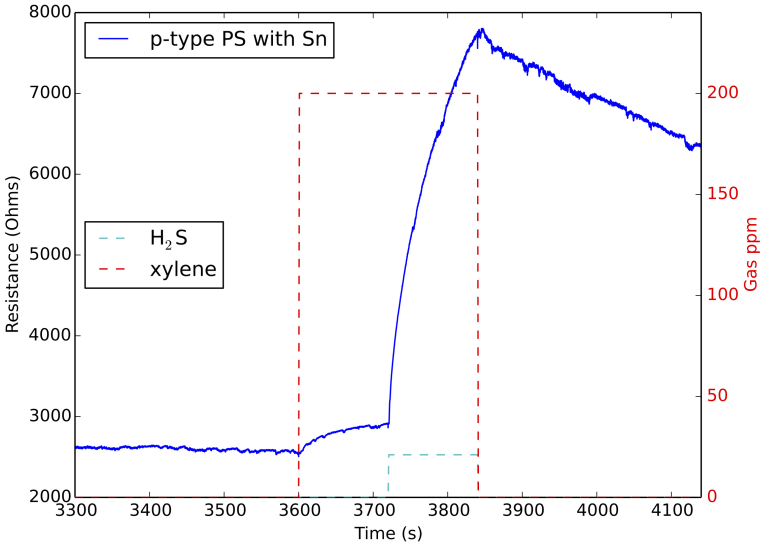

Figure B.2: Comparison of relative response as the xylene concentration is calculated to be (200 ± 20) ppm over the range denoted by the red box and the H_2S concentration is (20.98 ± 0.51) ppm over the range denoted by the aqua box for an SnO_x decorated p-type PSi sensor.

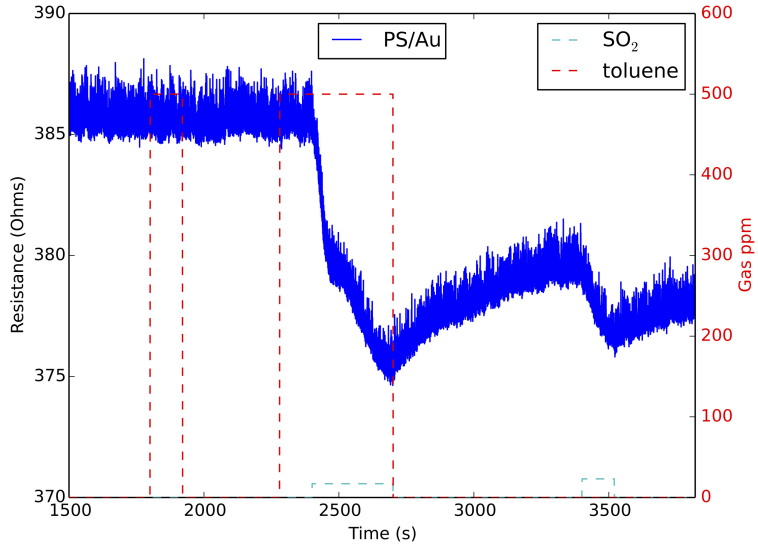

Figure B.3: P-type, Au_xO decorated, PSi sensor response to (500 ± 50) ppm toluene over the range denoted by the red dashed boxes and $16 \cdot 85\,(_{41})$ppm SO_2 over the range denoted by the aqua dashed boxes. The first minimum corresponds to SO_2 with toluene while the second minimum generated over a much shorter time scale corresponds to SO_2 alone. These minima are very similar and correspond to a conductance increase of $(10 \pm 2)\,\Omega$ for the etch conditions used in this experiment.

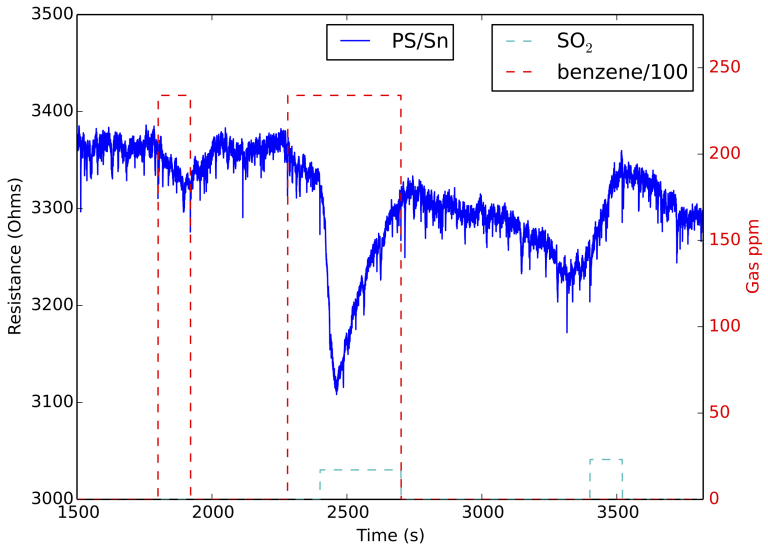

Figure B.4: P-type, SnO_x decorated, PSi sensor response to $> 20\,000$ ppm benzene over the range denoted by the red dashed boxes and (16.85 ± 0.41) ppm SO_2 over the initial the range and (23.44 ± 0.57) ppm over the latter range denoted by the aqua dashed boxes.

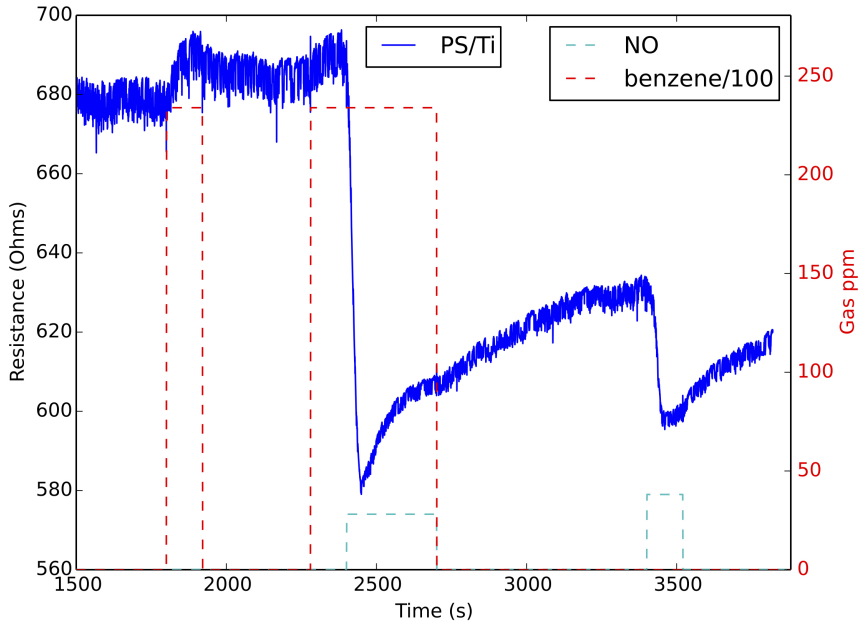

(a)

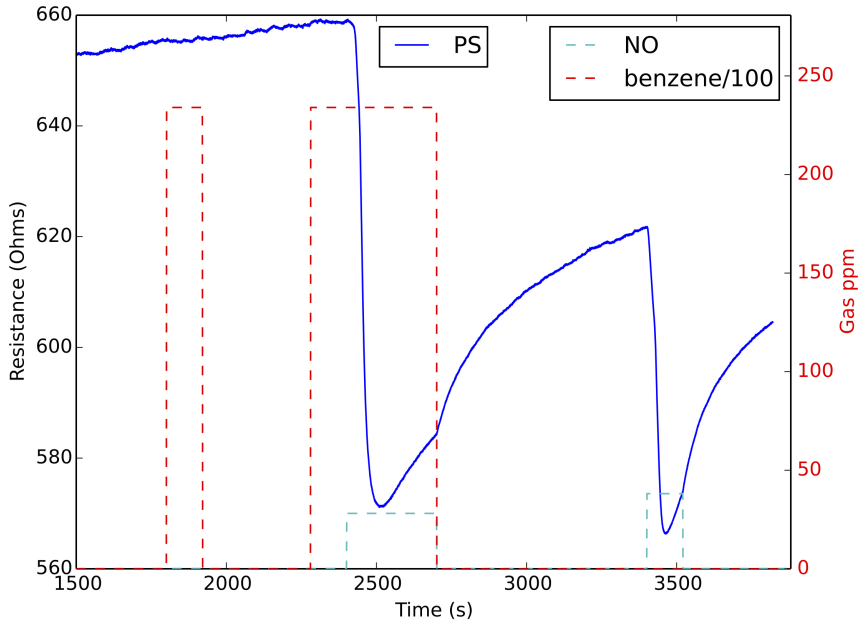

(b)

Figure B.5: (a) TiO_2 decorated p-type PSi sensor and (b) untreated p-type PSi sensor response to $> 20\,000$ ppm benzene over the range denoted by the red dashed boxes and (27.78 ± 0.68) ppm NO (first zone with 280 sccm N_2 with the aromatics) and (38.46 ± 0.94) ppm (second zone with 200 sccm without the aromatics) over the range denoted by the aqua dashed boxes.

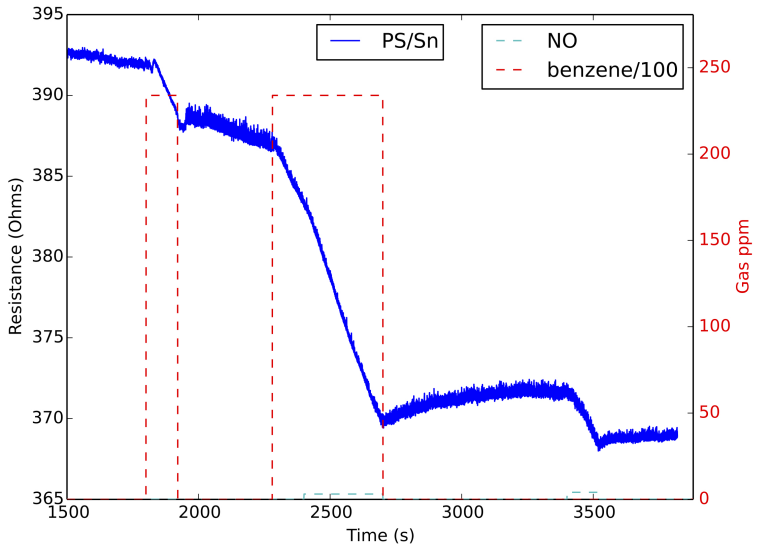

Figure B.6: SnO_x decorated p-type PSi sensor response to $> 20\,000$ ppm benzene over the range denoted by the red dashed boxes and (2.85 ± 0.07) ppm NO (first zone with 280 sccm N_2 with the aromatics) and (3.98 ± 0.10) ppm (second zone with 200 sccm without the aromatics) over the range denoted by the aqua dashed boxes.

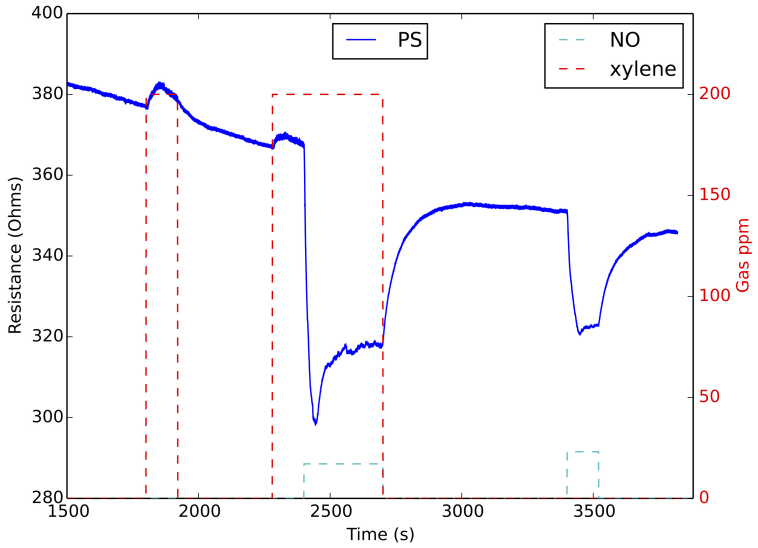

Figure B.7: P-type PSi sensor response to (200 ± 20) ppm xylene over the range denoted by the red dashed boxes and (27.78 ± 0.68) ppm NO (first zone with 280 sccm N_2 with the aromatics) and (38.46 ± 0.94) ppm (second zone with 200 sccm without the aromatics) over the range denoted by the aqua dashed boxes.

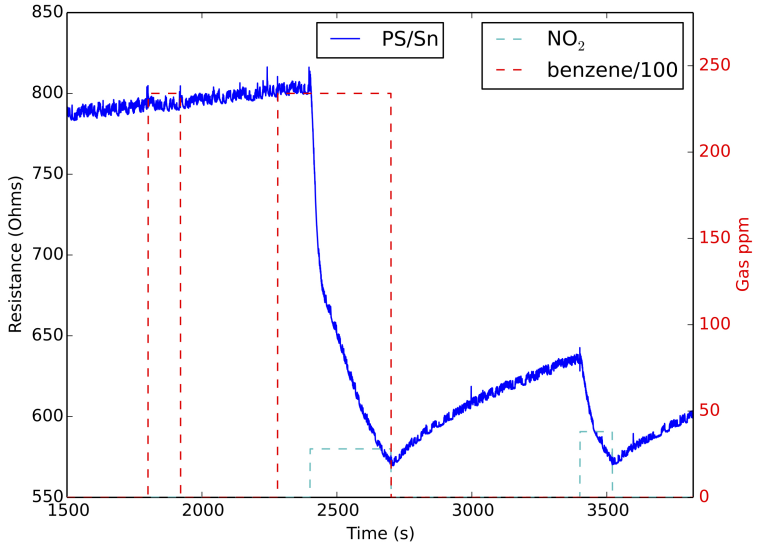

Figure B.8: P-type, untreated PSi sensor response to> 20 000 ppm benzene over the range denoted by the red dashed boxes and (27.78 ± 0.68) ppm NO_2 (first zone with 280 sccm N_2 with the aromatics) and (38.46 ± 0.94) ppm (second zone with 200 sccm without the aromatics) over the range denoted by the aqua dashed boxes. The first dominant minimum corresponds to NO_2 with benzene while the second minimum, generated over a much shorter time scale, corresponds to NO_2 alone.

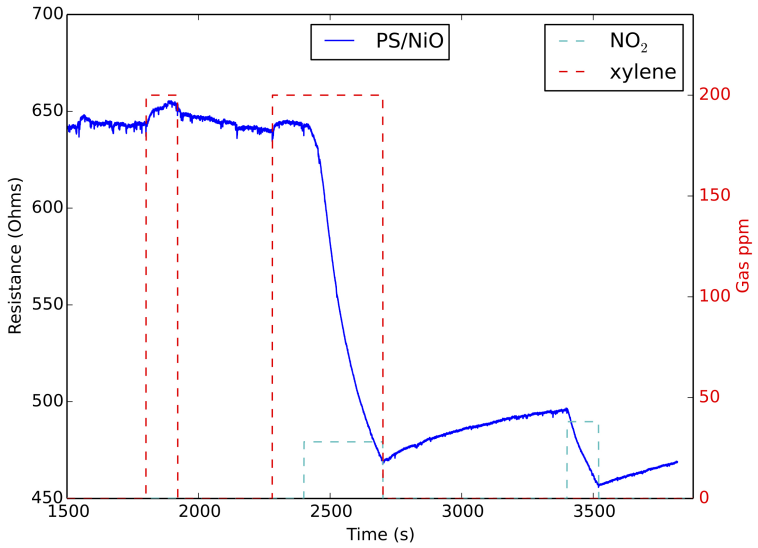

Figure B.9: P-type, NiO decorated PSi sensor response to (200 ± 20) ppm over the range denoted by the red dashed boxes and (27.78 ± 0.68) ppm NO_2 (first zone with 280 sccm N_2 with the aromatics) and (38.46 ± 0.94) ppm (second zone with 200 sccm without the aromatics) over the range denoted by the aqua dashed boxes.

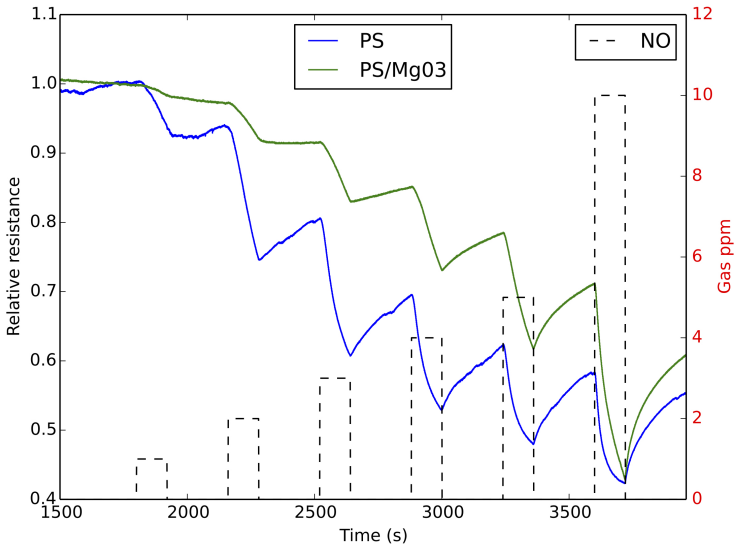

Figure B.10: Response to NO of an Mg^{2+} decorated p-type PSi interface before (solid blue) and after (green) treatment of the surface for 15 s with a 0.03 M solution. The boxes (black dashed) denote the analyte concentration from 1 ppm to 10 ppm over the time of analyte gas exposure to the sensors.

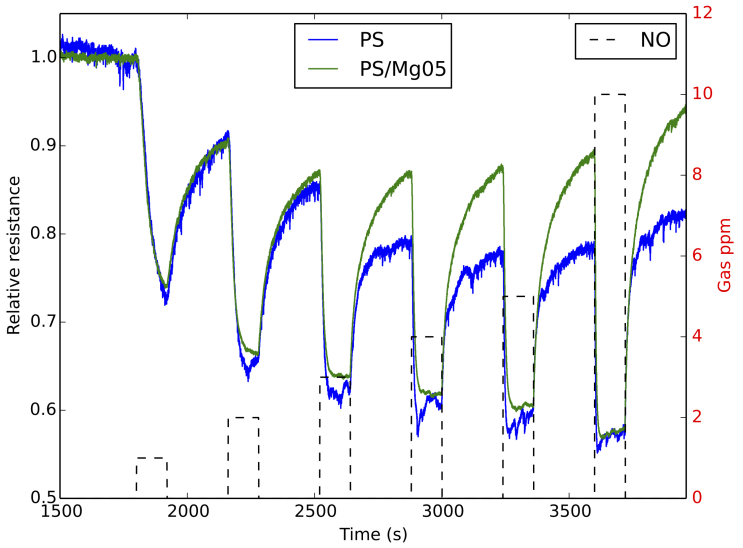

Figure B.11: Response to NO of an Mg^{2+} decorated p-type PSi interface before (solid blue) and after (green) treatment of the surface for 15 s with a 0.05 M solution. The boxes (black dashed) denote the analyte concentration from 1 ppm to 10 ppm over the time of analyte gas exposure to the sensors.

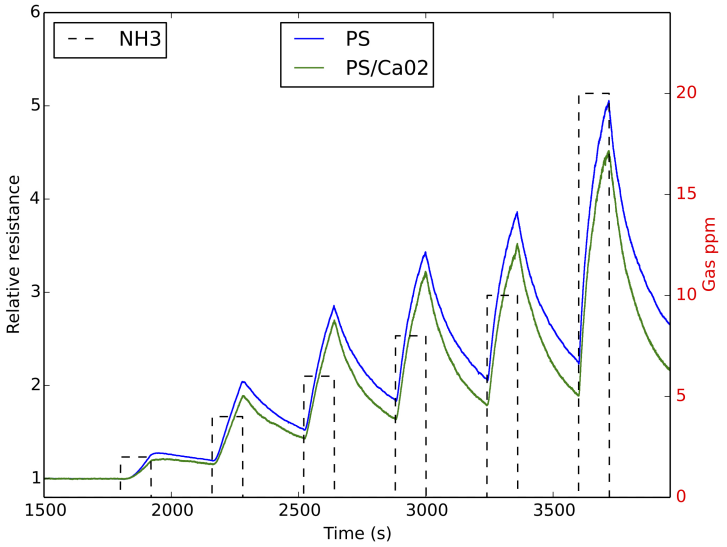

Figure B.12: Response to NH_3 of an Ca^{2+} decorated p-type PSi interface before (solid blue) and after (green) treatment of the surface for 15 s with a 0.02 M solution. The boxes (black dashed) denote the analyte concentration from 2 ppm to 20 ppm over the time of analyte gas exposure to the sensors.

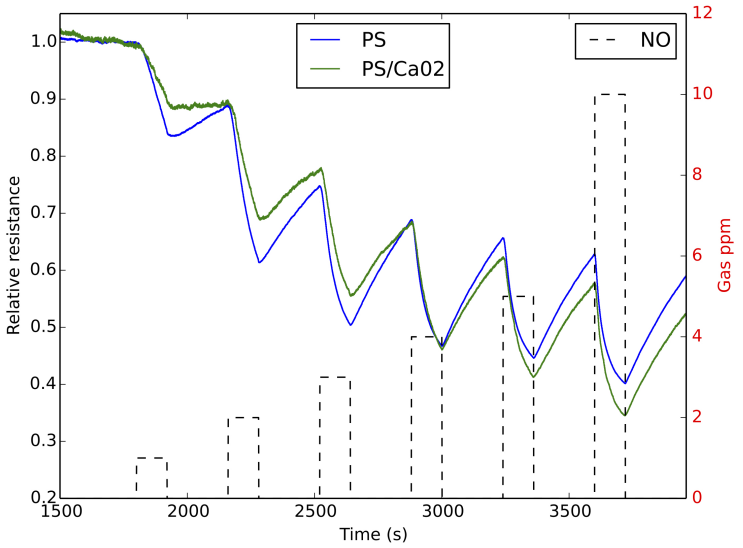

Figure B.13: Response to NO of an Ca^{2+} decorated p-type PSi interface before (solid blue) and after (green) treatment of the surface for 15 s with a 0.02 M solution. The boxes (black dashed) denote the analyte concentration from 1 ppm to 10 ppm over the time of analyte gas exposure to the sensors.

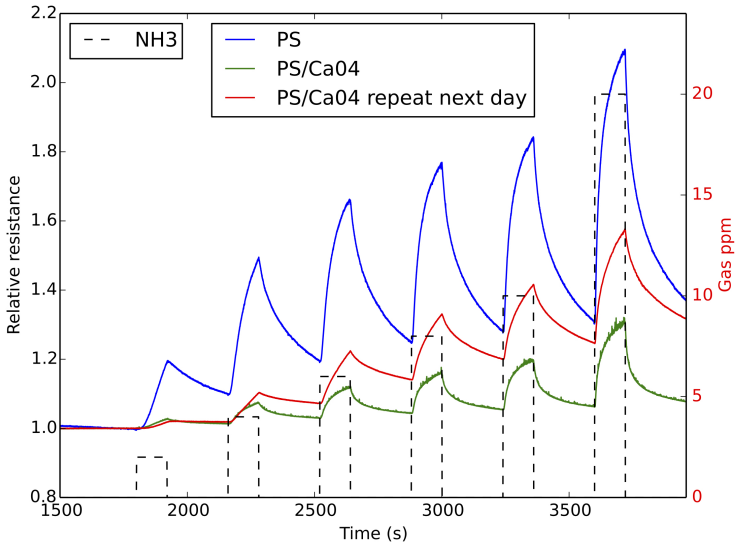

(a)

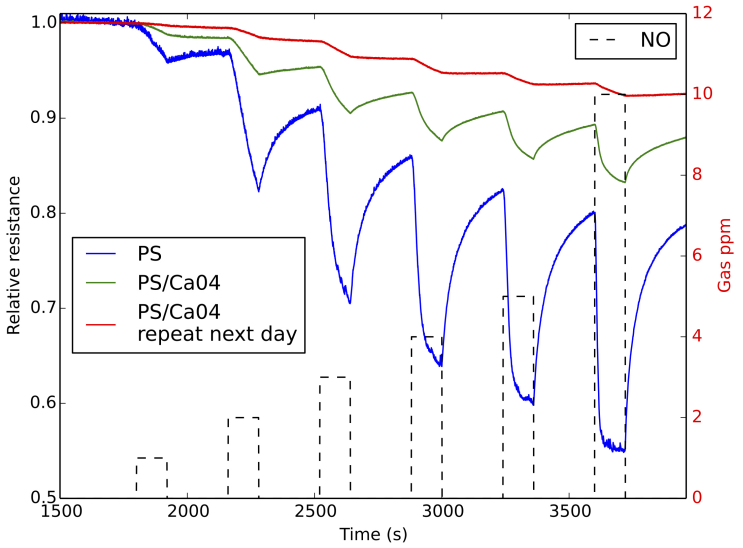

(b)

Figure B.14: Response to (a) NH_3 and (b) NO of a Ca^{2+} decorated p-type PSi interface before (solid blue) and after (green) treatment of the surface for 15 s with a 0.04 M solution. The boxes (black dashed) denote the analyte concentration from (a) 2 ppm to 20 ppm (NH_3) or (b) 1 ppm to 10 ppm (NO) over the time of analyte gas exposure to the sensors.

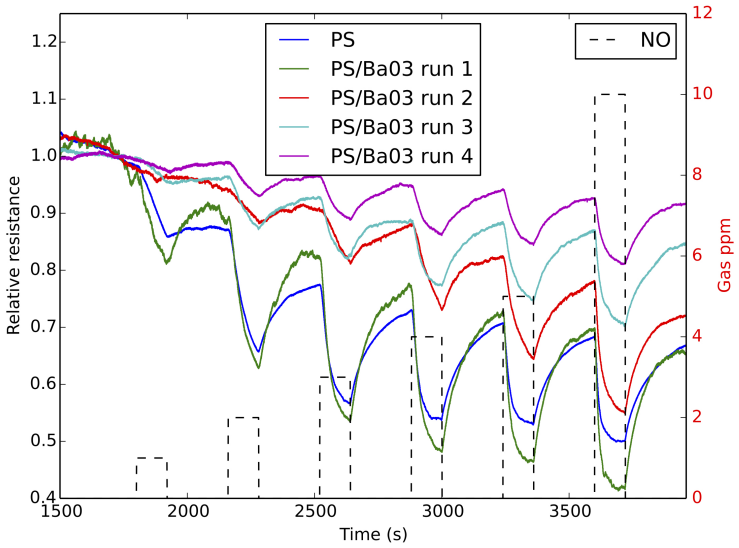

Figure B.15: Response to NO of an Ba^{2+} decorated p-type PSi interface before (solid blue) and after (all other colors) treatment of the surface for 15 s with a 0.03 M solution. Each subsequent run was collected over a series of days. The boxes (black dashed) denote the analyte concentration from 1 ppm to 10 ppm over the time of analyte gas exposure to the sensors.

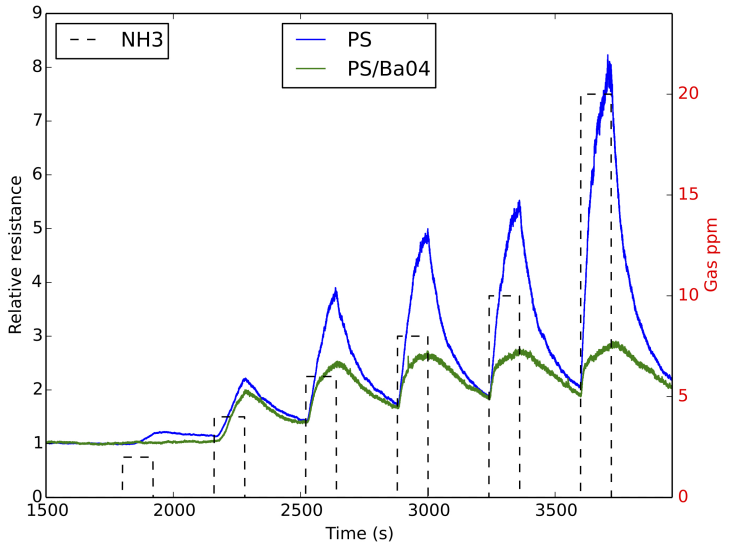

(a)

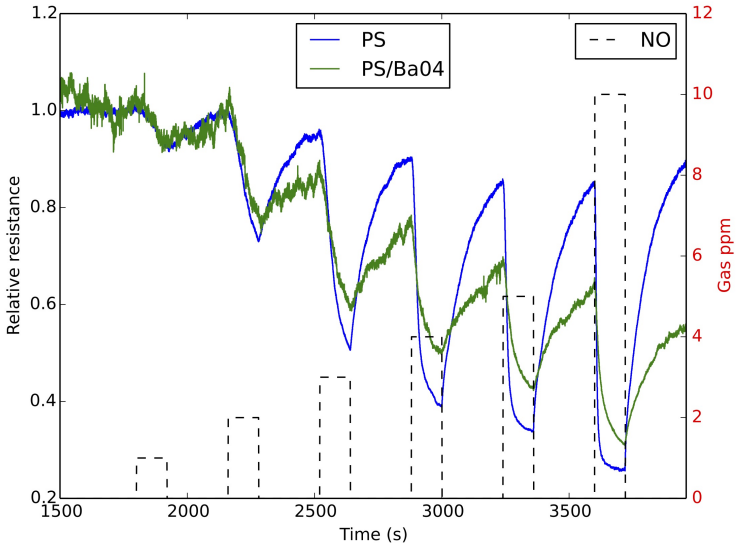

(b)

Figure B.16: Response to (a) NH_3 and (b) NO of a Ba^{2+} decorated p-type PSi interface before (solid blue) and after (green) treatment of the surface for 15 s with a 0.04 M solution. The boxes (black dashed) denote the analyte concentration from (a) 2 ppm to 20 ppm (NH_3) or (b) 1 ppm to 10 ppm (NO) over the time of analyte gas exposure to the sensors.

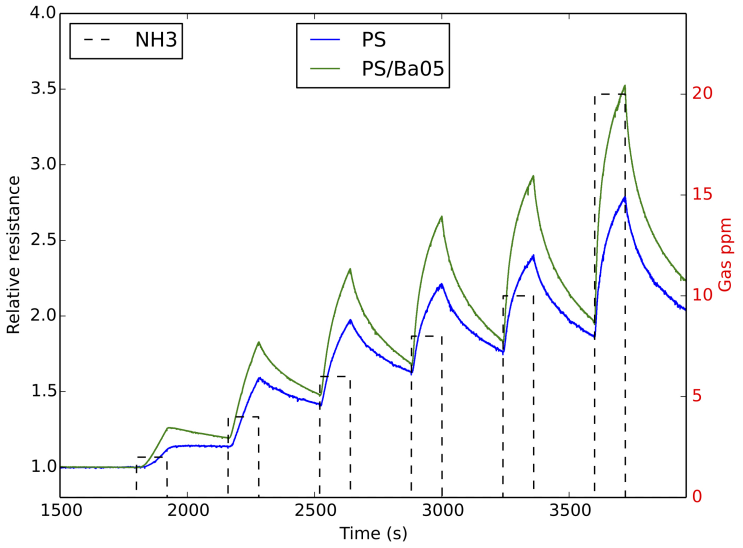

(a)

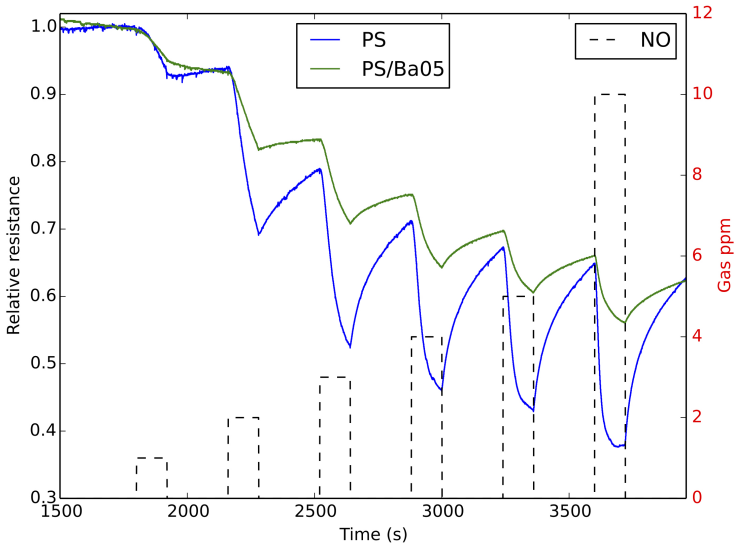

(b)

Figure B.17: Response to (a) NH_3 and (b) NO of a Ba^{2+} decorated p-type PSi interface before (solid blue) and after (green) treatment of the surface for 15 s with a 0.05 M solution. The boxes (black dashed) denote the analyte concentration from (a) 2 ppm to 20 ppm (NH_3) or (b) 1 ppm to 10 ppm (NO) over the time of analyte gas exposure to the sensors.

APPENDIX C

ACTIVITY OF TITANIA AND ZEOLITE SAMPLES DOSED WITH TRIETHYLAMINE

This work is the result of the collaborative efforts of Caitlin Baker, James L. Gole, Jonathan Brauer, Samuel Graham, Jianzhi Hu, Jeff. Kenvin, Andrew D. D'Amico, and Mark G. White.

C.1 Introduction

Recently, we discussed the catalytic activity of nitrogen and metal ion doped titania, comparing the activity of nanotitania to a commercial catalyst [43, 98]. The goal of these studies was to convert Lewis acid sites to basic sites employing a relatively simple nitration process at the nanoscale [30, 43, 98, 151]. Titanium oxide nanocolloids were treated with alkyl amines, such as triethylamine (TEA) in solution. It was apparent that nitrogen species were added to the colloid before the system was converted to its oxide. We show here our attempts to extend this approach to treating already formed oxides to determine if this technique will be effective with a similar TEA-treatment for Y zeolites.

Zeolites represent low-density, aluminosilicates and play an important role in a variety of petrochemical processes where they are used as molecular sieves, selective adsorbents, and catalysts [12, 40, 71, 79, 191, 276]. Zeolites are known to play an important role in petroleum refining and chemicals production [53]. The singular properties of zeolites are closely correlated to their physical structure, which consists of fully, corner-connected (Al,Si)O_4 tetrahedra as well as surface-based octahedral sites and results from their ability to form cavities and channels of various sizes.

These are usually occupied by charge-balancing cations, which can include H^+, Na^+, and Fe^{2+}, as well as solvent molecules.

For active molecular sieves and catalytic surfaces, there has been considerable interest in the design and synthesis of extra-large zeolite pores [61] and in the formation of basic sites in the normally acidic zeolite lattice (for example, tetrahedral AlO_4-sites, which bind a proton for charge neutrality) [276]. In complement to the generation of high pore volumes, it is desirable to demonstrate that the rigidity of the complex zeolite structure can be altered, perturbing but not destroying its intrinsic character. The modification of the properties of zeolites has been done using a variety of methods [183, 276]. In particular, amine-treatment of zeolites has been used in an effort to enhance the CO_2 storage capacity of zeolites [243]. An important modification of a typical zeolite, such as zeolite Y, with acidic catalytic sites would result if these sites can be converted to basic sites capable of binding and converting a reactant at the activating site [53]. It has been suggested that these basic sites could be nitrogen-based [61, 69].

Early attempts to produce basic sites in zeolites included the ion exchange of group IA and IIA cations. Here, the goal was to replace the Na ions normally used to balance the framework negative charge with ions of increasing electro-positivity so as to realize the benefits of these strong Brønsted bases [183]. Zeolites have also been decorated with strong Lewis bases as an alternate approach to create basic sites. For example, zeolite beta was dosed with ammonia at 300 °C in an attempt to develop basicity in this zeolite by developing a nitride surface species [243]. Aluminosilicates and aluminophosphates have also been treated with ammonia at higher temperatures to develop surface basicity [69]. Organic bases have been grafted to zeolites in another attempt to confer basicity to acidic zeolites [52]. Alkyl amines have been used to develop surface species onto silicon [288], and titania [283, 289]. We demonstrate here our attempts to change the properties of a titania nanocolloid and a crystalline, zeolite

Y, using a treatment with triethylamine, completed at a temperature slightly elevated from room temperature. In particular, we compare and contrast the effectiveness of the TEA treatment to alter the properties of a loosely-assembled nanosized colloid of titania with the properties of a fully-crystallized, rigid, zeolite Y.

C.2 Experimental

C.2.1 Catalyst Preparation

TiO_2 nanocolloids were formed by hydrolysis of Ti(IV) tetraisopropoxide. 250 ml of doubly ionized water and 80 ml of acetic acid were combined in a 1 l flask as the mixture was cooled to 0 °C in an ice bath under vigorous stirring. Ten mL of 2-propanol followed by 3.7 ml of $Ti[OCH(CH_3)_2]_4$ were added to a dropping funnel fixed to the flask as this solution was added slowly and drop-wise, under a dry nitrogen atmosphere, again with vigorous stirring. Continued stirring of the initial mixture for 24 h produces a clear colloidal solution. This clear solution can also be maintained under refrigeration for several months. For the present experiments, the nanocolloid ranged in size from 5 nm to 20 nm [98]. The highly porous TiO_2 nanocolloid was treated directly using triethylamine (TEA) in order to form $TiO_{2-x}N_x$ [43,98]. The reaction was found to take place readily and appeared complete within several seconds accompanied by heat release and the formation of a yellowish, partially opaque, mixture. XPS studies indicate the presence of 4 % to 8 % nitrogen in the nitridated samples, not only at the surface but also incorporated into several monolayers of the nano-particle agglomerates.

The inordinately-high heat release of the triethylamine reaction with the titania nanocolloid prompted us to characterized further this event by estimating the enthalpy of the reaction, $\Delta\hat{H}_{\mathrm{TEA/titania}}$, in the small, 2 ml bottle depicted in Figure C.1. A thermocouple system was attached to the bottle under black electrical tape and the temperature rise as a function of reaction time was recorded. A prescribed quantity

of TiO_2 nanocolloid, aqueous solution (0.0933 g titania and balance water to give a total mass of 0.204 g) was mixed with TEA (1.58 g). The maximum temperature rise was 16 °C for the reactants and bottle. The temperature rise could be related to the enthalpy of reaction/mixing assuming that the system was adiabatic and that average values of the heat capacities could be used to estimate the enthalpy change for the reagents and the glass container. In addition, we included the heat of mixing of TEA with water [33, 112, 193], $\Delta\hat{H}^0_{\text{mixing}} = -287$ cal/mol mixture, given by,

$$-\Delta\hat{H}_{\text{TEA/titania}} = (\Delta\hat{H}^0_{\text{mixing}} + [m_{\text{water}}\Delta H_{\text{water}} + m_{\text{titania}}\Delta H_{\text{titania}} + m_{\text{TEA}}\Delta H_{\text{TEA}} + m_{\text{glass}}\Delta H_{\text{glass}}])/\text{moles titania}, \quad \text{(C.1)}$$

where, m_i, is the mass of species i, and ΔH_i is the enthalpy per unit mass of species i. Because the titania nanocolloid samples contain a residual amount of acetic acid, a control experiment was conducted to assess the activity and heat release from the interaction of acetic acid and triethylamine (TEA). In an identical container to that shown in Figure C.1, acetic acid was diluted 1:1 with distilled water and this mixture was tested in the same manner as the nanocolloid/TEA mixture. Although the interaction of the acetic acid and TEA, as expected, leads to heat release, the corresponding temperature rise was less than 2 °C, demonstrating that the observed heat release can be attributed mainly to the nanocolloid/TEA interaction.

As a control experiment to the TEA-treatment of the titania nanocolloid, we used zeolites as sources of a microcrystalline, right metal oxide: the ammonium form of the zeolite, NH_4Y, and the proton form of the zeolite, HY, both having a silica/alumina ratio of 5.2. These materials were obtained from Zeolyst Products with the commercial designations of CBV 500 and CBV 600, respectively. The total aluminum ion concentration in these samples was estimated to be 4.83 mmol/g zeolite, from a consideration of the silica/alumina ratio provided by the vendor. Two methods were used to contact the NH_4Y and HY zeolites with the triethylamine (TEA). By method

Figure C.1: 2 ml bottle used to evaluate heat rise for the TiO_2-TEA reaction. The major portion of $TiO_{2-x}N_x$ is visible in the bottom of the container.

A, 5 g of zeolite was stirred in a 5 cm^3 triethylamine solution, which corresponds to 35.9 mmol of triethylamine, at 48 °C for 45 min and dried at 73 °C. By method B, the zeolite was contacted with TEA at 48 °C for 30 min in an open container with stirring, followed by heating at 73 °C in a closed container for 30 min, and then cooled to 48 °C in an open container with subsequent drying at 48 °C. We speculate that the heating at 73 °C in a closed container will develop a higher vapor pressure of TEA in the system and thus produce a higher loading of TEA on the zeolite. Treated samples were labeled NH_4YN and HYN followed by A or B to distinguish between treatment methods. No significant heat release was observed by either treatment method. A second control sample was established by heating a NH_4Y zeolite at 400 °C for 12 h to convert it to the acidic form, labeled H-400 °C.

C.2.2 Surface Area

The specific surface areas were obtained using the nitrogen vapor adsorption technique at 77 K. Data were recorded on the ASAP 2420, ASAP 2020 Accelerated Surface Area and Porosimetry Systems, and the 3FLEX Surface Characterization Analyzer at Micromeritics Instruments, Corporation (Norcross, GA). Samples were prepared at

temperatures ranging from 50 °C to 400 °C on the ASAP 2420. Most samples achieved a maximum surface area with an optimal preparation temperature of 300 °C. Prior to testing, the samples were pretreated in two preparation stages. The samples were first degassed on a SmartPrep 065 at 250 °C under nitrogen flow for 1 h. The second stage of preparation was performed on the ASAP 2420 where the samples were degassed under vacuum at 300 °C, the optimal preparation temperature, for 4 h.

C.2.3 Temperature Programmed Desorption, TPD, and Methanol Temperature Programmed Surface Reaction, TPSR

Methanol and CO_2 absorption isotherms over the zeolite were collected at 50 °C after pretreatment at 90 °C and 600 °C (TPSR) for methanol and 90 °C and 475 °C for CO_2. Methanol is a probe reaction that characterizes the samples for acidity and basicity from a consideration of the products generated over each sample, vide infra. Chemisorption of CO_2 to these same samples was used to confirm the basicity of the samples.

Several HY-Zeolite samples treated with TEA and untreated were subjected to temperature programmed desorption (TPD) under a He purge gas at a programming rate of 10 °C min^{-1} in a Micromeritics AutoChem II 2920 analyzer. The desorbed/evolved species were identified by an MKS Cirrus 2 Quadrupole mass spectrometer. This technique was used to describe the fate of the TEA species on the zeolite over the temperature range of 100 °C to 400 °C.

In a separate set of tests, the TEA-treated, Y-zeolite was saturated with MeOH before the TPD test was initiated. The motivation for this test was to determine what reaction sites remained on the surface, if any, after the TEA-treatment. If the MeOH does react, the reaction can be used to characterize the types of surface sites present on the surface (acid, base, or redox) from a consideration of the products observed. Acid sites give the product dimethyl ether, and base sites catalyze the reaction to form $CO + CO_2$ [33, 112, 193]. Under some conditions, redox sites also

give the products $CO + CO_2$ and formaldehyde. The samples were saturated with MeOH vapors, generated by doses of MeOH at 35 °C after which the temperature programmed surface reaction (TPSR) initiated by heating from 100 °C to 400 °C at 10 °C min^{-1}. The evolved gases were detected by mass spectrometry on an MKS Cirrus 2 Quadrupole mass spectrometer. The component signals were calculated using mass fragment signals m/z = 15, 16, 17, 18, 26, 27, 28, 29, 30, 31, 44, 45 and 86. The relative intensities of the components were obtained using NIST data (http://webbook.nist.gov/chemistry/).

C.2.4 XPS Characterization

The XPS experiments on the NH_4Y and NH_4YN zeolites were carried out on a Kratos Axis 165 using a monochromatic Al K-alpha x-ray source at a pass energy of 80 eV. The base pressure was 2×10^{-8} Torr and all scans were charge-neutralized.

C.2.5 Raman Spectroscopy

Samples were examined by Raman spectroscopy to determine the effect of the triethylamine molecules upon contacting the NH_4Y zeolite. Raman spectroscopy measurements, using a Horiba JobinYvon HR 800 system, were completed in the backscattered configuration with a 532 nm diode laser with a 2400 l/mm grating and LN_2 cooled, backside illuminated, Symphony detector. A 50X microscope objective was used to illuminate and collect the Raman signal. Integration times were 60 s. To reduce the fluorescence background in some samples, photo-bleaching was performed for 4 min prior to collecting the Raman data.

C.2.6 Solid State, MAS-NMR

High resolution ^{27}Al MAS-NMR testing on the NH_4Y and NH_4YN zeolites was completed at the Pacific Northwest National Laboratories/Environmental Molecular Sciences Laboratory (PNNL/EMSL) to determine how the amine treatment changed

the Al environment, if at all. The NMR experiments were completed in the William R. Wiley Environmental Molecular Sciences Laboratory at the Pacific Northwest National Laboratory using the 900 MHz NMR spectrometer, which features a medium-bore (63 mm) 21.1 Tesla Oxford magnet and a 4-channel Varian NMRS console. High-resolution ^{27}Al MAS NMR spectra were obtained for both the NH_4Y and TEA-treated NH_4Y zeolites. An additional study was also performed to describe the higher-order, quadrupole couplings involving the aluminum sites and the resulting spinning side bands. In addition, the NMR was recorded for a NaY and an Alumina-blank control samples.

C.2.7 XRD analysis

Powder, XRD spectra of the NH_4Y and NH_4YN zeolites were recorded on a Panalytical X'-pert Pro MPD diffractometer using the Cu $K_{\alpha 1}$ ($\lambda = 1.54\,\text{Å}$) line with a Ge, single crystal, monochromator.

C.2.8 FTIR Spectroscopy

Mid-infrared, transmission spectra ($4000\,\text{cm}^{-1}$ to $370\,\text{cm}^{-1}$) of the HY and HYN-A zeolites were obtained using a VERTEX 80v Fourier Transform Infrared Spectrometer with the OPUS 6.5 software. The samples were mixed with potassium bromide and subsequently this zeolite/KBr mixture was crushed in a marble, mortar and pestle. The resulting fine powder mixture was then pressed into a translucent pellet using an appropriate die press. The spectra were compared to a pure potassium bromide reference pellet.

C.3 Results

C.3.1 Catalyst Preparation

The initial preparation of the catalyst in the small 2 ml tubes was conducted concurrent with the measurement of the temperature rise attending this catalyst preparation.

The gross heating effect, that gave rise to the 16 °C increase in temperature of the mixture, was estimated to be no higher than 21.4 cal to give a value of 984 cal/mol mixture. We may begin to interpret these data by recognizing that this exothermic heat effect cannot be attributed to physisorption since almost all such events are endothermic.

So as to interpret these data further, we hypothesize that this exothermic event must be related only to those mechanisms that give rise to exotherms, such as, heats of mixing of reagents, chemisorption at surfaces, and exothermic chemical reactions. The heat of mixing of water with TEA was 287 cal/mol of mixture for a system showing 72 mol% TEA [270]. In the present case, the mixture is 72 mol% TEA, so the observed exotherm effect, 984 cal/mol mixture, is about three times the literature value for the heat of mixing of water in TEA. Thus, we must include the value, 287 cal/mol into the Equation C.1 so as to account for the heat of mixing of TEA with water. By doing so, we estimate the enthalpy of combining the TEA mixture with the titania sol-gel is −12.99 kcal/mol of titania in the mixture since titania is the limiting reagent (or catalyst) in this system. We reasoned that the titania was the limiting reagent in this mixing from a consideration of its molar content versus the liquid TEA (1.2 mmol titania versus 15.6 mmol TEA) and considering that only a fraction of the solid TEA was exposed to the TEA (surface area of TEA was $(159 \pm 3)\,\mathrm{m^2/g}$).

One might compare this observed figure to the heat effect for the catalytic decomposition of TEA over the titania catalyst according to the following stoichiometric equation where A is a Lewis acid site:

$$\mathrm{TEA} + 3\,\mathrm{A} \longrightarrow \mathrm{NH_3} + 3\,\mathrm{CH_2{=}CH_2} + 3\,\mathrm{A} \tag{C.2}$$

If this reaction does occur during the mixing of the sample with TEA, one can estimate the heat effect by using the standard heats of formation at 298 K, to calculate this enthalpy of reaction to be −13.8 kcal/mol TEA. From the stoichiometry of this reaction, one TEA surface reaction requires 3 Ti surface atoms, and the unit

cell of anatase exposes 2 Ti ions per surface face. The unit cell shows constants of $a = 0.378\,45\,\text{nm}$ and $c = 0.951\,43\,\text{nm}$ from which we can determine the Ti ion surface density of $5.55 \times 10^{18}\,\text{Ti atoms/m}^2$. For a sample having $159\,\text{m}^2/\text{g}$ of catalyst, we estimate the total Ti atom site density per mole of catalyst to be:

$$\begin{aligned}\left(5.55 \times 10^{18}\,\text{Ti atoms/m}^2\right)\left(159\,\text{m}^2/\text{g}\right)(79.9\,\text{g/mol titania}) \\ = 0.11\,\text{mol exposed Ti atoms/mol titania} \quad \text{(C.3)}\end{aligned}$$

We estimate the heat effect for the TEA decomposition reaction is 1.61 kcal/mol titania using a Lewis acid site density of 0.11 mol Lewis acid site/mol titania assuming that the Lewis acid sites do not turnover. It is assumed that the TEA decomposition reaction is proceeding at the reaction temperature of room temperature plus 16 °C, for this liquid phase reaction. The gas phase reaction requires a temperature in excess of 300 °C for the very acidic HZSM-5 catalyst (vide infra); whereupon the products ethylene and ammonia desorb at temperatures > 300 °C. It is also assumed that the ammonia product does not leave the titania reaction sites at this low temperature, thus, only one turnover or less will be observed. This calculated heat effect for the catalytic decomposition of TEA is much too low to explain the measured heat effect of −12.99 kcal/mol of titania. We conclude that some other stoichiometric reaction(s) are occurring that produce the bulk of the heat effect that we report here.

One possible interpretation of these calorimetric data involves reaction of the TEA with the titania nanocolloid to produce a titanium oxide containing a N atom for which the nitrogen could be furnished from the chemisorbed TEA. The control experiment for the mixing of acetic acid and TEA showed an exothermic heat effect that produced a temperature rise of ∼1 °C. Thus, we rule out this homogenerous acid/base between acetic acid and TEA as contributing much to the observed heat effect. Having ruled out several possible explanations, we conclude that TEA reacts with the titania nanocolloid to produce a N-containing solid product. In contrast to

this large exothermic heat effect observed when TEA was mixed with Ti nanocolloid, very little, if any heat effect was observed when mixing TEA with the Y-zeolite in aqueous solution. Given that the TEA/zeolite mixing produced very little heat, we conjecture that the TEA is not causing much change in the structure of the rigid zeolite.

C.3.2 Surface Area Testing

The BET surface areas for the nanotitania and zeolite samples are recorded in Tables C.1 and C.2 for the pretreatment temperature of 300 °C. This temperature resulted in the highest surface area for most of the zeolite samples but differed somewhat for titania and its oxynitride. The repeat titania sample and oxynitride sample was a separate sample of the material drawn from the same batch of titania of titanium oxynitrides. For both titania samples and its oxynitride, the variation in the BET SA was $6\,m^2/g$.

Table C.1: Summary of specific surface area of TiO_2 and the TEA treated material with a preparation temperature of 300 °C.

Catalyst	BET SA/m^2/g
TiO_2	146
TiO_2 repeat	152
$TiO_{2-x}N_x$	187
$TiO_{2-x}N_x$ repeat	193

The TiO_2 and its oxynitride have surprisingly high surface areas ($(149 \pm 3)\,m^2/g$ for the parent oxide and $(190 \pm 3)\,m^2/g$ for the oxynitride) compared to DeGussa P25 ($sim56\,m^2/g$) [43, 98]. This may result in large part because the titania nanocolloids used in this experiment are formed using the sol-gel technique and as a result are more porous than DeGussa P25 [43,98] . The zeolites used in this study show a considerably larger surface area than do the titania samples; however, the TEA treatment results in a decrease in the zeolite surface area of 30 % to 40 %. The ammonium form of

Table C.2: Summary of specific surface area of NH_4Y and HY zeolites and the TEA-treated materials with a preparation temperature of 300 °C.

Catalyst	BET SA/m^2/g
NH_4Y	548
HY-400 °C	515
HY; Z6/Untreated CBV600, H form	714
NH_4YN-A	299
NH_4YN-B	345
NH_4YN-B, repeat	251
HYN-A; Z2/method A, TEA-treated CBV600, H form	502
HYN-B; Z3/method B, TEA-treated CBV600, H form	632

the zeolite Y (NH4Y) heated to 300 °C showed a surface area of 548 m^2/g whereas the same zeolite heated to 400 °C showed a surface area of 515 m^2/g. The hydrogen form (HY) showed a surface area of 714 m^2/g. Two treatment methods were used to introduce N into the NH_4Y-zeolite: methods A and B. The zeolite treated by method A showed a surface area of 299 m^2/g. We made two separate batches of the CBV500 treated by Method B, denoted by NH_4YN-B. The surface areas of those two samples were 345 m^2/g and 251 m^2/g, which demonstrates the variability in the surface areas of this method B from batch to batch. The HY-zeolite treated by methods A and B (HYN-A and HYN-B) showed surface areas of 502 m^2/g and 632 m^2/g. The sample treated by method A is speculated to show a lower loading of TEA when compared to the sample prepared by method B. The unexpected response in surface areas with increasing loadings of TEA could be a result of the displacement of water from the samples.

The different response of the sample surface area upon treatment of the Ti nanocolloid and the Y-zeolite with TEA is somewhat surprising and this result combined with the heat effect upon mixing TEA with the oxide demonstates the contrasting response of the nanocolloid and the microcrystalline rigid zeolite for the TEA treatment. Increasing surface area of the Ti nanocolloid treated with TEA could be indicative of

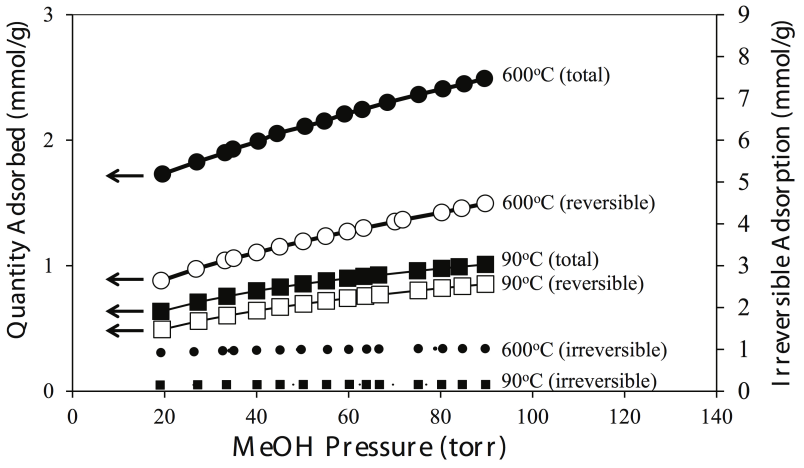

Figure C.2: Total and reversible methanol adsorption isotherms at 50 °C on amine-treated zeolite after pretreatment at 90 °C and after TPSR (600 °C).

sample reconstruction with the development of a porous solid. On the other hand, treatment of the zeolite samples with TEA resulted in lower surface areas, perhaps the result of pore plugging with the generation of alumina and coke residue inside the pore system of the samples.

C.3.3 Methanol and CO_2 Adsorption Isotherms

Adsorption isotherms for methanol and CO_2 are shown over the same pressure range in Figure C.3 and Figure C.3, respectively. All isotherms were collected at 50 °C, after pretreatment at the indicated temperatures. Methanol adsorption data were collected before the TPSR (90 °C pretreatment) and after the TPSR (600 °C pretreatment), and CO_2 isotherms were collected after comparable pretreatment. The zeolite always adsorbs more MeOH than CO_2, some of which may be surface adsorption and some of which may be pore filling. For MeOH, more irreversible adsorption is observed after the higher temperature pretreatment, corresponding to adsorption on acid sites. For CO_2, more irreversible adsorption is observed at low temperature, perhaps due to interaction with excess amine.

Figure C.4 shows the total quantity of adsorbed methanol (80 Torr) and CO_2

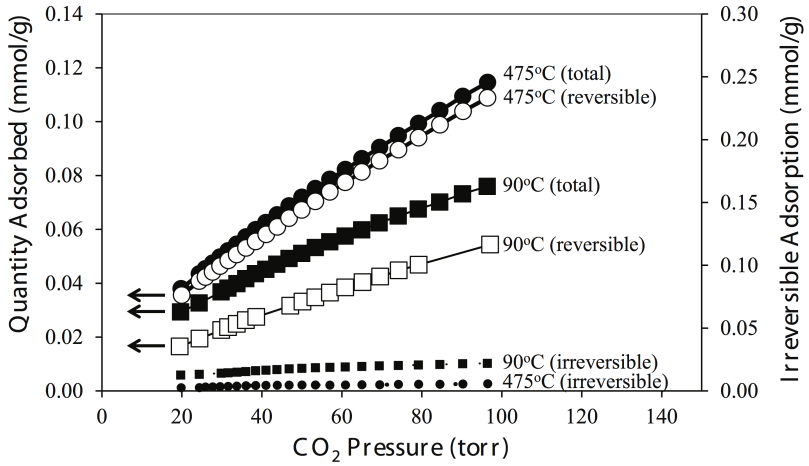

Figure C.3: Total and reversible CO_2 adsorption isotherms at 50 °C on amine-treated zeolite after pretreatment at 90 °C and 475 °C, with increased adsorption observed.

(500 Torr) at 50 °C. While the quantity of adsorbed methanol is greater than the amount of adsorbed CO2, Figure C.2 and Figure C.3, the increasing trends in total (and reversible) quantities adsorbed were comparable. From 90 °C to 475 °C, the quantity of irreversibly adsorbed methanol increases from 16 % to 41 % while the quantity of irreversibly adsorbed CO_2 decreased from 12 % to 2 %.

The contrasting behavior of CO_2 and MeOH adsorption with increasing temperatures is consistent with a model where the untreated zeolite shows predominantly acid sites with few basic sites. In addition, the TEA treatment preferentially covers the acid sites, leaving the basic surface sites uncovered for titration by CO_2.

C.3.4 TPD and Methanol TPSR

Alkyl amines are known to react with Brönsted acid sites in zeolites to produce NH_3 and alkenes which can be observed by TPSR characterization. In order to investigate the TEA interaction with the zeolite, temperature-programmed experiments were performed under helium flow on the untreated zeolite and as received TEA-treated zeolite by two different methods.

When methanol was adsorbed on the amine-treated zeolite before the TPSR,

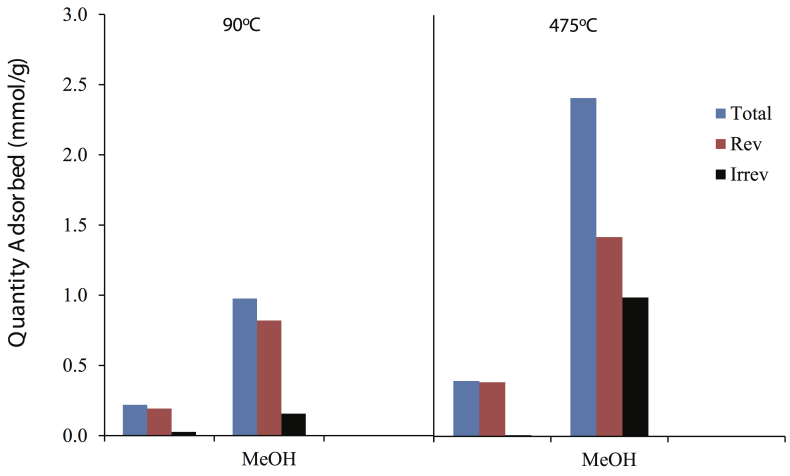

Figure C.4: Comparison of adsorption (total, reversible, and irreversible adsorption) of methanol and CO_2 on amine-treated zeolite at two different pretreatment temperatures, increasing adsorption with increasing temperature.

methanol desorbed unreacted with no indication of methanol reaction products (CO, CO_2, dimethyl ether, or formaldehyde), indicating the presence of only weak adsorption sites. When methanol was adsorbed after the first TPSR, unreacted (weakly adsorbed) methanol desorbed along with dimethyl ether, the product of methanol reaction with acid sites. This result indicates that the acid sites on the zeolite were blocked by amine but became accessible after the TEA was removed by heating.

The TPD data of the two, TEA-treated (HYN-A and HYN-B) and untreated Y-zeolite (HY) are shown in Figure C.5. Consider as a control sample, the untreated Y-zeolite TPD (top panel-Z6) where only water was observed in the purge gas, eluting at temperatures between 100 and 600 oC. Water was also observed to elute from the two, TEA-treated samples, HYN-A and HYN-B, over the same temperature range in these TPD spectra (middle panels-Z2 TPD and Z3 TPD). In comparison, the two TEA-treated Y-zeolites show the desorption of weakly adsorbed TEA at temperatures of 150-400oC, and the decomposition products of TEA to ethylene (300-500oC) and ammonia at temperatures between 350-600oC. These results show that the TEA is not removed from the samples by heating to temperatures lower than 150oC. The

ethylene and ammonia products suggest that the Hoffman elimination is occurring on the Brnsted sites where the TEA is reacting by a series reaction sequence as follows:

$$(CH_3CH_2)_3N + H^+ \longrightarrow (CH_3CH_2)_2NH + H^+ + CH_2{=}CH_2 \quad (C.4)$$

$$(CH_3CH_2)_2NH + H^+ \longrightarrow (CH_3CH_2)NH_2 + H^+ + CH_2{=}CH_2 \quad (C.5)$$

$$(CH_3CH_2)NH_2 + H^+ \longrightarrow NH_3 + H^+ + CH_2{=}CH_2 \quad (C.6)$$

This same reaction sequence was reported for the decomposition of TEA over H-beta zeolite [29]. The diethyl amine (DEA), Equation C.4, and the ethyl amine (EA) intermediate, Equation C.5, products react at different temperatures producing the asymmetric peak containing the ethylene products. Since this decomposition is catalyzed by Brønsted acid sites, the reactivity of the substrates is highest for the tertiary amine, TEA, less reactive for the secondary amine, DEA, and least reactivity for the primary amine, EA. Thus, we expect that some of the ethylene products will elute at temperatures different from the products of ethyl amine by Equation C.6: ammonia and ethylene. One might expect the ethylene and ammonia products of ethyl amine decomposition to elute together since they are co-products of the final Hoffman elimination reaction, Equation C.6, and this common elution temperature would be observed if the system was in reaction-rate control. In the present case, the delay in the elution of the ammonia vis-á-vis the ethylene strongly suggests that desorption of the products is the rate controlling process. Ammonia is a much stronger base than ethylene and thus it is expected that ethylene will desorb from the zeolite at a lower temperature than ammonia. Moreover, the elution of the TEA at temperatures below 350 °C shows that the continuous film of weakly adsorbed TEA is removed leaving behind isolated patches of H^+TEA^-. Thus, the selective decoration of TEA to the Brønsted sites is one attribute of this preparation method for adding N to the zeolite that distinguishes this method from those methods which develop a continuous film

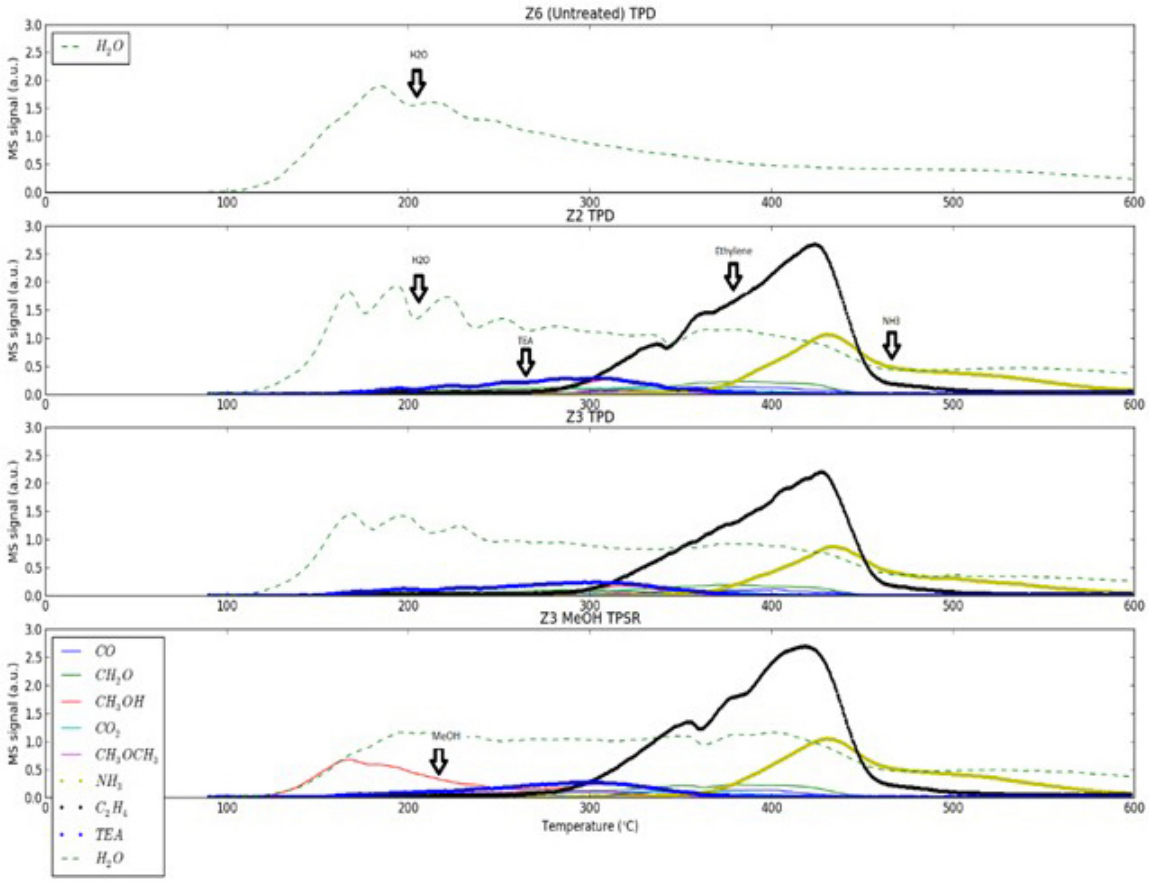

Figure C.5: TPD of untreated Y-zeolite (top), two, TEA-treated Y-zeolites (two middle panels) and TPSR of MeOH over TEA-treated Y-zeolite (bottom panel). Component signals were calculated from m/z = 15, 16, 17, 18, 26, 27, 28, 29, 30, 31, 44, 45, and 86. Relative intensity values were obtained from the NIST database (webbook.nist.gov).

on the sample.

The TPD curves shown in Figure C.5 for ethylene and ammonia products were integrated to estimate the relative areas under these curves. We suggest that the relative areas of the ethylene/ammonia products are proportional to the relative molar amounts of ethylene/ammonia. The areas of ethylene/ammonia were found to be in the ratio of 3.1 and 3.13 for the two TEA-treated Y-zeolites. The Hoffmann reaction shows a stoichiometry of 3 ethylene molecules per one ammonia molecule products. We suggest that the values of 3.1 and 3.13 mol ethylene per mol ammonia cannot be explained as evidence for incorporation of the N atoms into the samples, owing

to the small deviations of the observed values (3.1) from the expected values for no N-incorporations, 3.

The MeOH TPSR experiment, Figure C.5 bottom panel (Z3 MeOH TPSR), shows a TEA-treated Y zeolite, initially decorated with 150 µmol of MeOH per gram of solid. (58.0 ± 0.1) mg of sample were used for all experiments in this figure so that the peaks and signals are directly comparable. Samples were degassed for 2 h (1 h under high vacuum and 1 h under helium flow) at 90 °C before experiments. The TEA decomposition was observed for this sample over the same temperature ranges recorded for the TEA-treated, Y zeolite samples, middle two panels. Under heating at $10\,°C\,min^{-1}$, most of the MeOH (red line) desorbs over the temperature range of 100 °C to 250 °C without reacting before the strongly-adsorbed TEA is decomposed to ethylene and ammonia. No significant amounts of DME were observed in this TEA-treated sample suggesting that the amine treatment eliminated much of the strong surface acidity of the parent zeolite. Small amounts of carbon monoxide and formaldehyde, blue and green lines, were observed in the purge gas at catalyst temperatures of 300 °C to 450 °C. The appearance of these products of the MeOH reaction can be attributed to base catalysis [33, 112, 193].

A control experiment, not shown, was completed where the catalyst was the H^+Y zeolite that had not been treated with TEA. All other conditions were the same as that described for the MeOH TPSR of the TEA-treated zeolite. The DME selectivity for this control sample was 88 % at a MeOH conversion of 65 % indicating the existence of Bronsted acid sites in the sample; whereas, the selectivity to CO, CO_2, $H_2C{=}O$ (products of base catalysis) were 6 %, 1 %, and 5 %, respectively. The data of this control experiment using the H^+Y zeolite shows that even acid zeolites, not treated with TEA, show small amounts of base sites. Zeolyst data of elemental analysis of the H^+Y zeolites shows small amounts of Na were present in these acid zeolites (vide infra). Apparently not all of the Na ions can be removed from these samples.

C.3.5 Core Level XPS

XPS profiles for the nanotitania and nitridated nanotitania samples, prepared following the same procedure as those used in this study, have been discussed in detail [43, 98]. The Ti2p region near 460 eV, the O1s region near 530 eV, and the N1s region near 400 eV were studied. The nitrogen signal is consistent with the formation of NO sites in the titanium lattice [43, 98]. The Ti2p binding energy for the nanocolloids peaks is at 458.8 eV (versus DeGussa P25 at 459.5 eV). The nitridated titania nanocolloids show peaks at 458.6 eV, a shift of only 0.2 eV. The O1s peak for the nanocolloids shows a value of 530.4 eV, shifting to an asymetric peak; whereas the nitridated titania shows a value of 530.0 eV, a shift of 0.4 eV.

Table C.3 and Figure C.6 show the Al2p and Al2s, core level, XPS binding energies in eV for the untreated and TEA-treated NH_4Y zeolite. Depicted in Figure C.6 and also included in Table C.3 are the corresponding XPS binding energies for Si2p and Si2s in the same sample. These data demonstrate the large core level XPS Al2p and 2s and Si2p and 2s shifts which correspond to a decreasing electron binding energy of the order of 1 eV to 2 eV (the Al and Si are becoming less positive as they accept electron density) with increasing degree of TEA-loading. These values represent the largest XPS core binding energy changes that we have observed at the nanometer length scale [43, 98]. These results are consistent with a significant nitrogen interaction with surface sites of the zeolite.

The corresponding O1s electron binding energies shift to lower binding energies which are smaller in values than the BE shifts observed in the cations, but also significant, being on the order of 0.4 eV to 0.65 eV with increased TEA loading for the conditions under which the spectra were generated.

The results for aluminum and silicon are consistent with the accompanying shift in the N1s binding energy. The N1s BE reported for the untreated zeolite, 401.5 eV, is characteristic of ammonium ions that remain after the calcination. This BE value,

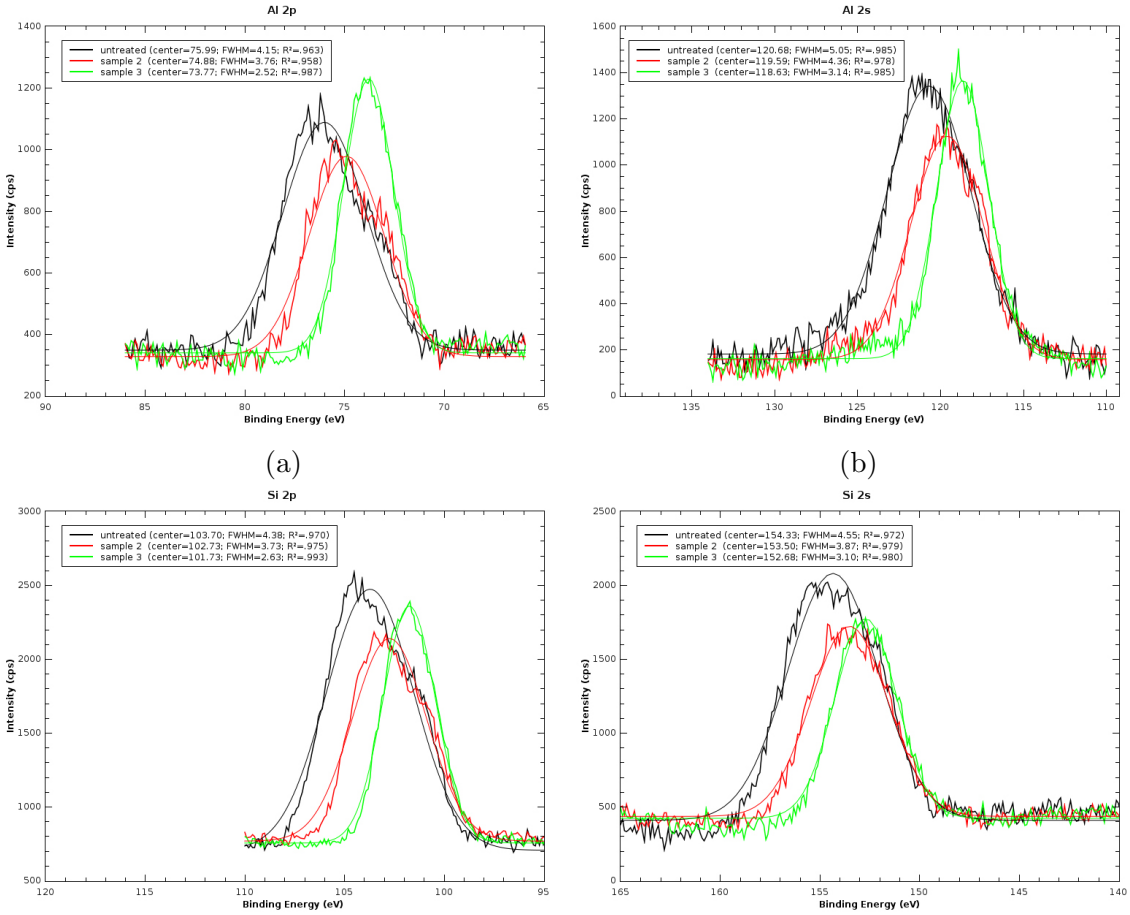

Figure C.6: (a) Al2p XPS spectra for Y5.2 faujasite and the TEA-treated faujasites, (b) Al2s XPS spectra. The binding energy shifts to considerably lower values on treatment with TEA. (c) Si2p XPS spectra for Y5.2 faujasite and the TEA-treated faujasites, (d) Si2s XPS spectra. The binding energy shifts to considerably lower values on TEA-treatments.

shifted up by almost 1.8 eV from that of neutral ammonia (398.8 eV) [190], is characteristic of an electron-deficient N as a result of the protonation of ammonia by an acidic proton. The shift results because the N1s binding energy is higher when the oxidation state of the nitrogen is more positive. This trend in shift vs. binding energy can be illustrated from a consideration of the XPS core binding energies in $NaNO_3$(408 eV) [268], in NO_2 (404.5 eV) [223] and in NO (400 eV to 401.5 eV) [57] compared to 398.8 eV in NH_3.

Now consider the N1s BEs for the NH_4Y zeolite decorated with TEA by methods A and B, where the values are 400.95 eV and 400.61 eV, respectively (Table C.3). These BEs reflect electrons leaving from protonated ammonia and protonated TEA. These values are to be compared to the N1s BEs of neutral triethylamine, which is 399 eV to 399.5 eV [190]. The N1s BE shows a systematic decrease in value, 401.59 eV to 400.95 eV to 400.61 eV, which is consistent with the sample becoming enriched in TEA, vide supra. These data show that the amine N experiences a shift of 1.1 eV to 1.5 eV to higher BEs upon contacting the surface of the zeolite. This shift to higher BEs is consistent with a loss of electron density from the amine N to the zeolite. We may speculate that this electron density is transferred to the zeolite O anions through H atoms residing on silanols, aluminols, and the on the O bridges between the framework Al and Si cations. This transfer of electron density to the oxygen atoms is confirmed by the negative shifts in binding energies observed in the O1s of 0.4 eV to 0.6 eV, Table C.3.

Table C.3: XPS Binding Energies (eV) of NH_4Y zeolite treated with TEA by Methods A and B.

Sample	Al2s	Al2p	Si2s	Si2p	N 1s	O1s
NH_4Y	120.68	75.99	154.33	103.7	401.59	531.25
NH_4YN-A	119.59	74.88	153.5	102.73	400.95	530.84
NH_4YN-B	118.63	73.77	152.68	101.73	400.61	530.58

C.3.6 Raman Spectroscopy

Raman Spectroscopy was performed to show the effect of heating to remove the ammonium ion from the NH_4Y zeolite (Figures C.7a and C.7b) and also the effect of amine treatment on the NH_4Y zeolite (Figures C.7c and C.7d). The background fluorescence has been subtracted from the $NH_4YN{-}B$ spectrum. The Raman signals assigned to the TEA-containing species in the samples are marked with the letter N.

The Raman spectra of the zeolite materials are distinguished by two major features: (1) a strong background fluorescence, which is suppressed in Figure C.7d, and (2) a notable narrowing of the Raman spectral features upon increased loading of TEA. The Raman spectra of Figures C.7c and C.7d suggest nitrogen incorporation upon treatment with triethylamine as well as indicating the formation of additional nitrogen-based sites (marked with a capital N in the figure).

The vibrational features of the zeolites have several common features [12, 53, 79, 276]. The modes between $700\,cm^{-1}$ and $1100\,cm^{-1}$ are primarily assigned to symmetric and asymmetric Z−O−Z (Z = Al or Si) stretching vibrations. The intense mode near $500\,cm^{-1}$ is attributed to the motion of the oxygen atom in the plane perpendicular to the Z−O−Z bond. This mode is slightly red-shifted for the $NH_4YN{-}B$ relative to the untreated zeolites and splits into two peaks at $490\,cm^{-1}$ and $510\,cm^{-1}$. Below $550\,cm^{-1}$, the bands are assigned to bending and rotational modes [12, 53, 79, 276].

We observe at least four new features in the spectra for the TEA-treated zeolites, which grow with increased amounts of TEA (vide supra). The loadings of TEA in these samples were not determined quantitatively; however, the procedure for preparing sample B is speculated to produce a higher loading of the amine than the procedure A. The sharp bands at $\sim 410\,cm^{-1}$, $750\,cm^{-1}$, $1150\,cm^{-1}$ and $1460\,cm^{-1}$ are likely associated with the bonding of a nitrogen-based species. See Table C.4 for a comparison of these data with the Raman data obtained from the literature (http://www.basechem.org/). The Raman spectrum of triethylamine shows strong

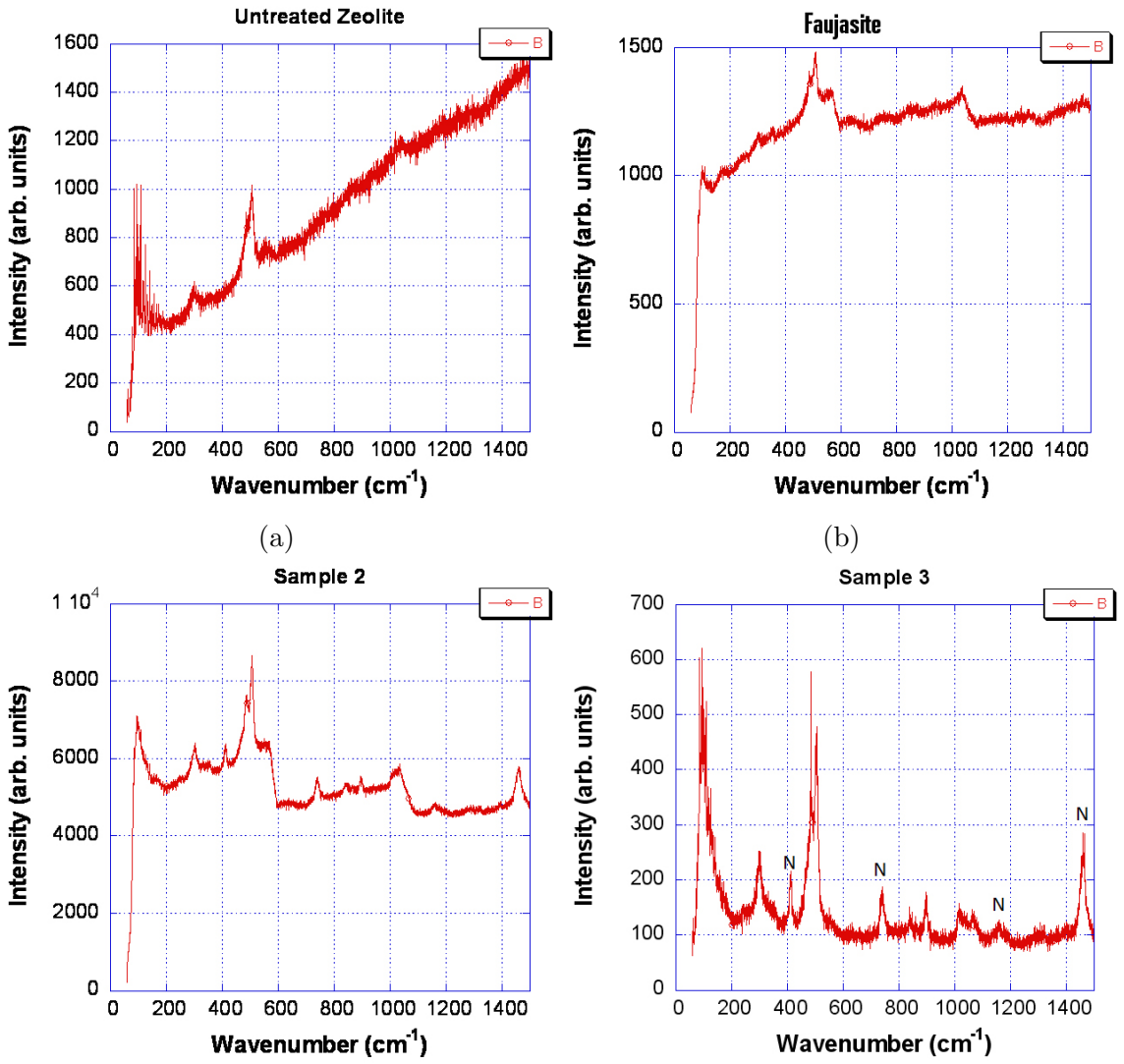

Figure C.7: Raman Spectroscopy of Faujasite Samples: (a) Raman spectrum for untreated Y5.2 ammonium-based faujasite superimposed on background fluorescence, (b) Raman spectrum for Y5.2 faujasite treated at 400 °C (sample 1) for 12 h to convert to an acidic faujasite whose Raman features are superimposed on the background fluorescence, (c) Raman spectrum for TEA-treated faujasite (sample 2, NH_4Y+TEA(A)) superimposed on the background fluorescence, (d) Raman spectrum for TEA-treated faujasite (sample 3, NH_4Y+TEA(B)) with background fluorescence removed.

Table C.4: Comparison of RAMAN spectra peaks (cm-1) of triethylamine liquid and TEA-treated NH4Y zeolite.

% Absorbance	TEA Liquid	NH_4YN-A	NH_4YN-B
96	2937		
62	2876		
46	1457	1450	1450
12	1295		
24	1096	1150	1150
29	1071	1070	1070
11	1022	1010	1010
13	1002		
16	923		
12	906	900	900
22	789	750	750
20	442	410	410

peaks at $1457\,cm^{-1}$, $1096\,cm^{-1}$ and $1071\,cm^{-1}$ and weaker peaks at the following wavenumbers: $1022\,cm^{-1}$, $1002\,cm^{-1}$, $923\,cm^{-1}$, $906\,cm^{-1}$, $789\,cm^{-1}$ and $442\,cm^{-1}$. One of the observed peaks can be assigned to TEA Raman spectrum ($1460\,cm^{-1}$) while the others cannot ($1150\,cm^{-1}$, $750\,cm^{-1}$ and $410\,cm^{-1}$). Peaks observed at $1070\,cm^{-1}$ and $900\,cm^{-1}$ for the untreated zeolite and the TEA liquid overlap. IR data of the TEA-treated zeolite show a correspondence of that spectrum with the spectrum of protonated TEA (vide supra). Therefore, we might expect that some of the peaks observed in the Raman spectrum might be different from the Raman spectrum of liquid TEA.

The observed narrowing of the Raman spectra (Figures C.7c and C.7d) upon treatment of the NH_4Y with triethylamine, while at first surprising, can be attributed to the formation of faujasite cage sites, which are much less confined. In other words, the Raman spectra are consistent with a loosening of the TEA-treated faujasite structure relative to that of the initial faujasite. This loosening is consistent with the complementary NMR characterization (vide infra).

C.3.7 ^{27}Al MAS-NMR

The ^{27}Al MAS-NMR results for the NH_4Y and NH_4YN zeolites (labeled as FAU and N-FAU in the figure) are shown in Figure C.8a. Major peaks for both samples were identified as the tetrahedrally-coordinated Al (Td) and octahedrally-coordinated Al (Oh). The Td peak for both solids appeared in the same position (61.6 ppm) whereas the Oh peak for the TEA-treated zeolite was shifted 2.8 ppm downfield of the untreated zeolite (8.8 ppm versus 6.0 ppm). Another small peak was observed for each sample (35.0 ppm and 31.4 ppm), which has been assigned to penta-coordinated Al. The peak at 8.8 ppm and the downfield shoulder at 11.9 ppm may show that the triethylamine is interacting with the Al ions in the extra-framework Al. There does not seem to be much direct interaction with the framework Al ions (Td) as the dashed line almost traces exactly the solid line (Figures C.8a and C.8b). These same samples were compared to two control samples: a sodium-form Y zeolite, NaY, having the same silica/alumina ratio (5.2), and an alumina sample (Figure C.8b). For the NaY control sample, only the Td peak was observed at a chemical shift of 63.9 ppm. Apparently, the effect of the H-form was to show a smaller chemical shift for Td Al. The Oh and penta-coordinated peaks are absent from this sample, which suggests that the formation of the acid form of the zeolite is attended with the extraction of Al ions from the framework to form the Oh and penta-coordinated Al species. The alumina shows only the Oh Al species at chemical shifts of -1 ppm, -9 ppm and -12 ppm. These peaks at -9 ppm and -12 ppm are similar to those observed in all zeolite samples.

The 900 MHz ^{27}Al MAS/NMR spectrum depicted in Figure C.9 supports our hypothesis to explain the Raman spectral narrowing on amine treatment. The parent NH_4Y zeolite sample displays spinning side bands, but the TEA-treated sample has lost these features for both the surface-based octahedral ($\sim$8.8 ppm) and framework tetrahedral ($\sim$61.6 ppm) sites, consistent with increased molecular motion. The

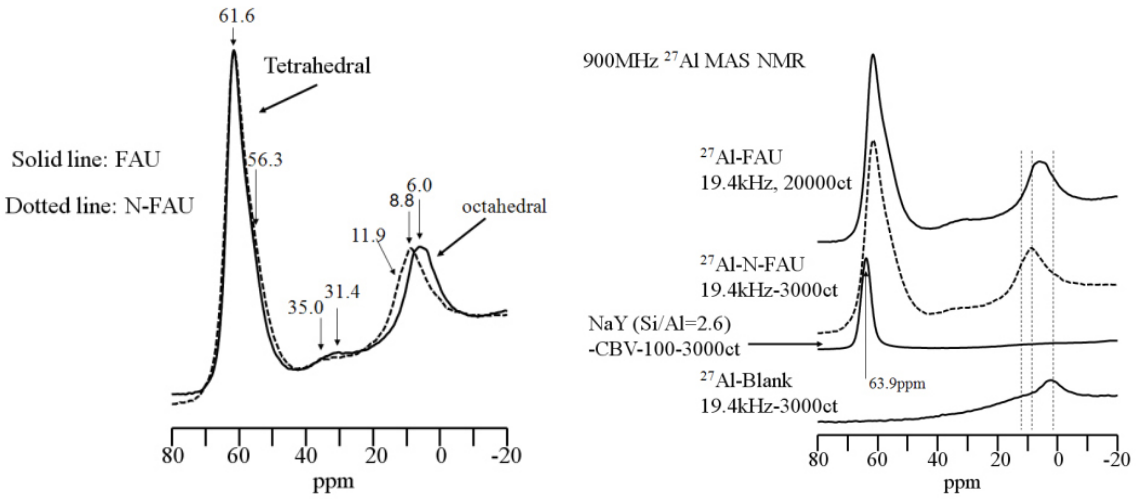

Figure C.8: High Resolution, ^{2}7Al MAS-NMR Testing of FAU and amine treated FAU. (a) zeolite Y and TEA-treated zeolite Y; (b) NH_4Y zeolite, NH_4Y^{+}TEA zeolite, sodium form NaY zeolite, alumina control sample (blank).

rolling baseline is due to the dead time associated with probe ring-down and receiver recovery. The disappearance of the spinning side bands upon TEA treatment may suggest increased framework, molecular motion.

While the ^{2}7Al line shape of the NH_4YN is similar to that of the parent zeolite, the tetrahedral peak is slightly broadened as the center of the octahedral peak shifts to 8.8 ppm. This result indicates that the nitrogen-based species most likely reside primarily on the surface of the zeolite. One interpretation of these results is that the TEA primarily adsorbs on acid sites near the Al species. However, the loss of spinning side bands for the tetrahedral site (Figure C.9) would also suggest a mode of nitrogen incorporation that loosens the faujasite structure (vide supra). The higher resolution spectra in Figures C.8a and C.8b suggest that we have observed an ∼2.5 ppm to 2.8 ppm change in the chemical shift from the zeolite ^{2}7Al NMR spectrum upon TEA-treated, consistent with the conversion of AlO_x bonding sites to $AlO_{x-1}N$ sites (http://www.basechem.org/).

Using the higher resolution data, Figure C.8, we estimated the fraction of the

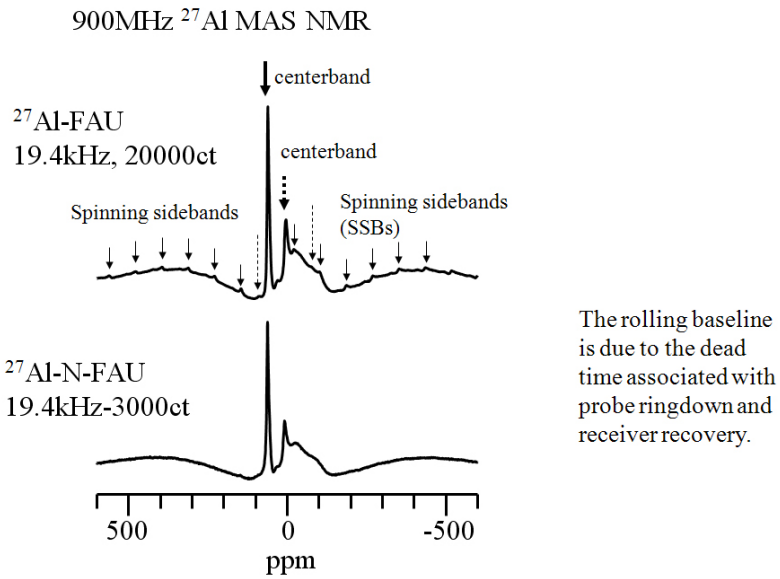

Figure C.9: Lower resolution 900 MHz ^{27}Al MAS-NMR spectrum.

aluminum ions residing the zeolite framework by taking a ratio of the area of the tetrahedral peak, Td, to the area of the octahedral peak, Oh. This fraction was 0.74 for the treated and untreated zeolites. Accordingly, the framework Al density in each sample is $0.74 \times 4.83\,\text{mmol/g} = 3.56\,\text{mmol/g}$ zeolite. The amount of amine added to the zeolite, 5 g, was 35.9 mmol amine or 7.18 mmol amine per gram zeolite, which is about 2 times the framework Al ion density of 3.56 mmol/g zeolite. Thus, the amount of TEA added is enough to titrate all of the framework acid sites in the sample initially, if all of the TEA were adsorbed only to framework Al and Brönsted acid sites. It must be remembered that the non-framework Al species can also interact with the TEA. Thus the degree of saturation of the framework Al and protonic sites depends upon the distribution of TEA between framework and non-framework Al.

C.3.8 Powder X-ray Diffraction Spectra

All of the P-XRD spectrum peaks for the NH_4Y zeolite, shown in Figure C.10, could be reconciled with those reflections present in authentic samples of Y zeolite . The peaks in the TEA-treated zeolite spectrum were uniformly lower in intensity and

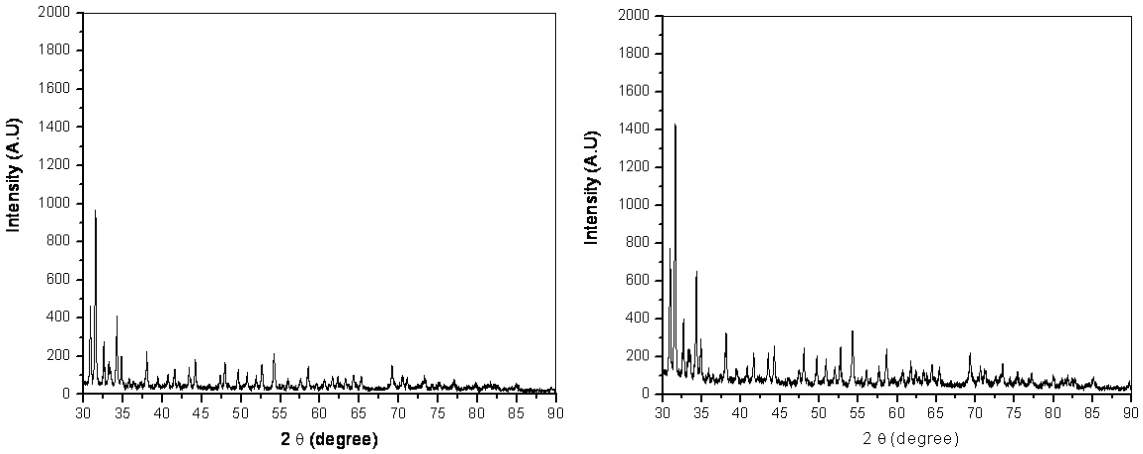

(a) (b)

Figure C.10: PXRD of (a) H^+Y-faujasite and (b) TEA-treated Y-faujasite.

broader than the corresponding peaks in spectrum of the untreated zeolite. No other peaks were present/absent between the spectra of the two samples. It could be conjectured that the TEA treatment slightly perturbed the crystal structure of the zeolite to form a less rigid crystalline structure than that of the untreated zeolite. The ^{27}Al MAS-NMR suggests this possibility since the areas under the Oh peaks in each spectrum were the same, indicative of very little removal of Al oxide from the sample.

It is instructive to compare these P-XRD results with the surface area/porosity results obtained from the surface area studies. Decreased crystallinity of the zeolite is consistent with loss of microporosity, resulting in lower specific surface area and lower specific pore volume. Since these extra amounts of amorphous products were not observed in the P-XRD, another technique, such as solid state MAS-NMR, was used to confirm the identities of these phases, vide supra. Finally, one might consider the smaller P-XRD peaks to be consistent with a lower symmetry in the crystal structure or a somewhat looser structure indicated by the change in the spinning side bands in the ^{27}Al MAS-NMR spectrum (vide supra).

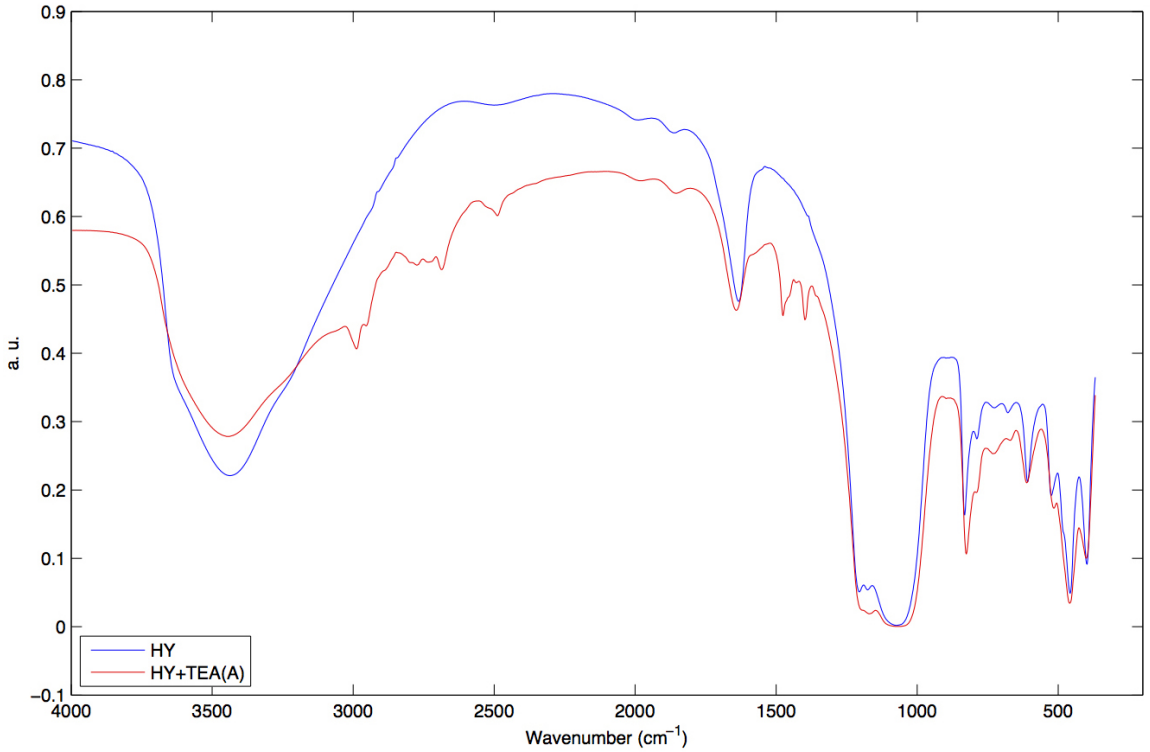

Figure C.11: Transmittance IR of HY zeolite and TEA-treated HY+TEA(A) zeolite.

C.3.9 IR Spectroscopy

Figure C.11 illustrates the differences in the mid-IR transmittance spectrum of HY zeolite and HYN-A. Table C.5 compares the assignment of the peaks in these two spectra upon consideration of the IR spectra of TEA liquid and the TEA-hydrochloride salt.

Peaks characteristic of the zeolite [102] appear in both spectra at the following wavenumbers: 3670, 3650 (ν, O−H); 3440 (ν, O−H); 1640 (δ, O−H); 1200, 1180, 1080 (Si−O−Si). The vibrations below 1080 are characteristic of the zeolite framework vibrations. Peaks at wavenumbers of 2988, 2952, 2774, 2686, and 2490 also appeared in the spectrum of the solid TEA$-H^+Cl^-$ salt and could be assigned to the ν, C−H (http://www.chemexper.com/cheminfo/servelt/org.dbcreator.Main). One peak at 2734 cm^{-1} compared well with a vibration (ν, C−H) of liquid TEA (SDBS of Organic Compounds). Peaks in the finger-print region could be attributed

Table C.5: Wavenumbers (cm^{-1}) for Peaks in % T for proton-form zeolite, HY, and method A treated zeolite, HYN-A.

HY	HYN-A	Assignments
3650	3670	ν,O−H
3440	3444	ν, O−H and ν C−H, H^+TEA^-
	2988	ν, C−H, H^+TEA^-
	2952	ν, C−H, H^+TEA^-
	2774	ν, C−H, H^+TEA^-
	2734	ν, C−H, TEA
	2686	ν, C−H^+TEA^-
2500	2500	not assigned
	2490	ν, C−H^+TEA^-
1640	1641	δ, O−H
	1476	δ, C−H^+TEA^-
	1397	ω, C−H^+TEA^-
1200	1198	Si−O−Si and C−N, TEA(?)
1180	1169	Si−O−Si
1080	1068	Si−O−Si and ω, C−H^+TEA^-
800	730	Zeolite framework
600	611	Zeolite framework
520	515	Zeolite framework
460	459	Zeolite framework
400	400	Zeolite framework

to the C−H deformation and wagging motions of the protonated TEA: 1476 (δ, C−H^+TEA^-), 1397(ω, C−H^+TEA^-), 1068 (ω, C−H^+TEA^-). One small vibration at 2500 cm^{-1} could not be assigned.

C.4 Discussion of Results

The TEA molecule can interact with the zeolite 1) by hydrogen-bonding with surface silanols and aluminols, 2) by forming strong chemisorption bonds to the framework protons and framework Al cations in the zeolite, and 3) by association with extra-framework alumina. Evidence is reported for these types of interactions of TEA with the surface of titania, which shows both acid and base sites [69]. The NMR data show that about 75 % of the Al species are incorporated into the zeolite leaving

about 25 % of the Al species as extra-framework alumina. From a consideration of the ^{27}Al MAS-NMR characterization of the zeolite and the silica to alumina ratio, we estimate that the average loading of TEA corresponds to 2 TEA molecules per framework Al ion which should be sufficient to insure coverage of at least one TEA per Brönsted/Lewis site provided that none of the TEA is sequestered by the extra-framework alumina. However, if some of the TEA migrate to the available extra-framework Al sites, we may set an upper limit on this TEA migration assuming 1 TEA per 1 Al site. Beginning with a loading of 2 TEA per framework Al, the amount of TEA available is 3/2 of the total Al available in the sample. The number of non-framework Al per framework Al is $0.25/0.75 = 1/3$. If all of the non-framwork Al were available for TEA sorption, then the amount of TEA on non-fraemwrok Al would be divided according to the relative amounts of Al, provided that TEA is attracted to each site equally well. Thus, 3/4 of the total adsorbed TEA is adsorbed to framework Al, making this stoichiometry of 2(3/4) TEA per framework Al and 2(1/4) TEA per non-framwork Al. That is, assuming the most favorable case for TEA redistribution, each framework Al will sequester 3 TEA molecules between two such sites; whereas, the non-framework Al will bind 1 TEA between 2 non-framework Al sites. From this simple calculation, we estimate that the loading of TEA at the framework Al sites to be bonded between 1.5 and 2 TEA molecules per framework Al site.

The zeolite contains both Brönsted acid, B, and Lewis acid, L, sites. The B site is a proton sited on an oxygen anion close to the Al cation and the L site is an Al cation showing a coordination of three and one uncoordinated position. The ratio of these sites depends upon the degree of hydration as governed by the following equation:

$$\mathrm{B} + \mathrm{heat} \longrightarrow \mathrm{L} + \mathrm{H_2O} \tag{C.7}$$

The TEA molecule should be able to coordinate to either of these sites. When TEA is coordinated to a B site, the proton can form the charged species: $\mathrm{H^+TEA}$;

whereas, the coordination to Al cation forms the complex TEA−Al. The zeolites were not dehydrated prior to the TEA treatment. The TPD experiments confirmed that these samples contained water, Figure C.5; thus, we expect that Brönsted sites should be present in these samples. The activity of the samples to catalyze the Hoffmann elimination reaction to form ammonia and ethylene is further evidence of proton acidity in the sample. We find direct evidence of the protonated TEA in the IR data and also find evidence of the weakly adsorbed TEA in both the IR and Raman spectra. These IR and Raman data are consistent with a model where the amine N donates electron density to the Brönsted site proton, which resides on the O bridging between the Si and Al cations. The XPS data of binding energies also supports this model where the amine N surrenders electron density when it interacts with the proton in the zeolite. As a result of this amine-proton interaction, we speculate that the O anion bonded to the proton retrieves some of the electron density formally residing on the proton in the untreated zeolite. Data of O1s BEs show that with this electron transfer, these O anions show BEs which are 0.4 eV to 0.6 eV lower than the undecorated zeolite Y. This increased electron density residing on the bridging O anions is partially redistributed to the adjacent Al and Si cations, which is reflected in a decrease of these BEs by 1 eV to 2 eV in the Al/Si XPS of the TEA-decorated Y zeolites. The data obtained from Raman, IR, XPS, and TPD experiments show that N species are retained in the TEA-treated Y-zeolites.

The formation of the H^+TEA^- species in the TEA-treated zeolite explains the absence of activity to form the dehydration product, DME, from MeOH. This result is completely consistent with the surface model that we have advanced here where Brönsted sites are "neutralized" by the triethylamine to form an unreactive, protonated amine resting on the surface. The small yields of carbon monoxide and formaldehyde were a surprising result because these products are associated with base-catalyzed and/or redox catalysis of methanol. Thus, the decoration by TEA

does eliminate all acidic catalytic activity, vide supra.

The formation of formaldehyde can be attributed to a reaction manifold that involves a redox reaction and a mechanism that involves a base site [249]. We rule out the redox chemistry since the metal cations in zeolite Y are considered to be irreducible and thus we must look to another chemistry inferred by the appearance of formaldehyde. Recently, it was reported that alkali-exchanged, faujasites, including zeolite Y, and alkali-doped alumina catalyzed the decomposition of MeOH to formaldehyde and CO [277]. This base catalysis explains the small yields of formaldehyde we observed over the untreated zeolite since it contained small amounts of sodium (0.2 wt% reported as Na2O).35 Thus, we believe that the genesis of formaldehyde, CO, and CO_2 observed in the untreated zeolite and the TEA-treated zeolite is attributed to a reaction manifold that is catalyzed by Brnsted base sites, such Na^+ and possibly OH^-.

The interaction of TEA with the Ti nanocolloid was different from that observed for the interaction with the already-formed, microcrystalline zeolite. In the case of the nanocolloid, the large heat effect of $-12.99\,\text{kcal/mol}$ titania suggests that this interaction between TEA and the Ti nanocolloid is much stronger than hydrogen-bonding and does lead to significant incorporation of N species into the final oxide. On the other hand, this type of heat effect is absent from the interaction between TEA and the Y-zeolite suggesting no such wide scale reaction between the amine and the zeolite. Moreover, the heat effect of TEA interacting with the Ti nanocolloid at near room temperature is consistent with a low activation energy process, such as ligand exchange with other ligands in solution. This ligand exchange process is not possible in a rigid, already-formed metal oxide such as the zeolite. For the zeolite, reactions with N-containing species were observed only at high temperatures, which is characteristic of a high activation energy process.

C.5 Conclusions

Room temperature treatment of porous nanotitania and Y-zeolite with triethylamine was found to significantly change the properties of these materials in contrasting ways. The titania nanocolloid reacts vigorously with TEA given an exothermic heat effect of $-12.99\,\mathrm{kcal/mol}$ titania; whereas, the microcrystalline Y-zeolite does not show such a heat effect. A BET analysis shows a surprisingly large surface area for the titania and not surprisingly a much larger surface area for Zeolite Y than the titania samples. The physical properties including the surface area are modified in contrasting ways upon treatment with TEA; the surface area increased by the TEA treatment for titania and decreased by the TEA treatment of the zeolite. The fate of the TEA on the surface of the zeolite, probed by IR spectroscopy and TPD, demonstrates that the TEA was strongly adsorbed as the TEA^+ cation, and this cation reacted by the Hoffman elimination reaction to form ethylene and ammonia upon heating. This strong chemisorption of the TEA to the zeolite, was found to effectively neutralize the Brönsted sites as catalyst for the methanol probe reaction to form the acid-catalyzed product–dimethyl ether. The TPSR data indicate that TEA strongly interacts (reacts) with the Brönsted acid sites of the zeolite, while no other sites remained strong enough to react with methanol were present on the surface. Instead, the base catalysis manifold for this reaction became evident, possibly via the action over the small amount of sodium ion left in the sample. Raman and IR data are consistent with a model whereby the amine N contributes electron density to a proton residing on the O atom shared by the zeolite framework Al and Si ions.

C.6 Acknowledgements

The authors thank the Georgia Institute of Technology for partial support of this work through the Creating Energy Options (CEO) Program. We also acknowledge the support from Micromeritics Instruments, Inc. Specifically, we acknowledge the

efforts of Ms. Yanette Pederson. The authors thank Professor Christopher Jones, School of Chemical and Biomolecular Engineering for this thoughtful advice and consultation.

APPENDIX D

PROGRAMS FOR SIMULATIONS AND MODELING

D.1 sensorsimulation.py

```
##================Sensor Simulation=================================

import pylab

import numpy as np

import csv as csv

import matplotlib.pyplot as plt

import math as math

from scipy.signal import gaussian

from scipy.optimize import curve_fit


##=================================================================##

##                  Global Variables                               ##

##=================================================================##


##=====Raw Input===============##

##Parameter Guesses

df= float(raw_input("Diffusion constant" +/

        "guess [normal = 0.0029]:  ") or 0.0029)

K1 = float(raw_input("Gas 1 Asdorption/" +/

        "Desorption [normal = 0.38]:  ") or 0.38)

A = float(raw_input("Fermi A coefficent " +/

        "guess [normal = 740000]:  ") or 740000)
```

```
E_F = float(raw_input("Fermi energy " +/
        "guess [normal = 0.808]:  ") or 0.808)
perform_fit = bool(int(raw_input("Perform f" +/
        "it? [1=True/0=False]:  ") or 1))
##Iteration cycles
tries_df = int(float(raw_input("Number of " +/
        "iterations for df [normal = 20]:  ") or 3))
cycles =  int(float(raw_input("Number of " +/
        "cycles [normal = 3]:  ") or 3))
try:
    force = bool(int(raw_input("Force iterated " +/
        "search for para? [1=True/0=False]: ") or 0))
except:
    force = False
if force == True:
    tries_para = int(float(raw_input("Number " +/
        "of iterations for para [normal = 40]:  ") or 40))
else:
    tries_para = 20


##=====Hard Coded Values=========##
#Dataset settings#
data_set = [('p11_s8_nh3_042814.lvm','experiment',1)]
short_data_file = True
gas_table = 'gas_table_NO.csv'
gas_type = 1    #1 = NH3, 2 = NO, 3 = H2S
sensor_type = 1 #1 = p-type, 2 = n-type
```

```
#Simulation Settings#
RM = 1
purge_time = 1700  #cut off from beginning
x_minimum = 0     #use this to zoom in.
x_maximum = 0   #cut off from end of run for plotting
sticky=1
report_sticky = True
sim_type = 1  #(1 = one gas; 2 = two gas)
sim = 'simulation'
window_size = 200 #widow size for gaussain window
window_sigma = 40 #standard div for gaussain window
#Other settings#
if data_set[0][2] == 4:
    dt = 0.05
elif data_set[0][2] == 3:
    dt = 0.1
elif data_set[0][2] == 2:
    dt = 1
else:
    dt = 0.05
n = 10
#Set up acid/base definition for response mechanism
if gas_type == 1:
    lewis = 1
elif gas_type == 2:
    lewis = -1
else:
```

```
    lewis = 1
#Set up p-type/n-type definition for response mechanism
if sensor_type == 1:
    p_ntype = 1
elif sensor_type == 2:
    p_ntype = -1
else:
    p_ntype = 1
##================================================================##
##                  Response Mechanism                            ##
##================================================================##

def fermi_response(C_avg, K1, A, E_F):
    '''This is the response mechanism with a langmuir adsoption,
    and then a Fermi sensor response
    *takes in C_avg, outputs resistance change
    *K1 is the adsoption coefficent, chemical property of
    gas/sensor
    *A is a coefficent for fermi response, physical property
    of sensor
    *E_F is the change in Fermi energy when saturated'''
    global lewis
    global p_ntype
    #Various response mechanisms for testing
    if RM == 1:
    #Combined BET adsorption - Fermi-Distribution
    #response mechanism
```

```
    ##calculate the relative change in Fermi energy
    #via BET Isotherm
        BET = 100
        dE = K1*C_avg/((BET-C_avg)*(1+(K1-1)*C_avg/BET))
    ##calculate sensor response via fermi distribution
        R_c = (1+A)/(1+A*np.exp(-E_F*dE*lewis*p_ntype))
    elif RM == 2:
    #Langmuir adsorption isotherm response mechanism
        dE = K1*C_avg/(1+K1*C_avg)
        R_c = 1 + A*dE*lewis
    elif RM == 3:
    #Linear response mechanism
        dE = C_avg
        R_c = 1 + A*dE*lewis
    elif RM == 4:
    #Fermi Distribution response mechanism
        dE = C_avg
        R_c = (1+A)/(1+A*np.exp(-E_F*dE*lewis*p_ntype))
    elif RM == 5:
    #Volkenstein response mechanism
        B = K1/(1+np.exp(-E_F))
        dE = B*C_avg/(1+B*C_avg)
        R_c = 1 + A*dE
    return R_c

##=================================================================##
##                  Plot Actual Data                               ##
```

```
##=============================================================##

def open_sensor_file(sensor_file):
    '''opens a file, skips the headers and returns an array'''
    inFile = open(sensor_file)
    if short_data_file:
        lines = inFile.readlines()[22:-1]
    else:
        lines = inFile.readlines()[36:-1]
    data = []
    for line in lines:
        fields = line.split('\t')
        data.append([int(float(fields[0])),
                     float(fields[1].strip('\r\n'))])
    data = np.array(data)
    return data


def normalize_response(data, data_type):
    '''seeks baseline and normalizes the data'''
    if data_type == 1: #time step of 0.05 seconds
        normalized_value = data[33000:36000,1].sum()/float(3000)
        x = 20
    elif data_type == 2: #time step in seconds
        normalized_value = data[1400:1800,1].sum()/float(400)
        x = 1
    elif data_type == 3: # time step of 0.1 seconds
        normalized_value = data[16000:18000,1].sum()/float(2000)
```

```
        x = 10
    elif data_type == 4: #time step of 0.05 seconds
        normalized_value = data[4000:4500,1].sum()/float(500)
        x = 20
    else:
        print 'Unknown data type'
        return None
    normalized_data = np.column_stack((data[:,0]/x,
                    data[:,1]/normalized_value))
    return normalized_data

def movingaverage(interval, window_size, window_sigma):
    '''This is a Gaussain low pass filter,
    used for noise reduction.  Parameters hard coded
    as global varible'''
    window = gaussian(int(window_size), window_sigma)
    window = window/sum(window) #renormalize
    return np.convolve(interval, window, 'same')

##============================================================##
##             Concentration calculator (new)                 ##
##============================================================##

def Cavg_calc_new(gastime, df, dt):
    '''New method of caclulating Cavg.  Combines the original
    gasDiffusion1 and Cavg_calc functions and improves processing
    time'''
```

```
global n


##======setting up evolution matrix================##
m = np.zeros([n+1,n+1])
##last row
a = np.zeros(n+1)
a[-2],a[-1] = [1,-1]
m[-1] = a
##middle
for i in range(1,n):
    a = np.zeros(n+1)
    a[i-1], a[i], a[i+1] = [1,-2,1]
    m[i] = a
delta = df*dt*n**2*m


#application of stickiness parameter
for i in range(n+1):
    for j in range(n+1):
        if delta[i,j] < 0:
            delta[i,j] = delta[i,j]*sticky


m = np.identity(n+1)+delta
##======apply evolution matrix=====================##
C = np.zeros([n+1,len(gastime)])
for i in range(0,len(gastime)-1):
    C[0,i] = gastime[i]
    C[:,i+1] = np.dot(m,C[:,i])
```

```
    ##removing concentration outside pores
    C_pore = C
    C_pore[0] = np.zeros(len(gastime))
    C_average = sum(C_pore)/float(n)
    return C_average

##=====================================================================##
##                  Gas Generation Functions                           ##
##=====================================================================##

def generateGas1(purge_time, gas_ppm, time_on, time_off):
    '''Generates gas picture for figures or simulations
    *purge_time is an int
    *gas_ppm is a vector of the different gas concentrations
    *time_on is time on for the gas
    *time_off is the time off for the gas
    '''
    gastime = []
    for time in range(purge_time):
        gastime.append(0)
    for i in gas_ppm:
        for j in range(time_on):
            gastime.append(i)
        for j in range(time_off):
            gastime.append(0)
    return gastime
```

```
def open_gas_file(gas_file):
    '''opens a file, skips the headers and
    returns an array'''
    inFile = open(gas_file)
    lines = inFile.readlines()[1:]
    data = []
    for line in lines:
        fields = line.split(',')
        data.append([int(float(fields[0])),
                     int(float(fields[1])),
                int(float(fields[2].strip('\r\n')))])
    data = np.array(data)
    return data


def generateGas2(gas_table):
    '''Generates gas picture for figures or simulations,
    using imported gas table'''
    gas = []
    counter = 1
    for i in gas_table:
        for j in range(int(i[2]/dt)):
            gas.append([i[0],i[1],counter])
            counter += 1
    gas = np.array(gas)
    return gas
```

```
def generateGas3(gas_table):
    '''Generates gas picture for figures or
    simulations, using imported gas table.
    *Includes linear concentration
    increase (opposed to step fuction)'''
    gas = []
    counter = 1
    for i in gas_table:
        counter2 = 1
        for j in range(int(i[2]/dt)):
            if j < 10/dt:
                gas.append([i[0]/(10/dt)*j,
                                i[1]/(10/dt)*j,counter])
                counter += 1
            else:
                gas.append([i[0],i[1],counter])
                counter += 1
    gas = np.array(gas)
    return gas


def generateGas4(gas_table):
    '''Generates gas picture for figures
    or simulations, using imported gas table.
    *Includes exponential concentration turn on
    and turn off (opposed to step function)'''
    gas = []
    counter = 1
```

```
for i in gas_table:
  counter2 = 1
  for j in range(int(i[2]/dt)):
      try:
          if i[0] != 0:
              if i[1] != 0:
                 gas.append([i[0]*(1-np.exp(-j/(5/dt))),
                   i[1]*(1-np.exp(-j/(5/dt))), counter])
                 counter += 1
              elif i[1] == 0:
                 gas.append([i[0]*(1-np.exp(-j/(5/dt))),
                   gas[-1][1]*np.exp(-j/(5/dt)), counter])
           elif i[0] == 0:
               if i[1] != 0:
                  gas.append([gas[-1][0]*np.exp(-j/(5/dt)),
                    i[1]*(1/(1+np.exp(-10*(j/(8/dt)-.5)))),
                    counter])
                  counter += 1
               elif i[1] == 0:
                  gas.append([gas[-1][0]*np.exp(-j/(5/dt)),
                    gas[-1][1]*np.exp(-j/(100/dt)), counter])
                  counter += 1
     except:
         gas.append([0, 0, counter])
         counter += 1
gas = np.array(gas)
return gas
```

```
##=====================================================================##
##                      Derivative Functions                           ##
##=====================================================================##


def deriv(x, y):
    '''This will take the first derivative of the data'''
    z = range(len(x) - 1)
    yp = []
    for i in z:
        dx = dt
        dy = y[i+1]-y[i]
        yp.append(dy/dx)
    yp.append(yp[-1])
    yp = np.array(yp)
    return yp


def deriv30(x, y):
    '''This will take the first derivative of the data'''
    z = range(len(x) - 600)
    yp = []
    for i in z:
        dx = dt*600
        dy = y[i+600]-y[i]
        yp.append(dy/dx)
    for i in range(600):
        yp.append(yp[-1])
```

```
    yp = np.array(yp)
    return yp

##=================================================================##
##                  Fitting Programs (new)                         ##
##=================================================================##

def df_fit(datay, gastime, dt, para_guess, df_guess, tries_df):
    '''Takes in all guess values and finds optimal df
    '''

    ##=====Initialize Everything========##
    df_guess0 = df_guess
    K1_guess, A_guess, E_F_guess = para_guess

    ##Run initial guess and calculate error
    Cavg_fit = Cavg_calc_new(gastime,df_guess0,dt)
    fity = fermi_response(Cavg_fit,K1_guess,A_guess,E_F_guess)
    SoS = np.sum(np.square(np.subtract(datay,fity)))

    ##=====Perform df Iterations===========##
    print 'Optimizing df'

    ##Initialize guess adjustments
    guess_add = df_guess0
    guess_subtract = df_guess0
    guess = df_guess0
```

```
i = 0
while i < tries_df:

    print '     Iteration #'+str(i+1)
    print '          [Mid] df: '+str(guess)+'| SoS:  '+str(SoS)

    ##Create high and low guesses
    guess_high = guess + guess_add
    guess_low = guess - guess_subtract
    if (guess_low < 0): guess_low = 0

    ##Run fit high and low simulations and calculate error
    Cavg_high = Cavg_calc_new(gastime, guess_high, dt)
    fity_high = fermi_response(Cavg_high,
                   K1_guess,A_guess,E_F_guess)
    SoS_high = np.sum(np.square(np.subtract(datay, fity_high)))
    print '          [High] df: '+str(guess_high)+\
                          '| SoS:  '+str(SoS_high)

    Cavg_low = Cavg_calc_new(gastime, guess_low, dt)
    fity_low = fermi_response(Cavg_low,
                   K1_guess,A_guess,E_F_guess)
    SoS_low = np.sum(np.square(np.subtract(datay, fity_low)))
    print '          [Low] df: '+str(guess_low)+\
                          '|  SoS: '+str(SoS_low)
```

```
        ##Compare and choose best fit
        if min(SoS, SoS_low, SoS_high) == SoS_low:
            guess = guess_low
            Cavg_fit = Cavg_low
            fity = fity_low
            SoS = SoS_low
            guess_add = guess_add/2
            guess_subtract = guess_subtract/2
        elif min(SoS, SoS_low, SoS_high) == SoS:
            guess_add = guess_add/2
            guess_subtract = guess_subtract/2
        elif min(SoS, SoS_low, SoS_high) == SoS_high:
            guess = guess_high
            Cavg_fit = Cavg_high
            fity = fity_high
            SoS = SoS_high
        i +=1
    print 'df: '+str(guess)+' | SoS: '+str(SoS)
    return [Cavg_calc_new(gastime, guess, dt), guess]

def para_fit(datay, C_avg, para_guess, tries_para):
    '''This is the fitting function for K1, A
    and E_F using the same method as df'''
    ##=====Initialize Everything========##
    K1_guess0, A_guess0, E_F_guess0 = para_guess
    fity = fermi_response(C_avg,K1_guess0,A_guess0,E_F_guess0)
    SoS = np.sum(np.square(np.subtract(datay,fity)))
```

```
##=====Perform K1 Iterations===========##
print 'Optimizing K1'

#Initialize guess adjustments
guess_add = K1_guess0
guess_subtract = K1_guess0
guess = K1_guess0

i = 0
while i < tries_para:
    print '     Iteration #'+str(i+1)
    print '          [Mid] K1: '+str(guess)+'| A: '+\
    str(A_guess0)+' | E_F: '+str(E_F_guess0)+' |SoS: '+str(SoS)

    #Create high and low guesses
    guess_high = guess+guess_add
    guess_low = guess-guess_subtract

    #Run high and low simulations and calculate error
    fity_high = fermi_response(C_avg,
                    guess_high, A_guess0, E_F_guess0)
    SoS_high = np.sum(np.square(np.subtract(datay,fity_high)))
    print '          [High] K1: '+str(guess_high)+\
                    '| A: '+str(A_guess0)+' | E_F: '+\
            str(E_F_guess0)+' |SoS: '+str(SoS_high)
```

```
    fity_low = fermi_response(C_avg,
                    guess_low, A_guess0, E_F_guess0)
    SoS_low = np.sum(np.square(np.subtract(datay,fity_low)))
    print '           [Low] K1: '+str(guess_low)+\
                    '| A: '+str(A_guess0)+' | E_F: '+\
            str(E_F_guess0)+' |SoS: '+str(SoS_low)

    #Compare and choose best fit
    if min(SoS, SoS_low, SoS_high) == SoS:
        guess_add = guess_add/2
        guess_subtract = guess_subtract/2
    elif min(SoS, SoS_low, SoS_high) == SoS_low:
        guess = guess_low
        fity = fity_low
        SoS = SoS_low
        guess_add = guess_add/2
        guess_subtract = guess_subtract/2
    elif min(SoS, SoS_low, SoS_high) == SoS_high:
        guess = guess_high
        fity = fity_high
        SoS = SoS_high
    i +=1
K1_opt = guess

##=====Perform A Iterations==========##
print 'Optimizing A'
```

```
#Initialize guess adjustments
guess_add = A_guess0
guess_subtract = A_guess0
guess = A_guess0

i = 0
while i < tries_para:
    print '     Iteration #'+str(i+1)
    print '          [Mid] K1: '+str(K1_opt)+'| A: '+\
                  str(guess)+' | E_F: '+str(E_F_guess0)+\
            ' |SoS: '+str(SoS)

    #Create high and low guesses
    guess_high = guess+guess_add
    guess_low = guess-guess_subtract

    #Run high and low simulations and calculate error
    fity_high = fermi_response(C_avg, K1_opt,
                  guess_high, E_F_guess0)
    SoS_high = np.sum(np.square(np.subtract(datay,fity_high)))
    print '         [High] K1: '+str(K1_opt)+\
                  '| A: '+str(guess_high)+' | E_F: '+\
            str(E_F_guess0)+' |SoS: '+str(SoS_high)

    fity_low = fermi_response(C_avg, \
    K1_opt, guess_low, E_F_guess0)
    SoS_low = np.sum(np.square(np.subtract(datay,fity_low)))
```

```
        print '           [Low] K1: '+str(K1_opt)+\
                        '| A: '+str(guess_low)+' | E_F: '+\
                        str(E_F_guess0)+' |SoS: '+str(SoS_low)

        #Compare and choose best fit
        if min(SoS, SoS_low, SoS_high) == SoS:
            guess_add = guess_add/2
            guess_subtract = guess_subtract/2
        elif min(SoS, SoS_low, SoS_high) == SoS_low:
            guess = guess_low
            fity = fity_low
            SoS = SoS_low
            guess_add = guess_add/2
            guess_subtract = guess_subtract/2
        elif min(SoS, SoS_low, SoS_high) == SoS_high:
            guess = guess_high
            fity = fity_high
            SoS = SoS_high
        i +=1
    A_opt = guess

    ##=====Perform E_f Iterations==========##
    print 'Optimizing E_F'

    #Initialize guess adjustments
    guess_add = E_F_guess0
    guess_subtract = E_F_guess0
```

```
guess = E_F_guess0


i = 0
while i < tries_para:
    print '     Iteration #'+str(i+1)
    print '          [Mid] K1: '+str(K1_opt)+\
                          '| A: '+str(A_opt)+' | E_F: '+\
                  str(guess)+' |SoS: '+str(SoS)

    #Create high and low guesses
    guess_high = guess+guess_add
    guess_low = guess-guess_subtract

    #Run high and low simulations and calculate error
    fity_high = fermi_response(C_avg,
                  K1_opt, A_opt, guess_high)
    SoS_high = np.sum(np.square(np.subtract(datay,fity_high)))
    print '         [High] K1: '+str(K1_opt)+\
                          '| A: '+str(A_opt)+' | E_F: '+\
                  str(guess_high)+' |SoS: '+str(SoS_high)

    fity_low = fermi_response(C_avg,
                  K1_opt, A_opt, guess_low)
    SoS_low = np.sum(np.square(np.subtract(datay,fity_low)))
    print '          [Low] K1: '+str(K1_opt)+\
                          '| A: '+str(A_opt)+' | E_F: '+\
                  str(guess_low)+' |SoS: '+str(SoS_low)
```

```
            #Compare and choose best fit
            if min(SoS, SoS_low, SoS_high) == SoS:
                guess_add = guess_add/2
                guess_subtract = guess_subtract/2
            elif min(SoS, SoS_low, SoS_high) == SoS_low:
                guess = guess_low
                fity = fity_low
                SoS = SoS_low
                #E_F can be negative
            elif min(SoS, SoS_low, SoS_high) == SoS_high:
                guess = guess_high
                fity = fity_high
                SoS = SoS_high
            i +=1
        E_F_opt = guess

        ##=====Final outputs====================##
        para = [K1_opt, A_opt, E_F_opt]
        covar = 'N/A'
        return [para, covar]

    def fermi_fit(datay, C_avg, para_guess, tries_para):
        '''Optimizes the rest of the varibles, returns
        simulation data
        *first tries non-linear least square fit
        *if that falls through use the same method for df'''
```

```
    global force
    if force == False:
        try:
            print 'Optimizing para. . .'
            para, covar = curve_fit(fermi_response,
                    C_avg, datay)
        except RuntimeError:
            print 'Optimizing para failed'
            para, covar = para_fit(datay, C_avg,
                    para_guess, tries_para)
    elif force == True:
        para, covar = para_fit(datay, C_avg,
                        para_guess, tries_para)

    ##printing final results
    K1_opt = para[0]
    A_opt = para[1]
    E_F_opt = para[2]
    print 'K1: '+str(K1_opt)+' | A: '+\
                    str(A_opt)+' | E_F: '+str(E_F_opt)
    print covar
    return [fermi_response(C_avg,
                    K1_opt, A_opt, E_F_opt), para]

##============================================================##
##                    Gas Wrapper Functions                   ##
##============================================================##
```

```
def oneGas():
    '''This is the gas wrapper function that
    runs the simulation and
    plots the response vs time'''

    print "Importing Sensor Data. . ."
    for data in data_set:
        data0 = normalize_response(open_sensor_file(data[0]),
                        data[2])
        txt_data = '['+ data[0] + ']'
    datay = movingaverage(data0[:,1], window_size,
                    window_sigma)
    datay = datay[:-window_size] #  Remove discontinuities

    print "Generating gas. . ."
    gas = generateGas4(open_gas_file(gas_table))
    gas = gas[:-window_size,:] #Remove items from gas table
    #so that simulation and experiment data have same length

    time = data0[int(purge_time/dt):-window_size,0]
    datay = datay[int(purge_time/dt):]
    gas = gas[int(purge_time/dt):]
    gas[:,2] = gas[:,2]-int(purge_time/dt)
    ##======Perform Fit======================##
    print "Running Fitting Program. . ."
    n = 0
```

```
para = [K1, A, E_F]
df_opt = df
if perform_fit == True:
    while n < cycles:
        print '##### Starting cycle # %d #####' %(n+1)
        Cavg, df_opt = df_fit(datay, gas[:,1], dt,
                para, df_opt, tries_df)
        simulated, para = fermi_fit(datay, Cavg, para,
                tries_para)
        print 'df: '+str(df_opt)
        SoS = np.sum(np.square(np.subtract(datay,simulated)))
        print 'SoS: '+str(SoS)
        n += 1
        print '##### Cycle # %d complete #####' %n
else:
    simulated = fermi_response(Cavg_calc_new(gas[:,1], df, dt),
                    K1, A, E_F)
    SoS = 0

print "Taking derivative. . ."
D_simulated = deriv(gas[:,2],simulated)

##======Finally Plotting=======================##
print "Plotting simulation"
fig, ax1 = plt.subplots(2, sharex = True)

## Plotting simulated data
```

```
ax1[0].plot(gas[:,2]*dt, simulated, color='b',label = sim)
ax1[1].plot(gas[:,2]*dt, D_simulated, color='b',
                label = 'First Derivative')
## Plotting Data
ax1[0].plot(gas[:,2]*dt, datay,'k', label = data[1])
d = deriv(gas[:,2],datay)
ax1[1].plot(gas[:,2]*dt,d,color='k')

## Plotting gas table
ax2 = ax1[0].twinx()
ax3 = ax1[1].twinx()
ax2.plot(gas[:,2]*dt,gas[:,1], 'r--',label='NH3')
ax3.plot(gas[:,2]*dt,gas[:,1], 'r--',label='NH3')
## Axis
ax1[0].set_ylabel('Relative Response', color='k')
ax1[1].set_ylabel('First Derivative of Response', color='k')
for tl in ax1[0].get_yticklabels():
    tl.set_color('k')
ax1[0].set_ylim([0.97*min(min(simulated),min(datay[100:])),
        1.01*max(max(simulated),max(datay))])
ax1[1].set_ylim([1.1*min(min(D_simulated),min(d[100:])),
        1.04*max(max(D_simulated),max(d[100:]))])
ax1[0],ax1[1].set_xlabel("Time (s)")
if lewis == 1:
    ax1[0].legend(loc = 'upper left')
else:
    ax1[0].legend(loc = 'upper right')
```

```
    ax2.set_ylabel('Gas ppm', color='r')
    ax3.set_ylabel('Gas ppm', color='r')
    for tl in ax2.get_yticklabels():
        tl.set_color('r')
    for tl in ax3.get_yticklabels():
        tl.set_color('r')
    ax2.set_ylim([0,30])
    ax3.set_ylim([0,30])
#     ax2.legend(loc = 'upper center')
#     ax2.set_position((.1, .15, .8, .75))
    ax1[:],ax2.set_xlim(xmin=x_minimum,
            xmax=gas[-1,2]*dt-x_maximum)

    ## Appending text
    if RM == 1:
        txt1 = '\
        \ndE = K1*C_avg/((BET-C_avg)*(1+(K1-1)*C_avg/BET))\
        \nR = (1+A)/(1+A*exp(-E_F*dE))'+\
        '\nSum of Squares = '+str(SoS)
    elif RM == 2:
        txt1 = '\
        \ntheta = K1*C_avg/(1+K1*C_avg)\
        \nR = 1 + A*theta'+\
        '\nSum of Squares = '+str(SoS)
    elif RM == 3:
        txt1 = '\
        \ndR = A*C_avg\
```

```
    \nR = 1 + A*theta'+\
    '\nSum of Squares = '+str(SoS)
elif RM == 4:
    txt1 = '\
    \ndE = C_avg\
    \nR = (1+A)/(1+A*exp(-E_F*dE))'+\
    '\nSum of Squares = '+str(SoS)
elif RM == 5:
    txt1 = '\
    \nB = K1/(1+exp(-E_F))\)\
    \ntheta = B*C_avg/(1+B*C_avg)\
    \nR = 1 + A*theta'+\
    '\nSum of Squares = '+str(SoS)



txt3 = 'df = ' + str(df_opt) +\
    '\nK = ' + str(para[0])+'\nA = ' + \
    str(para[1])+' | E_F = ' + str(para[2])

## report fitted data file
if report_sticky:
    fig.text(.01, .01, 'sticky: '+str(sticky))

fig.text(.6, .01, txt_data)

fig.text(.12,.91,txt1)
```

```
    fig.text(.5,.91,txt3)
    pylab.show()

##====================================================================##
##                    Run Code                                        ##
##====================================================================##

if sim_type == 1:
    oneGas()
else:
    twoGas()
```

D.2 LabVIEW Block Diagram

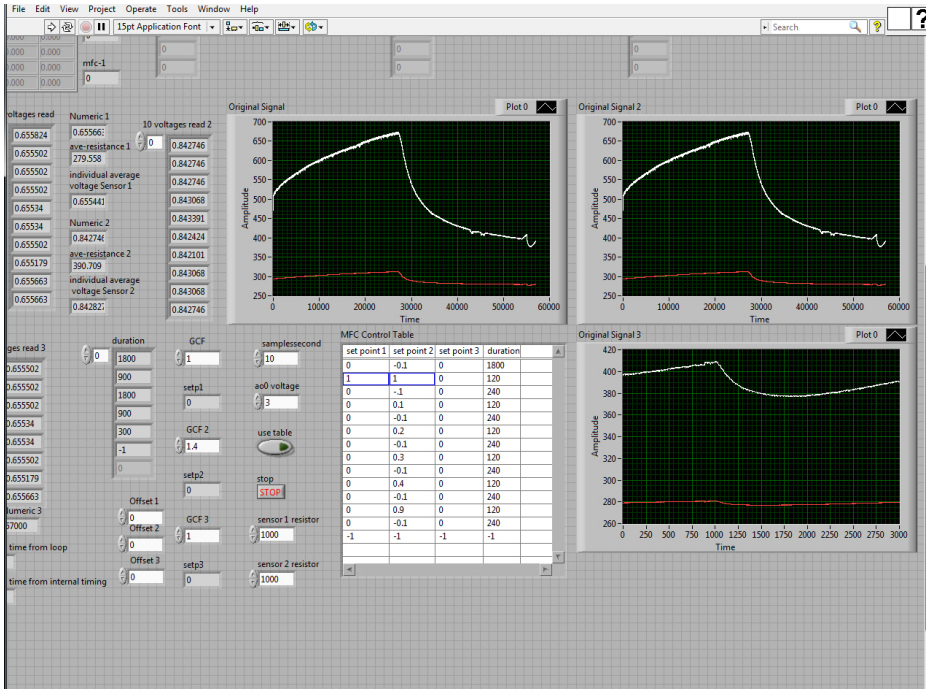

(a)

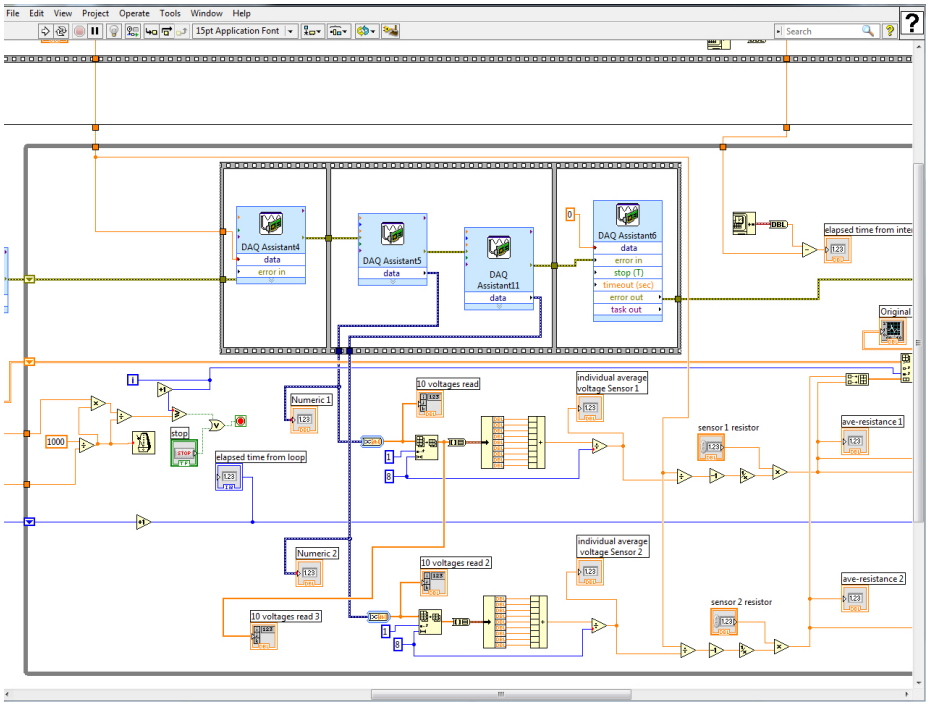

(b)

Figure D.1: (a) LabVIEW screenshot and (b) block diagram for operating the gas detection experiments for multiple sensors and multiple gases.

REFERENCES

[1] "e-CFR: Title 40: Protection of Environment PART 80—REGULATION OF FUELS AND FUEL ADDITIVES , Subpart I—Motor Vehicle Diesel Fuel; Nonroad, Locomotive, and Marine Diesel Fuel; and ECA Marine Fuel," 2006.

[2] "NIST X-ray Photoelectron Spectroscopy Database, Version 4.1," 2012.

[3] "Equipment." Georgia Tech Institute for Electronics and Nanotechnology, https://cleanroom.ien.gatech.edu/equipment/, 2015.

[4] "Processing at the ien." Georgia Tech Institute for Electronics and Nanotechnology, https://cleanroom.ien.gatech.edu/staff/process/landing/, June 2015.

[5] Abrams, B. L. and Vesborg, P. C. K., "Chapter 4 - Catalysts for Environmental Remediation—Examples in Photo- and Heterogeneous Catalysis," in *New and Future Developments in Catalysis* (Suib, S. L., ed.), pp. 63–85, Amsterdam: Elsevier, 2013.

[6] Allongue, P., de Villeneuve, C. H., Bernard, M. C., Péou, J. E., Boutry-Forveille, A., and Lévy-Clément, C., "Relationship between porous silicon formation and hydrogen incorporation," *Thin Solid Films*, vol. 297, pp. 1–4, Apr. 1997.

[7] Appel, J., "Freundlich's adsorption isotherm," *Surface Science*, vol. 39, pp. 237–244, Aug. 1973.

[8] Archer, M., Christophersen, M., and Fauchet, P. M., "Electrical porous silicon chemical sensor for detection of organic solvents," *Sensors and Actuators B: Chemical*, vol. 106, pp. 347–357, Apr. 2005.

[9] Archer, R. J., "Stain films on silicon," *Journal of Physics and Chemistry of Solids*, vol. 14, pp. 104–110, July 1960.

[10] Arita, Y., Kato, K., and Sudo, T., "The n+-IPOS scheme and its applications to IC's," *IEEE Transactions on Electron Devices*, vol. 24, pp. 756–757, June 1977.

[11] Ashcroft, N. W. and Mermin, N. D., *Solid State Physics*. New York: Holt, Rinehart and Winston, 1976.

[12] Auerbach, S. M., Carrado, K. A., and Dutta, P. K., *Handbook of Zeolite Science and Technology*. CRC Press, July 2003.

[13] Baker, C. and Gole, J. L., "Interface Modifications of Porous Silicon for Chemical Sensor Applications," *JSM Nanotechnol Nanomed*, vol. 2, no. 1, pp. 1021–1032, 2014.

[14] Baker, C. and Gole, J. L., "Selective detection of the inorganics NOx, SO2, and H2s in the presence of volatile BTEX contaminants toluene, benzene, and xylene," *Air Quality, Atmosphere & Health*, pp. 1–9, June 2015.

[15] Baker, C., Laminack, W., and Gole, J. L., "Sensitive and selective detection of H2s and application in the presence of toluene, benzene, and xylene," *Sensors and Actuators B: Chemical*, vol. 212, pp. 28–34, June 2015.

[16] Baker, C., Laminack, W., Tune, T., and Gole, J., "Magnetically induced enhancement of reversibly responding conductometric sensors," *Journal of Applied Physics*, vol. 115, p. 164312, Apr. 2014.

[17] Baker, D. and Tillman, J. R., "The preparation of very flat surfaces of silicon by electropolishing," *Solid-State Electronics*, vol. 6, pp. 589–596, Nov. 1963.

[18] Banica, F.-G., *Chemical Sensors and Biosensors : Fundamentals and Applications*. Somerset, NJ, USA: John Wiley & Sons, 2012.

[19] Baraton, M.-I. and Merhari, L., "Advances in Air Quality Monitoring via Nanotechnology," *Journal of Nanoparticle Research*, vol. 6, pp. 107–117, Feb. 2004.

[20] Baratto, C., Faglia, G., Comini, E., Sberveglieri, G., Taroni, A., La Ferrara, V., Quercia, L., and Di Francia, G., "A novel porous silicon sensor for detection of sub-ppm NO2 concentrations," *Sensors and Actuators B: Chemical*, vol. 77, pp. 62–66, June 2001.

[21] Baratto, C., Sberveglieri, G., Comini, E., Faglia, G., Benussi, G., La Ferrara, V., Quercia, L., Di Francia, G., Guidi, V., Vincenzi, D., Boscarino, D., and Rigato, V., "Gold-catalysed porous silicon for NOx sensing," *Sensors and Actuators B: Chemical*, vol. 68, pp. 74–80, Aug. 2000.

[22] Barla, K., Bomchil, G., Herino, R., Monroy, A., and Gris, Y., "Characteristics of SOI CMOS circuits made in n/n+/n oxidised porous silicon structures," *Electronics Letters*, vol. 22, no. 24, p. 1291, 1986.

[23] Beale, M. I. J., Benjamin, J. D., Uren, M. J., Chew, N. G., and Cullis, A. G., "An experimental and theoretical study of the formation and microstructure of porous silicon," *Journal of Crystal Growth*, vol. 73, pp. 622–636, Dec. 1985.

[24] Bengtsson, M., Ekström, S., Marko-Varga, G., and Laurell, T., "Improved performance in silicon enzyme microreactors obtained by homogeneous porous silicon carrier matrix," *Talanta*, vol. 56, pp. 341–353, Feb. 2002.

[25] BenChorin, M., Kux, A., and Schechter, I., "Adsorbate effects on photoluminescence and electrical conductivity of porous silicon," *Applied Physics Letters*, vol. 64, pp. 481–483, Jan. 1994.

[26] Berck, B., "Sorption of phosphine by cereal products," *Journal of Agricultural and Food Chemistry*, vol. 16, pp. 419–425, May 1968.

[27] Blackwood, D. J. and Akber, M. F., "In Situ Electrochemical Functionalization of Porous Silicon," *Journal of The Electrochemical Society*, vol. 153, pp. G976–G980, Nov. 2006.

[28] Boarino, L., Baratto, C., Geobaldo, F., Amato, G., Comini, E., Rossi, A. M., Faglia, G., Lérondel, G., and Sberveglieri, G., "NO2 monitoring at room temperature by a porous silicon gas sensor," *Materials Science and Engineering: B*, vol. 69–70, pp. 210–214, Jan. 2000.

[29] Bourgeat-Lami, E., Di Renzo, F., Fajula, F., Mutin, P. H., and Des Courieres, T., "Mechanism of the thermal decomposition of tetraethylammonium in zeolite .beta.," *The Journal of Physical Chemistry*, vol. 96, pp. 3807–3811, Apr. 1992.

[30] Breck, D. W., *Zeolites Molecular Sieves: Structure, Chemistry, and Use*. New York: Wiley, 1974.

[31] Breysse, M., Djega-Mariadassou, G., Pessayre, S., Geantet, C., Vrinat, M., Pérot, G., and Lemaire, M., "Deep desulfurization: reactions, catalysts and technological challenges," *Catalysis Today*, vol. 84, pp. 129–138, Sept. 2003.

[32] Burgess, J. L., "Phosphine exposure from a methamphetamine laboratory investigation," *Journal Of Toxicology. Clinical Toxicology*, vol. 39, no. 2, pp. 165–168, 2001.

[33] Campbell, A. N. and Kartzmark, E. M., "Heats of mixing and dielectric constants of some partially miscible liquid pairs," *Canadian Journal of Chemistry*, vol. 47, pp. 619–623, Feb. 1969.

[34] Campbell, J., Corno, J. A., Larsen, N., and Gole, J. L., "Development of Porous-Silicon-Based Active Microfilters," *Journal of The Electrochemical Society*, vol. 155, pp. D128–D132, Feb. 2008.

[35] Canham, L. T., "Silicon quantum wire array fabrication by electrochemical and chemical dissolution of wafers," *Applied Physics Letters*, vol. 57, pp. 1046–1048, Sept. 1990.

[36] Cao, E., Zuburtikudis, I., Al-Rifai, N., Roydhouse, M., and Gavriilidis, A., "Enhanced performance of oxidation of rosalva (9-decen-1-ol) to costenal (9-decenal) on porous silicon-supported silver catalyst in a microstructured reactor," *Processes*, vol. 2, pp. 141–157, Jan. 2014.

[37] Caro, J. and Gallego, M., "Environmental and biological monitoring of volatile organic compounds in the workplace," *Chemosphere*, vol. 77, pp. 426–433, Oct. 2009.

[38] Carstensen, J., Christophersen, M., Hasse, G., and Föll, H., "Parameter Dependence of Pore Formation in Silicon within a Model of Local Current Bursts," *physica status solidi (a)*, vol. 182, pp. 63–69, Nov. 2000.

[39] Caselli, M., de Gennaro, G., Marzocca, A., Trizio, L., and Tutino, M., "Assessment of the impact of the vehicular traffic on BTEX concentration in ring roads in urban areas of Bari (Italy)," *Chemosphere*, vol. 81, pp. 306–311, Sept. 2010.

[40] Cejka, J., Bekkum, H. v., Corma, A., and Schueth, F., *Introduction to Zeolite Molecular Sieves*. Elsevier, Oct. 2007.

[41] Chazalviel, J. N., Wehrspohn, R. B., and Ozanam, F., "Electrochemical preparation of porous semiconductors: from phenomenology to understanding," *Materials Science and Engineering: B*, vol. 69–70, pp. 1–10, Jan. 2000.

[42] Chen, M. Y., Klunk, M. D., Diep, V. M., and Sailor, M. J., "Electric-Field-Assisted Protein Transport, Capture, and Interferometric Sensing in Carbonized Porous Silicon Films," *Advanced Materials*, vol. 23, pp. 4537–4542, Oct. 2011.

[43] Chen, X., Lou, Y.-B., Samia, A. C. S., Burda, C., and Gole, J. L., "Formation of Oxynitride as the Photocatalytic Enhancing Site in Nitrogen-Doped Titania Nanocatalysts: Comparison to a Commercial Nanopowder," *Advanced Functional Materials*, vol. 15, pp. 41–49, Jan. 2005.

[44] Cho, S.-Y., Lee, K.-W., Kim, J.-W., and Kim, D.-H., "Rugate-structured free-standing porous silicon-based fiber-optic sensor for the simultaneous detection of pressure and organic gases," *Sensors and Actuators B: Chemical*, vol. 183, pp. 428–433, July 2013.

[45] Choinière, Y. and Munroe, J., "Air Quality Inside Livestock Barns," Jan. 1993.

[46] Chvojka, T., Vrkoslav, V., Jelnek, I., Jindřich, J., Lorenc, M., and Dian, J., "Mechanisms of photoluminescence sensor response of porous silicon for organic species in gas and liquid phases," *Sensors and Actuators B: Chemical*, vol. 100, pp. 246–249, June 2004.

[47] Ciston, J., Subramanian, A., Kienzle, D. M., and Marks, L. D., "Why the case for clean surfaces does not hold water: Structure and morphology of hydroxylated nickel oxide (1 1 1)," *Surface Science*, vol. 604, pp. 155–164, Jan. 2010.

[48] Ciston, J., Subramanian, A., and Marks, L. D., "Water-driven structural evolution of the polar MgO (111) surface: An integrated experimental and theoretical approach," *Physical Review B*, vol. 79, p. 085421, Feb. 2009.

[49] Collins, R. T., Fauchet, P. M., and Tischler, M. A., "Porous Silicon: From Luminescence to LEDs," *Physics Today*, vol. 50, pp. 24–31, Jan. 2008.

[50] Comini, E., Baratto, C., Faglia, G., Ferroni, M., Vomiero, A., and Sberveglieri, G., "Quasi-one dimensional metal oxide semiconductors: Preparation, characterization and application as chemical sensors," *Progress in Materials Science*, vol. 54, pp. 1–67, Jan. 2009.

[51] Corbett, J. W., Shereshevskii, D. I., and Verner, I. V., "Changes in the Creation of Point Defects Related to the Formation of Porous Silicon," *physica status solidi (a)*, vol. 147, pp. 81–89, Jan. 1995.

[52] Corma, A., Iborra, S., Miquel, S., and Primo, J., "Catalysts for the Production of Fine Chemicals: Production of Food Emulsifiers, Monoglycerides, by Glycerolysis of Fats with Solid Base Catalysts," *Journal of Catalysis*, vol. 173, pp. 315–321, Jan. 1998.

[53] Corma, A., Navarro, M. T., Rey, F., Rius, J., and Valencia, S., "Pure Polymorph C of Zeolite Beta Synthesized by Using Framework Isomorphous Substitution as a Structure-Directing Mechanism," *Angewandte Chemie International Edition*, vol. 40, pp. 2277–2280, June 2001.

[54] Crank, J., *The Mathematics of Diffusion*, vol. 2. Oxford: Clarendon Press, 1975.

[55] Cullis, A. G., Canham, L. T., and Calcott, P. D. J., "The structural and luminescence properties of porous silicon," *Journal of Applied Physics*, vol. 82, pp. 909–965, Aug. 1997.

[56] D'Arrigo, G., Spinella, C., Arena, G., and Lorenti, S., "Fabrication of miniaturised Si-based electrocatalytic membranes," *Materials Science and Engineering: C*, vol. 23, pp. 13–18, Jan. 2003.

[57] DeLouise, L. A. and Winograd, N., "Adsorption and desorption of no from Rh{111} and Rh{331} surfaces," *Surface Science*, vol. 159, pp. 199–213, Aug. 1985.

[58] Dippell, J. and Jaeschke, W., "A comparison between natural and anthropogenic emissions of the reduced sulfur compounds H2s, COS, and CS2 in a tropical industrialized region," *Journal of Atmospheric Chemistry*, vol. 25, pp. 251–270, Nov. 1996.

[59] Divins, N., Lopez, E., Llorca, J., Vega, D., Rodriguez, A., de Rivera, F., Angurell, I., and Rossell, M., "Macroporous silicon microreactor for the preferential oxidation of CO," in *2013 Spanish Conference on Electron Devices (CDE)*, pp. 139–142, Feb. 2013.

[60] Dixon, D. A. and Gutowski, M., "Thermodynamic Properties of Molecular Borane Amines and the [BH4-][NH4+] Salt for Chemical Hydrogen Storage Systems from ab Initio Electronic Structure Theory," *The Journal of Physical Chemistry A*, vol. 109, pp. 5129–5135, June 2005.

[61] Dogan, F., Hammond, K. D., Tompsett, G. A., Huo, H., Conner, W. C., Auerbach, S. M., and Grey, C. P., "Searching for Microporous, Strongly Basic Catalysts: Experimental and Calculated 29si NMR Spectra of Heavily Nitrogen-Doped Y Zeolites," *Journal of the American Chemical Society*, vol. 131, pp. 11062–11079, Aug. 2009.

[62] Driver, L. and Freedman, E., "Report to Congress on Hydrogen Sulfide Air Emissions Associated with the Extraction of Oil and Natural Gas. Final Report," Tech. Rep. PB-94-131224/XAB; EPA–453/R-93/045, Environmental Protection Agency, Research Triangle Park, NC (United States). Office of Air Quality Planning and Standards, Oct. 1993.

[63] Drott, J., Rosengren, L., Lindström, K., and Laurell, T., "Porous Silicon Carrier Matrices in Micro Enzyme Reactors-Influence of Matrix Depth," *Microchimica Acta*, vol. 131, pp. 115–120, June 1999.

[64] Dudel, F. P., Rieger, M. M., Pickering, J. P., Gole, J. L., Kohl, P. A., and Bottomley, L. A., "Photoluminescence in the Earliest Stages of Porous Silicon Formation," *Journal of The Electrochemical Society*, vol. 143, pp. L164–L166, Aug. 1996.

[65] Duffar, T., *Crystal Growth Processes Based on Capillarity: Czochralski, Floating Zone, Shaping and Crucible Techniques*. John Wiley & Sons, Mar. 2010.

[66] Ensafi, A. A., Abarghoui, M. M., and Rezaei, B., "A new non-enzymatic glucose sensor based on copper/porous silicon nanocomposite," *Electrochimica Acta*, vol. 123, pp. 219–226, Mar. 2014.

[67] Eranna, G., *Metal Oxide Nanostructures as Gas Sensing Devices*. CRC Press, Dec. 2011.

[68] Eranna, G., Joshi, B. C., Runthala, D. P., and Gupta, R. P., "Oxide materials for development of integrated gas Sensors—A comprehensive review," *Critical Reviews in Solid State and Materials Sciences*, vol. 29, no. 3-4, pp. 111–188, 2004.

[69] Ernst, S., Hartmann, M., Sauerbeck, S., and Bongers, T., "A novel family of solid basic catalysts obtained by nitridation of crystalline microporous aluminosilicates and aluminophosphates," *Applied Catalysis A: General*, vol. 200, pp. 117–123, Aug. 2000.

[70] Erson, R. C., Muller, R. S., and Tobias, C. W., "Investigations of porous silicon for vapor sensing," *Sensors and Actuators A: Physical*, vol. 23, pp. 835–839, Apr. 1990.

[71] Fachini, A. and Vasconcelos, M. T. S. D., "Effects of zeolites on cultures of marine micro-algae," *Environmental Science and Pollution Research*, vol. 13, pp. 414–417, Jan. 2006.

[72] Fehsenfeld, F., Calvert, J., Fall, R., Goldan, P., Guenther, A. B., Hewitt, C. N., Lamb, B., Liu, S., Trainer, M., Westberg, H., and Zimmerman, P., "Emissions of volatile organic compounds from vegetation and the implications for atmospheric chemistry," *Global Biogeochemical Cycles*, vol. 6, pp. 389–430, Dec. 1992.

[73] Ferrero, R., Marracci, M., Prioli, M., and Tellini, B., "Simplified model for evaluating ripple effects on commercial PEM fuel cell," *International Journal of Hydrogen Energy*, vol. 37, pp. 13462–13469, Sept. 2012.

[74] Föll, H., Christophersen, M., Carstensen, J., and Hasse, G., "Formation and application of porous silicon," *Materials Science and Engineering: R: Reports*, vol. 39, pp. 93–141, Nov. 2002.

[75] Föll, H., Carstensen, J., and Frey, S., "Porous and Nanoporous Semiconductors and Emerging Applications," *Journal of Nanomaterials*, vol. 2006, p. e91635, Dec. 2006.

[76] Frey, S., Keipert, S., Chazalviel, J.-N., Ozanam, F., Carstensen, J., and Föll, H., "Electrochemical formation of porous silica: toward an understanding of the mechanisms," *physica status solidi (a)*, vol. 204, pp. 1250–1254, May 2007.

[77] Fukuda, Y., Nagoshi, M., Suzuki, T., Namba, Y., Syono, Y., and Tachiki, M., "Chemical states of Ba in YBa2cu3o7- studied by x-ray photoelectron spectroscopy," *Physical Review B*, vol. 39, pp. 11494–11497, June 1989.

[78] Fuller, C. S. and Ditzenberger, J. A., "Diffusion of Donor and Acceptor Elements in Silicon," *Journal of Applied Physics*, vol. 27, pp. 544–553, May 1956.

[79] Galarneau, A., Di Renzo, F., Fajula, F., and Vedrine, J., *Zeolites and Mesopores at the Dawn of the 21st Century*. Amsterdam: Elsevier, 2001.

[80] Garde, R., Villain, F., and Verdaguer, M., "Molecule-Based Room-Temperature Magnets: Catalytic Role of V(III) in the Synthesis of VanadiumChromium Prussian Blue Analogues," *Journal of the American Chemical Society*, vol. 124, pp. 10531–10538, Sept. 2002.

[81] Gatteschi, D., Sessoli, R., and Villain, J., *Molecular Nanomagnets*. OUP Oxford, Mar. 2006.

[82] Gautier, G., Kouassi, S., Desplobain, S., and Ventura, L., "Macroporous silicon hydrogen diffusion layers for micro-fuel cells: From planar to 3d structures," *Microelectronic Engineering*, vol. 90, pp. 79–82, Feb. 2012.

[83] Golbabaei, F. and Islami, F., "Evaluation of Workers' Exposure to Dust, Ammonia and Endotoxin in Poultry Industries at the Province of Isfahan, Iran," *Industrial Health*, vol. 38, no. 1, pp. 41–46, 2000.

[84] Gold, S., Chu, K.-L., Lu, C., Shannon, M. A., and Masel, R. I., "Acid loaded porous silicon as a proton exchange membrane for micro-fuel cells," *Journal of Power Sources*, vol. 135, pp. 198–203, Sept. 2004.

[85] Gole, J. L., "Increasing energy efficiency and sensitivity with simple sensor platforms," *Talanta*, vol. 132, pp. 87–95, Jan. 2015.

[86] Gole, J. L. and Laminack, W., "General approach to design and modeling of nanostructure modified semiconductor and nanowire interfaces for sensor and microreactor applications," in *Chemical Sensors Simulation and Modeling Volume 3: Solid-State Devices* (Korotcenkov, G., ed.), pp. 87–136, Momentum Press, 1 ed., Dec. 2012.

[87] Gole, J. and Laminack, W., "(invited) nanostructure modified porous interfaces for enhanced sensing and directed microcatalysis," *ECS Transactions*, vol. 50, pp. 237–246, Apr. 2013.

[88] Gole, J. L., DeVincentis, J. A., Seals, L., Lillehei, P., and Narasimha, S., "Contrasting photovoltaic response and photoluminescence for distinct porous silicon pore structures," *Physical Review B*, vol. 61, pp. 7589–7594, Mar. 2000.

[89] Gole, J. L. and Dixon, D. A., "Potential role of silanones in the photoluminescence-excitation, visible-photoluminescence-emission, and infrared spectra of porous silicon," *Physical Review B*, vol. 57, pp. 12002–12016, May 1998.

[90] Gole, J. L. and Dixon, D. A., "Transformation, Green to Orange-Red, of a Porous Silicon Photoluminescent Surface in Solution," *The Journal of Physical Chemistry B*, vol. 102, pp. 33–39, Jan. 1998.

[91] Gole, J. L., Dudel, F. P., Grantier, D., and Dixon, D. A., "Origin of porous silicon photoluminescence: Evidence for a surface bound oxyhydride-like emitter," *Physical Review B*, vol. 56, pp. 2137–2153, July 1997.

[92] Gole, J. L., Goude, E. C., and Laminack, W., "Nanostructure-driven Analyte–Interface electron transduction: A general approach to sensor and microreactor design," *ChemPhysChem*, vol. 13, no. 2, pp. 549–561, 2012.

[93] Gole, J. L. and Lewis, S. E., "Nanostructure and morphology modified porous silicon sensors," in *SPIE Proceedings*, vol. 5732, pp. 573–583, 2005.

[94] Gole, J. L. and Ozdemir, S., "Nanostructure-directed physisorption vs chemisorption at semiconductor interfaces: The inverse of the HSAB concept," *ChemPhysChem*, vol. 11, no. 12, pp. 2573–2581, 2010.

[95] Gole, J. L., Ozdemir, S., and Osburn, T. B., "Novel Concept for the Formation of Sensitive, Selective, Rapidly Responding Conductometric Sensors," *ECS Transactions*, vol. 33, pp. 239–244, Oct. 2010.

[96] Gole, J. L., Prokes, S. M., Glembocki, O. J., Wang, J., Qiu, X., and Burda, C., "Study of concentration-dependent cobalt ion doping of TiO2 and TiO2xNx at the," *Nanoscale*, vol. 2, pp. 1134–1140, July 2010.

[97] Gole, J. L., Prokes, S. M., and Glembocki, O. J., "Efficient Room-Temperature Conversion of Anatase to Rutile TiO2 Induced by High-Spin Ion Doping," *The Journal of Physical Chemistry C*, vol. 112, pp. 1782–1788, Feb. 2008.

[98] Gole, J. L., Stout, J. D., Burda, C., Lou, Y., and Chen, X., "Highly efficient formation of visible light tunable TiO2-xNx photocatalysts and their transformation at the nanoscale," *The Journal of Physical Chemistry B*, vol. 108, pp. 1230–1240, Jan. 2004.

[99] Gole, J. L., Veje, E., Egeberg, R. G., Ferreira da Silva, A., Pepe, I., and Dixon, D. A., "Optical Analysis of the Light Emission from Porous Silicon: A Hybrid Polyatom Surface-Coupled Fluorophor," *The Journal of Physical Chemistry B*, vol. 110, pp. 2064–2073, Feb. 2006.

[100] Gole, J. and Laminack, W., "A Variable Response Phosphine Sensing Matrix Based on Nanostructure Treated p and n-Type Porous Silicon Interfaces," *IEEE Sensors Journal*, vol. 14, pp. 2731–2738, Aug. 2014.

[101] Gomzi, M., "Indoor air and respiratory health in preadolescent children," *Atmospheric Environment*, vol. 33, pp. 4081–4086, Oct. 1999.

[102] Gonghu, L., *FTIR studies on zeolite materials: characterization and environmental applications*. PhD thesis, University of Iowa, 2005.

[103] Granitzer, P., Rumpf, K., Pölt, P., Reichmann, A., and Krenn, H., "Self-assembled mesoporous silicon in the crossover between irregular and regular arrangement applicable for Ni filling," *Physica E: Low-dimensional Systems and Nanostructures*, vol. 38, pp. 205–210, Apr. 2007.

[104] Granitzer, P. and Rumpf, K., "Porous Silicon—A Versatile Host Material," *Materials*, vol. 3, pp. 943–998, Feb. 2010.

[105] Green, M. A., "Intrinsic concentration, effective densities of states, and effective mass in silicon," *Journal of Applied Physics*, vol. 67, pp. 2944–2954, Mar. 1990.

[106] Greenstone, M., "Did the Clean Air Act cause the remarkable decline in sulfur dioxide concentrations?," *Journal of Environmental Economics and Management*, vol. 47, pp. 585–611, May 2004.

[107] Grundmann, M., *The Physics of Semiconductors*. Graduate Texts in Physics, New York: Springer Berlin Heidelberg, 2nd ed., 2010.

[108] Hanada, T., Zaitsu, A., Kojima, S., Ukai, H., Nagasawa, Y., Takada, S., Kawakami, T., Ohashi, F., and Ikeda, M., "Solvent Use in Private Research Laboratories in Japan: Comparison with the Use in Public Research Laboratories and on Production Floors in Industries," *Journal of Occupational Health*, vol. 56, no. 5, pp. 393–398, 2014.

[109] Harper, J. and Sailor, M. J., "Detection of Nitric Oxide and Nitrogen Dioxide with Photoluminescent Porous Silicon," *Analytical Chemistry*, vol. 68, pp. 3713–3717, Nov. 1996.

[110] Harraz, F. A., "Porous silicon chemical sensors and biosensors: A review," *Sensors and Actuators B: Chemical*, vol. 202, pp. 897–912, Oct. 2014.

[111] Harraz, F. A., Ismail, A. A., Bouzid, H., Al-Sayari, S. A., Al-Hajry, A., and Al-Assiri, M. S., "A capacitive chemical sensor based on porous silicon for detection of polar and non-polar organic solvents," *Applied Surface Science*, vol. 307, pp. 704–711, July 2014.

[112] Hathaway, P. E. and Davis, M. E., "Base catalysis by alkali modified zeolites: III. Alkylation with methanol," *Journal of Catalysis*, vol. 119, pp. 497–507, Oct. 1989.

[113] Hernández-Ramírez, F., Tarancón, A., Casals, O., Arbiol, J., Romano-Rodríguez, A., and Morante, J. R., "High response and stability in CO and humidity measures using a single SnO2 nanowire," *Sensors and Actuators B: Chemical*, vol. 121, pp. 3–17, Jan. 2007.

[114] Hippo, D., Nakamine, Y., Urakawa, K., Tsuchiya, Y., Mizuta, H., Koshida, N., and Oda, S., "Formation Mechanism of 100-nm-Scale Periodic

Structures in Silicon Using Magnetic-Field-Assisted Anodization," *Japanese Journal of Applied Physics*, vol. 47, p. 7398, Sept. 2008.

[115] Holec, T., Chvojka, T., Jelnek, I., Jindřich, J., Němec, I., Pelant, I., Valenta, J., and Dian, J., "Determination of sensoric parameters of porous silicon in sensing of organic vapors," *Materials Science and Engineering: C*, vol. 19, pp. 251–254, Jan. 2002.

[116] Housecroft, C. and Sharpe, A. G., *Inorganic Chemistry*. Prentice Hall, 3rd ed., 2008.

[117] Huang, X.-J. and Choi, Y.-K., "Chemical sensors based on nanostructured materials," *Sensors and Actuators B: Chemical*, vol. 122, pp. 659–671, Mar. 2007.

[118] Hubbell, B., "Understanding urban exposure environments: new research directions for informing implementation of U.S. air quality standards," *Air Quality, Atmosphere & Health*, vol. 5, pp. 259–267, Aug. 2011.

[119] Hübner, M., Simion, C. E., Tomescu-Stănoiu, A., Pokhrel, S., Bârsan, N., and Weimar, U., "Influence of humidity on CO sensing with p-type CuO thick film gas sensors," *Sensors and Actuators B: Chemical*, vol. 153, pp. 347–353, Apr. 2011.

[120] Hui-Qing, C., Ming, H., Jing, Z., and Wei-Dan, W., "The light-enhanced NO2 sensing properties of porous silicon gas sensors at room temperature," *Chinese Physics B*, vol. 21, p. 058201, May 2012.

[121] Hull, R., *Properties of Crystalline Silicon*. London: INSPEC, IET, 1999.

[122] Hunter, E. P. L. and Lias, S. G., "Evaluated Gas Phase Basicities and Proton Affinities of Molecules: An Update," *Journal of Physical and Chemical Reference Data*, vol. 27, pp. 413–656, May 1998.

[123] Husairi, M., Rouhi, J., Alvin, K., Atikah, Z., Rusop, M., and Abdullah, S., "Developing high-sensitivity ethanol liquid sensors based on ZnO/porous Si nanostructure surfaces using an electrochemical impedance technique," *Semiconductor Science and Technology*, vol. 29, p. 075015, July 2014.

[124] Imai, K., "A new dielectric isolation method using porous silicon," *Solid-State Electronics*, vol. 24, pp. 159–164, Feb. 1981.

[125] Imai, K. and Yoriume, Y., "Application of IPOS technique to MOS ICs," *Japanese Journal of Applied Physics*, vol. 18, p. 281, Jan. 1979.

[126] Ishigami, M., Hiraki, K., Umemura, K., Ogasawara, Y., Ishii, K., and Kimura, H., "A Source of Hydrogen Sulfide and a Mechanism of Its Release in the Brain," *Antioxidants & Redox Signaling*, vol. 11, pp. 205–214, Aug. 2008.

[127] Jalkanen, T., Torres-Costa, V., Salonen, J., Björkqvist, M., Mäkilä, E., Martínez-Duart, J. M., and Lehto, V.-P., "Optical gas sensing properties of thermally hydrocarbonized porous silicon bragg reflectors," *Optics Express*, vol. 17, pp. 5446–5456, Mar. 2009.

[128] Jalkanen, T., Tuura, J., Mäkilä, E., and Salonen, J., "Electro-optical porous silicon gas sensor with enhanced selectivity," *Sensors and Actuators B: Chemical*, vol. 147, pp. 100–104, May 2010.

[129] Janata, J., *Solid state chemical sensors*. Academic Press, July 1985.

[130] Jensen, K. F., "Microreaction engineering — is small better?," *Chemical Engineering Science*, vol. 56, pp. 293–303, Jan. 2001.

[131] Jeske, M., Schultze, J. W., Thönissen, M., and Münder, H., "Electrodeposition of metals into porous silicon," *Thin Solid Films*, vol. 255, pp. 63–66, Jan. 1995.

[132] Kang, Y. and Jorné, J., "Morphological Stability Analysis of Porous Silicon Formation," *Journal of The Electrochemical Society*, vol. 140, pp. 2258–2265, Aug. 1993.

[133] Kanungo, J., Maji, S., Mandal, A. K., Sen, S., Bontempi, E., Balamurugan, A. K., Tyagi, A. K., Uvdal, K., Sinha, S., Saha, H., and Basu, S., "Surface treatment of nanoporous silicon with noble metal ions and characterizations," *Applied Surface Science*, vol. 256, pp. 4231–4240, Apr. 2010.

[134] Karacali, T., Hasar, U. C., Ozbek, I. Y., Oral, E. A., and Efeoglu, H., "Novel design of porous silicon based sensor for reliable and feasible chemical gas vapor detection," *Journal of Lightwave Technology*, vol. 31, pp. 295–305, Jan. 2013.

[135] Karplus, M. and Porter, R. N., *Atoms and molecules; an introduction for students of physical chemistry*. Philippines: W.A. Benjamin, 1970.

[136] Kelly, M. T., Chun, J. K. M., and Bocarsly, A. B., "A silicon sensor for SO2," *Nature*, vol. 382, pp. 214–215, July 1996.

[137] Kimura, H., "Hydrogen sulfide: its production, release and functions," *Amino Acids*, vol. 41, pp. 113–121, Feb. 2010.

[138] King, B. H., Ruminski, A. M., Snyder, J. L., and Sailor, M. J., "Optical-fiber-mounted porous silicon photonic crystals for sensing organic vapor breakthrough in activated carbon," *Advanced Materials*, vol. 19, no. 24, pp. 4530–4534, 2007.

[139] Kisliuk, P., "The sticking probabilities of gases chemisorbed on the surfaces of solids," *Journal of Physics and Chemistry of Solids*, vol. 3, no. 1–2, pp. 95–101, 1957.

[140] Koch, F., Petrova-Koch, V., and Muschik, T., "The luminescence of porous Si: the case for the surface state mechanism," *Journal of Luminescence*, vol. 57, pp. 271–281, Nov. 1993.

[141] Kolasinski, K. W., "Silicon nanostructures from electroless electrochemical etching," *Current Opinion in Solid State and Materials Science*, vol. 9, pp. 73–83, Feb. 2005.

[142] Korotcenkov, G. and Cho, B. K., "Porous Semiconductors: Advanced Material for Gas Sensor Applications," *Critical Reviews in Solid State and Materials Sciences*, vol. 35, no. 1, pp. 1–37, 2010.

[143] Korotcenkov, G. and Cho, B. K., "Silicon Porosification: State of the Art," *Critical Reviews in Solid State and Materials Sciences*, vol. 35, pp. 153–260, Aug. 2010.

[144] Ku, H., "Notes on the Use of Propagation of Error Formulas," *Journal of Research of the National Bureau of Standards - C. Engineering and Instrumentation*, vol. 70C, pp. 263–273, May 1966.

[145] Laminack, W., Pouse, N., and Gole, J. L., "Dynamic Interaction of NO2 with a Nanostructure Modified Porous Silicon Matrix: Acidity, Sensor Response, and the Competition for Donor Level Electrons," *ECS Journal of Solid State Science and Technology*, vol. 1, pp. Q25–Q34, Jan. 2012.

[146] Laminack, W., Baker, C., and Gole, J., "Sulfur-Hz(CHx)y(z = 0,1) functionalized metal oxide nanostructure decorated interfaces: Evidence of Lewis base and Brönsted acid sites – Influence on chemical sensing," *Materials Chemistry and Physics*, vol. 160, pp. 20–31, June 2015.

[147] Laminack, W., Hardy, N., Baker, C., and Gole, J. L., "Approach to Multi-gas Sensing and Modeling on Nanostructure Decorated Porous Silicon Substrates," *IEEE Sensors Journal*, 2015.

[148] Laminack, W. I. and Gole, J. L., "Development of a Fermi Energy Distribution Based Absorption Isotherm on Nanostructure Decorated Porous Silicon Substrates," *submitted*.

[149] Laminack, W. I. and Gole, J. L., "Light Enhanced Electron Transduction and Amplified Sensing at a Nanostructure Modified Semiconductor Interface," *Advanced Functional Materials*, vol. 23, pp. 5916–5924, Dec. 2013.

[150] Laminack, W. I. and Gole, J. L., "Nanostructure-directed chemical sensing: The IHSAB principle and the effect of nitrogen and sulfur functionalization on metal oxide decorated interface response," *Nanomaterials*, vol. 3, pp. 469–485, Aug. 2013.

[151] Laminack, W. I. and Gole, J. L., "Direct In Situ Nitridation of Nanostructured Metal Oxide Deposited Semiconductor Interfaces: Tuning the Response of Reversibly Interacting Sensor Sites," *ChemPhysChem*, vol. 15, pp. 2473–2484, Aug. 2014.

[152] Langmuir, I., "THE CONSTITUTION AND FUNDAMENTAL PROPERTIES OF SOLIDS AND LIQUIDS. PART I. SOLIDS.," *Journal of the American Chemical Society*, vol. 38, pp. 2221–2295, Nov. 1916.

[153] Lasia, A., "Definition of Impedance and Impedance of Electrical Circuits," in *Electrochemical Impedance Spectroscopy and its Applications*, pp. 7–66, Springer New York, 2014.

[154] Laurell, T., "Biocatalytic Porous Silicon Microreactors," *Sensors Update*, vol. 10, pp. 3–32, Jan. 2002.

[155] Lehmann, V., "The Physics of Macropore Formation in Low Doped nType Silicon," *Journal of The Electrochemical Society*, vol. 140, pp. 2836–2843, Oct. 1993.

[156] Lehmann, V. and Föll, H., "Formation Mechanism and Properties of Electrochemically Etched Trenches in n type Silicon," *Journal of The Electrochemical Society*, vol. 137, pp. 653–659, Feb. 1990.

[157] Lehmann, V. and Gösele, U., "Porous silicon formation: A quantum wire effect," *Applied Physics Letters*, vol. 58, pp. 856–858, Feb. 1991.

[158] Lehmann, V. and Grüning, U., "The limits of macropore array fabrication," *Thin Solid Films*, vol. 297, pp. 13–17, Apr. 1997.

[159] Lehmann, V., Stengl, R., and Luigart, A., "On the morphology and the electrochemical formation mechanism of mesoporous silicon," *Materials Science and Engineering: B*, vol. 69–70, pp. 11–22, Jan. 2000.

[160] Lescouëzec, R., Vaissermann, J., Ruiz-Pérez, C., Lloret, F., Carrasco, R., Julve, M., Verdaguer, M., Dromzee, Y., Gatteschi, D., and Wernsdorfer, W., "Cyanide-Bridged Iron(III)–Cobalt(II) Double Zigzag Ferromagnetic Chains: Two New Molecular Magnetic Nanowires," *Angewandte Chemie International Edition*, vol. 42, pp. 1483–1486, Apr. 2003.

[161] LévyClément, C., Lagoubi, A., and Tomkiewicz, M., "Morphology of Porous nType Silicon Obtained by Photoelectrochemical Etching I . Correlations with Material and Etching Parameters," *Journal of The Electrochemical Society*, vol. 141, pp. 958–967, Apr. 1994.

[162] Lewis, S. E., DeBoer, J. R., and Gole, J. L., "A pulsed system frequency analysis for device characterization and experimental design: Application to porous silicon sensors and extension," *Sensors and Actuators B: Chemical*, vol. 122, pp. 20–29, Mar. 2007.

[163] Lewis, S. E., DeBoer, J. R., Gole, J. L., and Hesketh, P. J., "Sensitive, selective, and analytical improvements to a porous silicon gas sensor," *Sensors and Actuators B: Chemical*, vol. 110, pp. 54–65, Sept. 2005.

[164] Lewis, S. E. and Gole, J. L., "Porous Silicon – Sensors and Future Applications," in *Nanosilicon* (Kumar, S., ed.), pp. 147–192, London: Elsevier, 2007.

[165] Lias, S. G., Bartmess, J. E., Liebman, J. F., Holmes, J. L., Levin, R. D., and Mallard, W. G., "Gas-phase ion and neutral thermochemistry," *Journal of Physical and Chemical Reference Data*, vol. 17, no. Supplementary No. 1, pp. 1–861, 1988.

[166] Liu, X., Cheng, H., and Cui, P., "Catalysis by silver nanoparticles/porous silicon for the reduction of nitroaromatics in the presence of sodium borohydride," *Applied Surface Science*, vol. 292, pp. 695–701, Feb. 2014.

[167] Liyanage, C. N. and Blackwood, D. J., "Functionalization of a porous silicon impedance sensor," *Thin Solid Films*, vol. 550, pp. 677–682, Jan. 2014.

[168] Llorca, J., Casanovas, A., Trifonov, T., Rodríguez, A., and Alcubilla, R., "First use of macroporous silicon loaded with catalyst film for a chemical reaction: A microreformer for producing hydrogen from ethanol steam reforming," *Journal of Catalysis*, vol. 255, pp. 228–233, Apr. 2008.

[169] Lokteva, E. S., Rostovshchikova, T. N., Kachevskii, S. A., Golubina, E. V., Smirnov, V. V., Stakheev, A. Y., Telegina, N. S., Gurevich, S. A., Kozhevin, V. M., and Yavsin, D. A., "High catalytic activity and stability of palladium nanoparticles prepared by the laser electrodispersion method in chlorobenzene hydrodechlorination," *Kinetics and Catalysis*, vol. 49, pp. 748–755, Sept. 2008.

[170] Losey, M. W., Schmidt, M. A., and Jensen, K. F., "Microfabricated Multiphase Packed-Bed Reactors: Characterization of Mass Transfer and Reactions," *Industrial & Engineering Chemistry Research*, vol. 40, pp. 2555–2562, June 2001.

[171] Löwe, H. and Ehrfeld, W., "State-of-the-art in microreaction technology: concepts, manufacturing and applications," *Electrochimica Acta*, vol. 44, pp. 3679–3689, June 1999.

[172] Lu, Y.-T. and Barron, A. R., "Nanopore-type black silicon anti-reflection layers fabricated by a one-step silver-assisted chemical etching," *Physical Chemistry Chemical Physics*, vol. 15, pp. 9862–9870, May 2013.

[173] Lundström, I., Shivaraman, S., Svensson, C., and Lundkvist, L., "A hydrogensensitive MOS fieldeffect transistor," *Applied Physics Letters*, vol. 26, pp. 55–57, Jan. 1975.

[174] Ma, S., Hu, M., Zeng, P., Li, M., Yan, W., and Qin, Y., "Synthesis and low-temperature gas sensing properties of tungsten oxide nanowires/porous silicon composite," *Sensors and Actuators B: Chemical*, vol. 192, pp. 341–349, Mar. 2014.

[175] Mädler, L., Roessler, A., Pratsinis, S. E., Sahm, T., Gurlo, A., Barsan, N., and Weimar, U., "Direct formation of highly porous gas-sensing films by in situ thermophoretic deposition of flame-made Pt/SnO2 nanoparticles," *Sensors and Actuators B: Chemical*, vol. 114, pp. 283–295, Mar. 2006.

[176] Mahan, G. D., *Condensed Matter in a Nutshell*. Princeton University Press, Oct. 2010.

[177] Malek, K. and Coppens, M.-O., "Knudsen self- and Fickian diffusion in rough nanoporous media," *The Journal of Chemical Physics*, vol. 119, pp. 2801–2811, Aug. 2003.

[178] Mallah, T., Thiébaut, S., Verdaguer, M., and Veillet, P., "High-Tc Molecular-Based Magnets: Ferrimagnetic Mixed-Valence Chromium(III)-Chromium(II) Cyanides with Tc at 240 and 190 Kelvin," *Science*, vol. 262, pp. 1554–1557, Dec. 1993.

[179] Mareš, J., Krištofik, J., and Hulicius, E., "Influence of humidity on transport in porous silicon," *Thin Solid Films*, vol. 255, pp. 272–275, Jan. 1995.

[180] Marsh, G., "Porous silicon a useful imperfection," *Materials Today*, vol. 5, pp. 36–41, Jan. 2002.

[181] Massera, E., Nasti, I., Quercia, L., Rea, I., and Di Francia, G., "Improvement of stability and recovery time in porous-silicon-based NO2 sensor," *Sensors and Actuators B: Chemical*, vol. 102, pp. 195–197, Sept. 2004.

[182] Miekisch, W., Schubert, J. K., and Noeldge-Schomburg, G. F. E., "Diagnostic potential of breath analysis—focus on volatile organic compounds," *Clinica Chimica Acta*, vol. 347, pp. 25–39, Sept. 2004.

[183] Milina, M., Mitchell, S., Michels, N.-L., Kenvin, J., and Pérez-Ramírez, J., "Interdependence between porosity, acidity, and catalytic performance in hierarchical ZSM-5 zeolites prepared by post-synthetic modification," *Journal of Catalysis*, vol. 308, pp. 398–407, Dec. 2013.

[184] Miller, J. S. and Drillon, M., eds., *Magnetism: Molecules to Materials*. Weinheim: Wiley-VCH Verlag GmbH & Co. KGaA, 2003.

[185] Molnár, G., Cobo, S., Real, J. A., Carcenac, F., Daran, E., Vieu, C., and Bousseksou, A., "A Combined Top-Down/Bottom-Up Approach for the Nanoscale Patterning of Spin-Crossover Coordination Polymers," *Advanced Materials*, vol. 19, pp. 2163–2167, Aug. 2007.

[186] Morin, F. J. and Maita, J. P., "Electrical Properties of Silicon Containing Arsenic and Boron," *Physical Review*, vol. 96, pp. 28–35, Oct. 1954.

[187] Morrison, S. R., "Selectivity in semiconductor gas sensors," *Sensors and Actuators*, vol. 12, pp. 425–440, Nov. 1987.

[188] Moseley, P. T., "Solid state gas sensors," *Measurement Science and Technology*, vol. 8, p. 223, Mar. 1997.

[189] Moshnikov, V. A., Gracheva, I., Lenshin, A. S., Spivak, Y. M., Anchkov, M. G., Kuznetsov, V. V., and Olchowik, J. M., "Porous silicon with embedded metal oxides for gas sensing applications," *Journal of Non-Crystalline Solids*, vol. 358, pp. 590–595, Feb. 2012.

[190] Moulder, J. F., Stickle, W. F., Sobol, P. E., and Bomben, K. D., *Handbook of X-ray Photoelectroscopy*. Eden Prairie: Physical Electronics, Inc., 1995.

[191] Mumpton, F. A., "La roca magica: Uses of natural zeolites in agriculture and industry," *Proceedings of the National Academy of Sciences*, vol. 96, pp. 3463–3470, Mar. 1999.

[192] Nakamura, T., Tiwari, B. P., and Adachi, S., "Direct synthesis and enhanced catalytic activities of platinum and porous-silicon composites by metal-assisted chemical etching," *Japanese Journal of Applied Physics*, vol. 50, p. 081301, Aug. 2011.

[193] Narasimharao, K., Hartmann, M., Thiel, H. H., and Ernst, S., "Novel solid basic catalysts by nitridation of zeolite beta at low temperature," *Microporous and Mesoporous Materials*, vol. 90, pp. 377–383, Mar. 2006.

[194] Nemati, M., Jenneman, G. E., and Voordouw, G., "Mechanistic study of microbial control of hydrogen sulfide production in oil reservoirs," *Biotechnology and Bioengineering*, vol. 74, pp. 424–434, Sept. 2001.

[195] Noort, H. M. v., Meenderink, B. C. M., and Molenaar, A., "In Situ 119sn Conversion Electron Mössbauer Study of the Surface of Tin Layers as Deposited by an Electroless Process," *Journal of The Electrochemical Society*, vol. 133, pp. 263–265, Feb. 1986.

[196] of Chemistry, R. S., "Chemspider." http://www.chemspider.com/, 2015.

[197] Ozdemir, S. and Gole, J. L., "The potential of porous silicon gas sensors," *Current Opinion in Solid State and Materials Science*, vol. 11, pp. 92–100, Oct. 2007.

[198] Ozdemir, S. and Gole, J. L., "A phosphine detection matrix using nanostructure modified porous silicon gas sensors," *Sensors and Actuators B: Chemical*, vol. 151, pp. 274–280, Nov. 2010.

[199] Ozdemir, S. and Gole, J. L., "Selectivity Improvements and Response Time Scale of Porous Silicon Conductometric Gas Sensors," *ECS Transactions*, vol. 33, pp. 111–115, Oct. 2010.

[200] Pacholski, C., Sartor, M., Sailor, M. J., Cunin, F., and Miskelly, G. M., "Biosensing Using Porous Silicon Double-Layer Interferometers: Reflective Interferometric Fourier Transform Spectroscopy," *Journal of the American Chemical Society*, vol. 127, pp. 11636–11645, Aug. 2005.

[201] Palestino, G., Legros, R., Agarwal, V., Pérez, E., and Gergely, C., "Functionalization of nanostructured porous silicon microcavities for glucose oxidase detection," *Sensors and Actuators B: Chemical*, vol. 135, pp. 27–34, Dec. 2008.

[202] Pancheri, L., Oton, C. J., Gaburro, Z., Soncini, G., and Pavesi, L., "Very sensitive porous silicon NO2 sensor," *Sensors and Actuators B: Chemical*, vol. 89, pp. 237–239, Apr. 2003.

[203] Park, H. G., Malen, J. A., Piggott, W., Morse, J., Greif, R., Grigoropoulos, C., Havstad, M., and Upadhye, R., "Methanol steam reformer on a silicon wafer," *Journal of Microelectromechanical Systems*, vol. 15, pp. 976–985, Aug. 2006.

[204] Parkhutik, V., "Porous silicon—mechanisms of growth and applications," *Solid-State Electronics*, vol. 43, pp. 1121–1141, June 1999.

[205] Parr, R. G., Donnelly, R. A., Levy, M., and Palke, W. E., "Electronegativity: The density functional viewpoint," *The Journal of Chemical Physics*, vol. 68, pp. 3801–3807, Apr. 1978.

[206] Pattekar, A. and Kothare, M., "A microreactor for hydrogen production in micro fuel cell applications," *Journal of Microelectromechanical Systems*, vol. 13, pp. 7–18, Feb. 2004.

[207] Pearson, R. G., "Hard and soft acids and bases—the evolution of a chemical concept," *Coordination Chemistry Reviews*, vol. 100, pp. 403–425, Apr. 1990.

[208] Pearson, R. G., *Chemical Hardness*. Weinheim: Wiley-VCH Verlag GmbH, 1997.

[209] Peng, C., Luttmann-Gibson, H., Zanobetti, A., Cohen, A., Souza, C. D., Coull, B. A., Horton, E. S., Schwartz, J., Koutrakis, P., and Gold, D. R., "Air pollution influences on exhaled nitric oxide among people with type II diabetes," *Air Quality, Atmosphere & Health*, pp. 1–9, Mar. 2015.

[210] Pichonat, T. and Gauthier-Manuel, B., "A new process for the manufacturing of reproducible mesoporous silicon membranes," *Journal of Membrane Science*, vol. 280, pp. 494–500, Sept. 2006.

[211] Pickering, C., Beale, M. I. J., Robbins, D. J., Pearson, P. J., and Greef, R., "Optical studies of the structure of porous silicon films formed in p-type degenerate and non-degenerate silicon," *Journal of Physics C: Solid State Physics*, vol. 17, p. 6535, Dec. 1984.

[212] Polisski, S., Goller, B., Lapkin, A., Fairclough, S., and Kovalev, D., "Synthesis and catalytic activity of hybrid metal/silicon nanocomposites," *physica status solidi (RRL) – Rapid Research Letters*, vol. 2, pp. 132–134, June 2008.

[213] Polisski, S., Goller, B., Wilson, K., Kovalev, D., Zaikowskii, V., and Lapkin, A., "In situ synthesis and catalytic activity in CO oxidation of metal nanoparticles supported on porous nanocrystalline silicon," *Journal of Catalysis*, vol. 271, pp. 59–66, Apr. 2010.

[214] Presting, H., Konle, J., Starkov, V., Vyatkin, A., and König, U., "Porous silicon for micro-sized fuel cell reformer units," *Materials Science and Engineering: B*, vol. 108, pp. 162–165, Apr. 2004.

[215] Prokes, S. M. and Glembocki, O. J., "Light emission properties of porous silicon," *Materials Chemistry and Physics*, vol. 35, pp. 1–10, Aug. 1993.

[216] Propst, E. and Kohl, P. A., "The Photoelectrochemical Oxidation of nSi in Anhydrous HF Acetonitrile," *Journal of The Electrochemical Society*, vol. 140, pp. L78–L80, May 1993.

[217] Qu, Y., Zhong, X., Li, Y., Liao, L., Huang, Y., and Duan, X., "Photocatalytic properties of porous silicon nanowires," *Journal of Materials Chemistry*, vol. 20, pp. 3590–3594, Apr. 2010.

[218] Rebrov, E. V., Seijger, G. B. F., Calis, H. P. A., de Croon, M. H. J. M., van den Bleek, C. M., and Schouten, J. C., "The preparation of highly ordered single layer ZSM-5 coating on prefabricated stainless steel microchannels," *Applied Catalysis A: General*, vol. 206, pp. 125–143, Jan. 2001.

[219] Ressine, A., Ekström, S., Marko-Varga, G., and Laurell, T., "Macro-/Nanoporous Silicon as a Support for High-Performance Protein Microarrays," *Analytical Chemistry*, vol. 75, pp. 6968–6974, Dec. 2003.

[220] Rieger, M. M. and Kohl, P. A., "Mechanism of (111) Silicon Etching in HF Acetonitrile," *Journal of The Electrochemical Society*, vol. 142, pp. 1490–1495, May 1995.

[221] Righettoni, M., Tricoli, A., and Pratsinis, S. E., "Si:WO3 Sensors for Highly Selective Detection of Acetone for Easy Diagnosis of Diabetes by Breath Analysis," *Analytical Chemistry*, vol. 82, pp. 3581–3587, May 2010.

[222] Roch, N., Florens, S., Bouchiat, V., Wernsdorfer, W., and Balestro, F., "Quantum phase transition in a single-molecule quantum dot," *Nature*, vol. 453, pp. 633–637, May 2008.

[223] Rodriguez, J. A., Jirsak, T., Dvorak, J., Sambasivan, S., and Fischer, D., "Reaction of NO2 with Zn and ZnO: Photoemission, XANES, and Density Functional Studies on the Formation of NO3," *The Journal of Physical Chemistry B*, vol. 104, pp. 319–328, Jan. 2000.

[224] Rönnebeck, S., Ottow, S., Carstensen, J., and Föll, H., "Crystal Orientation Dependence of Macropore Formation in n-Si With Backside-Illumination in HF-Electrolyte," *Journal of Porous Materials*, vol. 7, pp. 353–356, Jan. 2000.

[225] Roumanie, M., Delattre, C., Mittler, F., Marchand, G., Meille, V., de Bellefon, C., Pijolat, C., Tournier, G., and Pouteau, P., "Enhancing surface activity in silicon microreactors: Use of black silicon and alumina as catalyst supports for chemical and biological applications," *Chemical Engineering Journal*, vol. 135, Supplement 1, pp. S317–S326, Jan. 2008.

[226] Rudden, M. N. and Wilson, J., *Elements of Solid State Physics*. Chichester: Wiley-VCH Verlag GmbH & Co. KGaA, 2nd ed., 1993.

[227] Rumchev, K., Spickett, J., Bulsara, M., Phillips, M., and Stick, S., "Association of domestic exposure to volatile organic compounds with asthma in young children," *Thorax*, vol. 59, pp. 746–751, Sept. 2004.

[228] Sahm, T., Mädler, L., Gurlo, A., Barsan, N., Pratsinis, S. E., and Weimar, U., "Flame spray synthesis of tin dioxide nanoparticles for gas sensing," *Sensors and Actuators B: Chemical*, vol. 98, pp. 148–153, Mar. 2004.

[229] Sailor, M. J., *Porous Silicon in Practice: Preparation, Characterization and Applications*. John Wiley & Sons, Jan. 2012.

[230] Sanderson, W. T., Weber, A., and Echt, A., "Case Reports: Epidemic Eye and Upper Respiratory Irritation in Poultry Processing Plants," *Applied Occupational and Environmental Hygiene*, vol. 10, pp. 43–49, Jan. 1995.

[231] Schechter, I., Ben-Chorin, M., and Kux, A., "Gas Sensing Properties of Porous Silicon," *Analytical Chemistry*, vol. 67, pp. 3727–3732, Oct. 1995.

[232] Schmeisser, D., Böhme, O., Yfantis, A., Heller, T., Batchelor, D. R., Lundstrom, I., and Spetz, A. L., "Dipole Moment of Nanoparticles at Interfaces," *Physical Review Letters*, vol. 83, pp. 380–383, July 1999.

[233] Seals, L., Gole, J. L., Tse, L. A., and Hesketh, P. J., "Rapid, reversible, sensitive porous silicon gas sensor," *Journal of Applied Physics*, vol. 91, pp. 2519–2523, Feb. 2002.

[234] Selvam, P., Viswanathan, B., and Srinivasan, V., "XPS studies of the surface properties of CaNi5," *Journal of Electron Spectroscopy and Related Phenomena*, vol. 49, no. 2, pp. 203–211, 1989.

[235] Smith, K. R., Samet, J. M., Romieu, I., and Bruce, N., "Indoor air pollution in developing countries and acute lower respiratory infections in children," *Thorax*, vol. 55, pp. 518–532, June 2000.

[236] Smith, R. L. and Collins, S. D., "Porous silicon formation mechanisms," *Journal of Applied Physics*, vol. 71, pp. R1–R22, Apr. 1992.

[237] Sosulnikov, M. I. and Teterin, Y. A., "X-ray photoelectron studies of Ca, Sr and Ba and their oxides and carbonates," *Journal of Electron Spectroscopy and Related Phenomena*, vol. 59, pp. 111–126, July 1992.

[238] Splinter, A., Stürmann, J., Bartels, O., and Benecke, W., "Micro membrane reactor: a flow-through membrane for gas pre-combustion," *Sensors and Actuators B: Chemical*, vol. 83, pp. 169–174, Mar. 2002.

[239] Steinemann, A. C., MacGregor, I. C., Gordon, S. M., Gallagher, L. G., Davis, A. L., Ribeiro, D. S., and Wallace, L. A., "Fragranced consumer products: Chemicals emitted, ingredients unlisted," *Environmental Impact Assessment Review*, vol. 31, pp. 328–333, Apr. 2011.

[240] Steiner, P. and Lang, W., "Micromachining applications of porous silicon," *Thin Solid Films*, vol. 255, pp. 52–58, Jan. 1995.

[241] Stievenard, D. and Deresmes, D., "Are electrical properties of an aluminum–porous silicon junction governed by dangling bonds?," *Applied Physics Letters*, vol. 67, pp. 1570–1572, Sept. 1995.

[242] Stubenrauch, M., Fischer, M., Kremin, C., Stoebenau, S., Albrecht, A., and Nagel, O., "Black silicon—new functionalities in microsystems," *Journal of Micromechanics and Microengineering*, vol. 16, p. S82, June 2006.

[243] Su, F., Lu, C., Kuo, S.-C., and Zeng, W., "Adsorption of CO2 on Amine-Functionalized Y-Type Zeolites," *Energy & Fuels*, vol. 24, pp. 1441–1448, Feb. 2010.

[244] Su, J., Yu, H., Quan, X., Chen, S., and Wang, H., "Hierarchically porous silicon with significantly improved photocatalytic oxidation capability for phenol degradation," *Applied Catalysis B: Environmental*, vol. 138–139, pp. 427–433, July 2013.

[245] Sun, Y.-F., Liu, S.-B., Meng, F.-L., Liu, J.-Y., Jin, Z., Kong, L.-T., and Liu, J.-H., "Metal Oxide Nanostructures and Their Gas Sensing Properties: A Review," *Sensors*, vol. 12, pp. 2610–2631, Feb. 2012.

[246] Susarla, S., Medina, V. F., and McCutcheon, S. C., "Phytoremediation: An ecological solution to organic chemical contamination," *Ecological Engineering*, vol. 18, pp. 647–658, June 2002.

[247] Tank, C. M., Sakhare, Y. S., Kanhe, N. S., Nawale, A. B., Das, A. K., Bhoraskar, S. V., and Mathe, V. L., "Electric field enhanced photocatalytic properties of TiO2 nanoparticles immobilized in porous silicon template," *Solid State Sciences*, vol. 13, pp. 1500–1504, Aug. 2011.

[248] Tao, Y. and Esashi, M., "Local formation of macroporous silicon through a mask," *Journal of Micromechanics and Microengineering*, vol. 14, p. 1411, Oct. 2004.

[249] Tatibouët, J. M., "Methanol oxidation as a catalytic surface probe," *Applied Catalysis A: General*, vol. 148, pp. 213–252, Jan. 1997.

[250] Tebizi-Tighilt, F.-Z., Zane, F., Belhaneche-Bensemra, N., Belhousse, S., Sam, S., and Gabouze, N.-E., "Electrochemical gas sensors based on polypyrrole-porous silicon," *Applied Surface Science*, vol. 269, pp. 180–183, Mar. 2013.

[251] Thomas, N., Davis, J., Keen, J., Castledine, J., Brumhead, D., Goulding, M., Alderman, J., Farr, J., Earwaker, L., L'Ecuyer, J., Stirland, I., and Cole, J., "High-performance thin-film silicon-on-insulator CMOS transistors in porous anodized silicon," *IEEE Electron Device Letters*, vol. 10, pp. 129–131, Mar. 1989.

[252] Tiggelaar, R. M. and Gardeniers, J. G. E. h., "Silicon and Glass Microreactors," in *Micro Process Engineering* (Hessel, V., Renken, A., Schouten, J. C., and Yoshida, J.-I., eds.), pp. 1–24, Wiley-VCH Verlag GmbH & Co. KGaA, 2009.

[253] Tsao, S., "Porous silicon techniques for SOI structures," *IEEE Circuits and Devices Magazine*, vol. 3, pp. 3–7, Nov. 1987.

[254] Tune, T. C., Baker, C., Hardy, N., Lin, A., Widing, T. J., and Gole, J. L., "Formation of nanostructured Group IIA metal activated sensors: The transformation of Group IIA metal compound sites," *Applied Surface Science*, vol. 337, pp. 216–223, May 2015.

[255] Turner, D. R., "Electropolishing Silicon in Hydrofluoric Acid Solutions," *Journal of The Electrochemical Society*, vol. 105, pp. 402–408, July 1958.

[256] Turner, M. J. and Rhoderick, E. H., "Metal-silicon Schottky barriers," *Solid-State Electronics*, vol. 11, pp. 291–300, Mar. 1968.

[257] Uhde, E. and Salthammer, T., "Impact of reaction products from building materials and furnishings on indoor air quality—A review of recent advances

in indoor chemistry," *Atmospheric Environment*, vol. 41, pp. 3111–3128, May 2007.

[258] Uhlir, A., "Electrolytic Shaping of Germanium and Silicon," *Bell System Technical Journal*, vol. 35, pp. 333–347, Mar. 1956.

[259] Uhlir, A. and Uhlir, I. W., "Historical perspective on the discovery of porous silicon," *physica status solidi (c)*, vol. 2, pp. 3185–3187, June 2005.

[260] Ulupi, N., Salundik, Margisuci, D., Hidayatun, R., and Sugiarto, B., "Growth Performance and Production of Ammonia and Hydrogen Sulfide in Excreta of Broiler Chickens Fed Basil (Ocimum basilicum) Flour in Feed," *International Journal of Poultry Science*, vol. 14, no. 2, pp. 112–116, 2015.

[261] Unagami, T. and Kato, K., "Study of the Injection Type IPOS Scheme," *Japanese Journal of Applied Physics*, vol. 16, p. 1635, Sept. 1977.

[262] van der Pauw, L. J., "A method of measuring specific resistivity and Hall effect of discs of arbitrary shape," *Philips Research Reports*, vol. 13, no. 1, pp. 1–9, 1958.

[263] van der Pauw, L. J., "A Method of Measuring the Resistivity and Hall Coefficient on Lamellae of Arbitrary Shape," *Philips Technical Review*, vol. 20, pp. 220–224, 1958.

[264] Vasiliu, M., Feller, D., Gole, J. L., and Dixon, D. A., "Structures and Heats of Formation of Simple Alkaline Earth Metal Compounds: Fluorides, Chlorides, Oxides, and Hydroxides for Be, Mg, and Ca," *The Journal of Physical Chemistry A*, vol. 114, no. 34, pp. 9349–9358, 2010.

[265] Verdaguer, M. and Matsushita, M., "Reports on experimental demonstrations: Or molecular magnetism is attractive!," *Polyhedron*, vol. 24, p. 2900, Nov. 2005.

[266] Verdaguer, M. and Villain, F., "Comment le magnétisme vient aux molécules (How molecules become magnetic)," in *Experimental Lecture Series*, (Paris), ESPCI ParisTech, Feb. 2007.

[267] Vial, J. C., Bsiesy, A., Gaspard, F., Hérino, R., Ligeon, M., Muller, F., Romestain, R., and Macfarlane, R. M., "Mechanisms of visible-light emission from electro-oxidized porous silicon," *Physical Review B*, vol. 45, pp. 14171–14176, June 1992.

[268] Wagner, C., Riggs, W., Davis, L., Moulder, J., and Muilenberg, G., *Handbook of X-Ray Photoelectron Spectroscopy*. Eden Prairie: Perin-Elmer, Physical Electronics Division, 1979.

[269] Wang, C., Yin, L., Zhang, L., Xiang, D., and Gao, R., "Metal Oxide Gas Sensors: Sensitivity and Influencing Factors," *Sensors*, vol. 10, pp. 2088–2106, Mar. 2010.

[270] Wang, X. and Wachs, I. E., "Designing the activity/selectivity of surface acidic, basic and redox active sites in the supported K2o–V2o5/Al2o3 catalytic system," *Catalysis Today*, vol. 96, pp. 211–222, Oct. 2004.

[271] Watanabe, Y., Arita, Y., Yokoyama, T., and Igarashi, Y., "Formation and Properties of Porous Silicon and Its Application," *Journal of The Electrochemical Society*, vol. 122, pp. 1351–1355, Oct. 1975.

[272] Watanabe, Y. and Sakai, T., "Application of a thick anode film to semiconductor devices," *Reviews of the Electrical Communications Laboratories*, vol. 19, no. 7-8, p. 899, 1971.

[273] Webb, P. A. and Orr, C., *Analytical methods in fine particle technology*. Norcross: Micromeritics Instrument Corporation, 1997.

[274] Weber, T. W. and Chakravorti, R. K., "Pore and solid diffusion models for fixed-bed adsorbers," *AIChE Journal*, vol. 20, pp. 228–238, Mar. 1974.

[275] Weiss, S. M. and Fauchet, P. M., "Electrically tunable porous silicon active mirrors," *physica status solidi (a)*, vol. 197, pp. 556–560, May 2003.

[276] Weitkamp, J. and Puppe, L., *Catalysis and Zeolites: Fundamentals and Applications*. Berlin: Springer Science & Business Media, June 1999.

[277] Wieland, W. S., Davis, R. J., and Garces, J. M., "Side-Chain Alkylation of Toluene with Methanol over Alkali-Exchanged Zeolites X, Y, L, and ," *Journal of Catalysis*, vol. 173, pp. 490–500, Jan. 1998.

[278] Wu, Y., Hu, M., Qin, Y., Wei, X., Ma, S., and Yan, D., "Enhanced response characteristics of p-porous silicon (substrate)/p-TeO2 (nanowires) sensor for NO2 detection," *Sensors and Actuators B: Chemical*, vol. 195, pp. 181–188, May 2014.

[279] Yan, D., Hu, M., Li, S., Liang, J., Wu, Y., and Ma, S., "Electrochemical deposition of ZnO nanostructures onto porous silicon and their enhanced gas sensing to NO2 at room temperature," *Electrochimica Acta*, vol. 115, pp. 297–305, Jan. 2014.

[280] Yang, W. and Parr, R. G., "Hardness, softness, and the fukui function in the electronic theory of metals and catalysis," *Proceedings of the National Academy of Sciences*, vol. 82, pp. 6723–6726, Oct. 1985.

[281] Yang, W., Parr, R. G., and Pucci, R., "Electron density, Kohn–Sham frontier orbitals, and Fukui functions," *The Journal of Chemical Physics*, vol. 81, pp. 2862–2863, Sept. 1984.

[282] Ye, S.-Y., Tanaka, S., Esashi, M., Hamakawa, S., Hanaoka, T., and Mizukami, F., "Thin palladium membrane microreactors with oxidized porous silicon support and their application," *Journal of Micromechanics and Microengineering*, vol. 15, p. 2011, Nov. 2005.

[283] Yu, J., Wang, J., Zhang, J., He, Z., Liu, Z., and Ai, X., "Characterization and photoactivity of TiO2 sols prepared with triethylamine," *Materials Letters*, vol. 61, pp. 4984–4988, Nov. 2007.

[284] Yu, M.-F., Atashbar, M., and Chen, X., "Mechanical and electrical characterization of beta;-Ga2o3 nanostructures for sensing applications," *IEEE Sensors Journal*, vol. 5, pp. 20–25, Feb. 2005.

[285] Zaleski, R. T., Qian, H., Zelenka, M. P., George-Ares, A., and Money, C., "European solvent industry group generic exposure scenario risk and exposure tool," *Journal of Exposure Science and Environmental Epidemiology*, vol. 24, pp. 27–35, Jan. 2014.

[286] Zeidler, M. R., Kleerup, E. C., and Tashkin, D. P., "Exhaled nitric oxide in the assessment of asthma," *Current Opinion in Pulmonary Medicine*, vol. 10, pp. 31–36, Jan. 2004.

[287] Zhang, X. G., "Morphology and Formation Mechanisms of Porous Silicon," *Journal of The Electrochemical Society*, vol. 151, pp. C69–C80, Jan. 2004.

[288] Zhu, X.-Y., Mulder, J. A., and Bergerson, W. F., "Chemical Vapor Deposition of Organic Monolayers on Si(100) via SiN Linkages," *Langmuir*, vol. 15, pp. 8147–8154, Nov. 1999.

[289] Zuyuan, W., Fuxiang, Z., Yali, Y., Jie, C., Qing, S., and Naijia, G., "One-Pot Synthesis of Visible-Light-Responsive TiO2 in the Presence of Various Amines," *Chinese Journal of Catalysis*, vol. 27, pp. 1091–1095, Dec. 2006.